Aggregation behavior of Pluronic P123 in bulk solution and under confinement at elevated temperatures near its cloud point

Dissertation zur Erlangung des
naturwissenschaftlichen Doktorgrades
der Julius-Maximilians-Universität Würzburg

vorgelegt von

Benedikt Sochor

aus Magdeburg

Würzburg, Juni 2021

Eingereicht am: 21.06.2021
bei der Fakultät für Physik und Astronomie

1. Gutachter: Prof. Dr. Randolf Hanke
2. Gutachter: Prof. Dr. Robert Luxenhofer

der Dissertation

Vorsitzender: Prof. Dr. Vladimir Dyakonov

1. Prüfer: Prof. Dr. Randolf Hanke
2. Prüfer: Prof. Dr. Robert Luxenhofer
3. Prüfer: Prof. Dr. Thorsten Ohl

im Promotionskolloquium

Tag des Promotionskolloquium: 15.09.2021

Preface

My words may be poor
but they will have to do.

(Hans Abrahamsen,
"let me tell you")

This thesis is part of the PhD-program at the Physics department of the University of Würzburg. It describes experiments, which were performed from August 2017 until February 2021 including three beamtimes at the Joint Institute for nuclear research (JINR, Dubna, Russia) in March 2019, the Advanced Photon Source (APS, Chicago, USA) in April 2019 and the Institute Laue-Langevin (ILL, Grenoble, France) in February 2020 as well as a one-month research stay funded by the DAAD at the Institute of Solid-State Chemistry (UB RAS, Yekaterinburg, Russia) in October 2019.

Besides the presented results, several other scientific and collaborative projects lead to a total of 6 peer-reviewed publications in journals and conference proceedings:

Proceedings:

- Schummer, B., **Sochor, B.**, Popov, I.D. and Gerth, S. Stabilization of Cadmium Sulfide Nanoparticles using Block-Copolymers. *Proceedings 10th International Conference on Nanomaterials - Research & Application* (2019), 590-596

- Kuznetsova Y.V., Popov I.D., **Sochor B.**, Schummer, B., Dorosheva, I.B. and Rempel, S.V. The effect of matrix on CdS nanoparticles photoluminescence. *AIP Conference Proceedings 2174* (2019), 020130, DOI: 10.1063/1.5134281

Journal articles:

- Gangloff, N., Höferth, M., Stepanenko, V., **Sochor, B.**, Schummer, B., Nickel, J., Walles, H., Hanke, R., Würthner, F., Zuckermann, R.N. and Luxenhofer, R. Linking two worlds in polymer chemistry: The influence of block uniformity and dispersity in amphiphilic block copolypeptoids on their self-assembly. *Biopolymers* (2019), 110:e23259, DOI: 10.1002/bip.23259

- Kuznetsova, Y.V., Letofsky-Papst, I., **Sochor, B.**, Schummer, B., Sergeev, A.A., Hofer, F. and Rempel, A.A. Greatly enhanced luminescence efficiency of CdS nanoparticles in aqueous solution. *Colloids and Surfaces A: Physicochemical and Engineering Aspects 581* (2019), 123814, DOI: 10.1016/j.colsurfa.2019.123814

- Popov I.D., **Sochor B.**, Schummer B., Kuznetsova Y.V., Rempel, S.V., Gerth, S. and Rempel, A.A. Baking nanoparticles: Linking the synthesis parameters of CdS nanoparticles in a glass matrix with their size and size distribution. *Journal of Non-Crystalline Solids 529* (2020), 119781, DOI: 10.1016/j.jnoncrysol.2019.119781

- **Sochor, B.**, Düdükcü, D., Lübtow, M.M., Schummer, B., Jaksch, S. and Luxenhofer, R. Probing the Complex Loading-Dependent Structural Changes in Ultrahigh Drug-Loaded Polymer Micelles by Small-Angle Neutron Scattering. *Langmuir 36* (2020), 13, 3494-3503, DOI: 10.1021/acs.langmuir.9b03460

During the 3.5 years, preliminary results were presented in two oral and three poster contributions at international schools, meetings and conferences:

Talks:

- **Sochor, B.** Determination of micellar aggregation number using SAXS-measurements with absoulte calibrated intensites. *7th German-Russian Traveling Seminar* (2017), Ural Federal University, Yekaterinburg, Russia

- **Sochor, B.** Determination of micellar aggregation number using SAXS-measurements with absoulte calibrated intensites and densometry. *10th International Conference on Nanomaterials - Research & Application* (2018), Brno, Czech Repubic

Posters:

- **Sochor, B.**, Schummer, B., Düdükcü, D., Gerth, S and Hanke, R. Determination of micellar aggregation number using SAXS-measurements with absoulte calibrated intensites and densometry. *Jülich Soft Matter Days* (2018), Forschungszentrum Jülich, Germany

- **Sochor, B.**, Schummer, B., Gerth, S. and Hanke, R. Tri-block copolymer Pluronic P123: form phase diagram, aggregation number and hysteresis in micellar shape. *HERCULES European School* (2019), Grenoble, France

- **Sochor, B.**, Düdükcü, D., Lübtow, M.M., Schummer, B., Jaksch, S. and Luxenhofer, R. Probing the Complex Loading-Dependent Structural Changes in Ultrahigh Drug-Loaded Polymer Micelles by Small-Angle Neutron Scattering. *MLZ User-Meeting und Deutsche Neutronenstreutagung* (2020), online

Following the ILL data policy, the reflectometry data of the beamtime in February 2020 is publicly accessible (DOI: 10.5291/ILL-DATA.9-10-1597). A detailed description with a copy of the logbook and all data, raw and processed, of the remaining experiments in this thesis can be obtained from the author upon reasonable request.

Abstract

This thesis aims to investigate the form-phase diagram of aqueous solutions of the triblock copolymer Pluronic P123 focusing on its high-temperature phases. P123 is based on polyethylene as well as polypropylene oxide blocks and shows a variety of different temperature-dependent micelle morphologies or even lyotropic liquid crystal phases in aqueous solutions. Besides the already well-studied spherical aggregates at intermediate temperatures, the size and internal structure of both worm-like and lamellar micelles, which appear near the cloud point, is determined using light, neutron and X-ray scattering. By combining the results of time-resolved dynamic light as well as small-angle neutron and X-ray scattering experiments, the underlying structural changes and kinetics of the sphere-to-worm transition were studied supporting the random fusion process, which is proposed in literature. For temperatures near the cloud point, it was observed that aqueous P123 solutions below the critical crystallization concentration gelate after several hours, which is linked to the presence and structure of polymeric surface layers on the sample container walls as shown by neutron reflectometry measurements. Using a hierarchical model for the lamellar micelles including their periodicity as well as domain and overall size, it is possible to unify the existing results in literature and propose a direct connection between the near-surface and bulk properties of P123 solutions at temperatures near the cloud point.

Kurzzusammenfassung

Ziel dieser Dissertation ist die Untersuchung des Form-Phasendiagrams des Dreiblock-Copolymers Pluronic P123 mit dem besonderen Fokus auf dessen Phasenverhalten bei hohen Temperaturen. P123 besteht aus Polyethylen- und Polypropylenoxid-Blöcken und zeigt in wässriger Lösung vielfätige, temperaturabhängige Mizellformen oder sogar Flüssigkristallphasen. Neben den bereits intensiv untersuchten sphärischen Aggregaten bei mittleren Temperaturen, werden die Größen und inneren Strukturen der wurmartigen und lamellearen Aggregate mittels Licht-, Neutronen- und Röntgenstreumethoden untersucht, welche nahe des Trübungspunktes der Lösungen auftreten. Durch die Kombination von zeitaufgelösten dynamischen Licht- und Kleinwinkelstreuung-Experimenten wurden die strukturellen Änderungen und kinetischen Prozesse während des Kugel-Wurm-Übergangs untersucht, welche den bereits in der Literatur vorgeschlagenen zufälligen Fusionsprozess weiter bestätigen. Es wurde beobachtet, dass wässrige P123-Lösungen unterhalb der kritischen Kristallisationskonzentration nach mehreren Stunden gelieren, was durch Neutronenreflektometrie mit dem Auftreten und der Struktur von oberflächennahen Monolagen auf den Messzellwänden in Verbindung gebracht wurde. Wenn ein hierarchisches Model für die lamellaren Mizellen verwendet wird, das deren Periodizität, Domänen- und Gesamtgröße berücksichtigt, ist es außerdem möglich, die bisherigen Ergebnisse in der Literatur zu vereinigen und eine direkte Verbindung zwischen dem Aggregationsverhalten von P123 auf Oberflächen und in Lösung bei Temperaturen nahe des Trübungspunktes zu ziehen.

Acknowledgments

A PhD-project always seems like an one-man-show or solo project, since only one person is rewarded with an academic title in the end. But this is of course never true! Although, there are tendencies to create “lone-wolf” scientists, I want to make sure to acknowledge the contribution of everyone involved in this thesis and thank them for their help, effort and time. Without any of them, this 3.5 year long journey would have never come to a successful end!

First, I want to thank my supervisor Professor Randolf Hanke. He brought me in contact with X-ray physics as a second-year undergraduate student and I heard every lecture of him on this topic during my studies. After accepting me as a Master-student in 2016, he gave me the opportunity to continue as one of his PhD-students. Although his time schedule would need a day with more than 24 hours, he followed my progress during this project with great enthusiasm and support, giving me complete freedom and invaluable opportunities to grow as an independent scientist.

I also want to thank Professor Robert Luxenhofer, who not only agreed to review my thesis and join the examining board but helped and mentored me during my whole PhD time. After meeting for the first time in beginning of my project, he introduced me to the field of drug delivery and polymer science. As a methodist, he helped me to find the people, who could ask the right questions to further improve myself. Working with him and the PhD students in his group has shown me how fruitful, exciting and important interdisciplinary work is! It helped to push myself and critically rethink my methods, work and results, which ultimately improved this thesis and myself as a scientist. I will forever be thankful for acknowledging my work on these collaborative projects through authorship on several publications and joint proposals at the FRM-II in Munich.

The next person I want to thank is Dr. Simon Zabler. Whenever Prof. Hanke was not in Würzburg, he would be around to help with whatever needs to be done. Despite managing a university and Fraunhofer group, no stress level could be high enough to prevent him from smiling and listening to you when there was a problem. I want to thank him for all the late-evening and late-night discussions, interest in the progress of my project and willingness to find money for all the trips to different schools, beamtimes and conferences. Due to him, I participated in the HERCULES school in Grenoble, which has changed my life forever.

Another extremely important person for the success of this project, and a very influential person for me, is Dr. Stefan Gerth. Having him as my advisor since the beginning of my master project was one of the greatest gifts and honors, I could have ever asked for. My project is based on his preliminary findings and results regarding Pluronic P123. Although he was not employed at the University Würzburg, he agreed to be my advisor. His encyclopedic knowl-

edge about almost any aspect of modern and X-ray physics, instrumentation and science in general and his willingness to spend large proportions of his spare time to discuss these topics with me always helped tremendously. He agreed to revise every proposal, paper or document and even my thesis. I would not have gotten my PhD without him. There is no doubt about that. I will forever be grateful of that!

I also have to thank Dr. Bernhard Schummer. He was probably the person, who I spend the most time in the last 4 years. First, he was my supervisor during my master and PhD project, but he also became my mentor and friend. I owe him for everything that I achieved, because none would have been possible without him. He had to endure all different moods, the good and especially the bad, which will naturally occur in the course of a PhD project. But he never shied away, always stayed positive and helped me to get over any obstacle. He traveled the world with me and I never had to ask for him to help me. He is a true hero and friend.

Most results of this thesis are based on experimental data, which was gathered around the world at Frank Laboratory for Neutron Physics (FLNP) in Dubna (Russia), the Argonne National Laboratory (ANL) in Lemont (Illinois, US) and the Institute Laue-Langevin (ILL) in Grenoble (France). Here I want to, first, thank the organizing, administrative and scientific committees and, second, the beamline and laboratory staff for considering my proposals, granting beamtime and the incredible effort and help during the experiments, which would have never been successful without these people.

During two stays in March of 2018 and 2019, both Dr. Aleksander Kuklin and Dr. Oleksandr Ivankov welcomed me to FLNP in Dubna and helped me during my first ever neutron experiments. On a historic site like Dubna with its numerous Nobel laureates and unique neutron reactor IBR-2, they gave me an invaluable introduction to small-angle neutron scattering (SANS), guidance on how to perform a successful SANS-experiment and the opportunity to discuss my previous data and results with two renowned experts in the field of soft matter science and scattering techniques. I want to thank both of them for their openness and willingness to share their expertise with me.

The next batch of data was acquired during remote beamtimes in October 2018 and April 2019 at the Advanced Photon Source of the ANL. Although we never met in person, I want to emphatically thank Dr. Soenke Seiffert for performing the measurements, showing me incredible tricks in scattering data reduction and giving me the opportunity to use synchrotron radiation for my experiments in the first place. Another person at the ANL, who was integral to not only my thesis but countless PhD projects before, is Dr. Jan Ilavsky. He is the author of the NIKA, IRENA and INDRA tool-suite, which is written in IgorPro. Despite more modern and recent scattering data analysis software, IRENA and especially NIKA are incredibly well-written and served as a foundation for my own data reduction and fitting scripts. Together with Jans almost constant availability and encouragement to write my own code, this Phd project would not have been successful without him.

I also want to thank Dr. Philipp Gutfreund, who is the beamline responsible of FIGARO at the ILL. During our joint beamtime in February 2020, his dedication, effort and experience with Pluronic just made the reflectometry experiment working. Due to his extreme openness,

kindness and humor as well as his passion for science, engineering and neutrons, I fell in love with reflectometry and surface research in general. I look forward to be a more frequent guest at his beamline with new and interesting projects. Here , I also want to thank Prof. Dr. Tobias Unruh and Dr. Matthias Weißer from the Institute for Crystallography and Structural Physics at the University Erlangen-Nürnberg for their generous loan of several silicon blocks, which were used during the experiments at FIGARO.

In the course of my time as a PhD student, I visited Russia three times. Every time I met with Ivan Popov, Dr. Yulia Kuznetsova and Prof. Andrey Rempel in Yekaterinburg. The first time was during the German-Russian traveling Seminar in 2017. Since then a successful and fruitful collaboration was established, which culminated in my one-month stay at the Institute of Solid State Chemistry in Yekaterinburg in October 2019. In this regard, I would also like to gratefully acknowledge funding by the DAAD. During that time, I got the invaluable chance to gain experience in nanoparticle fabrication and characterization and the opportunity to do extended light scattering experiments with my Pluronic samples. I want to thank all three for their time, hospitality and passion to keep the collaboration going.

From the work group of Prof. Luxenhofer, I would like to thank Dr. Michael Lübtow and Lukas Hahn. In the same context, I want to thank Dr. Sebastian Jaksch from Froschungszentrum Jülich at the FRM-II neutron reactor in Garching. Together, we worked on projects related to drug delivery adn biofabrication , analyzed neutron scattering data and went on beamtimes in Munich. I am very grateful for the opportunity to work with all of them and hope to continue our collaborations.

In general, I would like to thank the whole staff and my collegues at the chair of X-Ray Microscopy. With the constant cheerful and encouraging atmosphere, working there was a joy and I do not want to miss a second of it. I would also like to thank the undergraduate and graduate students Thasihan Thavarasavel, Holger Diehm and Özgür Düdükcü, who I helped supervising. Although none of them contributed to this thesis, I greatly appreciate their work and hope that they will continue to succeed in their respective careers.

But of course all the mentioned people I would have never met and all the exciting experiences I would have never been able to make without the constant help and support of my family.

Fist, I want to thank my grandparents, who supported me during my whole studies. Although my grandfather passed away before I graduated, I know that he and my grandmother will be proud of me.

My dearest and indescribable thanks go to my parents and brother. They were always there for me when I needed them and I know that they will always be there. They guided me through the hard times with their support and celebrated the ups and highs with me during all my life. I will always love them and hope to continue making them proud of me.

At last, I want to thank my girlfriend and partner Emma, who I met during the Hercules School in Spring 2019. Meeting her has changed my life forever. She helped me a lot during the final stages of my PhD thesis with countless hours of proof reading, corrections and discussions. She was always there for me and I will never forget that. Jeg elsker dig, Emma!

Contents

Introduction

One of the most fundamental criteria for grouping matter is its aggregation state: solid, liquid, gaseous or plasma [1]. Most elements and materials on earth can be described by only the first three states, but plasmas play an important role in the description of the universes dynamics [2, 3] and can be occasionally seen in nature as well, e.g. in form of lightnings. The transitions between the different states are called phase transitions, which are canonically measured for different temperatures and pressures. Each transition is a result of the internal energy minimization of the system and there are several more phase transition for more complex materials, e.g. solid-state phase transitions in semicondutors induced by doping [4] or under extreme conditions [5]. A similar rich phase behavior can be observed for a variety of complex fluids.

In the last decades, colloidal, polymer and protein solutions or microemulsions garnered significant scientific traction due to their variety and tunability of properties and applications. These soft condensed matter systems range from metallic nanoparticle dispersions, which have size-dependent luminescence properties [6], over organic colorant, which form supramolecular aggreagtes in aqueous showing increased fluoresence [7, 8] and even electric conductivity [9], to protein solutions, where their structure can be altered [10] or completely re-built for applications as biological sensors [11, 12, 13]. Despite proteins, soft matter systems based on solutions with nanodiamonds [14, 15, 16] or different polymer blends, which show tensid-like self-assembly, can be used as pharmaceutical formulations in nanomedicine [17, 18, 19, 20] or ink material in biofabrication [21, 22, 23, 24, 25]. Here, also the interactions between the potential carrierer system and cellular membranes are a pressing topic, which need to be carefully studied and tested [26, 27, 28, 18, 29, 30, 31].

The pharmaceutical applications are based on the ability of these polymers to "encapsulate" the drug or nanoparticle by forming so-called micelles. In aqueous solution, this behavior is observed for tensid-like, amphiphile compounds, which means that consist of both hydrophillic and hydrophobic components. One of the historically well-documented and studied amphiphile polymer variants is the family of polypropylene (PPO) and polyethylene oxide (PEO) based tri-block copolymers, commerically called Pluronics or Poloxamers [32, 33]. They were originally designed for the use as lubricants or detergents in cosmetics [33] but were also discussed as stabiliser-systems for drug delivery shortly afterwards [34, 35]. The original product range included many different Pluronic variants with different block lengths and hydrophobic balances, but one of the most prominent is called P123 ($EO_{20}PO_{70}EO_20$), which is also one of heaviest and most hydrophobic of the available Pluronics [36].

Aqueous P123 solutions show a rich temperature- and concentration-dependent phase diagram. At low temperatures, both its PPO middle block and PEO end groups are soluble in water, but with increasing temperature both block units undergo conformational changes, which result in lower polarity and hence in a lower hydration of the polymer chains [37, 38]. This dehydration is more pronounced for PPO and above a the critical micellization temperature, spherical micelles consisting of a hydrophobic core (PPO) and surrounded by a less hydrophobic shell (PEO) are formed. With further increase in temperature, the micelles start to assemble and grow in size while adopting rod- or worm-like shapes [39]. The process kinetics of this second transition have timescales in the order of hours to days corresponding to a random fusion and fragmentation model of spherical micelles to form larger, worm-like clusters [40]. By surpassing a certain temperature, which is called the cloud point ($T \approx 90°C$), an increasing cloudiness of the solutions will be visible due to the Mie-scattering of even bigger aggregates with an lamellar ordering [41, 42]. In concentrated solutions (above 27 weight percent) the micelles self-assemble into crystalline structures (lytropic liquid crystal (LLC) phases) [43, 44]. Here cubic and hexagonal ordering can be observed, which is correlated to the spherical or worm-like shape of the micelles [45]. These LLC phases are still heavily studied due to their scientific use as a structure-directing agents in the fabrication of mesopourous materials [46, 47, 48, 49, 50]. For solutions on a surface, it was shown using neutron reflectometry, that the crystallinity undergoes a distinct temperature dependent hysteresis between heating and cooling of the sample [51]. This hysteresis in crystallinity appears also in bulk solution without the confinement to an interface [52], which makes P123 an ideal model-system for studying the interplay between surface and solution properties.

While the spherical micelle and LLC regime has been extensively studied over the past 30 years for a variety of different Pluronics [53, 54, 36, 55, 56, 57, 58, 59, 60, 61, 62, 63, 39, 64, 65, 66, 67, 45, 51, 68], the same does not apply for the worm-like [69, 70, 40, 71] and lamellar aggregates [41, 42, 72]. The different studies also yielded ambiguous results in key parameters like the aggregation number, size and internal structure of the micelles. Yet, these information are in high demand for different micelle mythologies e.g. for polymers with a direct biological or pharmaceutical relevance [22, 20, 73]. The aim of this thesis is to study the full temperature-dependent phase diagram of Pluronic P123 and the structural properties of its micelles - with special focus on its worm-like and lamellar aggregates - using light, X-ray and neutron scattering. Although Pluronics have been studied using imaging [69] and different spectroscopic techniques [74, 37, 38], scattering methods such as dynamic light (DLS) and small-angle X-ray (SAXS) or neutron scattering (SANS) are versatile and powerful tools to simultaneously measure the micellar size and structure in solutions. In combination with additional neutron reflectometry experiments, the structural changes inside the micelles can be analyzed for different model interactions. Here, a new possible pathway for the already reported near-surface crystallization [57] will be revealed.

1. Theory

The theories of scattering and reflection are historically connected and linked to the theory of light or, more precisely, to the theory of waves. Despite already existing work on wave phenomena by Hyugens [75], the corpuscle or particle theory of light by Newton [76] was most popular and acknowledged until the early 19th century. Here, the groundbreaking double slit experiments by Young [77] as well as the works on light dispersion and diffraction by Fresnel [78] culminated in the neat formulation of light as electromagnetic waves by Maxwell [79] with its famous equations:

$$\begin{aligned} \nabla \cdot \mathbf{E} &= \frac{\rho}{\epsilon_0} , \\ \nabla \cdot \mathbf{B} &= 0 , \\ \nabla \times \mathbf{E} &= -\frac{\partial}{\partial t}\mathbf{B} , \\ \nabla \times \mathbf{B} &= \mu_0 \left(\mathbf{J} + \epsilon_0 \frac{\partial}{\partial t}\mathbf{E} \right) . \end{aligned} \tag{1.1}$$

E and **B** denote the electric and magnetic vector fields, while ϵ_0 and μ_0 are the vaccum permittivity and permeability, respectively. Although all classical light phenomena, i.e. dispersion, diffraction, reflection and absorption, were summarized in this set of universal equations, two major problems remained unsolved: a correct description of the black body emission spectrum and the unusual discharging of illuminated metal plates.

In 1860, Kirchhoff [80] reported on emission and absorption spectra of different heated materials and stated that they should be independent of any material properties. His assumption was the basis for a first sophisticated model by Wien [81], but it failed to cover experimental data of Paschen [82], Lummer, Pringsheim [83], Rubens and Kurlbaum [84] in the infrared and far-infrared wavelength regime. The breakthrough came with a revolutionary approach by Planck [85, 86, 87] and his famous law for the spectral radiance

$$L(\nu, T) = \frac{2h\nu^3}{c^2} \frac{1}{e^{\frac{\Delta E}{k_B T}} - 1} \tag{1.2}$$

of a black body, where ν is the radiation frequency, T the temperature of the black body, c the radiation propagation speed and k_B Boltzmann constant. Using an atomistic and probabilistic oscillator model based on thermodynamics, he introduced a finite energy spacing [87]

$$\Delta E = h \cdot \nu . \tag{1.3}$$

He called it the energy quantization of the radiation field and later h was named Planck constant. He is considered as one of the founders of quantum theory. This novel idea of quantization was so radical that it sparked skepticism and was not commonly accepted right away. It should proofed to be inevitably correct by works on the so-called photoelectric effect.

In 1839, Becquerel [88] was the first to describe this effect. He observed a measurable electric potential in galvanic cells with identical electrodes when one of them is illuminated by ultraviolet (UV) light. Hertz [89] and Hallwachs [90] could proof that metal plates discharge under UV radiation using spark gap experiments, but they couldn't give an conclusive explanation. The discovery of the electron by Thompson [91] with a similar experimental setup and dedicated investigations by Lenard [92], who showed that electrons were emitted and that their energy was solely depending on the frequency of the used light, Einstein [93] combined these results and came to his interpretation of the photoelectric effect. He concluded that, in terms of thermodynamics, a monochromatic light beam acts like an ensemble of independent energy quanta $h\nu$ and they should act like quanta or particles upon interaction with matter. The last part of this conclusion is his famous "heuristic principle" (approach based on experience and experiment). His suggestion for the kinetic energy of the emitted photo electrons [93]

$$E_{\text{kin}}^{\text{electron}} = h \cdot \nu - W \,, \tag{1.4}$$

where W denotes the potential barrier of the material, was later experimentally proven by Millikan [94].

The concepts, which were introduced by Planck and Einstein, inspired the then PhD-student De Broglie [95] to reverse the Energy-frequency relation $E = h \cdot \nu$ of photons and apply it to massive particles. He associated every particle with a fictitious wave giving them a frequency or wavelength [95]

$$\lambda = \frac{2\pi}{|\mathbf{k}|} = \frac{c}{\nu} = \frac{c \cdot h}{E} = \frac{h}{p} \,. \tag{1.5}$$

His predicted diffraction of electrons by crystalline structures was later realized by Davidson and Germer [96]. In addition to the quantum theory, matter waves - especially electron waves - gave rise to a new field in physics called wave mechanics. Schrödinger [97] used the wave description of electrons to formulate his eponymous differential equation [97]

$$\left(-\frac{\hbar^2}{2m}\nabla^2 + V \right) \cdot \Psi = \mathrm{i}h\frac{\partial}{\partial t}\Psi \,, \tag{1.6}$$

where $\hbar = h/2\pi$, ∇^2 is the Laplace-operator, m is the particle mass, Ψ is the particle wave function and V and E his potential and total energy, respectively. Hereby, he calculated the correct energy levels and orbitals of the hydrogen atom without any additional assumptions [98].

The atomic structure was still up for debate at that time. With the discovery of the electron, it was possible to distinguish between core and shell particles, but the exact atomic composition of heavier elements was still unknown. Rutherford already postulated the existence of

a neutral core particle in 1920 [99], but he thought of it as a strongly bound proton-electron pair. Susequent measurements with Beryllium, which was hit by alpha radiation, showed a new and highly penetrating type of radiation [100, 101]. This so called "Beryllium-radiation" was later shown to be made of neutral and massive particles, which had a similar mass to the proton, by Chadwick in 1932 [102]. Since it was uncharged, the newly discovered particle was called neutron. Following De Broglie's interpretation, its wave character was shown in diffraction experiments using thermal neutrons by Wollan and Shull [103, 104].

In this chapter, photons and neutrons will be treated in their wave description. Hence, incoming light and particles will be referred to as beams consisting of planar wave fronts

$$\mathbf{E} = \mathbf{E}_0 \, e^{-i(\mathbf{k}\cdot\mathbf{r}+\omega t)} \quad \text{or} \tag{1.7a}$$

$$\Psi = \Psi_0 \, e^{-i(\mathbf{k}\cdot\mathbf{r}+\omega t)} \, . \tag{1.7b}$$

Here $\mathbf{E}$ represents the electric field component of an electromagnetic light wave with its amplitude $\mathbf{E}_0$, wave vector $|\mathbf{k}| = \frac{2\pi}{\lambda}$, oscillation frequency $\omega = 2\pi\nu$ as well as propagation direction $\mathbf{r}$ and time t. The same definitions apply for the matter wave Ψ, which represents neutrons. Each wave front is a solution of either the Maxwell equations (1.1) (in case of (1.7a)) or the Schrödinger equation (1.6) (in case of (1.7b)) within their boundary and normalization conditions, respectively.

In the following, the interaction of light and neutron waves with matter will be discussed. Afterwards, compact summaries will provide the necessary theoretical basics and equations for each of the used experimental techniques.

1.1. Interaction of light and neutron waves with matter

Although both photons and neutrons can be expressed similarly as waves, they have inherently different physical properties (see table 1.1). Photons are carrier particles of the electromagnetic force and predominantly interact with shell electrons of atoms. Neutrons, on the other hand, have negligible interaction probabilities with electrons due to them being uncharged and having a significantly higher mass. Their interaction with matter is dominated by the atomic nucleus and its compositions.

	photon	neutron
electric charge	uncharged	uncharged
spin	$\hbar$	$\hbar/2$
rest mass	0	m_n
velocity	c_0/n	$\sqrt{2k_BT/m_n}$

Table 1.1. Comparison of photon and neutron properties. c_0 is the speed of light in vacuum and n is the refractive index of the medium, which the light is passing through.

Despite these differences, they both exhibit the same set of fundamental interactions with matter due to their wave nature (see figure 1.1):

absorption when passing through media,
refraction and **reflexion** at an interface and
scattering by diffuse media.

The type of interaction strongly depends on the energy or wavelength. In soft matter studies, the commonly used energies range from few electron volts (eV) up to several keV for photons and lay in the meV-regime for neutrons. Consequently, all high energy related interactions above these thresholds will not be discussed here.

Another wave property is the polarization, which gives the oscillation direction. This direction can be classified in components parallel (p-polrization) or perpendicular (s-polarization) to the propagation plane in space. Waves can be linear, elliptically or unpolarized [105]. Linear polarization has only one distinct oscillation direction, while elliptically polarized waves alternate between p- and s-states. Laser and synchrotron radiation is naturally linearly polarized [106, 105], while neutrons from nuclear fission reactors and spallation sources are unpolarized with no preferred spin configuration [107]. At the cost of loosing intensity, neutron beams can polarized using special magnetic crystals or mirrors [107].

In the following, each fundamental interaction will be briefly highlighted, while treating light and neutron waves independently.

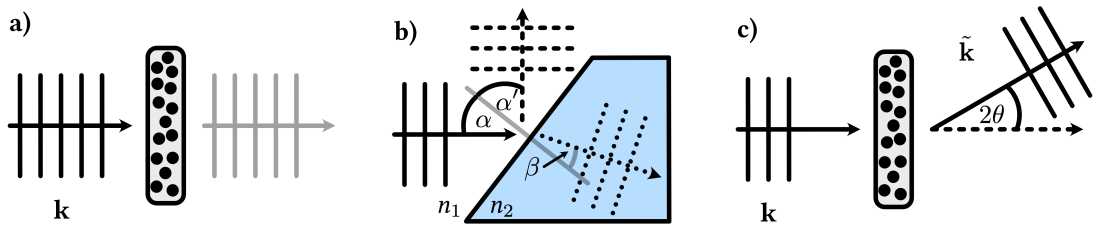

Figure 1.1. Different interactions of waves with matter: a) absorption, b) reflection (dashed wave front) or refraction (dotted wave front) at an interface of two media, c) diffraction and d) scattering.

Absorption is the reason for the observed attenuation of light and neutron beams when they pass through a sample or medium (see figure 1.1,a). In the wave picture, absorption is introduced by the complex refractive index

$$n = n' - \mathrm{i}\beta \tag{1.8}$$

with its real part n' and complex part β. In classical electrodynamics, the refractive index describes the slower propagation speed of waves in the medium compared to vacuum (see table 1.1). This change in velocity gives rise to a propagation time difference

$$\Delta t = t_{\mathrm{vac}} - t_{\mathrm{medium}} = \frac{d}{c_0} - \frac{d}{\frac{c_0}{n}} = (n-1)\frac{d}{c_0}\,. \tag{1.9}$$

Here, d is the thickness of this medium, c_0 the speed of light in vacuum and n the refractive of this medium. In a classical textbook calculation, the electric filed component of the light wave after the medium can be derived by inserting equations (1.8) and (1.9) in (1.7a):

$$\mathbf{E}_{\mathrm{medium}} = \mathbf{E}_0\, \mathrm{e}^{\mathrm{i}(\omega t_{\mathrm{medium}} - \mathbf{k}\cdot\mathbf{r})} = \mathbf{E}_0\, \mathrm{e}^{\mathrm{i}\omega(t-\frac{r}{c_0})}\, \mathrm{e}^{-\mathrm{i}\omega(n'-1)\frac{d}{c_0}}\, \mathrm{e}^{-\omega n''\frac{d}{c_0}}\,. \tag{1.10}$$

Looking at the intensity of the electromagnetic wave $I = \mathbf{E}\cdot\mathbf{E}^*$ (with $\mathbf{E}^*$ being the complex conjugate of $\mathbf{E}$) leads to the so called BOUGUER-LAMBERT-BEER law [108, 109, 110]

$$I_{\mathrm{medium}} = I_0\, \mathrm{e}^{-2\omega n''\frac{d}{c_0}} = I_0\, \mathrm{e}^{-\mu d} \tag{1.11}$$

with the intensities I_0 and I_{medium} before and after the medium, respectively, and the absorption coefficient

$$\mu = 2\frac{\omega}{c_0}\beta = 2k\beta\,. \tag{1.12}$$

This coefficient can also be normalized to the medium density and is then called the mass absorption coefficient [108].

μ is often associated with the cross section σ, which is a "particle picture property", has units like an area in barn (1 barn=10^{-24}cm^2) and is a measure for the interaction probability. Al-

though absorption effects will be mostly neglected in the following chapters, the neutron and X-ray absorption cross section shall be briefly mentioned due to their importance in tomography and microscopy techniques.

The process of X-ray absorption is based on the photoelectric effect [93]. Incoming photons interact with the atomic shell electrons. In the atomic model by Bohr [111], they get absorbed by the atom and their energy is transfered to an electron in the K-shell, L-Shell etc. with their corresponding binding energies. As a result the electrons get expelled with the excess energy (see equation (1.4)) and leave the atom in an excited state. The resulting "hole" in the atomic shell structure gets filled by electron transitions from other shells causing the emission of subsequent fluorescence photons.

If a neutron is absorbed by the samples nuclei, it will excite them and lead to two possible reactions: the fission of the nucleus or the emission of either a proton, α-particle or γ-quantum [107]. Values for the neutron absorption cross sections of all stable nuclei have been measured, published [112] and are available in multiple databases, e.g. from the National Institute of Standards and Technology (NIST) [113].

Refraction and Reflection are two processes taking place when waves hit the interface between two media with different refractive indices n_1 and n_2. Both can be explained using Fermat's principle. In a very simple form, it states that rays will always chose the path of least propagation time between two points when passing through a medium [105]. In its mathematical form, the total time

$$T = \int_{\Omega'} \mathrm{d}t = \int_{\Omega} \frac{\mathrm{d}r}{c'} \tag{1.13}$$

of a light ray with velocity c' along its path Ω or its total optical length

$$L_{opt} = c_0 \cdot T = c_0 \int_{\Omega} \frac{\mathrm{d}r}{c'} = \int_{\Omega} n \, \mathrm{d}r \ , \tag{1.14}$$

which depends on the refractive index n, needs to be stationary, i.e. is independent of small deviations [105]. Although Fermat's principle is strictly not based on the wave propagation formalism, it can be directly linked to the wave approach introduced by Huygens [114]. The path of the refracted light can be seen as the only possible, completely coherent and phase-correct superposition of Huygens spherical elementary waves [114]. Applying Fermat's principle (1.14) on a light wave, which is passing from one medium with refractive index n_1 to another with n_2 (see figure 1.1,b), will lead to

$$n_1 \cdot \sin\alpha = n_2 \cdot \sin\beta \quad \text{and} \tag{1.15a}$$

$$\alpha = \alpha' \ . \tag{1.15b}$$

The first equation is the famous Decartes-Snells law of refraction [115], which gives a relation between the direction of the incoming and refracted wave. The second equation shows

the intuitive result that both incoming and reflected wave have the same angle with the interface. A more detailed formalism about reflection will be given in chapter 1.4.

	E [eV]	λ [nm]	k [cm^{-1}]	n'	μ [cm^{-1}]	β
visible light	1.959	633	$9.93 \cdot 10^{4}$	1 + 0.46 [116]	$2.02 \cdot 10^{-2}$ [117]	$1.02 \cdot 10^{-7}$
X-rays [118]	8266	0.15	$4.19 \cdot 10^{8}$	$1 - 6.76 \cdot 10^{-6}$	69.41	$8.29 \cdot 10^{-8}$
neutrons [112]	0.036	0.15	$4.19 \cdot 10^{8}$	$1 - 1.50 \cdot 10^{-6}$	$0.20 \cdot 10^{-2}$	$2.39 \cdot 10^{-12}$

Table 1.2. Typical optical properties of visible light, X-rays and neutrons when interacting with quartz glas (SiO_2). The wavelengths are typical for the performed experiments. k was calculated using equation (1.5). The values for n' and μ were taken from their respective references. β was calculated using equation (1.12).

Visible light, X-rays and neutrons have distinctively different optical properties (see table 1.2). These variations are due to their different interaction mechanisms with matter and energy regimes. This strong energy (wavelength or frequency) dependence is called dispersion. It is best and easily observed for white visible light when it hits a prism and gets dispersed in the colors of the rainbow. Similarly, there are materials and crystals acting as prisms for neutrons [119].

Since both X-rays and neutrons have $n' < 1$, they exhibit a uniquely different reflection behavior compared to visible light. This feature is used for the construction of focusing lenses for X-rays [120] and waveguides for neutrons [121]. A microscopic explanation for the unusual values of n' will be given in chapter 1.4.

Scattering processes involve a change of direction of the incoming waves (see figure 1.1,c) depending on the properties of the matter, which they hit. There is a variety of different scattering types depending on the kind of interaction, energy scale, sample size and shape. Additionally, the interaction can be inelastic or elastic, i.e. without or with energy being transfered from the waves to the matter. Any inelastic processes (Raman scattering [122] for visible light, Compton scattering [123] for X-rays and inelastic neutron scattering [124, 125]) will not be discussed in further detail, since they either need a high degree of crystallinity or their contribution is too weak or they are indistinguishable from the elastic case.

The elastic scattering of electromagnetic waves at the atomic electrons is dominated by three processes: Thomson [126], Rayleigh [127, 128, 129] and Mie scattering [130]. In their theoretical treatise, they are all based on the stimulated emission and interference of dipole radiation by the electrons caused by the incoming oscillating electric field. The reader is referred to the excellent original publications for more details. Yet, in the following, a more generalized set of equations by van de Hulst [131] will be used to describe and compare the three main scattering processes.

An incoming wave front as seen in equation (1.7a) will cause outgoing spherical waves

$$\mathbf{E}' = S(\theta)\,\frac{\mathrm{e}^{-\mathrm{i}(\tilde{\mathbf{k}}\cdot\tilde{\mathbf{r}}+\omega t)}}{\mathrm{i}\left|\tilde{\mathbf{k}}\right|\left|\tilde{\mathbf{r}}\right|} = S(\theta)\,\frac{\mathrm{e}^{-\mathrm{i}(\tilde{\mathbf{k}}\cdot\tilde{\mathbf{r}}+\mathbf{k}\cdot\mathbf{r})}}{\mathrm{i}\left|\tilde{\mathbf{k}}\right|\left|\tilde{\mathbf{r}}\right|}\,\mathbf{E}\,, \tag{1.16}$$

upon interaction with a disturbance in its way. These spherical waves can have a different propagation directions $\mathbf{k}' \cdot \mathbf{r}'$ and amplitudes $S(\theta)$ compared to the incoming plane ones $\mathbf{E}$ (see equation 1.7a). Taking different polarization states in account, equation (1.16) needs to be modified and reads as [131]

$$\begin{pmatrix}\tilde{\mathbf{E}}_\mathrm{p}\\ \tilde{\mathbf{E}}_\mathrm{s}\end{pmatrix} = \begin{pmatrix}S_2(\theta) & S_3(\theta)\\ S_4(\theta) & S_1(\theta)\end{pmatrix}\frac{\mathrm{e}^{-\mathrm{i}(\tilde{\mathbf{k}}\cdot\tilde{\mathbf{r}}+\mathbf{k}\cdot\mathbf{r})}}{\mathrm{i}\left|\tilde{\mathbf{k}}\right|\left|\tilde{\mathbf{r}}\right|}\begin{pmatrix}\mathbf{E}_\mathrm{p}\\ \mathbf{E}_\mathrm{s}\end{pmatrix}. \tag{1.17}$$

In case of spherical particles the scattering amplitude matrix becomes [131]

$$\begin{pmatrix}S_2(\theta) & S_3(\theta)\\ S_4(\theta) & S_1(\theta)\end{pmatrix} = \mathrm{i}\left|\tilde{\mathbf{k}}\right|^3\alpha\begin{pmatrix}\cos(2\theta) & 0\\ 0 & 1\end{pmatrix}, \tag{1.18}$$

with the isotropic polarizability α and scattering angle 2θ (see figures 1.1,c and 1.2). The polarizability α links the dipole moment

$$\mathbf{p} = \alpha\,\mathbf{E} \tag{1.19}$$

of the electrons with the incoming electric field component of the light wave and describes the strength of the "dipole response". Using equation (1.17), the scattering intensity can be calculated, which yields the famous result by Rayleigh [129]:

$$\tilde{I}_\mathrm{Ray} = \frac{(1+\cos 2\theta)^2\left|\tilde{\mathbf{k}}\right|^4|\alpha|^2}{2|\tilde{\mathbf{r}}|^2}\,I\,, \tag{1.20}$$

where I denotes the intensity of the incoming planar wave front (see figure 1.2). Here, the

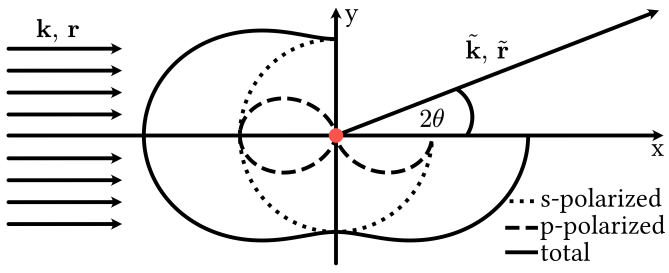

Figure 1.2. Angular distribution of the Rayleigh and Thompson scattering intensities. The incoming wave front of natural light is unpolarized and hits an arbitrary, isotropic polarizable sample (red dot).

scattering takes place at homogeneous, spherical particles, which are smaller than the wavelength of the used light. These spheres can be associated with atoms or small molecules and their k^4 or λ^{-4} dependency in equation (1.20) is the reason for the blue sky during the day and the red shades during sunrise and sunset [128].

In case of Thomson scattering, the electromagnetic waves only interact with a single and free electron and [131]

$$\alpha = \frac{-e^2}{m_e \tilde{\mathrm{k}}^2 c_0^2} \,. \tag{1.21}$$

Using (1.20) and (1.21) leads to the elimination of the energy dependency of the Thomson scattering intensity

$$\tilde{I}_{\mathrm{Thom}} = \frac{e^4}{2 m_e^2 c_0^4 |\tilde{\mathbf{r}}|^2} \left(1 + \cos 2\theta\right)^2 I \,. \tag{1.22}$$

The assumption of quasi-free electrons is e.g. valid for high energy X-ray photons, which energies are much higher than the binding energies of atomic electrons. A more detailed look on the connection between equation (1.22) and material properties, which can be obtained by small-angle scattering, will be discussed in chapter 1.3.

The theory of Mie scattering is applicable for arbitrary particle shapes and sizes in the ranges near or above the lights wavelength [130, 131]. It provides a direct link to the optical diffraction theory of Fresnel [78]. If particle sizes exceed the wavelength by a factor of 20 [131], diffraction phenomena from geometrical optics start to play a role in the interpretation of the scattering patterns. In the framework of equation (1.17), Mie scattering can be approximated by [131]

$$\begin{aligned} S_3(\theta) &= S_4(\theta) = 0 \quad \text{and} \\ S_1(\theta) &= S_2(\theta) = \frac{\tilde{\mathrm{k}}^2}{2\pi} \cdot G \cdot D(\varphi, \theta) \end{aligned} \tag{1.23}$$

with the geometric area $G = \int\int \mathrm{d}x\,\mathrm{d}y$ of the particle shadow and

$$D(\varphi, \theta) = \frac{1}{G} \int\int \mathrm{e}^{-i\mathrm{k}(x\cos\varphi + y\sin\varphi)\sin\theta}\,\mathrm{d}x\,\mathrm{d}y \,, \tag{1.24}$$

which is a complex function vanishing for $\theta = 0$. In terms of intensity, this yields[131]:

$$I_{\mathrm{Mie}} = \frac{G^2}{\lambda^2 \tilde{r}^2} I \left|D(\varphi, \theta)\right|^2 . \tag{1.25}$$

The elastic scattering of neutrons can be treated exclusively in the particle wave or Schrödinger formalism. With its magnetic moment, the neutrons are very sensitive to the nuclear composition of atoms and specifically their different isotopes. This fact will give rise to the so-called neutron scattering length, which is a element specific material property. A rigid calculation on this topic will be given in chapter 1.3.1.

1.2. Dynamic light scattering

The scattering of visible light is prominently used for the investigation of dilute macromolecular solutions and soft matter. Continuing on the work of Rayleigh and Mie (equations (1.20) and (1.25)), Debye [132] and Zimm [133, 134] further investigated the angular and polarization dependency of the scattered light by fluids. They developed experimental methods and a theory linking the observed intensities with the sizes and masses of the molecules and particles in liquids and solutions. At that time, the experimental set-ups were inefficient and too time-consuming for an immediate impact. After the development of lasers, Pecora [135] and Cummins et al. [136] further improved the existing scattering methods by introducing optical mixing and temporal correlation spectroscopy into the experimental set-up and subsequent data acquisition and analysis. Their work was the basis for dynamic light scattering (DLS), which is nowadays a canonical and integral technique in any laboratory workflow regarding material research. An overview for current state-of-art equipment and applications is given in [137, 138].

In a DLS experiment, monochromatic light from a laser is guided on a sample (see figure 1.3). These can be dilute solutions of proteins, polymers, other macromolecules or nanoparticles. These particles will scatter the laser light according to either Rayleigh or Mie theory depending on their size (see chapter 1.1). For the following considerations and calculations the exact mechanism will be irrelevant. The scattered intensity is monitored under a certain fixed angle using some detection device, e.g. a photo diode or 2D pixel array. Due to the thermal movement of the particles in the solvent, the scattering intensity on the detector will fluctuate over time (see figure 1.3). After starting at the time t_0 and measuring for a time period T, the average intensity will be [139]

$$\langle I \rangle = \frac{1}{T} \int_{t_0}^{t_0+T} I(t)\,\mathrm{d}t = \lim_{T\to\infty} \frac{1}{T} \int_0^T I(t)\,\mathrm{d}t \ . \tag{1.26}$$

Since the intensity changes for every time-step t_j, the correlation between these intensities is an important quantity. Such a correlation function can be defined as [139]

$$\langle I(0)I(\tau)\rangle = \lim_{T\to\infty} \int_0^T I(t)\, I(t+\tau)\,\mathrm{d}t \approx \lim_{N\to\infty} \frac{1}{N} \sum_{j=1}^{N} I_j\, I_{j+n}. \tag{1.27}$$

$I(0)$ and $I(\tau)$ are the intensities at the very beginning and an arbitrary time τ, respectively. For the approximation in the last step, the following relations were introduced: $t = j\Delta t$, $\tau = n\Delta t$, $T = N\Delta t$ and $t + \tau = (j + n)\Delta t$. Δt is the sampling between two time-steps.

Since the incoming light is scattered by the particles in the solution, the observed intensity will depend on their number density [139]

$$\rho(\mathbf{r}, t) = \sum_j \delta(\mathbf{r} - \mathbf{r}_j) \tag{1.28}$$

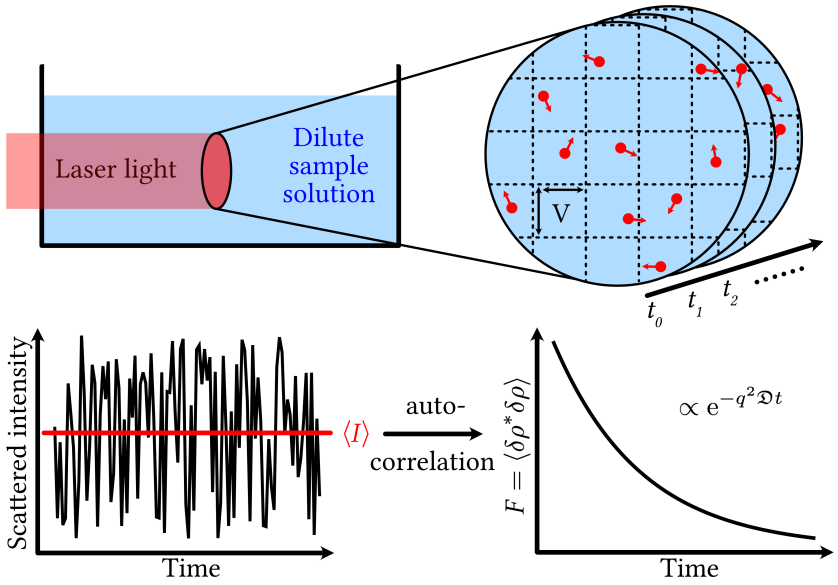

Figure 1.3. Sketch of a dynamic light scattering experiment, its time-dependent scattering intensity and correlation function. ⟨I⟩ shows the time-average of the scattering intensity.

at a certain point **r** and time t in the illuminated volume. Hence, the fluctuating intensity is caused by a fluctuation [139]

$$\delta\rho(\mathbf{r}, t) = \rho_0 - \rho(\mathbf{r}, t) \tag{1.29}$$

in the number density, where ρ_0 symbolizes the time-average. After a lengthy calculation, which shall be omitted here, it is possible to show that the intensity correlation function $\langle I(0)I(\tau)\rangle$ is proportional to the function [139]

$$F(\mathbf{q}, t) = \langle \delta\rho^*(\mathbf{q}, 0)\delta\rho(\mathbf{q}, t)\rangle \tag{1.30}$$

with the complex conjugate denoted by *, the FOURIER transformation

$$\delta\rho(\mathbf{q}, t) = \int \delta\rho(\mathbf{r}, t)\, e^{i\mathbf{q}\cdot\mathbf{r}}\, d^3r \tag{1.31}$$

of the number density fluctuation in equation (1.29) and the scattering vector **q** of length

$$q = |\mathbf{q}| = \frac{4\pi n}{\lambda} \sin\theta\,, \tag{1.32}$$

where n is the refractive index of the sample, λ the wavelength of the laser light and θ half of the scattering angle (see figures 1.1 and 1.2). The summation in equation (1.28) should be discussed in more detail. If a particle is in the illuminated volume, it will be added to ρ. By dividing this volume in a grid of identical smaller cells with the cell volume V (see figure 1.3),

a new parameter [139]

$$b_j = \begin{cases} 1 & \text{if } j \in V \\ 0 & \text{if } j \notin V \end{cases} \tag{1.33}$$

can be introduced, which counts the particles in each sub-volume for each individual time step. In sufficiently dilute solutions, all particles or macromolecules will rarely encounter each other and their motion can be assumed as statistically independent. If the volume V of each cell is large compared to the average travel path due to diffusion, the quantity b_j will show almost no variation over time. Under these assumptions and by combining equations (1.28, (1.29) and (1.33), equation (1.30) can be written as [139]

$$F(\mathbf{q}, t) = \sum_j^N \langle b_j(0)\rangle\langle e^{i\mathbf{q}[\mathbf{r}_j(t)-\mathbf{r}_j(0)]}\rangle = \langle N\rangle \cdot F_s \tag{1.34}$$

where $\sum_j^N \langle b_j(0)\rangle = \langle N\rangle$ is the total particle number and [139]

$$F_s = \langle e^{i\mathbf{q}[\mathbf{r}_j(t)-\mathbf{r}_j(0)]}\rangle \tag{1.35}$$

is the so-called self-intermediate scattering function. Due to the assumption that the particles will rarely leave their sub-volume V during the measurement, equation (1.34) is also their auto-correlation function.

All particles in the solution move through the solvent by diffusion. Since all measurable particle properties are encoded in the F_s-function in (1.35), it has to fulfill the diffusion equation

$$\frac{\partial}{\partial t} F_s(\mathbf{q}, t) = -q^2 \mathfrak{D} F_s(\mathbf{q}, t) \tag{1.36}$$

with the diffusion constant $\mathfrak{D}$. For spherical particles, $\mathfrak{D}$ is connected with the hydrodynamic radius of the particle R_H by the Einstein-Stokes relation [140, 141]:

$$\mathfrak{D} = \frac{k_B T}{6\pi\eta R_H} \,. \tag{1.37}$$

Here, T is the temperature of the sample solution and η the solvent viscosity. Using the boundary condition $F_s(\mathbf{q}, t = 0) = 1$, equation (1.36) can be solved, which leads to the fundamental equation for the auto-correlation of the scattered intensities [139]:

$$F(\mathbf{q}, t) = \langle N\rangle\, e^{-q^2\mathfrak{D}t} = \langle N\rangle\, e^{-\frac{k_B T}{6\pi\eta R_H} t} \,. \tag{1.38}$$

This auto-correlation is usually directly calculated during the experiment by dedicated hardware. The subsequent data analysis for the determination of $\mathfrak{D}$ and R_H is already integrated in commercially available DLS systems and can often handle non-spherical particle shapes. This so-called cumulant method is very robust and assumes a linear combination of exponential functions, which can be related to different particle orientations and dimensions.

1.3. Small-angle scattering

This chapter will treat the theory of small-angle X-ray (SAXS) and neutron scattering (SANS), which were pioneered in the late 1930s [142, 143] and 1970s [144, 145, 146, 147], respectively. Both techniques are nowadays important standard tools for material characterization in chemistry, biology and nano-science.

The scattering theories of X-rays and neutrons are distinctly different, which is due to their interaction mechanisms, independent historical development and user communities. Despite these differences, section 1.3.1 will emphasize on the unified formalism of both X-rays and neutrons in the context of soft matter studies. The later chapters, 1.3.2until 1.3.4, will tackle the most common data analysis procedures and the concept of absolute intensities.

1.3.1. Scattering Theory of X-rays and neutrons

Elastic X-ray scattering is described by the Thompson formula (see equation 1.22). In its classical form, it only shows the scattering by single electrons. Any matter or atoms, besides hydrogen or ions, consists of an assortment of electrons. Each one will act as a Thompson scatterer upon X-ray illumination. The more generalized description for the collective scattering of many electrons is called the Rayleigh-Debye-Gans-theory [148, 149, 127]. Since X-rays are high energy photons, their interaction with matter, especially soft matter, can be considered as weak. Consequently, the physical basis of the theory is that the photons interact with the volume element $\mathrm{d}V$ of the scatterer, which will act as independent dipoles. The subsequent emitted radiation is a superposition of all elements $\mathrm{d}V$ (see figure 1.4). Staying in the van de Hulst notation, the polarizability of an atom reads as [131]

$$\tilde{\alpha} = \frac{1}{V} \int \alpha \cdot \mathrm{d}V \ , \tag{1.39}$$

where α is equal to the single-electron-polarizability in equation (1.21). By applying an appropriate coordinate system and using the paraxial approximation , equation (1.17) can then be rewritten to read:

$$\begin{pmatrix} \tilde{\mathbf{E}}_\mathrm{p} \\ \tilde{\mathbf{E}}_\mathrm{s} \end{pmatrix} = -\frac{e^2}{m_e c_0^2 r} \int \rho_e \mathrm{e}^{-\mathrm{i}(\tilde{\mathbf{k}}-\mathbf{k})r} \, \mathrm{d}V \begin{pmatrix} \cos(2\theta) & 0 \\ 0 & 1 \end{pmatrix} \begin{pmatrix} \mathbf{E}_\mathrm{p} \\ \mathbf{E}_\mathrm{s} \end{pmatrix} , \tag{1.40}$$

with the newly introduced electron density $\rho_e = Z/V$, the total electron number Z, the distance from the origin $|\tilde{\mathbf{r}}| = r$, and the already mentioned scattering vector (with $|\mathbf{k}| = |\tilde{\mathbf{k}}|$) [150]

$$|\mathbf{q}| = \left|\tilde{\mathbf{k}} - \mathbf{k}\right| = \frac{4\pi}{\lambda} \sin\theta \, . \tag{1.41}$$

In case of an incoming plane wave front and natural unpolarized light, the total scattered field will be

$$\mathbf{E}_\mathrm{scatt} = -\mathbf{E}_0 \, \frac{e^2}{m_e c_0^2} \, \frac{\mathrm{e}^{-\mathrm{i}\mathbf{k}\cdot\mathbf{r}}}{r} \int \rho_e \mathrm{e}^{-\mathrm{i}\mathbf{q}\mathbf{r}} \, \mathrm{d}V \, \frac{1+\cos 2\theta}{2} \, . \tag{1.42}$$

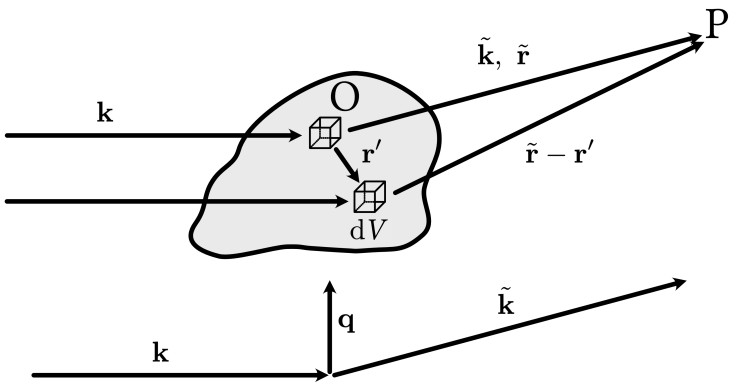

Figure 1.4. Scattering geometry introducing the wave vector $\mathbf{q}$. The chosen coordinate system has its origin in the volume element noted by "O". The incoming wave front $\mathbf{k}$ is scattered by independent volume elements dV in the particle, which interfere at a distant observation point "P".

Here, $\mathbf{E}_0$ is the amplitude of the incoming wave front, r the distance from the sample and $\frac{1+\cos 2\theta}{2}$ is called the polarization factor. The amplitude of the scattered wave is altered by

$$f_X(\mathbf{q}) = -\frac{e^2}{m_e c_0^2} \int \rho_e \, \mathrm{e}^{-\mathrm{i}\mathbf{q}\cdot\mathbf{r}} \, \mathrm{d}V = -r_e \int \rho_e \, \mathrm{e}^{-\mathrm{i}\mathbf{q}\cdot\mathbf{r}} \, \mathrm{d}V \tag{1.43}$$

with the classical Thompson electron radius r_e (in cgs units). This function is the Fourier-transformation of the electron density ρ_e and is called atomic form factor in scattering theory [151, 152, 153]. When discussing small-angle scattering, the polarization factor is often omitted, since its contribution is almost negligible for small values of 2θ. In wide-angle scattering experiments and for polarized sources, it is important to correctly apply the polarization factor during data reduction and handling.

In case of neutrons, the elastic scattering case can be described quantum mechanically using the so-called Lippmann-Schwinger equation [154, 155]

$$\Psi_s(\tilde{\mathbf{r}}) = \Psi_0(\tilde{\mathbf{r}}) - \frac{m_n}{2\pi\hbar^2} \int \mathrm{d}\mathbf{r}'^3 \, \frac{\mathrm{e}^{\mathrm{i}k|\tilde{\mathbf{r}}-\mathbf{r}'|}}{|\tilde{\mathbf{r}} - \mathbf{r}'|} \, V(\mathbf{r}') \, \Psi_s(\mathbf{r}') \, \mathrm{d}\mathbf{r}' \tag{1.44}$$

with the wave function Ψ_s of the scattered neutron field, the wave function $\Psi_0 = \frac{1}{(2\pi)^{3/2}} \mathrm{e}^{\mathrm{i}\mathbf{k}\cdot\tilde{\mathbf{r}}}$ of the incoming neutrons, the neutron mass m_n, the wavenumber $k = |\mathbf{k}| = |\tilde{\mathbf{k}}|$ and the neutron-matter interaction potential $V(\mathbf{r}')$. The notation of $\tilde{\mathbf{r}}$ and $\mathbf{r}'$ is in accordance with figure (1.4). It is an iterative equation and the application of perturbation theory on the stationary (time-independent) Schrödinger equation (1.6). For an in-depth introduction, the reader is referred to classical literature on quantum mechanics [156, 157] or more specialized courses on quantum scattering theory [158]. To further simplify the problem in equation (1.44), only single scattering will be considered and any multi-scattering events will be neglected, which is valid

for very diluted or thin samples. This condition is equal to the first order Born-approximation in the kinematic scattering theory. Here, the interaction between neutrons and matter is assumed to be weak enough so that $\Psi_s(\mathbf{r}') \approx \Psi_0(\mathbf{r})$ in the integral on the right hand side of equation (1.44). As a result, the scattered wave function will be [159, 160, 161]

$$\Psi_s^{\text{Born}}(\tilde{\mathbf{r}}) = \Psi_0(\tilde{\mathbf{r}}) + f(\mathbf{q})\,\frac{e^{ikr}}{r} \tag{1.45}$$

with the neutron scattering amplitude

$$f(\mathbf{q}) = -\frac{m_n}{2\pi\hbar^2}\int e^{i\mathbf{q}\cdot\mathbf{r}'}\; V(\mathbf{r}')\;\mathrm{d}\mathbf{r}'\,, \tag{1.46}$$

which is the Fourier transform of the interaction potential $V(\mathbf{r}')$. The interaction range of this potential is very short compared to the wavelength of thermal neutrons. Mathematically, this circumstance can be modeled with the so-called FERMI-pseudo potential [162]

$$V_{\text{Fermi}}(\mathbf{r}') = \frac{2\pi\hbar^2}{m_n}\; b\;\delta(\mathbf{r}')\,, \tag{1.47}$$

where b is the so-called neutron scattering length and $\delta(\mathbf{r}')$ is the delta function. One of the properties of this function is that its Fourier transform gives unity. Consequently, when applying the Fermi-potential in equation (1.48), the neutron form factor is simply [107, 151]

$$f_n(\mathbf{q}) = -b\,. \tag{1.48}$$

In contrast to the X-ray form factor (1.43), it is a simple constant value, which depends on the nuclear composition of the elements. Depending on the total magnetic moment of the nucleus (proton and neutron ratio), the interaction with thermal free neutrons can either be attractive or repulsive and the sign of b can change. For all known stable elements and their isotopes, values of the neutron scattering length are experimentally determined and can be found in literature [113, 112].
In a sample solution not only one particle is present but an assembly of them. If all of them

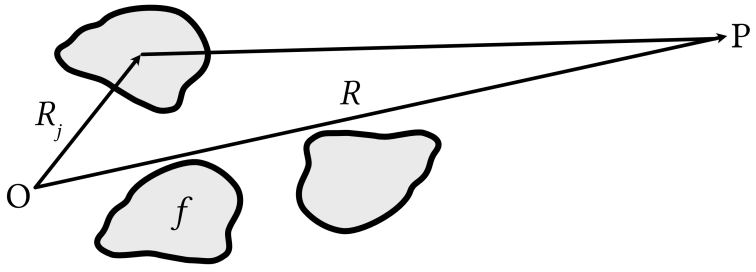

Figure 1.5. Scattering of a discrete distribution of particles. Each particle is represented by its scattering amplitude f and has its unique position R_j from the origin "O".

are uniform in size and shape, the scattering wave functions and amplitudes f_X or f_n of each individual particle are identical. Then the total scattering wave function of the sample [151, 152]

$$\Psi_{\text{scatt}}^{\text{total}} = \sum_j f_j(\mathbf{q})\, \mathrm{e}^{-\mathrm{i}\mathbf{q}\cdot\mathbf{R}_j} \frac{\mathrm{e}^{\mathrm{i}kR}}{R} = F(\mathbf{q})\, \frac{\mathrm{e}^{\mathrm{i}kR}}{R} \tag{1.49}$$

is the superposition of these individual wave functions (see figure 1.5) with the total scattering amplitude

$$F(\mathbf{q}) = \sum_j f_j(\mathbf{q})\, \mathrm{e}^{-\mathrm{i}\mathbf{q}\cdot\mathbf{R}_j} \,. \tag{1.50}$$

During an small-angle scattering experiment any time-dependence, e.g. in the sense of chapter 1.2, is lost due to macroscopic measurement times compared to molecular movements and diffusion. Due to the constant movement of the particles, their discrete assembly can be replaced by

$$\sum_j f_j(\mathbf{q})\, \mathrm{e}^{-\mathrm{i}\mathbf{q}\cdot\mathbf{R}_j} \longrightarrow \int_V \rho^{\mathrm{s}}\, \mathrm{e}^{-\mathrm{i}\mathbf{q}\cdot\mathbf{R}}\, \mathrm{d}\mathbf{R} \,. \tag{1.51}$$

Here, the scattering length density ρ^{s} was introduced. Since both f_X and f_n are lengths by their units, ρ^{s} is given in cm^{-2}. It is connected to the macroscopic density ρ by

$$\begin{aligned} \rho_X^{\mathrm{s}} &= \frac{N_A\, \rho}{\sum_i n_i M_i} \sum_i n_i \cdot Z_i\, r_e \quad \text{and} \\ \rho_n^{\mathrm{s}} &= \frac{N_A\, \rho}{\sum_i n_i M_i} \sum_i n_i \cdot b_i \end{aligned} \tag{1.52}$$

with Avogadros number N_A, the samples stoichiometric composition n_i, the molar masses M_i of its elements, their electron number Z_i, their respective neutron scattering lengths b_i and the classical Thompson electron radius r_e (see equation (1.43)). Integration over the whole sample volume V, will restore the units of the scatting amplitude. The subsequent ensemble-averaged scattering intensity will be [151]

$$I_{\text{scatt}} = \left\langle \Psi \cdot \Psi^* \right\rangle \propto \left\langle |F(\mathbf{q})|^2 \right\rangle \,, \tag{1.53}$$

where the spatial average over all particles in solution and their orientations $\langle \cdot \rangle$ is introduced.

1.3.2. Model-independent analysis

The analysis of equation (1.53) is the subject of the following two chapters. The first presented approach is model-independent and uses no *a priori* assumptions for the particle shape or composition. Its theories tackle special cases of equation (1.53) in the low- or high-$\mathbf{q}$ regime, like the Guinier and Porod laws, or attempt to calculate the real-space scattering intensity using the inverse Fourier-transformation.

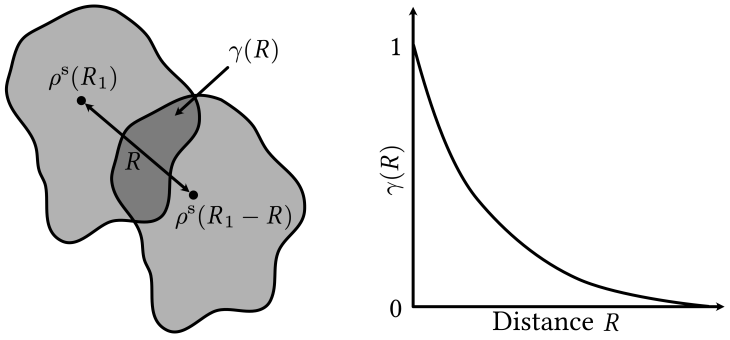

Figure 1.6. Graphic representation of the spatial autocorrelation function.

Spatial autocorrelation function

Starting from equation (1.53), the quantity $\left\langle |F(\mathbf{q})|^2 \right\rangle$ needs to be calculated. Using the integral representation of $F(\mathbf{q})$ [151],

$$|F(\mathbf{q})|^2 = F(\mathbf{q}) \cdot F^*(\mathbf{q}) = \int_V \int \rho^s(\mathbf{R}_1)\, \rho^s(\mathbf{R}_2)\, \mathrm{e}^{-\mathrm{i}\mathbf{q}\cdot(\mathbf{R}_1-\mathbf{R}_2)}\, \mathrm{d}\mathbf{R}_1\, \mathrm{d}\mathbf{R}_2 \ . \tag{1.54}$$

With the coordination shift $\mathbf{R} = \mathbf{R}_1 - \mathbf{R}_2$ and $\mathbf{R}_2 = \mathbf{R}_1 - \mathbf{R}$, this leaves [151]

$$|F(\mathbf{q})|^2 = \int_V \int \rho^s(\mathbf{R}_1)\, \rho^s(\mathbf{R}_1 - \mathbf{R})\, \mathrm{e}^{-\mathrm{i}\mathbf{q}\cdot\mathbf{R}}\, \mathrm{d}\mathbf{R}_1\, \mathrm{d}\mathbf{R} = \int_V \gamma(\mathbf{R})\, \mathrm{e}^{-\mathrm{i}\mathbf{q}\cdot\mathbf{R}}\, \mathrm{d}\mathbf{R} \ . \tag{1.55}$$

Here, the spatial autocorrelation function [163]

$$\gamma(\mathbf{R}) = \int_V \rho^s(\mathbf{R}_1)\, \rho^s(\mathbf{R}_1 - \mathbf{R})\, \mathrm{d}\mathbf{R}_1 \tag{1.56}$$

of the particle is introduced. This function is heavily used in imaging techniques, since it has unique properties when FOURIER transformed [164]. It is an decaying function with increasing distance R (see figure 1.6). To obtain the scattering intensity, it is necessary to find the orientation average of $|F(\mathbf{q})|^2$. Averaging will always lead to the loss of information, which is the essence of a scattering experiment. This means that the autocorrelation function $\gamma(|\mathbf{R}| = R)$ will only depend on absolute values of the distances, since all possible orientations of $\mathbf{R}$ will be considered. The orientation average of the phase factor $\mathrm{e}^{-\mathrm{i}\mathbf{q}\cdot\mathbf{R}}$ is given by the famous DEBYE formula [148]

$$\left\langle \mathrm{e}^{-\mathrm{i}\mathbf{q}\cdot\mathbf{R}} \right\rangle = R^2\, \frac{\sin qR}{qR} \tag{1.57}$$

with $q = |\mathbf{q}|$ and $R = |\mathbf{R}|$. Combining all these considerations will lead to the orientation averaged scattering intensity

$$I_{\mathrm{scatt}}(q) = 4\pi \int_0^\infty \gamma(R)\, R^2\, \frac{\sin qR}{qR}\, \mathrm{d}R \ . \tag{1.58}$$

Pair distance distribution function

The Fourier-transformation is inseparably linked with scattering processes. The scattering amplitude $F(\mathbf{q})$ and the scattering length density $\rho^s(\mathbf{R})$ are a Fourier pair as is its square $|F(\mathbf{q})|^2$ and the spatial autocorrelation function $\gamma(\mathbf{R})$. It follows from equation (1.58) that the scattering intensity is the Fourier transform of the function [165, 153]

$$p(R) = \gamma(R) \cdot R^2 = R^2 \cdot \left\langle \int_V \rho^s(\mathbf{R}_1)\, \rho^s(\mathbf{R}_1 - \mathbf{R})\ \mathrm{d}\mathbf{R}_1 \right\rangle . \tag{1.59}$$

This is the convolution of the one-dimensional orientation-averaged autocorrelation function with all possible displacements. Since $\gamma(R)$ will vanish for all displacements larger than the particle itself, R can be identified with the possible distances inside the particle. From here, $p(R)$ is nothing more than a "distance histogram" [151] of the particle. Hence, $p(R)$ is called the pair-distance distribution function. Its maximum is the most probable distance to be observed in the particle. The R-values, for which $p(R) = 0$, will give the biggest possible distance inside the particle. For a spherical particle, the most probable distance would be its radius, while its maximum distance would be its diameter (see figure 1.7).

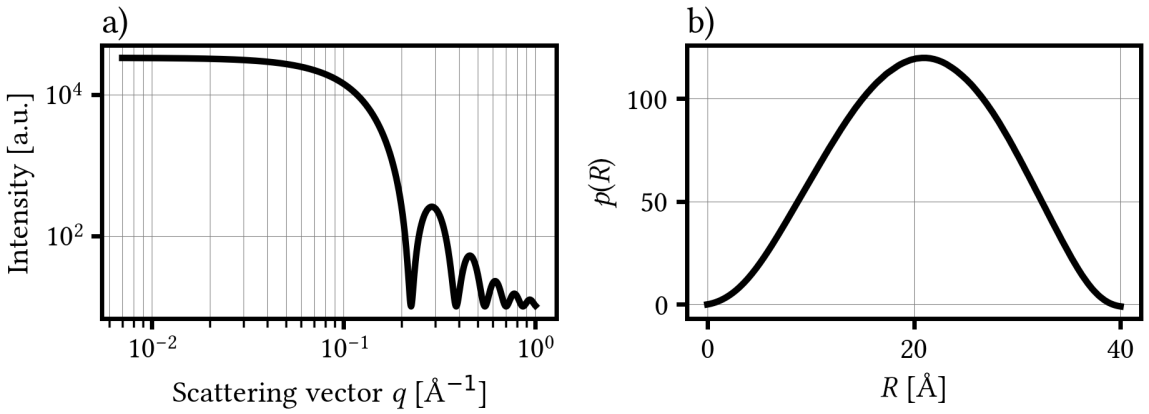

Figure 1.7. a) The scattering intensity of simple spheres with a 2 nm radius and b) their respective $p(R)$ function, which was calculated using the Atsas software [166].

Although $I_{\mathrm{scatt}}(q)$ and $p(R)$ are connected by a Fourier-transformation, it is impossible to directly apply the back transformation, since $I_{\mathrm{scatt}}(q)$ cannot be completely measured in q-space ($0 \leq q \leq \infty$) [151]. There are numerical methods introduced by Glatter, which are called indirect Fourier transformation [165]. Here, the $p(R)$ function is modeled in real-space using cubic spline functions. The coefficients of these polynomial spline functions have an analytical expression when Fourier transformed, which gives the desired connection with the scattering intensity. The guess in real-space is modified until the modeled $p(R)$ fits the experimental intensities. However, it gets more complex for different particle geometries than spheres or cylinders, since any three-dimensional shape information is lost during the averaging process.

Guinier approximation

Without the need of numerical methods, it is possible to further analyze equation (1.58). In the low q-regime near $qR = 0$, the phase factor can be approximated by the TAYLOR series [152]

$$\frac{\sin qR}{qR} = \frac{qR - \frac{1}{6}(qR)^3 + \mathcal{O}\big((qR)^5\big)}{qR} = 1 - \frac{1}{6}(qR)^2 + \mathcal{O}\big((qR)^4\big)\,, \tag{1.60}$$

where $\mathcal{O}((qR)^x)$ are the following higher order terms of the series expansion. Inserting equation (1.60) in (1.58) will lead to the famous GUINIER-law [143]

$$I_{\text{scatt}}^{\text{Guinier}}(q) \approx 4\pi \int_V \gamma(R) \cdot R^2 \,\mathrm{d}R \cdot \left(1 - \frac{q^2 R_G^2}{3}\right) \approx I_{\text{scatt}}(q=0) \cdot \mathrm{e}^{-\frac{q^2 R_G^2}{3}} \tag{1.61}$$

with the scattering intensity

$$I_{\text{scatt}}(q=0) = \int_V \gamma(R) \cdot R^2 \,\mathrm{d}R = (\rho^s)^2 \cdot V^2\,. \tag{1.62}$$

at $q = 0$, the pair-distance distribution function $p(R)$ and the newly defined radius of gyration

$$R_G^2 = \frac{\int_V p(R) \cdot R^2 \,\mathrm{d}R}{\int_V p(R)\,\mathrm{d}R}\,. \tag{1.63}$$

In the last step, the TAYLOR series of a Gaussian function $\mathrm{e}^{-aq^2} \approx (1 - aq^2)$ with $a = \frac{R_G^2}{3}$ was used. The radius of gyration has an analytical form for the most simple and common particle geometries (see table 1.3). When studying polymers, their shape and motion in solution is highly complex. Both depends on their interaction with the solvent, which can be characterized by the FLORY exponent ν. The special case is $\nu = 0.5$, which means a perfectly free polymer showing random walk behavior when moving through the solvent. With more complex interaction models, the values for ν can vary significantly [167].

	variables	R_G	p
sphere	radius R	$\sqrt{\frac{3}{5}}R$	4
disk	radius $R \gg$ thickness d	$\sqrt{\frac{1}{2}}R$	2
cylinder	radius $R \ll$ length L	$\sqrt{\frac{1}{12}}L$	1
mass fractals	correlation length R_l	$R_l^{1/\nu}$	$1/\nu$

Table 1.3. Values for R_G and the POROD exponential p for the most common geometrical objects. The first three relations were taken from [152, 153]. The mass fractal definition is taken from [167] and ν is the FLORY exponent, which describes the solvent-fractal interaction.

Porod theorems

Besides Guinier, Porod was the second important founding fathers of SAS theory. He developed three crucial ideas for the interpretation of scattering data from diluted samples, namely the scattering contrast, scattering invariant and the power law approach named after him.

If the sample consists of two phases, e.g. the homogeneous particles of arbitrary size and shape and their solvent, the sharp interface between them will result in the scattering amplitude [168]

$$\begin{aligned} F(q) &= \int_{\phi V} \rho_1^s(R)\, \mathrm{e}^{-\mathrm{i}\mathbf{q}\cdot\mathbf{R}}\, \mathrm{d}R + \int_{(1-\phi)V} \rho_2^s(R)\, \mathrm{e}^{-\mathrm{i}\mathbf{q}\cdot\mathbf{R}}\, \mathrm{d}R \\ &= \int_{\phi V} \Delta\rho^s(R)\, \mathrm{e}^{-\mathrm{i}\mathbf{q}\cdot\mathbf{R}}\, \mathrm{d}R + \rho_2^s \int_V \mathrm{e}^{-\mathrm{i}\mathbf{q}\cdot\mathbf{R}}\, \mathrm{d}R \end{aligned} \tag{1.64}$$

where $\rho_1^s(R)$ and $\rho_2^s(R)$ are the scattering length densities of the two phases with their volume fractions ϕ and $(1 - \phi)$, respectively.

$$\Delta\rho^s(R) = \rho_1^s(R) - \rho_2^s(R) \tag{1.65}$$

is the so-called scattering contrast between the two phases. The second term in equation (1.64) will always result in a constant scattering intensity when the orientational average is applied. This background intensity only holds information about the solvent. For the analysis of the particles or sample in this solvent, only the scattering contrast $\Delta\rho^s(R)$ will be needed.

Since both $\gamma(R)$ and $I_{\mathrm{scatt}}(q)$ are connected by equation (1.58), there exists a back transformation [151, 152]:

$$\gamma(R) = \frac{1}{2\pi^2} \int_0^\infty I_{\mathrm{scatt}}(q) \cdot q^2\, \frac{\sin qR}{qR}\, \mathrm{d}q \ . \tag{1.66}$$

A special case occurs for vanishing particle shifts or distances R. When $R = 0$, this back transformation yields

$$\gamma(0) = \frac{1}{2\pi^2} \int_0^\infty I_{\mathrm{scatt}} \cdot q^2\, \mathrm{d}q \ . \tag{1.67}$$

Applying the newly introduced scattering contrast $\Delta\rho^s$ and the value for $\gamma(0)$ from equation (1.56), will give the so-called scattering invariant [169, 170, 171]

$$Q = \frac{1}{V} \int_0^\infty q^2 \cdot I_{\mathrm{scatt}}\, \mathrm{d}q = 2\pi^2 \phi(1-\phi)(\Delta\rho^s)^2 \ . \tag{1.68}$$

The quantity Q only depends on universal material properties like the scattering contrast between and the volume fractions of the sample and its matrix or solvent, respectively. Because of that, it is completely invariant of the particle shape and size. The integral over the whole scattering curve (see figure 1.8) can be taken as a good measure whether any irregularities happened during following experiments with the same sample, e.g. evaporation or radiation damage.

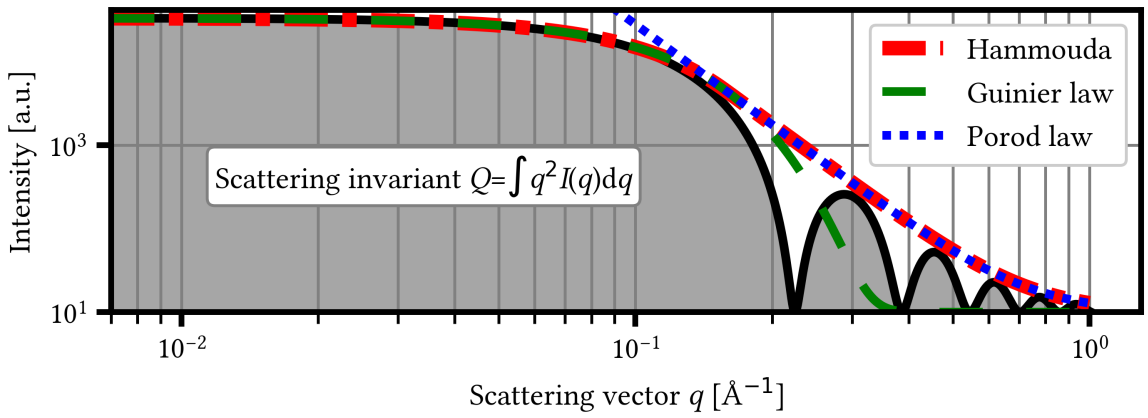

Figure 1.8. Representation of the Guinier and Porod law, generalized Hammouda model and the scattering invariant for the simulated scattering curve of a sphere with radius R = 2 nm (solid black line).

The scattering by an particle is determined by its size and shape as described by the auto-correlation function $\gamma(R)$. In contrast to the GUINIER approximation, which is dealing with the low-**q** or high-**R** regime, the scattering for very small displacements R is either caused by the particles bulk volume or its surface [153]. Consequently, $\gamma(R)$ can be interpreted as the probability function whether two points separated by R will be in the bulk volume or on the surface of the particle [172]. In the high-**q** or low-**R** regime, the decreasing auto-correlation function can then be approximated by [152]

$$\gamma_{\mathrm{Porod}} = 1 - \frac{\mathrm{S}}{4\mathrm{V}}\mathrm{R} + \mathcal{O}\left(\mathrm{R}^2\right) \tag{1.69}$$

with the particles volume V, surface S and displacement R. The higher orders are connected to the particle shape in a more complicated way and give oscillating functions [152]. Inserting equation (1.69) into (1.58) and subsequent integration, will yield the famous POROD approximation [152, 173]:

$$I_{\mathrm{scatt}}^{\mathrm{Porod}}(q) = \frac{C}{q^4} = \frac{2\pi(\Delta\rho^s)^2 S'}{q^4} \tag{1.70}$$

where $S' = \frac{S}{V}$ is the specific particle surface. The exponent in the denominator changes for different particle shapes and geometries and is connected to mathematical fractal theory (see table 1.3).

Unified model

For low and high q-values, equations (1.70) and (1.61), respectively, fail to adequately describe the scattering curve, since their assumptions are not valid anymore. Yet, both models cross at a certain q-value (see figure 1.8) hinting the possibility to unify them [172]. On this basis,

Hammouda was able to formulate a generalized Guinier-Porod law [174]

$$I_{\text{Hammouda}}(q) = \begin{cases} \frac{G}{q^s}\, \mathrm{e}^{-\frac{q^2 R_G^2}{3-s}}, & \text{for } q \leq q_1 \\ \frac{D}{q^d}, & \text{for } q \geq q_1 \end{cases} \tag{1.71}$$

with the Guinier and Porod prefactors G and D, the Porod exponents s and d and the radius of gyration R_G. To guarantee a consistent transition at the crossing value q_1, both intensities and their first derivatives have to be equal [174]. As a result, both q_1 and D can be calculated analytically [174]:

$$q_1 = \frac{1}{R_G} \left(\frac{(d-s)(3-s)}{2} \right)^{\frac{1}{2}} \tag{1.72}$$

$$D = \frac{G}{R_G^{(d-s)}}\, \mathrm{e}^{-\frac{(d-s)}{2}} \left(\frac{(d-s)(3-s)}{2} \right)^{\frac{(d-s)}{2}}, \tag{1.73}$$

leaving only 4 individual parameters to refine. Equation (1.71) was already used in literature to model the different form phases of an aqueous Pluronic P85 solution over a wide temperature range up to 90°C [41]. The radius of gyration will give an approximation of the observed size domains, while the Porod exponent provides information of the particle shape, symmetry and geometry.

1.3.3. Model-based analysis

In case of identical particles, the general form for the scattering intensity in equation (1.53) can be further simplified to read [151]

$$I_{\text{scatt}} = N \left\langle |F(\mathbf{q})|^2 \right\rangle = N\, F_0^2\, P_0(q) \tag{1.74}$$

with the total particle number N and normalized particle form factor

$$P_0(q, R) = \frac{\left\langle |F(\mathbf{q})|^2 \right\rangle}{\left\langle |F(0)|^2 \right\rangle} = \frac{\left\langle |F(\mathbf{q})|^2 \right\rangle}{F_0^2}. \tag{1.75}$$

In the following, it will be the task to find analytical expressions of equation (1.75) for different particle shapes and models.

Form factors

Here, the form factor models will be shown, which has been used during the data analysis in chapter 5: the simple sphere, ellipsoid and a spherical core-shell model (see figures 1.9 and 1.10, a).

The most simple particle form is a homogeneous sphere with constant scattering length den-

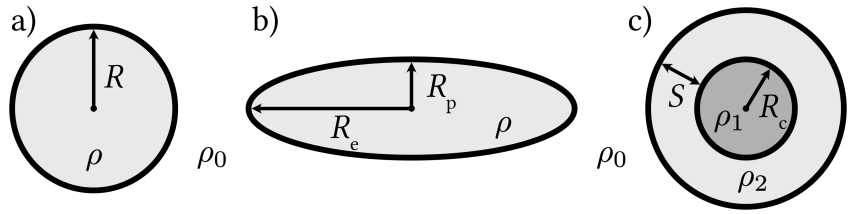

Figure 1.9. Schematic representation of the simple fitting models and their fit parameters: a) homogeneous sphere, b) homogeneous ellipsoid and c) core-shell sphere. For a more detailed description of the individual parameters see chapter 1.3.3

sity ρ. It is completely rotationally symmetric and has an analytical expression for the form factor calculation [175, 176]:

$$P_0^{sphere}(q,R) = 9\left(\frac{\sin qR - qR\cdot\cos qR}{qR}\right)^2 \tag{1.76}$$

with the sphere radius R. Including the prefactor

$$F_0^2 = (\Delta\rho^s)^2\ \frac{V_p^2}{V} \tag{1.77}$$

with the scattering contrast $\Delta\rho^s = \rho - \rho_0$ between the sphere and the solvent, the particle volume $V_p = \frac{4}{3}\pi R^3$ and the scattering volume V, The overall scattering intensity of a homogeneous sphere reads as

$$I_{\text{sphere}} = \frac{N}{V}\,(\Delta\rho^s)^2\ V_p^2\ P_0^{\text{sphere}}(q,R)\,. \tag{1.78}$$

The form factor of an ellipsoid is not an analytical function anymore. It has a lower symmetry than a sphere and its orientation to the incoming wavefront needs to be taken into account during averaging. By introducing the angle α between the scattering vector $\mathbf{q}$ and its perpendicular ellipsoid axis $r = \sqrt{R_e^2\sin^2\alpha + R_p^2\cos^2\alpha}$ [143, 175],

$$P_0^{\text{ellipsoid}}(q,R_e,R_p) = \int_0^{\frac{\pi}{2}} P_0^{\text{sphere}}(q,r)\sin\alpha\,\mathrm{d}\alpha \tag{1.79}$$

with R_e being the ellipsoids equatorial and R_p its polar axis, respectively (see figure 1.9). The subsequent scattering intensity has a very similar to the spherical case:

$$I_{\text{ellipsoid}} = \frac{N}{V}\,(\Delta\rho^s)^2\ V_p^2\ P_0^{\text{ellipsoid}}(q,R_e,R_p)\,, \tag{1.80}$$

where $\Delta\rho^s$ is the scattering contrast between the particle and the solvent and $V_p = \frac{4}{3}\pi R_e R_p^2$ is the ellipsoids volume.

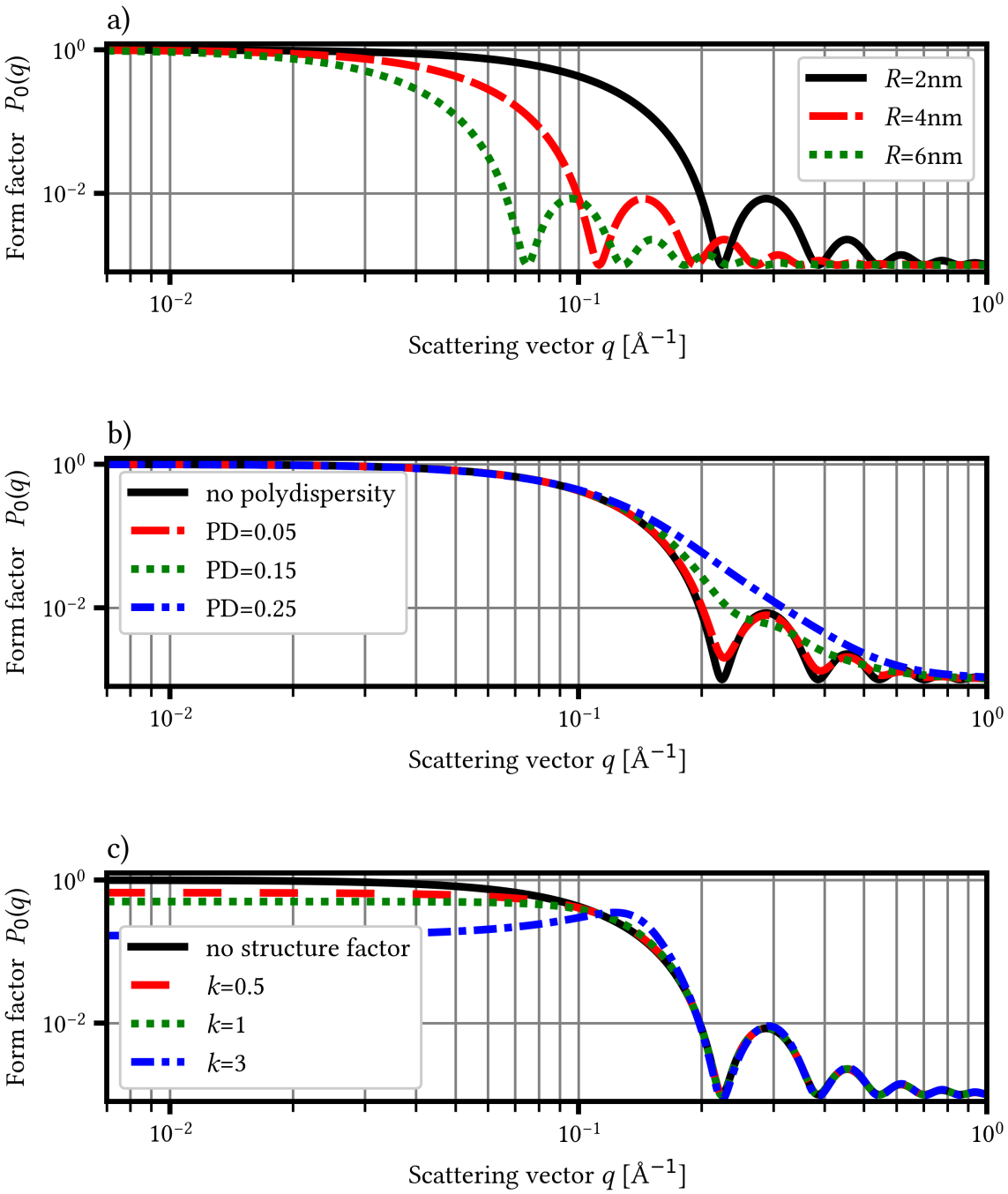

Figure 1.10. Different approaches in model-based analysis to account for (a) different particle sizes, (b) polydispersity (non-uniform particle sizes) and (c) long range order for high particle concentrations. The black solid curves always represent the simulated scattering curve of a sphere with R = 2 nm. To show the polydispersity effect, a Gaussian distribution was used (PD = $\frac{\sigma}{x_0}$). For the structure factor, the Beaucage model was used with ξ = 4 nm.

A more advanced model is that of a core-shell particle consisting of concentric shells. Here, the scattering length density is not constant for the whole particle, but varies for certain areas (see figure 1.9). Depending on the desired complexity, multiple shell levels can be added. The form factor for a composition of a particle core with one additional shell is [152]

$$P_0^C S(q, \rho_c^s, \rho_s^s, R_c, S) = \frac{9}{V_p^2}\Bigg((\rho_c^s - \rho_s^s) V_c \frac{\sin qR_c - qR_c \cos qR_c}{qR_c} + \\ + (\rho_s^s - \rho_0^s) V_p \frac{\sin qR_p - qR_p \cos qR_p}{qR_p} \Bigg)^2 \tag{1.81}$$

with the scattering length densities ρ_c^s, ρ_s^s and ρ_0^s of the particles core, shell and its surrounding solvent, the core radius R_c, the shell thickness S, the radius of whole particle $R_p = R_c + S$ and the volumes $V_c = \frac{4}{3}\pi R_c^3$ and $V_p = \frac{4}{3}\pi(R_c + S)^3$ of the core and of the whole particle, respectively. The scattering intensity can be calculated in accordance to equation (1.78).

Polydisersity

Only *monodisperse* particles with an uniform size and shape will show highly oscillating scattering patterns. If the particle sizes follow a certain distribution, they are called *polydisperse* and the scattering intensity will not exhibit a sharp oscillating structure (see figure 1.10, b). There is a very intuitive explanation for the apparent smearing effect taking place. Different particle sizes give rise to individual scattering curves with shifts in their maxima and minima positions. For an ensemble of differently sized particles, the total scattering intensity is the superposition of each of their scattering curves. Hence, the smearing is due to the summation of slightly shifted maxima and minima. For broader size distributions, the smearing will be more severe than for smaller ones (see figure 1.10, b).

The samples polydispersity can be modeled using certain distribution functions $D(x)$, which are applied during the calculation of I_{scatt}:

$$I_{\text{scatt}} = N \int_0^\infty D(x)\, F_0^2\, P_0(q, x)\, \mathrm{d}x \ . \tag{1.82}$$

The variable x can be any model parameter and $D(x)$ and desired distribution function. In most cases, a Gaussian distribution

$$D(x) = \frac{1}{K} \mathrm{e}^{-\frac{(x-x_0)^2}{2\sigma^2}} \tag{1.83}$$

with the mean value x_0, its standard deviation σ and the normalization constant

$$K = \int_0^\infty D(x)\, \mathrm{d}x \tag{1.84}$$

is sufficient to describe the polydispersity in a sample. It is also possible to use multiple distribution functions for different parameters with an increasing calculation and fitting time.

Resolution effects

Besides the samples polydisperstiy, the smearing of the oscillations can be caused by the resolution function of the experimental set-up [177, 178]. Its main contributions are the imperfect monochromization and collimation of the used radiation. Both effects would lead to a wrongful detection of neutrons or photons. This resolution effect is more pronounced in neutron scattering experiments, since both their wavelength selection and collimation is less precise than for photons. Hence, the experimental resolution has to be taken into account for SANS data analysis. By assuming a gaussian distribution in both the wavelength uncertainty and beam profile due to spacial collimation, the scattering intensity is convoluted with the resolution function $\mathfrak{R}(q, \langle q \rangle)$, which gives the probability of the wave vector $\langle \mathbf{q} \rangle$ to appear at the wrong position $\mathbf{q}$ [179, 177, 178]:

$$I_{\text{scatt}}^{\text{res}} = \int_0^\infty \mathfrak{R}(q, \langle q \rangle)\, I_{\text{scatt}}\, \mathrm{d}q \tag{1.85}$$

with

$$\mathfrak{R}(q, \langle q \rangle) = \frac{q}{\sigma'^2}\, \mathrm{e}^{-\frac{(q+\langle q \rangle)^2}{2\sigma'^2}}\, I_0\left(\frac{q\,\langle q \rangle}{\sigma'}\right) \tag{1.86}$$

and

$$\sigma'^2 = \langle g \rangle^2 \sigma \left(\frac{\lambda}{\Delta\lambda}\right)^2 + 4\langle k \rangle^2 \sigma\,(\Delta\theta)^2 \ . \tag{1.87}$$

Here, $I_0(x)$ is the Bessel function of first kind and zeroth order. $\sigma\left(\frac{\lambda}{\Delta\lambda}\right)$ and $\sigma(\Delta\theta)$ are Gaussian widths due to the finite wavelength distribution and radiation collimation, respectively. They can either be determined experimentally [177] or pre-calculated using the geometrical configuration of the setup [178].

Structure factors

Up to now, only the individual scattering of independent particles was mentioned. This is valid for very dilute or low concentrated samples, but the correlation between an ensemble of particles can have interference effects, i.e. in analogy to crystallography. In case of fluids, the structure effect is more subtle compared to single crystal or powder diffraction, but it is still important to consider for a correct data analysis.

The long range interaction between the particles is described by the so-called structure factor $S(q)$. Depending on the polydispersity of the sample, its application for the scattering intensity in equation (1.74) is different [175]. If *no polydispersity* is applied in the model, the scattering

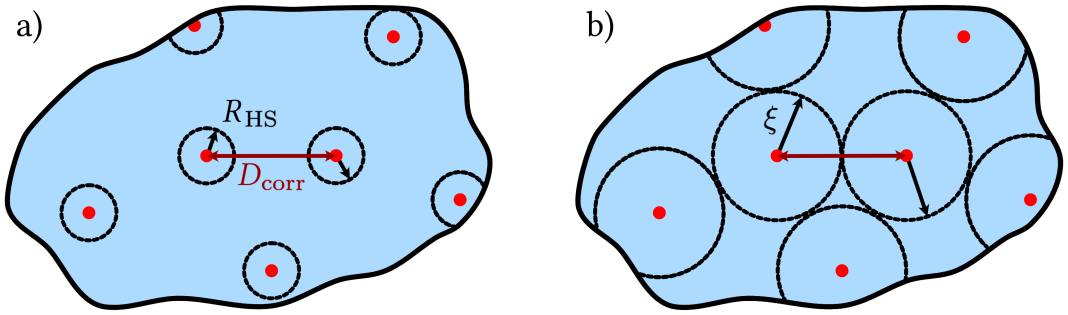

Figure 1.11. Different correlation length for a) the structure factor of hard spheres and b) the BEAUCAGE interference model. With the model parameters in a), the hard sphere potential radius R_{HS} and their volume fraction φ, the inter-micelle correlation distance $D^{a)}_{corr} = R_{HS}/\varphi$. In b), the whole scattering volume is filled with touching hard potential spheres of radius ξ, and the subsequent correlation length is then simply $D^{b)}_{corr} = 2\xi$.

intensity is simply

$$I_{scatt}^{no\ poly} = N\ F_0^2\ P_0(q)\ S(q)\ . \tag{1.88}$$

The polydispersity of the particles in the sample causes different interference patterns than the monodisperse case and has to be treated in a more complex way. In the *local approximation*, each particle is assumed to be surrounded by only identical other particles. This means that they are grouped throughout the sample. For a given size distribution function $D(x)$, the scattering intensity reads as [175]

$$I_{scatt}^{local} = N \int_0^\infty D(x)\ F_0^2\ P_0(q,x)\ S(q,x)\,\mathrm{d}x\ . \tag{1.89}$$

The so-called *decoupling approximation* is used when the particles in the sample are more or less spherical, have roughly the same shape and only a small size distribution [180, 175]. Here, the scattering intensity [180]

$$I_{scatt}^{decoup} = N\ \overline{\langle |F(\mathbf{q})|^2 \rangle} \left(1 + \beta(q)\,[S(q) - 1]\right) \tag{1.90}$$

is a more complex function with

$$\overline{\langle |F(\mathbf{q})|^2 \rangle} = \int_0^\infty D(x)\ F_0^2\ P_0^2(q,x)\,\mathrm{d}x \quad \text{and} \tag{1.91}$$

$$\beta(q) = \frac{\overline{|\langle F(q) \rangle|^2}}{\overline{\langle |F(\mathbf{q})|^2 \rangle}} = \frac{\left(\int_0^\infty D(x)\ F(q,x)\,\mathrm{d}x\right)^2}{\int_0^\infty D(x)\ F^2(q,x)\,\mathrm{d}x}\ , \tag{1.92}$$

where $F^2(q)$ is the unnormalized form factor model from equation (1.74).

There are different models for the theoretical calculation of $S(q)$. They are based on liquid

state theory, which uses the Ornstein-Zernecke equation [181] with an appropriate Percus-Yevick closure relation [182]. Only for spherical interaction potential shapes, $S(q)$ has an analytical form. The most commonly used model is the hard-sphere structure factor. Here, the interaction potential of each particle is modeled by an impenetrable sphere around them. The expression for $S(q)$ reads then as [183, 175]

$$S_{\mathrm{HS}}(q) = \frac{1}{1 + 24\ \varphi_{\mathrm{HS}}\ \frac{G(qR_{\mathrm{HS}})}{qR_{\mathrm{HS}}}} \tag{1.93}$$

with

$$\begin{aligned} G(qR_{\mathrm{HS}} = x) =& \alpha\ \frac{\sin x - x \cdot \cos x}{x^2} \\ &+\beta\ \frac{2x \sin x + [2 - x^2] \cos x - 2}{x^3} \\ &+\gamma\ \frac{-x^4 \cos x + 4\left[(3x^2 - 6)\cos x + (x^3 - 6x)\sin x + 6\right]}{x^5} \end{aligned} \tag{1.94}$$

and the prefactors

$$\alpha = \frac{(1 + 2\varphi_{\mathrm{HS}})^2}{(1 - \varphi_{\mathrm{HS}})^4}\ , \quad \beta = -6\ \varphi_{\mathrm{HS}}\ \frac{(1 + \frac{\varphi_{\mathrm{HS}}}{2})^2}{(1 - \varphi_{\mathrm{HS}})^2} \quad \text{and} \quad \gamma = \frac{\alpha\ \varphi_{\mathrm{HS}}}{2}\ , \tag{1.95}$$

where R_{HS} is the the radius of the hard potential sphere around the particles and φ_{HS} is the subsequent volume fraction of these potential spheres in the solution (see figure 1.11,a). It has to be emphasized, that the particle dimension is not identical with the radius of the potential spheres around them. In this model, the mean inter-particle distance or correlation length is not a fit parameter and can be approximated by $D_{\mathrm{corr}} = R_{\mathrm{HS}}/\varphi_{\mathrm{HS}}$.

A more phenomenological approach for the structure factor is the interference or Beaucage model [172]. It assumes that the whole sample volume is filled with touching spheres with a radius ξ, which is related to the mean inter-particle distances (see figure 1.11,b), and the packing parameter κ [172]:

$$S_{\mathrm{BM}}(q) = \frac{1}{1 + 3\ \kappa\ \frac{\sin q\xi - q\xi \cos q\xi}{(q\xi)^3}}\ . \tag{1.96}$$

Possible values for κ range from 0 to 5.92, which is equivalent for a complete unordered system with no long-range interaction and hexagonal densely packed spheres, respectively. The mean inter-particle distance or correlation length $D_{\mathrm{corr}} = 2\xi$ is a direct fit parameter in this model, which makes it applicable for a wide range sample geometries during data analysis.

1.3.4. Scattering cross section and absolute intensity scale

The interaction probability of photons and neutrons is measured using cross sections (see chapter 1.1). For scattering events, the macroscopic differential cross section is defined as [151, 157]:

$$\frac{\mathrm{d}\Sigma}{\mathrm{d}\Omega} = n\,\frac{\mathrm{d}\sigma}{\mathrm{d}\Omega} = n\,\frac{I_{\mathrm{scatt}}}{I_0}\,R^2\,. \tag{1.97}$$

Here, n is the number density, $\frac{\mathrm{d}\sigma}{\mathrm{d}\Omega}$ the classical differential cross section from high-energy particle physics, I_{scatt} and I_0 is the scattered or incoming intensity of photons or neutrons, respectively, R is the distance from the sample to the detector and $\mathrm{d}\Omega$ is the solid-angle element they are scattered into. The macroscopic cross section is equivalent with the theoretical intensity in equation (1.58). In soft matter studies, the units for $\frac{\mathrm{d}\sigma}{\mathrm{d}\Omega}$ are cm^2 and cm^{-1} for $\frac{\mathrm{d}\Sigma}{\mathrm{d}\Omega}$.

In an scattering experiment, $\frac{\mathrm{d}\Sigma}{\mathrm{d}\Omega}$ is not readily available, since the measured intensity is usually a count rate (s^{-1}) and more complicated [184]:

$$I_{\mathrm{exp}} = \frac{N_{\mathrm{scatt}}}{t} = I_0(\lambda)\cdot A\cdot\Delta\Omega\cdot\eta(\lambda)\cdot T_{\mathrm{sample}}\cdot d_{\mathrm{sample}}\cdot\frac{\mathrm{d}\sigma}{\mathrm{d}\Omega} + \mathrm{BG} \tag{1.98}$$

with the number of scattered photons or neutrons N_{sactt} per time frame t, the incoming flux I_0, the illuminated detector area A, the illuminated and pixel size limited solid angle element $\Delta\Omega$, the detector efficiency η, the sample transmission T_{sample} and thickness d_{sample}, the desired differential cross section $\frac{\mathrm{d}\sigma}{\mathrm{d}\Omega}$ and the background intensity BG. There are two different experimental approaches to obtain the quantity in equation (1.97), which are called primary and secondary calibration methods. For a primary calibration, it is necessary to measure I_{scatt} and I_0 at the same time [184]. Adequate experimental conditions are rare and need either a specialized set-up (e.g. Bonse-Hart layout [185]) or a thorough design and understanding of the I_0 measurement process. The more common procedure is the secondary calibration method, where the measured intensities are compared and scaled to theoretically calculated or experimentally obtained values of $\frac{\mathrm{d}\Sigma}{\mathrm{d}\Omega}$. Here, water [186], vanadium [187] or glassy carbon [188] are the most frequently used calibration materials. In case of water, the differential scattering cross section is

$$\frac{\mathrm{d}\Sigma}{\mathrm{d}\Omega}_{\mathrm{H2O}}(T) = \rho_s^2\cdot k_B\cdot T\cdot\kappa_T \tag{1.99}$$

and only depends on the Boltzmann-constant k_B and material properties like its scattering length density ρ_s, temperature T and isothermal compressibility κ_T. These temperature dependency of ρ_s and χ_T is well-studied and can be found in literature [189]. The ratio of calculated, theoretical intensities and those from the experiment will provide an appropriate scaling factor, which can be used during data processing.

1.4. Reflectivity at surfaces

Material properties can vary greatly when looking at it as bulk, its surfaces or even interfaces of different media. The latter is the basis for topological materials, which are one of the most prominent research fields in physics nowadays. Reflectivity measurements are one of the primary tools for surface and interface science. Since reflectivity or surface scattering are wave-phenomena, the theory of both X-ray and neutron reflectivity is almost identical despite their different interactions with matter. Yet, these differences lead to the great advantage of neutrons over X-rays (see figure 1.12). With the neutron cross section of silicon being several

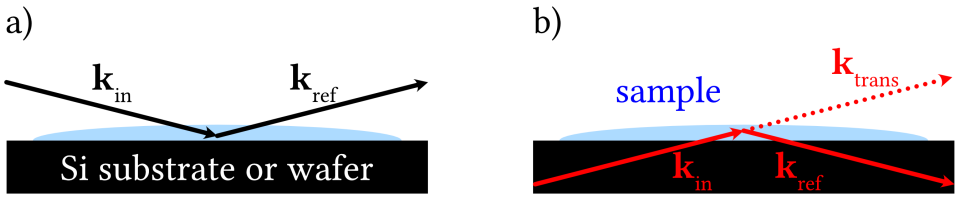

Figure 1.12. Possible scattering geometries in reflectivity experiments. a) direct scattering geometry from the top of the sample film, b) inverse scattering geometry through the substrate.

orders of magnitude lower compared to X-rays, it is possible to use the so-called inverse scattering geometry for neutron reflectiviy measurements (see figure 1.12,b). It circumvents the necessity of ultra-thin film samples and is able to detect "hidden" layers or interfaces close to the substrate or sample holder. This chapter is devoted to the fundamental equations (chapters 1.4.1 and 1.4.2), which are necessary for the data analysis of specular reflectivity (chapter 1.4.3).

1.4.1. Fresnel theory of reflectivity

The classical theory by Fresnel calucaltes the refracted and reflected wave fronts at an interface between two media with different refractive indices n_1 and n_2 (see figure 1.13). Here,

$$\Psi_0 = \Psi_{0,0}\, e^{-i(\mathbf{k}_0\cdot\mathbf{r}+\omega t)}\ ,\ \Psi_r = \Psi_{0,r}\, e^{-i(\mathbf{k}_r\cdot\mathbf{r}+\omega t)} \text{ and } \Psi_t = \Psi_{0,t}\, e^{-i(\mathbf{k}_t\cdot\mathbf{r}+\omega t)} \tag{1.100}$$

are the wave functions of the incoming, reflected and transmitted (refracted) neutron or X-ray wave fields with their respective amplitudes $\Psi_{0,i}$ and wave vectors $\mathbf{k}_i$. In the elastic case, $|\mathbf{k}_0| = |\mathbf{k}_r| = |\mathbf{k}_t|\frac{n_1}{n_2} = \frac{2\pi}{\lambda}$. Each vector consists of components in perpendicular ($\mathbf{e}_\perp$) and parallel ($\mathbf{e}_\parallel$) direction to the interface:

$$\mathbf{k} = k_\perp \cdot \mathbf{e}_\perp + k_\parallel \cdot \mathbf{e}_\parallel\ . \tag{1.101}$$

For reasons of continuity,

$$\Psi_{0,t} = \Psi_{0,0} + \Psi_{0,r} \quad \text{and} \quad (\mathbf{k}_0\cdot\mathbf{r})_{n_1\to n_2} = (\mathbf{k}_r\cdot\mathbf{r})_{n_1\to n_2} = (\mathbf{k}_t\cdot\mathbf{r})_{n_1\to n_2} \tag{1.102}$$

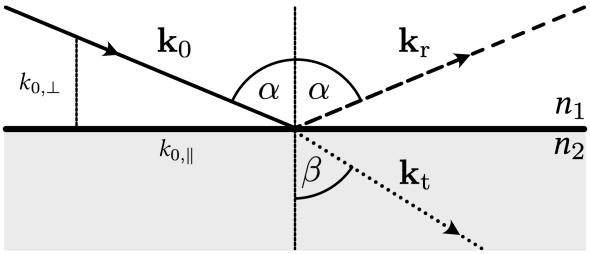

Figure 1.13. Coordinate system for the calculation of the FRESNEL equations of reflectivity. n_1 and n_2 are the different refractive indices at the interface. $\mathbf{k}_0$, $\mathbf{k}_r$ and $\mathbf{k}_t$ are the incoming, refelcted and transmitted wave front, respectively, with their perdenpdicular ($\perp$) and parallel ($\parallel$) components towards the interface.

directly at the boundary condition on the interface. These equations are universal for both X-rays and neutrons and were first solved by FRESNEL in 1823 for the photon case [78]. At the end of his calculation, which can be found in almost every textbook on electromagnetism [105, 190], the FRESNEL coefficients for [105]

$$\text{reflection} \quad r = \frac{\Psi_{0,r}}{\Psi_{0,0}} = \frac{k_{0,\perp} - k_{t,\perp}}{k_{0,\perp} + k_{t,\perp}} = \frac{n_1 \cos\alpha - n_2 \cos\beta}{n_1 \cos\alpha + n_2 \cos\beta} \quad \text{and} \tag{1.103}$$

$$\text{transmission} \quad t = \frac{\Psi_{0,t}}{\Psi_{0,0}} = \frac{2k_{0,\perp}}{k_{0,\perp} + k_{t,\perp}} = \frac{2n_1 \cos\alpha}{n_1 \cos\alpha + n_2 \cos\beta} \tag{1.104}$$

will be found. They are used to calculate the [105]

$$\text{reflectivity} \quad R = r \cdot r^* = \left| \frac{k_{0,\perp} - k_{t,\perp}}{k_{0,\perp} + k_{t,\perp}} \right|^2 \quad \text{and} \tag{1.105}$$

$$\text{transmittance} \quad T = 1 - R = t \cdot t^* = \left| \frac{2k_{0,\perp}}{k_{0,\perp} + k_{t,\perp}} \right|^2 , \tag{1.106}$$

which represents the probability for the wave getting reflected at the interface or penetrating into the other medium. If the wave propagates from the medium with higher to the one with lower refractive index, $R = 1$ and $T = 0$ above a certain critical angle (i.e. $n_2 > n_1$ and $\alpha = 90°$ in figure 1.13). This phenomenon is called total reflection and, according to the DECARTES-SNELLS law (see equation 1.15a), its critical angle is [190]

$$\sin\alpha_c = \frac{n_2}{n_1} . \tag{1.107}$$

For visible light, this effect can trap light inside a medium, e.g. glass prism, water or thin oil film, which has a larger n_2 compared to vacuum or air ($n_1 = 1$). In classical literature about electromagnetism, this phenomenon is called total internal reflection for this reason. Since both X-rays and neutrons have refractive indices $n_2 < 1$, the whole scenario is shifted and they exhibit total external reflection with values for α_c very close to 90°.

1.4.2. Scattering theory of specular reflectivity

In contrast to classical Fresnel theory of reflectivity, scattering theory can give a microscopic explanation for the optical properties, i.e. the refractive index, of a material or sample. It will link n_{med} with its atomic composition using the scattering length density $\rho^{\text{s}}_{\text{med}}$, which was introduced in chapter 1.3. Although both X-rays and neutrons will end up with the same mathematical expressions, its calculation takes different approaches in both cases. Since the following chapters will exclusively treat neutron reflectometry, the X-ray case will be omitted here (for further details see [191]). The interaction of neutrons with an isotropic sample or medium is modeled by its mean interaction potential [192]

$$\overline{V} = \int_V V_{\text{Fermi}}(\mathbf{r})\,\mathrm{d}\mathbf{r} = \frac{2\pi\hbar^2}{m_n}\, b\, \rho_{\text{atom}} = \frac{2\pi\hbar^2}{m_n}\, \rho^{\text{s}} \tag{1.108}$$

with the Fermi potential V_{Fermi} from equation 1.47, the number of atoms per unit volume ρ_{atom} and the scattering length density $\rho^{\text{s}} = b \cdot \rho$. If the medium consists of more than one element or material, ρ^{s} represents the mean scattering length density of the whole layer. By inserting equation (1.108) into the stationary Schrödingers equation (time-independent variant of equation (1.6)), it takes the form [192]

$$\frac{\mathrm{d}^2\Psi}{\mathrm{d}r^2} + k^2\,\Psi = 0 \quad \text{with} \quad k^2 = \frac{2m_n}{\hbar^2}(E - V_{\text{mean}})\,. \tag{1.109}$$

$E = \frac{\hbar^2 k_0^2}{2m_n} = \frac{h^2}{2m_n\lambda^2}$ is the vacuum energy of the neutrons. In classical optical theory, the refractive index is then defined by [192]

$$n^2_{\text{med}} = \frac{k^2}{k_0^2} = \frac{E - V}{E} = 1 - \frac{V}{E} = 1 - \frac{\lambda^2\rho^{\text{s}}}{2\pi} \tag{1.110}$$

with the neutron wavelength λ. Since the refractive index is very close to one for small neutron wavelength, the final result yields [192]:

$$n_{\text{med}} \approx 1 - \frac{\lambda^2\rho^{\text{s}}}{2\pi}\,. \tag{1.111}$$

In scattering theory it is more convenient to use the scattering angle θ instead of the optical angle α (see figures 1.13 and 1.14). The change of definition leads to a π-shift and the subsequent critical scattering angle [192]

$$\cos\theta_{\text{c}} = \frac{n_{\text{med}}}{n_{\text{vac}}}\,. \tag{1.112}$$

Since the critical optical angles α_{c} are close to 90°, θ_{c} is usually very small and a Taylor expansion yields [192]

$$\theta_{\text{c}} \approx \sqrt{\frac{\rho^{\text{s}}}{\pi}}\,\lambda \tag{1.113}$$

with its corresponding scattering vector

$$q_c = \frac{4\pi}{\lambda} \sin\theta_c \approx 4\sqrt{\pi\rho^s} \ . \tag{1.114}$$

The specular reflectivity gives information about the of the sample perpendicular to the substrate, i.e. its atomic composition and layering. There are two different theoretical approaches known from classic optics [190]: the dynamical theory, which explicitly derives the wave functions on their way through the medium, and the kinematical approach, which directly links the samples layer composition (scattering length densities and thicknesses) with the observed reflectivity pattern.

Dynamical approach - PARRATTS formalism

The dynamical theory of reflectivity was first derived for X-rays by PARRATT in 1954 [193]. Starting with a single layer of certain thickness d, the propagating waves will be either reflected or refracted according to FRESNEL theory. This gives rise to the so-called multi-scattering events inside the layer (see figure 1.14). The total reflected wave is the superposition of all possible multi-scattering events and its FRESNEL coefficient is [194]

$$r = r_{0,1} + t_{0,1}r_{1,2}t_{1,0}\, e^{-i\varphi} + t_{0,1}r_{1,2}r_{1,0}r_{1,2}t_{1,0}\, e^{-i2\varphi} + t_{0,1}r_{1,2}r_{1,0}r_{1,2}r_{1,0}r_{1,2}t_{1,0}\, e^{-i3\varphi} + \dots \ . \tag{1.115}$$

Here, $r_{i,j}$ or $t_{i,j}$ is the reflection or transmission coefficient for the transition at the interface from medium i to medium j and $\varphi = d_1 q_1 = d_1 \frac{4\pi}{\lambda} \sin\theta_1$ is the phase difference of the respective waves. Factoring out $t_{0,1}r_{1,2}t_{1,0}\, e^{-i\varphi}$ in equation (1.115) leads to the geometric series and the total reflection coefficient takes the form [194]

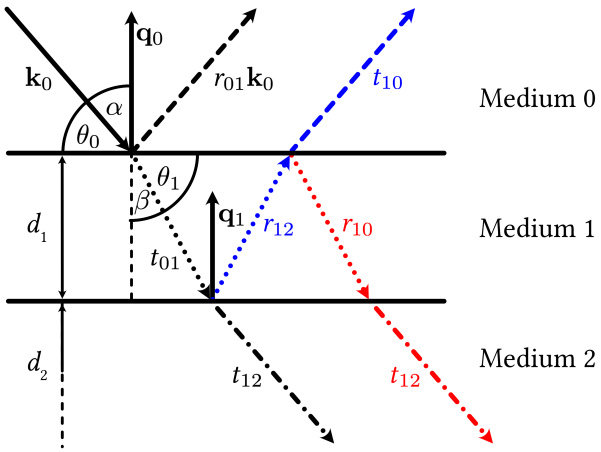

Figure 1.14. Exemplary sketch of possible multi-scattering events. The abbreviations r_{ij} and t_{ij} represent the FRESNEL coefficients at the respective interface. The amplitudes of the related wave functions are simply the product of these coefficients on their way through the sample.

$$
\begin{aligned}
r =& r_{0,1} + t_{0,1} r_{1,2} t_{1,0}\, \mathrm{e}^{-\mathrm{i}\varphi} \left(1 + r_{1,0} r_{1,2}\, \mathrm{e}^{-\mathrm{i}\varphi} + r_{1,0}^2 r_{1,2}^2\, \mathrm{e}^{-\mathrm{i}2\varphi} + \dots\right) \\
=& r_{0,1} + t_{0,1} r_{1,2} t_{1,0}\, \mathrm{e}^{-\mathrm{i}\varphi} \left(\sum_{n=0}^{\infty} r_{1,0}^n r_{1,2}^n\, \mathrm{e}^{-\mathrm{i}n\varphi}\right) \\
=& r_{0,1} + t_{0,1} r_{1,2} t_{1,0}\, \mathrm{e}^{-\mathrm{i}\varphi} \left(\frac{1}{1 - r_{1,0} r_{1,2}\, \mathrm{e}^{-\mathrm{i}\varphi}}\right) \\
=& \left(r_{0,1} + r_{1,2}\, \mathrm{e}^{-\mathrm{i}\varphi}\right) \left(\frac{1}{1 + r_{0,1} r_{1,2}\, \mathrm{e}^{-\mathrm{i}\varphi}}\right) .
\end{aligned}
\tag{1.116}
$$

In the last step, it was used that $r_{0,1} = -r_{1,0}$ and $t_{1,0} t_{0,1} = 1 - r_{0,1}^2$ for non-absorbing media [194, 105]. The last bracket in equation (1.116) represents the multi-scattering correction. Similarly, an expression for the total transmission coefficient can be derived [195]:

$$
\mathrm{t} = \frac{t_{0,1}\, t_{1,2}\, \mathrm{e}^{-\mathrm{i}\varphi}}{1 + r_{0,1} r_{1,2}\, \mathrm{e}^{-\mathrm{i}\varphi}} \tag{1.117}
$$

If the single layer is extended to a multilayer with j independent layers each with a thickness d_j (see figure 1.14), Parratts recursive formula [193]

$$
X_j = \frac{r_{j,j+1} + X_{j+1}\, \mathrm{e}^{-\mathrm{i}d_j q_{j+1}}}{1 + r_{j,j+1} X_{j+1}\, \mathrm{e}^{-\mathrm{i}d_j q_{j+1}}} . \tag{1.118}
$$

will follow for the amplitude ratio $X_j = \frac{r_j}{t_j}$ between the reflected and transmitted wave in the jth layer. $r_{j,j+1}$ is calculated using Frenels equation (1.103). Since all refractive indices are close to one, equation (1.103) can be approximated using Decartes-Snells law (1.15a) and equation (1.41) to read as [194]

$$
r_{j,j+1} = \frac{q_{j+1} - q_j}{q_{j+1} + q_j} \tag{1.119}
$$

with

$$
q_j = \sqrt{q^2 - q_{\mathrm{c},j}^2} . \tag{1.120}
$$

Here, q is the scattering vector in vacuum (X-rays) or the substrate (neutrons) and $q_{\mathrm{c},j}$ is the critical wave vector of the jth layer. The critical value is always calculated with respect to vacuum using equation (1.114). The recursion formula is initiated with $X_{j+1} = 0$, which represents no possible reflection due to either a thick substrate (in case of X-rays) or bulk sample (neutrons). After $j + 1$ iterations, the reflectivity [195]

$$
R = |X_0|^2 \tag{1.121}
$$

between the sample and vacuum (X-rays) or the substrate (neutrons) is reached (see figure 1.12).

Kinematical apporach

Up to now, a sample consisted of a certain assortment of optical interfaces resulting in multiple reflected and transmitted waves, whose interference was explicitly calculated. In the kinematical theory, the appearing reflectivity pattern is not attributed to sharp interfaces but to a continuous change of material properties, namely the scattering length density, throughout the sample. Equation (1.119) can be rewritten as [194]

$$r_{j,j+1} = \frac{q_{j+1} - q_j}{q_{j+1} + q_j} = \frac{\sqrt{1 - \left(q_{\mathrm{c},j+1}/q\right)^2} - \sqrt{1 - \left(q_{\mathrm{c},j}/q\right)^2}}{\sqrt{1 - \left(q_{\mathrm{c},j+1}/q\right)^2} + \sqrt{1 - \left(q_{\mathrm{c},j}/q\right)^2}} \,. \tag{1.122}$$

For $q \gg q_\mathrm{c}$,

$$r_{j,j+1} \approx \frac{q_{\mathrm{c},j+1}^2 - q_{\mathrm{c},j}^2}{4q^2} = \frac{4\pi\left(\rho_{j+1}^\mathrm{s} - \rho_j^\mathrm{s}\right)}{q^2} \tag{1.123}$$

with the scattering length densities ρ^s of the respective layers. The kinematical theory ignores all multi-scattering events. Every neutron is scattered and reflected only once at each interface between layers. Consequently, the total reflection coefficient is the simple summation over all layers [196, 194, 197]

$$r = \sum_{j=0}^{\infty} r_{j,j+1}\, \mathrm{e}^{-\mathrm{i}d_j q} = \frac{4\pi}{q^2} \sum_{j=0}^{\infty} \left(\rho_{j+1}^\mathrm{s} - \rho_j^\mathrm{s}\right)\, \mathrm{e}^{-\mathrm{i}d_j q} \tag{1.124}$$

with the individual layer thickness d_j. If the layers are assumed to be infinitesimal thin, the discrete summation becomes [196, 194, 197]

$$r = \frac{4\pi}{q^2} \int_{-\infty}^{\infty} \frac{\mathrm{d}\rho^\mathrm{s}(z)}{\mathrm{d}z}\, \mathrm{e}^{-\mathrm{i}zq}\, \mathrm{d}z \;, \tag{1.125}$$

where the z-axis points in the direction perpendicular to the substrate. In the inverse scattering geometry, the neutrons first hit the substrate-sample interface with its critical angle $\theta_\mathrm{c}^{-\infty}$ and scattering vector $q_\mathrm{c}^{-\infty}$. The reflectivity $R = 1$ for scattering angles $\theta \leq \theta_\mathrm{c}^{-\infty}$ and $q \leq q_\mathrm{c}^{-\infty}$. To account for that fact, the modified scattering variable [196]

$$q' = q - q_\mathrm{c}^{-\infty} \tag{1.126}$$

can be introduced and the subsequent total reflectivity is [194, 198]

$$R = r \cdot r^* = \frac{(4\pi\rho_{-\infty}^\mathrm{s})^2}{q^4} \left| \frac{1}{\rho_{-\infty}^\mathrm{s}} \int_{-\infty}^{\infty} \frac{\mathrm{d}\rho^\mathrm{s}(z)}{\mathrm{d}z}\, \mathrm{e}^{-\mathrm{i}zq'}\, \mathrm{d}z \right|^2 \tag{1.127}$$

with the scattering length density $\rho^s_{-\infty}$ of the substrate. Solving the square convolution $|\cdot|^2$ leads to an alternative version of equation (1.127) [199]:

$$\frac{R}{R_F} = 2\int_0^\infty \mathrm{p}^*(z)\ \cos\left(zq'\right)\mathrm{d}z \quad \text{with} \quad R_F = \left|(q_{sub} - q_{bulk})/(q_{sub} + q_{bulk})\right|^2 . \tag{1.128}$$

The newly introduced function $p^*(z)$ is the symmetrical auto-correaltion or Patterson function [200]

$$p^*(z) = \int_0^\infty \frac{\mathrm{d}\rho^s}{\mathrm{d}z}(z') \cdot \frac{\mathrm{d}\rho^s}{\mathrm{d}z}(z + z')\,\mathrm{d}z' \tag{1.129}$$

of the first derivative of the scattering length density perpendicular to the surface. Its Fourier transformation is R/R_F, which normalizes the reflectivity data by the rapid q^{-4} decay of the substrate interface and amplifies the structural pattern of the sample. The prefactor $\frac{1}{\rho^s_{-\infty}}$ in equation (1.128) can be omitted when $\rho^s(z)$ is given in units of $\rho^s_{-\infty}$. Due to its striking resemblance with the pair-distance distribution function in small-angle scattering (see equation (1.58 in chapter 1.3.2), the auto-correlation function p^*(z) can be calculated using methods based on the indirect Fourier transformation [198, 199] or other numerical recipes, which calculate the correlation functions in real space [195].

1.4.3. Analysis of reflectivity data

There are two approaches for analysing specular reflectivity data, which either use the dynamical theory and *a priori* knowledge about the scattering length density profile perpendicular to the surface or work independent of any model with equation (1.127) from kinematical theory. Both approaches are equally valid, under the appropriate conditions and using sufficient corrections [198]. Yet, most commonly available data analysis software is based on Parratts formalism due to its robust simplicity and numerical rapidness.
The aim of a reflectometry experiment is to solve the samples structure close to the surface using the scattering length density profile $\rho^s(z)$, which is defined as

$$\rho^s(z) = \begin{cases} \rho^s_{substrate} & \text{for} \quad z < 0, \\ \rho^s_1 & \text{for} \quad 0 \le z < d_1, \\ \quad\vdots & \\ \rho^s_j & \text{for} \quad d_j \le z < d_{j+1}, \\ \rho^s_{bulk} & \text{for} \quad z \ge d_{j+1}, \end{cases} \tag{1.130}$$

where j indicate the layer number, ρ^s_j its scattering length density and d_j its thickness (see figure 2.5). The scattering length density is linked with samples macroscopic density, which can give information about its molecular and phase composition, e.g. the sample-solvent ratio. At each interface between consecutive layers j and $j+1$ the reflection coefficient $r_{j,j+1}$ from equation (1.119) is calculated and inserted into Parratts formula (1.118). If $q < q_c$ for the substrate-sample interface, no transmission can occur and $R = 1$, which leads to the characteristic and sharp edge in the resulting reflectivity pattern (see figure 1.16, b).

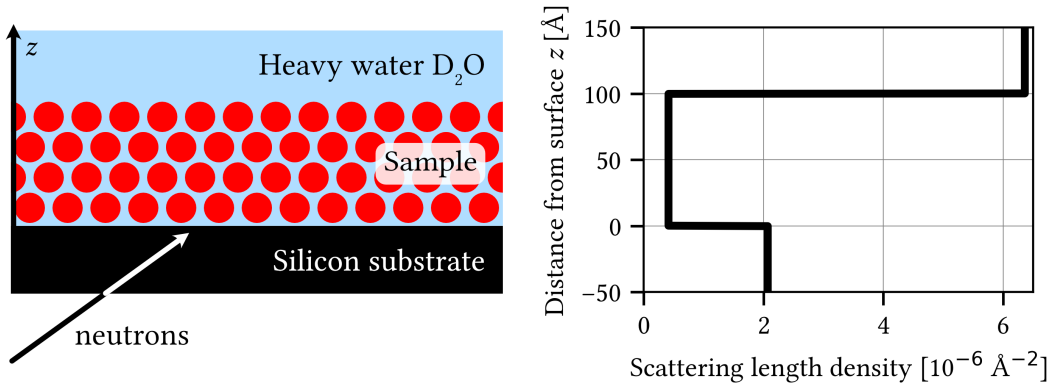

Figure 1.15. Model of the scattering length density profile $\rho(z)$ based on the sample structure. The profile function represents the scattering length density and consequently the material, which the neutrons encounter on their way through the sample. In neutron experiments, the origin $z = 0$ is always placed at the interface between substrate and sample. In the present case, the sample consists of one 100 Å thick layer, which has a constant scattering length density. The exact values are $\rho^{\mathrm{s}}_{\mathrm{substrate}} = 2.07 \cdot 10^{-6}\text{Å}^{-2}$, $\rho^{\mathrm{s}}_{\mathrm{sample}} = -0.44 \cdot 10^{-6}\text{Å}^{-2}$ and $\rho^{\mathrm{s}}_{\mathrm{bulk}} = 6.36 \cdot 10^{-6}\text{Å}^{-2}$, which represent silicon a substrate, polymer sample and heavy water, respectively.

In real samples, the interfaces are not perfect and the transitions in $\rho^{\mathrm{s}}(z)$ are smeared due to interdiffusion between different layers [192]. This effect can be approximated using a Gaussian distribution with a standard deviation of σ_j around a mean value z_j and the sharp step-function will be replaced by the standard error function [192, 195]

$$\operatorname{erf}\left(\frac{z - z_j}{\sigma_j}\right) = \frac{2}{\pi}\int_0^{(z-z_j)/\sigma_j} \mathrm{e}^{-t^2}\,\mathrm{d}t \ . \tag{1.131}$$

Consequently, the area of interdiffussion has a thickness of $2\sigma_j$ (see figure 1.16) and the reflection coefficients in equation (1.119) become

$$r^{\sigma_j}_{j,j+1} = r_{j,j+1} \cdot \mathrm{e}^{-2\sigma_j^2 q_j q_{j+1}} \ . \tag{1.132}$$

The parameter σ will be called roughness from now on. With increasing σ the oscillations in the reflectivity pattern are damped while the FRESNEL q^{-4}-decay is amplified (see figure 1.16).

In addition to the smearing by the interface roughness, the experimentally obtained data is certainly influenced by resolution effects of both the used neutrons and instrumentation. PARRATTS reflectivity model can be modified to take these effects into account [199]:

$$R^{\mathrm{res}} = \int_0^{\infty} \mathfrak{R}(q, \langle q \rangle)\, R\, \mathrm{d}q \tag{1.133}$$

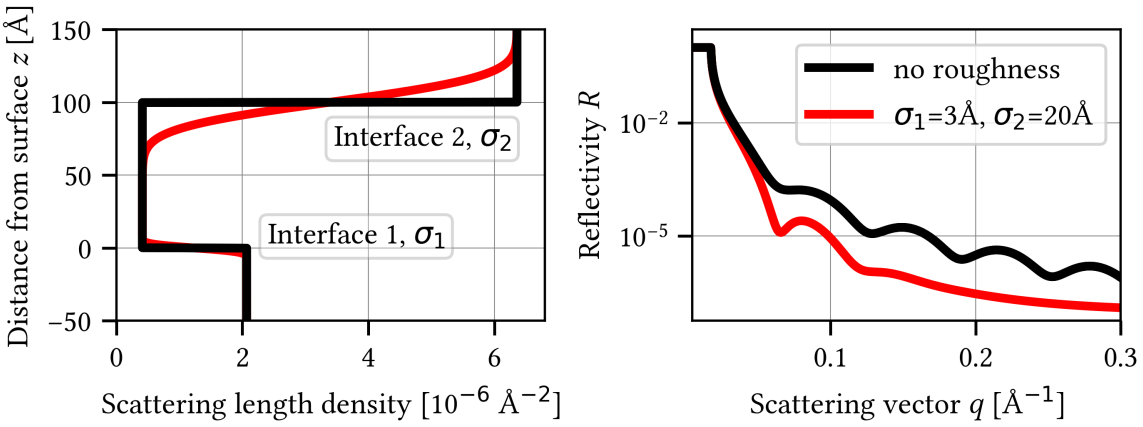

Figure 1.16. Influence of the interface roughness on the specular reflectivity.

with the resolution function $\mathfrak{R}(q, \langle q \rangle)$ from equation (1.86) and (1.87) in chapter 1.3.3. The influence of this function is the same as it was discussed in the context of small-angle scattering: it damps the oscillation in the reflectivity pattern. In the case of neutrons, it is necessary to apply the correct resolution model in order to obtain meaningful results for the scattering length profile. Yet, the geometric component of $\mathfrak{R}(q, \langle q \rangle)$ can be neglected for neutron reflectometry (see equation (1.87) and its discussion in chapter 1.3.3), since their wavelength distribution is the dominant contribution on the finite resolution with values for $\frac{\Delta\lambda}{\lambda}$ up to 10%.

2. Sample system

Since their first correct scientific description by Staudinger in 1920 [201], polymers became an irrevocable part of modern economy and society with a worldwide production volume of 370 Mt (megatons) in 2018 [202]. Despite their obvious use as plastics and packing materials, polymers offer a wide-range of applications due to their chemical versatility.

Pluronics are industrial polymers, which are based on the two organic compounds propylene (PO) and ethylene oxide (EO) and are commercially available at BASF. Depending on their chemical composition, i.e. EO-PO ratio, block lengths and molar masses, the resulting polymers will be solids or liquids. They quickly outgrew their initial use as lubricants and additives for detergents or cosmetics [32] with early pharmaceutical applications in the 1980s [35, 203]. Since more than three decades, their aggregates, crystallization and adsorption behavior was already subject to extensive fundamental research [54], which led to their standardized use as structure directing agents in the synthesis of mesopourous silica [47] and functionalized surfaces [204].

Chapter 2.1 will cover general concepts, an introduction to the mathematical description of polymer solutions by Flory and the theoretical framework of polymer brushes, which are produced by adsorption onto a surface. In Chapter 2.2, the triblock copolymer Pluronic P123 will be introduced, focusing on its current state of the art and novel scientific applications. Although P123 is one of the most commonly used Pluronic variations, several other Pluronic variations with different EO-PO ratios and molecular weights are described in literature. Consequently, this chapter will summarize the results of a multitude of Pluronics with careful discussion of the results in the context of Pluronic P123. At last, chapter 2.3 will treat the chemical methods for the preparation of hydrophilic and hydrophobic silicon surfaces.

2.1. Polymer physics

The field of polymer physics describes the motion and physical properties of polymer materials. It was pioneered by Huggins[205], Flory [206], Edwards [207] and de Gennes [208] in the 20th century, who developed a theoretical framework for the description of polymer chains in different solvents using statistical and scaling methods. The following chapters will clarify the essential concepts of polymer physics (chapter 2.1.1) and only treat those equations of Flory theory for solutions (chapter 2.1.2) and surfaces (chapter 2.1.3), which will be relevant for later data analysis. For a full introduction, the reader is referred to the excellent textbooks by the already mentioned pioneering authors [209, 210] and Rubinstein [211].

2.1.1. General concepts

A **polymer** is a molecule consisting of elementary, chemical and structural units, which are called **monomers**. The process of forming a polymer is called **polymerization**, which convalently binds the monomers to form a chain-like repeating structure. If there is only one species of monomers, the resulting structure is called a **homopolymer** (see figure 2.1).

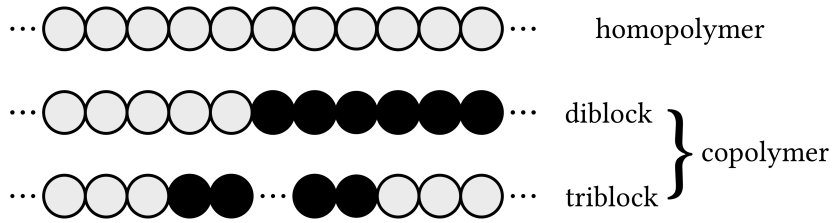

Figure 2.1. Schematic drawing of different polymer types. The grey and black spheres represent two different monomers.

With more than one monomer species, the macromolecule is called a **heteropolymer**. The unique properties of these molecules are based on the chemical structure of their different monomers and the chain sequencing. Primary examples of heteropolymers are protiens, which can inherit multiple amino acids. One of the special cases is a **copolymer**, which consists of exactly two different monomers.The two monomers usually form blocks. A **diblock** copolymer consists of two separated monomer block, while a **triblock** copolymer has a middle and two end blocks. The molar mass of a polymer is [211]

$$M = \sum_i N_i \cdot M_i^{\text{mono}} \tag{2.1}$$

with the molar mass of its monomer species M_i^{mono} and their degree of polymerization N_i, which is the number of monomers in each block. During polymerization, the polymers composition and architecture is fixed, but polymers can still adopt multiple different conformations. A conformation is the spatial structure of a polymer, which is determined by the relative location of its monomers. Most conformations are self-similar or fractal. Since the polymer is moving and adapting different conformation, it is hard to find a reliable definition for its size.

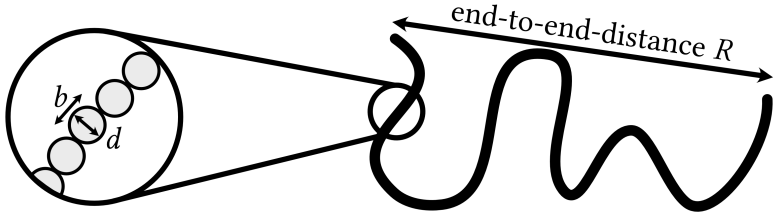

Figure 2.2. One conformation of a chain-like polymer and the definition of its end-to-end distance R. The monomer units have the molecular dimensions b and d.

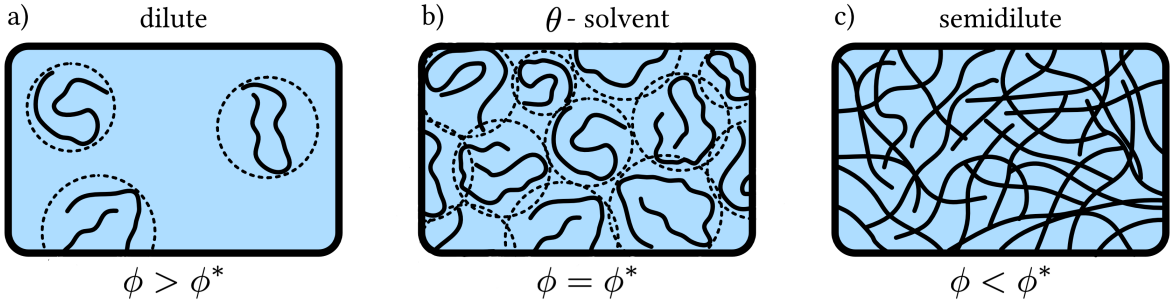

Figure 2.3. Representation of a polmyer solutions different solubility states. ϕ is the macroscopic volume fraction of the polymers in solution, while ϕ^* is the overlap volume fraction.

The conformation-averaged end-to-end distance R is linked with the degree of polymerization N by [209]

$$N \propto \langle R^2 \rangle \,. \tag{2.2}$$

Depending on its fractality, any smaller section with radius r of the polymer is then propotional to its monomer content g (see figure 2.2) [211]:

$$g \propto \left(\sqrt{\langle r^2 \rangle} \right)^{\mathfrak{D}} \,. \tag{2.3}$$

Here, $\mathfrak{D}$ is the fractal dimension, which is influenced by different conditions of the polymer, e.g. its composition or the surrounding solvent and temperature.
The solubility of polymers in a solvent can be classified using its volume fraction [211]

$$\phi = \frac{c_m}{\rho} = c_m \frac{V^{\text{mono}}}{M^{\text{mono}}} N_\text{A} \,, \tag{2.4}$$

where c_m is the polymers mass concentration, ρ its density, V^{mono} the monomer volume and M^{mono} its molar mass. Since the polymers can be entangled with themselves in certain conformations, another important quantity is the so-called overlap volume fraction [211]

$$\phi^* = \frac{N \cdot V^{\text{mono}}}{V_p} \tag{2.5}$$

which compares the "stretched" polymer volume $N \cdot V^{\text{mono}}$ with the pervaded volume

$$V_p = R^3 \,, \tag{2.6}$$

where R is the end-to-end distance of the certain conformation. The pervaded volume can also be seen as the solution volume, which is covered by the whole polymer. Then, ϕ^* gives the fraction of actual polymer in this volume. If $\phi < \phi^*$, the polymer solution is called dilute [211] (see figure 2.3, a). The distance between the polymers is larger than their size. In the

case that $\phi = \phi^*$, the solution is densely filled with polymers (figure 2.3, b). For $\phi > \phi^*$, the polymer solution is called semidilute (figure 2.3, c). Although $\phi < 1$, the physical properties of the solution are dominated by the polymers and only small changes in concentration can change them drastically [211].

2.1.2. Flory theory of polymer solutions

Real polymer chains do not only interaction with the surrounding solvent, but the monomers are interacting with each other as well. The probability of finding two monomer in a given distance r form each other is given by the so-called Mayer-f-function [212]

$$f(r) = \mathrm{e}^{\frac{U(r)}{k_B T}} - 1 \,, \tag{2.7}$$

where $U(r)$ is the interaction potential between the monomers, k_B is Boltzmanns constant and T is the temperature. Its three-dimensional spacial integral is called the excluded volume [206, 211]

$$v = -\int f(r)\,\mathrm{d}^3 r = \int \left(1 - \mathrm{e}^{\frac{U(r)}{k_B T}}\right) \mathrm{d}^3 r \,, \tag{2.8}$$

which gives a measure whether the interaction between monomers is attractive or repulsive. Depending on the value of v, the polymer-solvent interaction and its solubility can be characterized as

- a **good solvent**, if $v < 0$ with slightly more favorable inter-monomer interactions compared to monomer-solvent ones,
- a θ-**solvent**, if $v = 0$, which happens at the so-called θ-temperature, where all polymer chains have their ideal conformations with no penalty for monomer-monomer contact, and
- a **poor solvent**, if $v > 0$, the attractive monomer interactions dominate and the monomers are close together and less hydrated.

To further quantify the monomer and solvent interaction energies, the theories of Flory [206] and Huggins [205] can be used. Both assumed that the monomers of a polymer are uncorrelated and evenly distributed in its pervaded volume $V_p = R^3$ with $R > b \cdot N^{\frac{1}{2}}$. The monomer interaction energy is then given by [205, 206]

$$E_{\mathrm{int}} = N \cdot k_B T \cdot \frac{N}{R^3} \cdot v \,. \tag{2.9}$$

The first factor is again the degree of polymerization N, which gives the number of monomers in a polymer chain. The second factor $k_b T$ is the assumed energy cost for excluding a monomer from the excluded volume v. The last factor $\frac{N}{R^3} v$ gives the probability of two monomers being in the same excluded volume [211]. When the monomers change their position, the polymer

conformation and its entropy is changed as well. This entropic energy contribution is modeled by [211]

$$E_{\text{ent}} = k_B T \cdot \frac{R^2}{N \cdot b^2} , \tag{2.10}$$

with the monomer size b. Equation (2.10) is the energy that would be required to stretch the polymer to its end-to-end-distance R. Hence, the total FLORY-HUGGINS-energy is [211]

$$E_{\text{FH}} = E_{\text{int}} + E_{\text{ent}} = k_B T \left(\upsilon \cdot \frac{N^2}{R^3} + \frac{R^2}{N \cdot b^2} \right) . \tag{2.11}$$

Minimization of equation (2.11) yields the ideal chain size [206, 205]

$$R_{\text{F}} = \upsilon^{\frac{1}{5}} \cdot b^{\frac{2}{5}} \cdot N^{\frac{3}{5}} , \tag{2.12}$$

which can be extended to a universal power law [210]

$$R \propto N^{\frac{1}{\nu}} \tag{2.13}$$

in a more generalised treatment [209]. Here, ν is the so-called FLORY exponent, which is connected with the fractality $\mathfrak{D}$ of the polymer by

$$\frac{1}{\nu} = \mathfrak{D} . \tag{2.14}$$

For an ideal chain in a θ-solvent, $\nu = \frac{1}{2}$ and $\mathfrak{D} = 2$ as expected for a Gaussian monomer distribution [209, 207, 210, 205, 211]. Depending on other additional correlation between the monomers, the energies in equation (2.11) are altered, which will lead to different values of ν. Equations (2.13) and (2.14) are the fundamental connection between the theoretical field of polymer physics and experimental methods like light, neutron and X-ray scattering.

2.1.3. Surface adsorption and polymer brushes

If polymers come in contact with a surface, it is possible that they gain a certain amount of energy due to adsorption. At the same time, their confinement to a certain height or thickness above the surface will result in an entropic energy penalty. By assuming an even distribution of monomers at different distances from the surface up to a certain thickness d_{ads}, the energetic gain of surface interaction is [211]

$$E_{\text{surf}} = -N \cdot \delta k_B T \cdot \frac{b}{d_{\text{ads}}} \tag{2.15}$$

with the a dimensionless constant δ ($0<\delta<1$). The first factor gives the total number of monomers in the polymer, the second is the energy gain of one monomer when it comes in contact with the surface and the last one gives the number of monomers in the adsorbed layer. With the subsequent entropic conformation energy loss due to the confinement, the total energy reads

as [211]

$$E = E_{\text{conf}} + E_{\text{surf}} = N \cdot k_B T \cdot \left(\frac{b}{d_{\text{ads}}} \right)^{\nu} - N \cdot \delta k_B T \cdot \frac{b}{d_{\text{ads}}} \,. \tag{2.16}$$

The entropic contribution E_{conf} needs the Flory-coefficient ν to account for the different conformations of the polymer depending on the interaction with the solvent and surface. Minimizing equation (2.16) with respect to d_{ads} yields the optimal layer thickness

$$d_{\text{ads}}^{\text{opt}} = b \; \delta^{-\frac{\nu}{1-\nu}} \tag{2.17}$$

and energy of surface adsorption

$$E_{\text{ads}} = E\left(d_{\text{ads}}^{\text{opt}}\right) = N \; k_B T \; \delta^{\frac{1}{1-\nu}} \,. \tag{2.18}$$

Both equations are very simple and do not account for additional effects and entropic contributions, e.g. stacking and proximity effects near the surface, but give a good first estimate for the fractality and conformation of the polymers near the surface as well as the necessary surface energies.

A special case of surface structures is the so-called Alexander-de Gennes polymer brush [213, 214] (see figure 2.4). Here, the polymers are assumed to be placed on the surface with a certain density σ. A second assumption is that the polymer chains reach into the solution with a certain distance H, after which no polymers will be found. The associated length scale of polymer density at the surface [213, 214]

$$\xi = \frac{1}{\sqrt{\sigma}} = \sigma^{\frac{1}{2}} \tag{2.19}$$

is called correlation length and represents their mean spacing. Since the polymers are homogeneously distributed, the adsorbed layer is filled with correlation "blobs" ξ^3 (see figure 2.4,

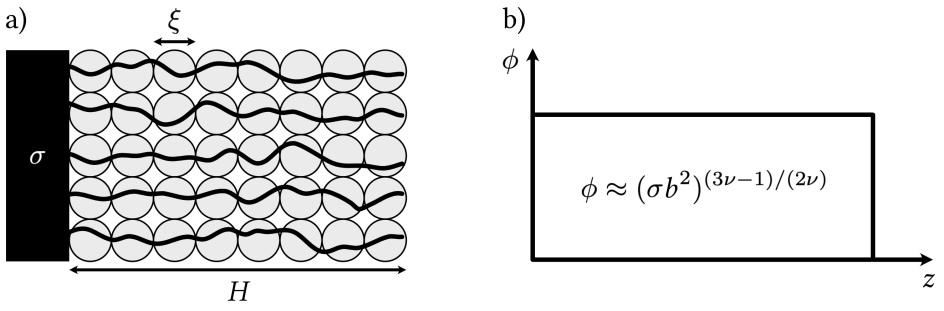

Figure 2.4. The Alexander-de Gennes brush. a) schematic representation of the polymer density σ near the surface, their associated correlation "blobs" ξ and the brush height H. b) corresponding volume fraction profile perpendicular to the surface.

a). The resulting brush height is given by [213, 214]

$$H = \xi \cdot \frac{N}{g} = N\ \sigma^{\frac{1-\nu}{2\nu}}\ b^{\frac{1}{\nu}} \tag{2.20}$$

with the number of monomers per correlation volume

$$g = \left(\frac{\xi}{b}\right)^{\frac{1}{\nu}} = \sigma^{-\frac{1}{2\nu}}\ b^{-\frac{1}{\nu}}\ , \tag{2.21}$$

the degree of polymerization N, the surface density σ and the molecular monomer size b. Since the correlation "blobs" are not completely filled with polymers, the volume fraction profile of the brush perpendicular to the surface is then (see figure 2.4, b) [213, 214]

$$\phi = \begin{cases} g\ \frac{b^3}{\xi^3} = \left(\sigma\ b^2\right)^{\frac{3\nu-1}{2\nu}} & \text{for} \quad z < H, \\ 0 & \text{for} \quad z > H \end{cases} . \tag{2.22}$$

There are more models for polymer brushes, which assume more complex geometries for more specialized cases. Another popular and general model [30] uses a parabolic formula for the volume fraction, but is not analytically solvable anymore. The Alexander-de Gennes brush is a good estimate for homogeneous layer structure, i.e. a polymer melt.

If the polymers adsorption is more complex, less homogeneous or if multiple polymer sections touch the surface, multi-chain adsorption has to be considered [209, 211]. A model for this purpose is the so-called de Gennes self-similar carpet [209]. Although the polymers chains try to minimize their energies by surface contacts, which leads to a high monomer concentration near the surface, the subsequent crowded chains elements start to repel each other. The optimal thickness of the near surface layer can be determined by equation (2.17). Only the polymer sections close to the surface gain energy through contacts, while polymer sections further away do not gain any energy, but relax the high concentrations at the surface to reasonable values in the bulk solution [211]. This results in a decaying volume fraction profile perpendicular to the surface [211]:

$$\phi = \begin{cases} \phi_0 & \text{for} \quad z < d_{\text{ads}}, \\ \left(\frac{z}{b}\right)^{-\frac{3\nu-1}{\nu}} & \text{for} \quad R > z > d_{\text{ads}}, \\ 0 & \text{else} \end{cases} \tag{2.23}$$

with the near-surface volume fraction ϕ_0, the adsorption layer thickness d_{ads} from equation (2.17),the monomer size b, the Flory-coefficient ν and the mean end-to-end distance of the polymer in the solution R from equation (2.13). Equations (2.22) and (2.23) can be combined to calculate ϕ_0 and then describe the partial adsorption of block polymers.

2.2. Pluronic P123

Pluronic P123 is a commercial triblock copolmyer consisting of propylene (PO) and ethylene oxide (EO), which was first synthesized by Vaughn et al. (Wyandotte Chemicals Co) in the early 1950s [33] and later patented by Schmolka (BASF) [215, 216]. The polymers are also available under other product names such as Poloxamers, Synperonics or Kolliphors, which are pharmaceutical Pluronic variants with a higher chemical purity. The following chapters will give some general chemical information about Pluronic 123 and the Pluronic nomenclature (2.2.1), summarize the state-of-the-art of P123s temperature dependent aggregation behavior up to its cloud point (chapter 2.2.2) as well as its surface studies (chapter 2.2.3).

2.2.1. General chemical information

Pluronics are synthesized by sequential addition of PO (C_3H_6O) and EO (C_2H_4O) to a seeding molecule, propylene glycol ($C_3H_8O_2$), with low molecular weight [32]. The resulting Pluronic polymer will consist of a PO middle block and two EO end groups of the same length. Due to the different solubilites of PO and EO in polar solvents like water, Pluronics are amphiphilic compounds, i.e. they are hydrophobic and hydrophilic at the same time. The polymeric propylene oxide in the middle block acts hydrophobic for molar masses above $750\frac{g}{mol}$, while an increasing ethylene oxide fraction guarantees water solubility [32, 33]. Depending on the degree of polymerization of both the PO and the two EO blocks, the Pluronics will have different physical properties.

Their product name starts either with a “L” for a liquid polymer, “P” for a pasty product or “F” for a flaky solid [33]. The last digit multiplied by 10 gives a rough estimate for the EO ratio of the whole polymer, while the remaining first one or two digits multiplied by 340 give the approximate molar weight of the PO middle block. In general, the polymers are liquid for low EO ratios and tend to solidify with increasing EO block lengths [54, 33]. In case of Pluronic P123, the polymer is pasty, has an EO ratio of 30% and its PO block weighs roughly $4000\frac{g}{mol}$.

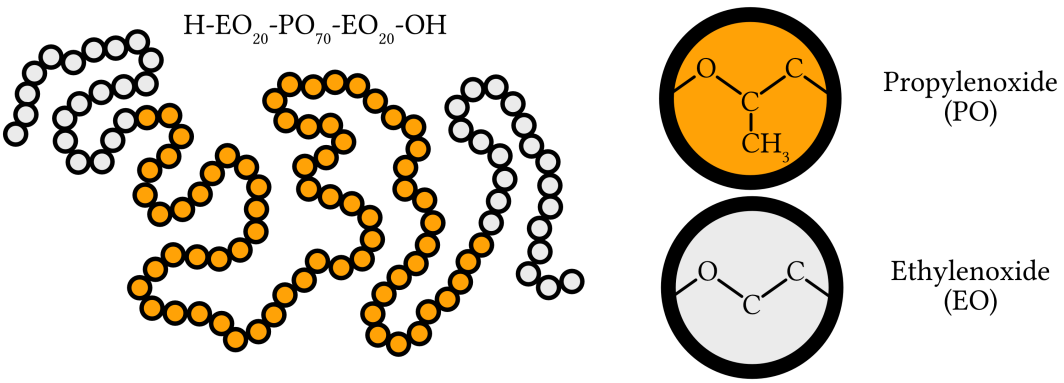

Figure 2.5. Sketch of Pluronic P123.

Pluronic	structure	molar mass $\left[\frac{g}{mol}\right]$	EO weight percent
P123	$EO_{20} - PO_{70} - EO_{20}$	5750	30
P103	$EO_{17} - PO_{60} - EO_{17}$	4950	30
P85	$EO_{25} - PO_{40} - EO_{25}$	4600	50
F127	$EO_{101} - PO_{56} - EO_{101}$	12600	70

Table 2.1. Chemical properties of different Pluronic variations, which are heavily studied in literature [54].

With the molar masses

$$M(\mathrm{PO}) \approx 58\frac{g}{mol} \quad \text{and} \quad M(\mathrm{EO}) \approx 42\frac{g}{mol}\,, \tag{2.24}$$

the PO middle block and each of the EO end groups have degrees of polymerization of 70 and 20, respectively (see table 2.1). There were more than 75 different Pluronic variations with numerous applications as lubricants, surface active agents or additives in detergents [32]. Heavier Pluronic variations like P123 gathered scientific attention due to their ability to form hydrogels and even liquid crystal structures at certain concentrations [54]. Since important milestones in literature are spread across several Pluronics, the results of the two structurally similar polymers P85 and P103 as well as the antagonistic variant F127, i.e. reversed hydrophobic-hydrophlilic balance, will be discussed (see table 2.1).

2.2.2. Aggregation behavior in aqueous solution

Due to their amphiphilic properties, aqueous Pluronic solutions generally show very strong self-assembly. Depending on the temperature and polymer concentration, the polymers form micelles with different shapes or aggregate to even bigger and more complex structures.

At low temperatures (5-10°C), Pluronic P123 is well-soluble in water and appear as independent polymer chains, which are called **unimers** (see figure 2.6). Both propylene (PO) and ethylene oxide (EO) homopolymers are also reported to be soluble up to ambient temperatures [217, 218], with the restriction of small molar masses for poly(propylene oxide) (PPO) [217]. Poly(ethylene oxide) (PEO) homopolymers with very high chain lengths and molar masses still have lower critical solution temperatures around 100°C when dissolved in water [218]. Only at higher temperatures, aqueous PEO solutions start to phase separate, i.e. behave like oil in water. In case of Pluronic P123, the PO middle block, which is too heavy and would phase separate on its own, is made soulble by the addition of the two EO end groups. The microscopic explanation is connected with the polymers structure on the molecular level and the conformation of its block groups. Using RAMAN and FOURIER-transform infrafred spectroscopy, GUO et al. investigated the temperature-dependent conformational states of different Pluronics (including P103). In the low temperature regime, both the PO middle block and the EO end groups are

hydrophilic and disordered [37, 38]. Cau et al. showed that more polar gauche conformations are present in the both polymer blocks performing ^{1}H-NMR epxeriments [74]. Their almost helical shape at low temperatures results in a high hydration and more polymer-solvent interactions compared to inter-monomer ones [38]. The associated sizes of the unimers vary for different Pluronics with radii of gyration between 1.7-2.5 nm for P85 [42] and F127 [39], respectively. Compared to theoretical values of ideal chains with a gaussian distribution of monomers, the experimentally obtained radii are systematically to low [39]. In combination with an increasing mobility of the methyl group ($-CH_3$) [74] and subsequent straightening of the PO middle block due to more trans conformations [37], the unimers are thought to resemble so-called unimolecular micelles [39]. These are structures, where the PO block is thought to be more compact and densely packed than the EO end groups.

With increasing temperature both block units of P123 undergo conformational changes resulting in lower polarity and hence in a lower hydration of the polymer chains [74, 37, 38]. The dehydration is more pronounced for PPO and above a well-defined temperature (critical micellization temperature) the polymer aggregate and form spherical **micelles** (see figure 2.6), which are larger clusters of polymer chains. Above the critical micellization temperature, the PO middle block is dominated by trans conformations [74, 38] and almost completely anhydrous [37]. Through ^{1}H-NMR measurements it is clear that the micellar core consists exclusively of PPO from different polymer chains and behaves like a polymer melt with liquid properties [74]. The PEO blocks, on the other hand, remain in a disordered, hydrated state and form a corona or shell around the PPO core of the micelles [54]. Numerous theoretical studies already investigated the inner structure of the micelles [53, 59, 58, 62] reporting hydration levels between 5 [58] and 30 % [59, 62] for the PPO core and at least 50 % for the PEO corona at near ambient temperatures (25-30°C) [53, 59, 58, 62]. However, the transition from the unimer into the micellar phase is not sharp as seen in the temperature dependence of the micelles size, which follows an empirical power law equation [39, 42]. First, the unimers form rather small aggregates, which then grow to sizes of 16 – 20 nm above the critical micellization temperature [54, 74, 40, 39, 42, 219]. With further increasing temperature the micelles continue to grow in size, although the growth rates are much smaller [219]. This is most likely due to the development of more trans conformations in the PEO blocks resulting in lower hydration of the corona as well as longer and straighter EO chains [74]. At too low concentrations, the polymers are unable to stastically find other ones to form aggregates. The critical micellization concentration has a strong temperature dependency [36, 220], but Pluronics generally need very small concentrations in aqueous solutions (in the range of 10 µM or 10^{-3} weight percent) to form micelles at ambient temperatures [221]. With increasing concentrations, the micelles start to order in solution, which can be observed in an increasing viscosity [220] and the presence of structure peaks in small-angle-scattering experiments [39, 42]. Highly concentrated aqueous Pluronic solutions gelate above a certain critical gelation concentration at ambient temperatures [220]. For P123 solutions, the gelation concentration is 28 weigth percent [57]. Here, the micelles even self-assemble into crystalline structures (lytropic liquid crystal (LLC) phases) ranging from cubic to hexagonal and even lamellar ordering [55, 43, 44].

With further increase in temperature, the spherical aggregates start to rapidly grow in size

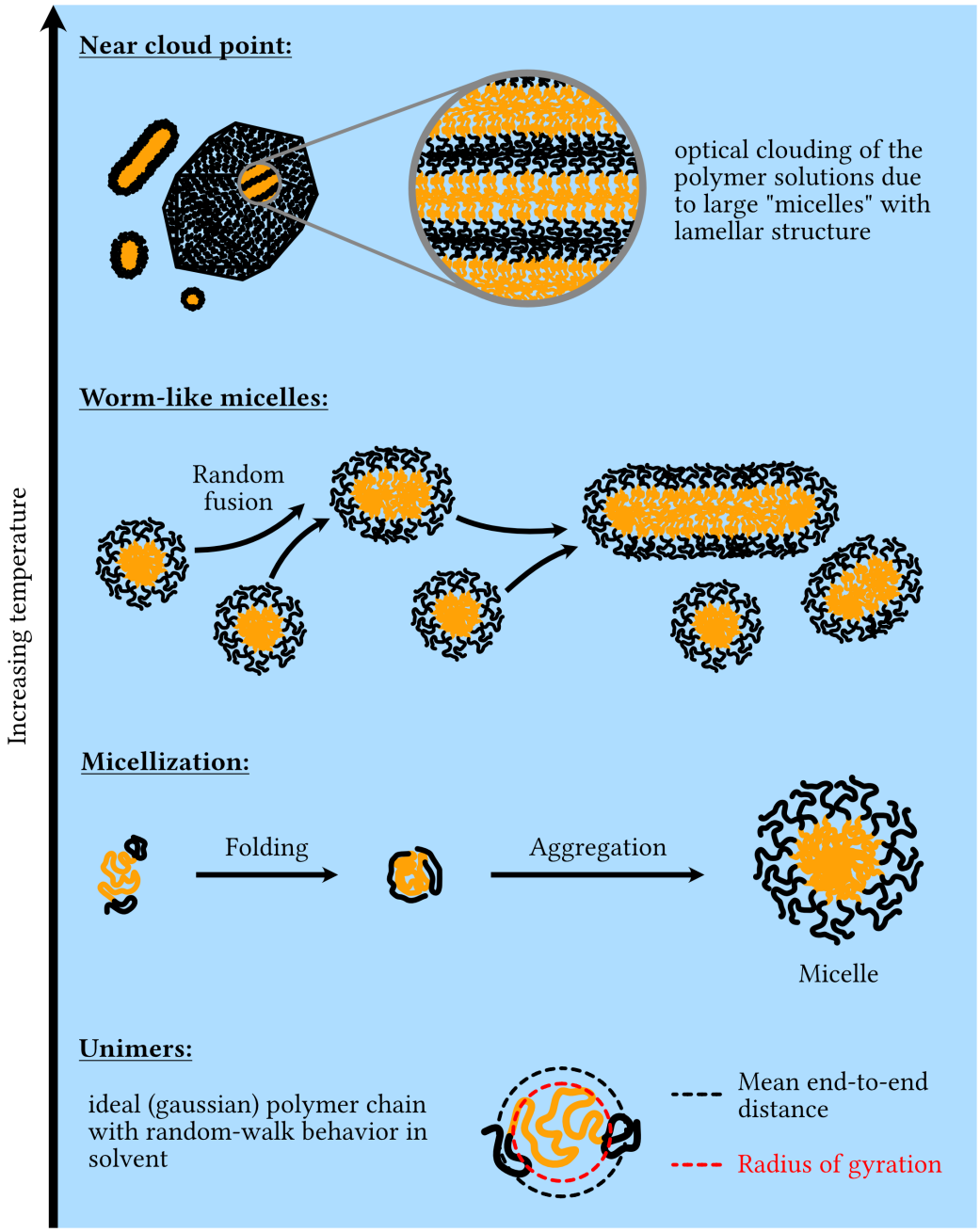

Figure 2.6. Cartoon of Pluronic P123s temperature dependent aggregation behavior. At low temperatures, the individual polymer chains with its PO middle block (orange) and EO end groups (black) are dissolved and well-hydrated in the surrounding solvent. With increasing temperature, P123s solubility decreases and the chains start to aggregate and form micelles with spherical, worm-like and lamellar structures.

and undergo a structural phase transition to form elongated **worm-like micelles**. The transition temperature depends on the Pluronic variant as well as the solvent and shifts towards lower temperature with increasing polymer concentrations [69, 39]. The kinematics of both transitions, from unimer to micelles and from spherical to worm-like micelles, were already subject of several studies [69, 222, 40, 223, 224, 225, 226]. In contrast to the equilibrium kinetics, which are dominated by the insertion and exclusion of unimers from individual micelles [223, 224], the non-equilibrium exhibit timescales in the order of hours to days, which correspond to a random fusion and fragmentation model of spherical micelles forming larger clusters [40, 225, 226]. Nonetheless, there is always a stable equilibrium between spherical and worm-like micelles and both species are presents [69, 39]. As an microscopic explanation for transition to worm-like micelles, two possible theories are discussed. First, it is well documented, that the micellar core grows with increasing temperatures [54, 39, 42, 220]. Near the transition temperature for the formation of worm-like micelles, the core reaches a size at which either the incorporated PPO blocks would have to reach their fully stretched, all-trans configuration to span it or EO monomers would appear in the core as well [39, 42]. Both is entropically very unstable and highly penalized [61], leading to the fusion process of spherical micelles. The second theory investigates possible conformational transitions in the PEO corona, which are documented for PEO homopolymers in aqueous solutions in the regime around the transition temperature to worm-like micelles [227, 228]. There is no final conclusion in literature, which of the two possibilities is correct or if a combination of both is necessary. In highly concentrated solutions, the formation of worm-like micelles is responsible for a change in crystalline ordering in the LLC phases of different Pluronics [56, 44]. The gels of P123 with hexagonal ordering are of particular interest as structure defining agents in the fabrication process of mesoporous silica, e.g. SBA-15 [47, 48, 49, 50].

By surpassing a certain temperature an increasing cloudiness of the solutions will be visible. The temperature, where the solution becomes completely opaque is called **could point** and in case of Pluronic P123 it is 93°C [36, 229]. The solutions milkiness is due to the dominant Mie scattering of larger aggregates, whose sizes are on the scale of the wavelength of visible light. However, the spherical and worm-like micelles do not simply agglomerate, since another distinct structural transition to a **lamellar structure** takes place [53, 41, 39, 42, 230]. Such regular structures are usually observed for extremely high concentrations above 50 weight percent, when aqueous Pluronic solutions start to phase separate. The temperature-driven formation of the lamellar phase, even at lower concentrations, is attributed to a transition of the PEO blocks into a fully dehydrated state near 90-100°C [227, 42, 218]. Mortensen et al. showed in small-angle neutron scattering experiments that the lamellar ordering would not yield the expected anisotropic scattering patterns associated with highly ordered lamellae, but only one very broad correlation peak, which they associated with large swollen lamellae domains [42]. For Pluronic P85 and F127, lamellar periodicities of 230 and 180Å are reported, respectively, which would correspond to almost entirely stretched PPO and PEO blocks [39]. But even under shear, these lamellae would not align, which is a hint towards the presence of multiple domains with different stacking directions [39]. One of the few systematic studies of Pluronics near their cloud point by Hammouda proposed a transition to large micelles with an internal

lamellar structure near the cloud point [41]. This is corroborated by prior theoretical calculations [230] and recent molecular dynamcis simulations [53], which showed that the observed lamellar periodicity can be caused by the stacking of both spherical and worm-like micelle with these associated sizes.

All phase transitions are reversible in temperature, but a distinct hysteresis changes the reversed transition temperatures between heating and cooling of the sample [70, 52, 231, 45] significantly. This hysteresis can be observed in the micellar shape [70, 231] and in the LLC phases [52, 45]. Although, there is no explanation in literature about the mechanism for this hysteretical behavior, it was already used to form thermodynamically stable worm-like micelles [70] and supercooled hexagonal LLC phases [52], which are still present at ambient conditions or after even dilution when heat cycles around their transition temperatures are applied.

2.2.3. Adsorption behavior onto surfaces

Pluronic copolymers are so-called surfactants (*surface active agent*), which are compounds that explicitly target inter- or surfaces and decrease their respective interfacial tensions. The micellization process of Pluronics can be also interpreted as a minimization of the surface tension between the hydrophobic PO middle blocks and the surrounding water using only their surfactant properties [232]. Besides their initial use as detergents, emulsifiers, foaming agents and dispersants [54, 32, 33], Pluronics are used nowadays as coatings for the preparation of highly functionalized surfaces for biological applications [204, 233, 234, 235, 236] or as colloidal stabilizers [237, 238, 239].

The adsorption of Pluronics was already the subject of numerous studies [240, 241, 242, 243, 244, 57, 245, 238, 62, 60, 246, 247, 248, 249, 250, 251, 252, 253, 51]. The key properties for applications, i.e. the absorbed amount of polymer on the surface, the adsorbed layer architecture and stability, were systematically investigated for different Pluronics [241, 242, 243, 245, 248, 250, 251, 252], at varying polymer concentrations (above and below the critical micellization concentration) [245, 238, 246, 253], temperatures [238, 246, 253], on hydrophilic [243, 62, 249, 251] and hydrophobic surfaces [241, 242, 62, 247, 249, 250, 252] as well as different surface geometries [240, 248] and under shear [244, 57, 51]. All investigated Pluronics were able to attach to the surfaces and create some form of layered structure close to the surface [245, 250, 251]. The main differences lie in the Pluronic composition. Adsorbed layers of versions with higher EO ratios, e.g. F127, tend to be less stable, while higher PO variants, e.g. P123, can form stronger interactions, especially with hydrophobic surfaces. Above the critical micellization concentration in bulk solution, the absorption is most efficient [241, 242, 243], but higher concentration usually do not cause more adhesion of polymer chains onto the surfaces due to saturation. On the contrary, the adsorbed amount of polymers strongly correlates with the applied temperatures. For temperatures below the critical micellization temperature, a monolayer of Pluronic is formed on top of the surface [242, 238]. Above the this temperature, an increase in adsorbed material can be observed, which is attributed to the surface adhesion of micellar structures [242, 238]. This effect continues up to the cloud point, where the micelles in solution seem

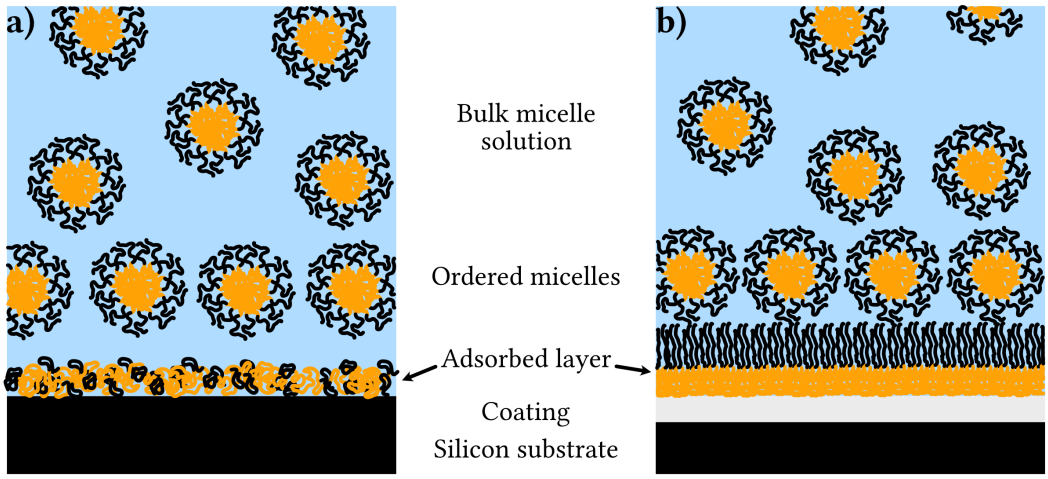

Figure 2.7. Schematic representation of Pluronic adsorption on a) hydrophillic and b) hydrophobic surfaces. The orange part stands for the poly(propylene oxide) middle block, while the black part of the polymer chains symbolizes the two poly(ethylene oxide) end groups of Pluronic P123.

to collapse onto the surfaces resulting in a rapid, exponential growth of polymeric material adsorbed to them [246, 253]. Yet, the stability and structure of the interfacial polymer layers is controlled by the surface hydrophobicity [62, 247]. For strong hydrophilic surfaces, e.g. acidic cleaned or flammed, their interaction with the Pluronic chains is gouverned by the EO end groups [246, 249, 251]. The resulting layers can quite easily be removed by rinsing [243] or using shear [57]. With increasing hydrophobicity, e.g. different surface preparations or coatings, the PO blocks start to form bonds with the surfaces and the EO end groups are pushed back into the solvent[241, 251, 252]. For heavier and more hydrophobic Pluronics (higher PO ratios), e.g. P123, the initial PO layer almost behaves like a melt [252], similar to the micellar core. Such layers are sturdier to rinsing and generally harder to remove from the surface [242, 246]. The overall layer thickness is surprisingly independent of the molar weight of the Pluronics and increases for higher PO ratios [247, 248, 250]. An explanation are the stretched and hydrated EO blocks in the solvent, which cause larger overall hydrodynamic layer thicknesses [248, 252].

The first adsorpted layer and its structure also influences the bulk solution near the surface (see figure 2.7). Especially in the micellar phase (above the critical micellization concentration and temperature), the micelles in bulk solution will show a different behavior whether they are close to a hydrophilic or hydrophobic surface [57]. Using shear, it is possible to initilaize crystallization of the solutions near the surfaces [57, 254, 255, 51]. This near-surface crystallization of P123 is reported to only work with hydrophilic surfaces [57]. Higher shear rates will disturb this ordering, but the crystalline structure reappears even when no shear is applied [57].

2.3. Surface preparation

For reflectometry experiments it is essential to use well-defined surfaces, which do not corrupt the applied sample and the subsequent data analysis. Silicon wafers are an excellent substrate material, because they are readily available, have a very low surface roughness and offer the possibility to prepare dedicated hydrophilic or hydrophobic surface properties. The hydrophobicity of a surface is linked to its surface energy [256]

$$\gamma = \frac{E_{\mathrm{sur}}}{A} \tag{2.25}$$

with the total free energy E_{sur} of the surface and the its area A. To understand the influence of γ on the surface wettability, the adsorption of a liquid droplet on a solid substrate can be considered (see figure 2.8). The liquid will form a contact line (or area) with the solid and the energies of the interface between the liquid and the solid (γ_{ls}), the liquid and air (γ_{la}) as well as between the solid and air (γ_{sa}), need to obey YOUNGS condition [257, 258, 259]

$$\gamma_{\mathrm{sa}} - \gamma_{\mathrm{ls}} - \gamma_{\mathrm{la}} \cdot \cos\theta_c = 0 \tag{2.26}$$

at its edge. Here, θ_c is the so-called contact angle, which is the experimental quantity to determine the surface energy. The interfacial energies between two the phases i and j can be calculated by [258]

$$\gamma_{ij} = \gamma_i + \gamma_j - 2\Phi\sqrt{\gamma_i \gamma_j} \tag{2.27}$$

where γ_i and γ_j denote the surface energies of both phases. $\Phi = 1$ for liquids, but is generally close to unity for other interfaces as well [258]. Assuming that $\gamma_{\mathrm{s}} - \gamma_{\mathrm{sa}}$ is negligible [257], equations (2.26) and (2.27) can be combined to yield [256]

$$\gamma_{\mathrm{s}} = \frac{\gamma_{\mathrm{l}}}{4}(1 + \cos\theta_c)^2 . \tag{2.28}$$

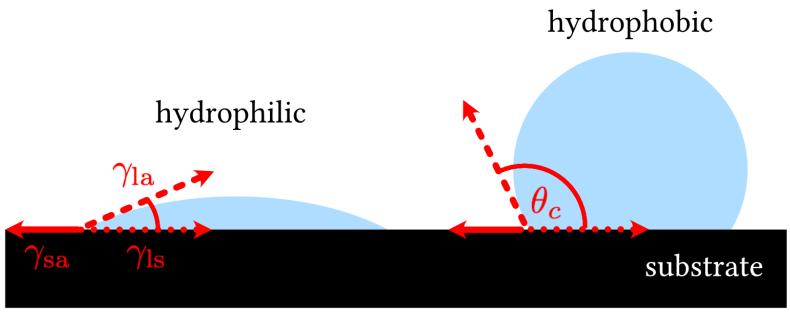

Figure 2.8. Illustration of the surface energy influence on the shape of a liquid droplet on top of a solid surface.

Higher surface energies of the solid substrate will result in smaller contact angles for selected liquids, and *vice versa*. It follows that hydrophilic surfaces have high surface energies and small contact angles (below 10°), while hydrophobic surfaces with lower surface energies show high contact angles (above 90°). In the following two procedures will be shown for the preparation of either hydrophilic or hydrophobic silicon surfaces.

Acidic cleaning

Untreated silicon surfaces have contact angles of 40–50° for polar solvents like water [260, 261]. Yet, these values can be drastically decreased if the surfaces are thoroughly cleaned using strong acids [261], e.g. Caro's acid (peroxymonosulfuric acid) [262].

Peroxymonosulfuric acid (H_2SO_5) is an equal mixture of concentrated sulfuric acid (>99% H_2SO_4) and unstabilized hydrogen peroxide (30% H_2O_2). The chemical reaction

$$H_2O_2 + H_2O_2 \rightleftharpoons H_2SO_5 + H_2O \tag{2.29}$$

is strongly exothermic and unstable, which is the reason why the mixture can only be used for one cleaning process at a time before disposal [263]. Due to the chemical aggressiveness of Caro's acid, which is able to break organic bonds, additional safety precautions have to be taken. The silicon surfaces should be cleaned using Teflon vessels and it is imperative to work under a fume hood. In addition, it is absolutely prohibited to make any contact between H_2SO_5 and organic solvents. There is high risk of explosion [264]! Even without additional heating, a treatment of the silicon substrate with Caro's acid will produce hydrophilic surfaces surface energies $\gamma \geq 72\ \frac{\mathrm{mN}}{\mathrm{m}}$ and contact angles $\theta_c \leq 10°$ for water [263, 261].

Coating with octadecyltrichlorosilane

To obtain hydrophobic surfaces, the silicon surfaces have to be first cleaned and then coated with certain compounds. Some of the most common coating materials are so-called self-assembled monolayers (SAM) of different silanes [265]. Here, octadecyltrichlorosilane (OTS, $C_{18}H_{37}SiCl_3$) was used, which are hydrocarbon chains consisting of a trichlorsilan ($SiCl_3$) head group, initiating the surface bonding, and an organic tail with a theoretical length of 23 Å [263, 265].

In the method of Lessel et al., the coating solution is first synthesized by mixing bicyclohexyl ($C_{12}H_{22}$), carbon tetrachloride (CCl_4) and OTS. Afterwards the surface is dipped into the solutions several times to form dense and uniform SAMs [265]. There different models for the adsorption process of the head group, which are still discussed in literature [266, 267, 268]. With this method, homogenous coatings of 26 Å thickness and very low roughness (σ = 5 Å) are produced. The resulting hydrophobic, coated silicon surfaces have surface energies in the range of 25 $\frac{\mathrm{mN}}{\mathrm{m}}$ and water contact angles $\theta_c \geq 110°$ [265].

3. Instrumentation

Since the experiments, which will be described in chapter 4, employ both photons and neutrons, the following sections will treat their production as well as the necessary instrumentation for manipulation and detection.

Photons can be produced by various reactions in nature. Leaving matter-antimatter interactions aside, which results in high energy γ radiation, the two processes for the production of visible light or X-rays are atomic energy level transitions [269] and accelerated charged particles like electrons [270]. Highly intense and coherent light sources with wavelengths in the visible regime are nowadays readily available in form of lasers (***l**ight **a**mplification by **s**timulated **e**mission of **r**adiation*). From its initial prediction by Einstein [271, 272], it took more than 40 years for the first experimental realization of a laser by Maiman using a ruby crystal in 1960 [273]. The first continous laser based on Helium and Neon followed in 1961 by Javan et al. [274], which is still one of the most commonly used laser types. For a comprehensive review and introduction, the reader is referred to excellent literature on the subject, e.g. the textbook by Hecht [105]. In chapter 3.1, the experimental set-up for dynamic light scattering will be described using a He-Ne laser.

X-rays are also produced by transitions between the inner atomic energy levels. The photon energies (wavelengths) are several orders of magnitude higher (lower) compared to optical lasers, but the emitted X-rays have less spatial and temporal coherence. To better compare different light sources, the spectral brightness or brilliance [106]

$$B = \frac{\Delta N}{\Delta t \cdot \Delta A \cdot \Delta\Omega \cdot \frac{\Delta\lambda}{\lambda}} \tag{3.1}$$

can be defined, which describes the number of photons ΔN per time Δt, area ΔA, solid angle element $\Delta\Omega$ and relative spectral bandwidth $\frac{\Delta\lambda}{\lambda}$. In terms of brightness, lasers are several orders of magnitude more brilliant than laboratory X-ray sources [275]. Highly brilliant X-ray radiation is produced by synchrotrons. These storage rings accelerate charged particles like protons or electrons to energies above several GeV using alternating electrically accelerating and magnetically deflecting elements [276, 277]. Inside the magnetic dipoles the particles change direction and irradiate [270]. There are different magnet types ranging from simple bending magnets up to more complex arrangements (wigglers and undulators), which force the electrons on oscillatory trajectories, and emit highly brilliant radiation [278, 279]. In general, higher particle energies will lead to higher available X-ray energies, but the exact spectra have a more complex analytical expression, which shall be omitted here. The reader is referred to the excellent standard textbook on synchrotron radiation by Attwood [106]. At large syn-

chrotron facilities, the radiation, which is produced in each magnetic dipole, is transferred to so-called beamlines. These are experimental endstations for dedicated scientific topics, e.g. X-ray spectroscopy, scattering or imaging. In chapter 3.2, the Advanced photon source (APS) at the Argonne National Laboratory (USA) and its small-angle X-ray scattering beamline 12-ID will be described in more detail.

Neutrons are produced by nuclear reactions [100, 102], fission [280], spallation [281, 282] and fusion [283]. After the discovery of radioactivity and α -radiation by Becquerel [284, 285], Marie Curie and Piere Curie around 1900 [286, 287, 288], free neutrons were detected by Bothe, Becker [100] and Chadwick [102] using a mixture of pollonium and berrylium powders. With pollonium being a strong α-emitter, the subsequent reaction reads as [289]

$$^{9}\mathrm{Be} \; + \; ^{4}_{2}\mathrm{He} \; \longrightarrow \; ^{12}\mathrm{C} \; + \; n \; + \; 5.704 \; \mathrm{MeV} \, . \tag{3.2}$$

Such α-Be or α-Li sources were historically relevant and are still used as calibration standards. Yet, their low "brightness" of $10^{7} \; \frac{\text{neutrons}}{\text{s}}$ [289], simultaneous production of high energy γ radiation and resulting non-thermal, hot neutrons makes them not useful for experimental work nowadays. A more powerful method for the production of neutrons are nuclear fission reactors. The pioneering work of Fermi, Frisch , Hahn, Meitner and Strassmann in the 1930s [290, 291, 292, 293, 294, 295, 296, 297], lead to the first artificial and controlled chain reaction in the "Chicago-Pile 1" in 1942, which was the first functioning nuclear reactor [298]. In modern fission reactors either uranium or polonium are used as fuel materials, which decay into two lighter elements [289, 299]:

$$\begin{aligned} ^{235}_{92}\mathrm{U} \; + \; ^{1}_{0}\mathrm{n} \; &\longrightarrow \; ^{144}_{56}\mathrm{Ba} \; + \; ^{89}_{36}\mathrm{Kr}^{*} \; + \; 3 \, ^{1}_{0}n \; + \; 173 \; \mathrm{MeV} \, , \\ ^{239}_{94}\mathrm{Pu} \; + \; ^{1}_{0}\mathrm{n} \; &\longrightarrow \; ^{144}_{56}\mathrm{Ba} \; + \; ^{94}_{38}\mathrm{Sr} \; + \; 2 \, ^{1}_{0}n \; + \; 191 \; \mathrm{MeV} \, . \end{aligned} \tag{3.3}$$

Equations (3.3) are the most probable reactions, but fission into 3 elements is possible as well [289]. The reaction is started either by spontaneous fission of the fuel materials [300] or by the insertion of a seeding neutron source, e.g. californium [301, 302, 303]. The produced neutrons have too high energies and need to be "cooled" down to few meV in order to increase their interaction probability with the remaining fuel material. This is done by so-called moderators, which are light elements with a very low neutron absorption cross section like water, graphite or helium [299]. If there are enough neutrons produced to obtain a self-sustaining chain reaction, the reactor is in its critical state. Here, reflectors keep the neutrons available for additional fission reactions. Typical reflector materials are water [299] or nickel alloys [304]. To prevent a dangerous overcritical reactor state or to stop the the chain reactions, control rods are used, which are typically made of highly neutron absorbing elements like boron or cadmium [304]. Depending on the reactor layout, they can achieve neutron flows between $10^{13} - 10^{15} \; \frac{\text{neutrons}}{\text{s}}$ [299]. In chapter 3.3 and 3.4, the pulsed neutron source IBR-2 at the Joint Intitute for Nuclear Research (JINR) and the reactor at the Institute Laue-Langevin (ILL) will be described including their respective small-angle neutron scattering and reflectometry beamlines.

3.1. Malvern ZetaSizer Nano ZS

For the dynamic light scattering (DLS) experiments, the commercial Zetasizer Nano ZS (Malvern panalyticals, United Kingdom) was used. Besides the dynamic scattering measurements, it is also possible to determine the zeta potential of the particles in solution, which is their electric surface potential. Since Pluronic micelles have an uncharged and highly hydrated poly(ethylene oxide) shell, their surface potentials are negligible and the experiments were only done in the instrument's DLS mode.

The Zetasizer uses a 4 mW strong He-Ne laser, which emits red light with a wavelength of 632 nm [305]. The light is collimated, focused and brought onto the sample solution inside a quartz glass cuvette with 10 mm optical path lengths. The scatted light is detected in the backscattering geometry at 175° relative to the incident direction [305]. This set-up allows for reducing the influence of larger contaminations in the cuvette, e.g. dust particle, which have a strong forward scattering signal, and for measuring higher sample concentrations, because the influence of multiple scattering is reduced at scattering angles close to 180° [305]. Before the scatted laser light hits the detector, it is attenuated so that the detector is not saturated and overloads. The recorded detector signal is processed by a correlator, which calculates the temporal correlation function the scattered intensities (see equation 1.27)).

3.2. Beamline 12-ID at the Argonne National Laboratory

The Argonne National Laboratory of the United States Department of Energy houses the Advanced Photon source (APS), which is one of the brightest synchrotrons in the world, as well as several other facilities for biological, material and nuclear research and supercomputing [306].

The Advanced Photon Source

The APS is a 3rd generation synchrotron with a diameter of 175 m and electrons are accelerated to 7 GeV using an upstream linear accelerater and smaller booster ring. In the main 1 km long sotrage ring, the electron bunches are kept at this energy and travel through bending magnets, wigglers and undulators to produce synchrotron radiation for the surrounding beamlines with accessible X-ray energies from 3 up to 100 keV [307]. Since the electrons travel in bunches through the ring, the resulting radiation is not continuous but pulsed with a temporal spacing of 12 ns [307]. The APS contains 34 sectors, which are located on each of the magnetic dipoles. Each sector can house multiple beamlines giving the APS a total of 89 endstations for various experimental techniques [307].

Outline of beamline 12-ID

The small-angle X-ray scattering beamline 12-ID is located downstream of an undualtor in sector 12 at the X-ray Science Division of the APS. Undulators consist of a periodic arrangements

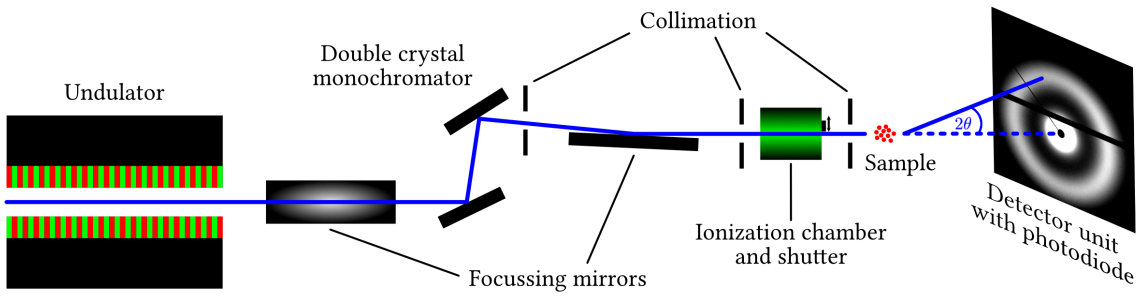

Figure 3.1. Sketch of beamline 12-ID at the APS with its undulator source, X-ray optics, monochromator and detection unit.

of magnetic dipoles, which force the electrons to oscillatory motions. If the electron bunch is properly collimated and small, the X-rays from each oscillation will interfere constructively or destructively and generate a peak spectrum with a high brightness [308]. Its wavelength and the size of the emitted radiation cone both depend on the electron energy as well as the undulator wavlength, which is the length between two homopolar magnetic elements, its overall length, period and gap [106]. In case of 12-ID, two undulators with wavelengths of 2.7 and 3.0 mm are available offering X-ray energies from 4 up to 40 keV [307]. For a detailed characterization of the undulators and a thorough formalism of their X-ray spectra see [106, 308, 309].

The outgoing light beam has a flat, elliptical shape and non-negligible divergence, which makes it convenient to apply focusing and beam shaping optics in order to maximize the photon flux at the sample position (see figure 3.1). Two mirrors for vertical and horizontal focussing, two cryogenically cooled silicon crystals and several scatterless beam-defining collimation slits yield a monochromatic beam ($\frac{\Delta\lambda}{\lambda} = 10^{-4}$) with sub-millimeter cross sections at the sample position, which is 60 m downstream of the undulator source [309]. The photon flux at the sample position is $10^{17} \frac{1}{\mathrm{s \cdot cm^2}}$ To safely change samples, reduce unnecessary radiation exposure and enable precise time-resolved measurements, the beam passes through an ionisation chamber with a high-speed shutter that can block the beam from reaching the experimental hutch and samples [309]. Depending on the incoming number of photons and time, for which the shutter is open, the ionization chamber measures the integrated photon flux. This quantity is later used during data reduction and calibration. The scattered photons by the sample are collected on a 2D direct-converting and single-photon-counting detector, while the central beam is caught using a beam stop with an integrated photo diode.

3.3. YuMO spectrometer at the Frank Laboratory for Neutron Physics

The Frank Laboratory for Neutron Physics (FLNP) is part of the Joint Institute for Nuclar Research (JINR) in Dubna. In addition to the IBR-2 research reactor, the FLNP houses an accelerator based pulsed neutron source, called IREN, as well as different tagged neutron sources for particle physics research [310]. Another important part of the JINR is the Flerov Laboratory for Nuclear Reactions (FLNR), where multiple new transuranium elements were discovered including Rutherfordium ($_{104}$Rf), Dubnium ($_{105}$Db) and the newest discoverd element Tennessine ($_{117}$Ts) [311].

The IBR-2 reactor

The IBR-2 reactor is a pulsed reactor with a periodic mechanical modulation of reactivity [304]. Its nominal mean power of 2 MW is reached by roughly 70 kg of plutonium oxide as fuel material and 430 ng of californium-252 as the initial neutron source for the chain reaction. The core is sodium-cooled and surrounded by stationary reflectors, control and safety units as well as water moderators (see figure 3.2), which point towards the connected beamlines and thermalize the fast neutrons from the fission reaction down to thermal energies (few meV) [299, 304]. However, the core is kept in a subcritical state unless the two rotating reflectors at its front side approach the active zone. The system is brought into a prompt supercritical state and short pulses of neutrons are generated. Depending on the reflector rotation, the pulse spacing and width can vary between 40-200 ms and 200-300 µs, respectively [304, 312]. The maximum obtainable thermal neutron flux at the pulse maximum behind the water moderator is 10^{16} $\frac{\text{neutrons}}{\text{s}\cdot\text{cm}^2}$ [299, 304, 312]. Since its last modernization in 2011, IBR-2 will operate in its current set-up

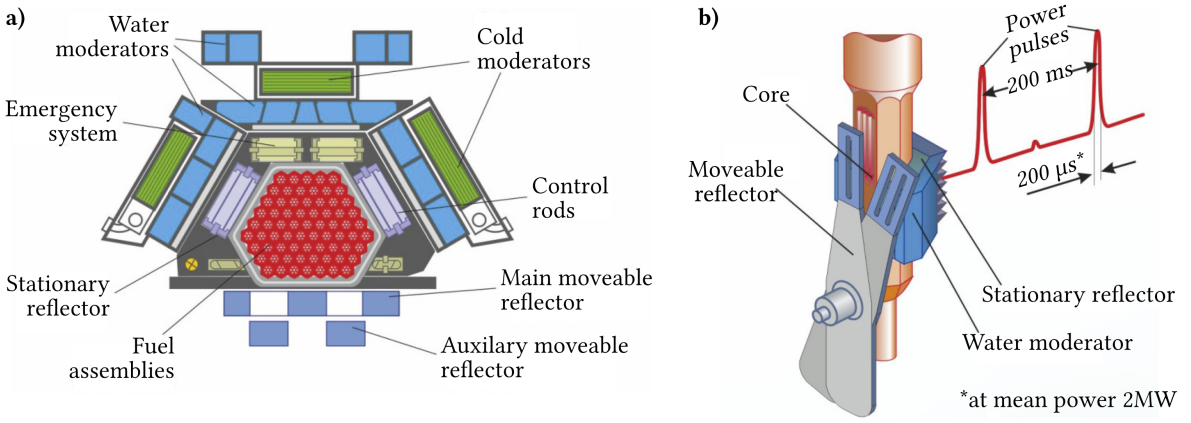

Figure 3.2. Illustration of the IBR-2 reactor at the JINR in Dubna. a) schematic overview of the reactor core and b) the neutron pulse generation with using moveable reflectors. The graphics are taken from [304] and modified according to the terms and condition of the Creative Commons Attribution license (CC 4.0 BY).

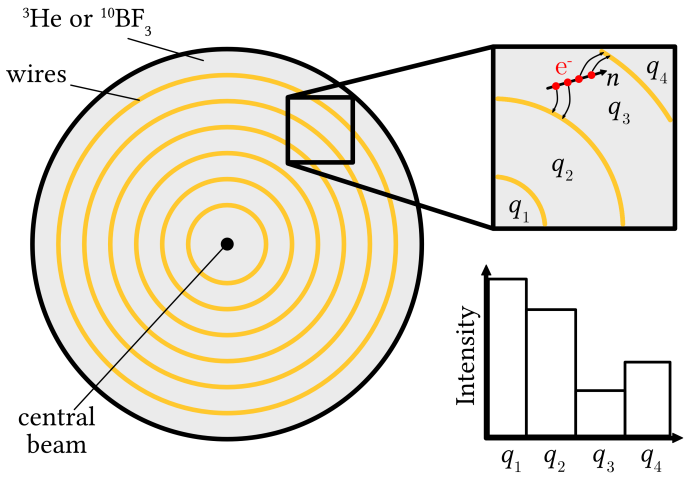

Figure 3.3. Functionality of a gas-filled ring detector for neutrons. It is a metallic container, which is filled with ^{3}He and consists of concentric wires. Due to the high absorption cross section of ^{3}He, the incoming thermal neutrons ionize the gas inside the detector and the produced particles are drawn towards the charged wires. The number of scattered neutrons is proportional to the deposited electric in each ring element (between two wires), which represents one q-region in **k**-space. Using a quick readout electronic, it is possible to further increase the q-sampling via drift-time corrections.

until 2030. Then, a new reactor architecture will introduced based on neptunium oxide fuel elements and cryogenic, aromatic hydrocarbon moderators, which will both increase the flux by a factor of 200 and reach the ultra-cold neutron regime [313, 312].

Outline of the YuMO spectrometer

The YuMO spectrometer is a small-angle neutron scattering beamline, which uses the time-of-flight measurement method and is named after its principal designer Yurii M. Ostanevich [314]. The incoming neutrons from the water moderator of the reactor are passed through another rotating disk with a well-defined slit, the so-called chopper, which cuts out the few fast and cold neutrons to reduce the scattering background, before hitting additional collimating optics [315, 316, 314]. Afterwards the collimated neutron beam hits the sample and scatters off of it. Through precise timing of the neutron pulse production in the reactor core, it is possible to determine the time of arrival on the ring detector for the scattered neutrons inside each pulse and hence their velocity or wavelength. Thus, each pulse is creating multiple scattering curve overs the whole accessible q-range and the summation of multiple pulses will result in scattering profiles with a high dynamic range [315]. The YuMO beamline has two ring detectors (see figure 3.3) to further increase its q-range and simultaneously measure both the sample and vanadium calibration standard.

3.4. FIGARO at the Institute Laue-Langevin

The research reactor at the Institue Laue-Langevin (ILL) is loacted alongside the European Synchrotron Radiation Facility (ESRF) in Grenoble. Since its inauguration in 1971, the reactor at the ILL is still the brightest continuous neutron source in the world and is scheduled to be used until the European Spalation Source is offering stable access to the user community in the 2030s.

The ILL high-flux reactor

ILL's nuclear reactor has only one fuel element containing roughly 10 kg of ^{235}U in a very small volume [299] and the chain reaction follows equation (3.3). The initial neutrons are a result of the spontaneous fission of ^{235}U [300]. This core element is surrounded by heavy water, which acts as the coolant, neutron moderator and reflector at the same time. Due to the extremely high fuel density, it is possible to extract up to 10^{15} $\frac{\text{neutrons}}{\text{s}\cdot\text{cm}^2}$ with a nominal power of 57 MW. The chain reaction is controlled by a control rod made of boron, which can be inserted into the fuel core. The produced neutrons are thermalized by the heavy water and extracted by several neutron guide tubes roughly 45 cm away from the core [299]. At this distance most fast neutrons are cooled down by repeated scattering interactions with the heavy water to thermal energies and velocities. In addition to the thermal neutrons, the ILL reactor has one hot and two cold neutron sources, which consist of heated graphite (T = 2300°C) and liquid deuterium (T = −250°C). Neutrons hitting these spots change their spectrum towards lower or higher wavelengths, respectively.

Outline of FIGARO

The **F**luid **I**nterfaces **G**razing **A**ngles **R**eflect**o**meter (FIGARO) is connected to the reactor core by a 28 m long neutron guide consisting of Ni/Ti-coated supermirrors. All remaining fast neutrons from the core with wavelengths $\lambda < 1.5$ Å cannot pass this guide due to its design and coating [317]. Afterwards, the thermal and cold neutron beam reaches the frame overlap mir-

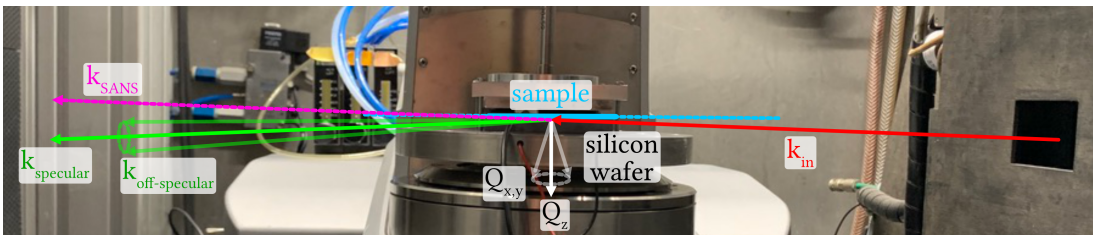

Figure 3.4. Illustration of the inverse scattering geometry. The incoming neutrons ($\mathbf{k}_{in}$) are transmitted, scattered and reflected at the interface between sample and silicon wafer. Besides the specular reflectivity ($\theta_{ref} = \theta_{in}$), which is measured along q_z perpendicular to the interface, off-specular scattering occurs, which gives information about the in-plane environment at the interface in the q_x and q_y directions. The transmitted neutrons can cause an additional small-angle scattering signal.

rors and chopper assembly, where the continuous neutron flux is cut into white beam pulses with a wide neutron wavelength spectrum in order to use the time-of-flight method. In the first two Ni-coated mirrors, the cold neutrons (high wavelength part of the spectrum) are filtered out so that the long and short wavelength in sequential pulses can always be separated [317]. The subsequent four boron-coated choppers are used to generate neutron pulses with a well-defined velocity/wavelength spectrum and wavelength resolution by carefully adjusting their rotation speeds, slit widths and relative movement to each other [318]. The pulsed neutron beam then hits two deflection mirrors adjusting the incident angle on the sample, a collimation system allowing for different beam shapes and sizes and an oscillating attenuator giving intensity normalized time-of-flight spectra, which are necessary during data reduction [317]. After interacting with the sample, the reflected and scattered neutrons are recorded by a 512 × 256 mm (width and height) area detector. It is filled with a mixture of ^{3}He and CF_4 and its complex internal design gives a vertical and horizontal spacial resolution of 2 and 8 mm, respectively [317]. Due to the exact timing of the pulse creation by the chopper assembly, it is possible to use the time-of-flight spectroscopy and precisely determine the arrival time of the neutrons in the detector elements. The detector is housed in an evacuated, 2.5 m long flight tube, where he can be moved to adjust incident angles of +3.8 down to -2.7° [317].

4. Experiments

This chapter will give an overview of the different experiments with visible light, X-rays and neutrons. Besides the synthesis of the aqueous Pluronic solutions and the instrumental parameters, this will include an explanation of the used data reduction and calibration routines, which were either performed by the instrument itself (dynamic light scattering) or by hand using certain procedures described in literature (small-angle neutron and X-ray scattering, neutron reflectrometry). The first four sections (4.1, 4.2, 4.3 and 4.4) will treat the experiments sorted by each individual method, while section 4.5 will present the kinetic measurements, which were done in a unified fashion using light and small-angle scattering. Although figures of experimental data will be shown here, the actual data analysis will be done in chapter 5 using the formalism introduced in the chapters 1.2, 1.3 and 1.4.

4.1. Dynamic light Scattering

Sample preparation

For the experiments, aqueous solutions with different Pluronic concentrations were prepared. Here, adequate amounts of polymer and distilled (H_2O) or heavy water (D_2O) were weighed and mixed at low temperatures in a refrigerator (5-10°C) to accelerate the solution process. Pluronic P123 (CAS-Nr.: 9003-11-6) and the heavy water (CAS-Nr.: 7789-20-0, degree of deuteration: 99%) were received by Sigma Aldrich. Pluronic solutions with either distilled or heavy water as the solvent will have different mass concentrations due to the higher density of heavy water compared to normal water. The mass concentrations for both solvents are

$$c_{H_2O} = \frac{m_{P123}}{m_{P123} + m_{H_2O}} \quad \text{and} \tag{4.1}$$

$$c_{D_2O} = \frac{c_{H_2O} \cdot \rho_{H_2O}}{\rho_{H_2O} - x \cdot (c_{H_2O} - 1) \cdot (\rho_{D_2O} - \rho_{H_2O})} \tag{4.2}$$

where m_{P123} and m_{H_2O} are the weighed masses of Pluronic P123 and distilled water, ρ_{H_2O} and ρ_{D_2O} are the densities of distilled and heavy water at a given temperature and x is the degree of deuteration of the used heavy water. Using equations 4.1 and 4.2, it is possible to account for this effect during sample preparation. All measured solution were mixed to have equal concentrations with respect to H_2O as the solvent. For the dynamic light scattering experiments, aqueous solutions with 0.5, 1, 3, 5, 7, 8, 10 and 15 weight percent were prepared. In addition, the samples containing 1, 5 and 10 weight percent of polymer were mixed in heavy water as well and used for the kinetic measurements (see chapter 4.5).

Experimental parameters

The samples were measured at different temperatures in the range from 5 – 88°C, both using a heating and subsequent cooling ramp. Temperature-dependent measurements are a fully automatized process in the instrument including heating, cooling, auto-correlation determination, aperture selection to prevent detector overflow and data analysis. After reaching each temperature, the samples were already in thermodynamic equilibrium due to the heating and cooling time as well as the small temperature increments. At each temperature, the samples were then measured three consecutive times for 10 seconds to ensure reproducibility of the obtained results.

Data handling

The obtained scattering intensity is used to calculate the time-dependent auto-correlation function by the instrument itself. For the internal data analysis, the first-order normalized auto-correlation function of the electric field component of the scattered laser light

$$g^1(\tau) = K\sqrt{\frac{\langle I(t)\cdot I(t+\tau)\rangle}{\langle I(t)\rangle^2} - 1} \tag{4.3}$$

is necessary. Here, K is an instrument constant and τ is the so-called delay time, which is the temporal spacing of the auto-correlation function. Applying equation (1.38) to polydisperse systems (multiple different particle sizes are present) [137, 139, 319],

$$g^1(\tau) = \sum_i G_i(q\mathfrak{D}_i)\,\mathrm{e}^{-q\mathfrak{D}_i t} = \int_0^\infty G(\Gamma)\,\mathrm{e}^{-\Gamma t}\,\mathrm{d}t \ , \tag{4.4}$$

where q is the scattering vector, $\mathfrak{D}_i$ is the diffusion constant of each individual particle size, which is present in the sample, and $\Gamma = q\mathfrak{D}$ is the so-called decay constant. Equation (4.4) is a Laplace transformation and the transformed auto-correlation function $G(\Gamma)$ contains the information about the size distribution. There are several numerical approaches to solve equation (4.4), but the most commonly used are the cummulant method [319] or inverse Laplace transformation using the CONTIN algorithm [320, 321]. Although the cummulant technique is robust and most commonly used, it is usually not ideal for polydisperse systems, since it gives the intensity-weighted average over all particle sizes in the solution. Since the scattering intensity increases for larger particle, even very few of them can greatly alter the averages and lead to incorrect results. For this reason, only the instrumental volume-weighted size distributions will be used, which were obtained by the inverse transformation of equation (4.4).

4.2. Small-angle X-ray scattering

Sample preparation

The samples were prepared in the same manner as described earlier using equation (4.1). Pluronic P123 was used from the same lot as the one used for the dynamic light scattering experiments. Aqueous solutions containing 1, 5 and 10 weight percent of P123 were prepared in Würzburg before the beamtime, send to (APS) one week in advance and stored there at 5°C.

Experimental parameters

The experiments were performed at beamline 12-ID (see chapter 3.2). Each sample was measured in a quartz glass capillary with diameters of 1.5 mm and a wall thickness of 10 µm. The X-ray energy was fixed at 18 keV and a temperature-controlled capillary rack was used to simultaneously measure all samples including a water reference. The exposure time for each detector image was 0.2 seconds and the sample-detector distance was chosen so that q-values between 0.005 and 0.5 $Å^{-1}$ were accessible. The samples underwent several heating and cooling cycles with ramps of 0.5 $\frac{°C}{min}$ and data was continuously acquired during the whole experiment. Due to the very slow temperature program it was not necessary to wait for the solution reaching thermodynamic equilibrium at each measurement point.

Data handling

During data reduction, the 2D-detector images were azimuthally integrated around the beam stop to produce the 1D- scattering curves. Different detector regions were masked, i.e. if they

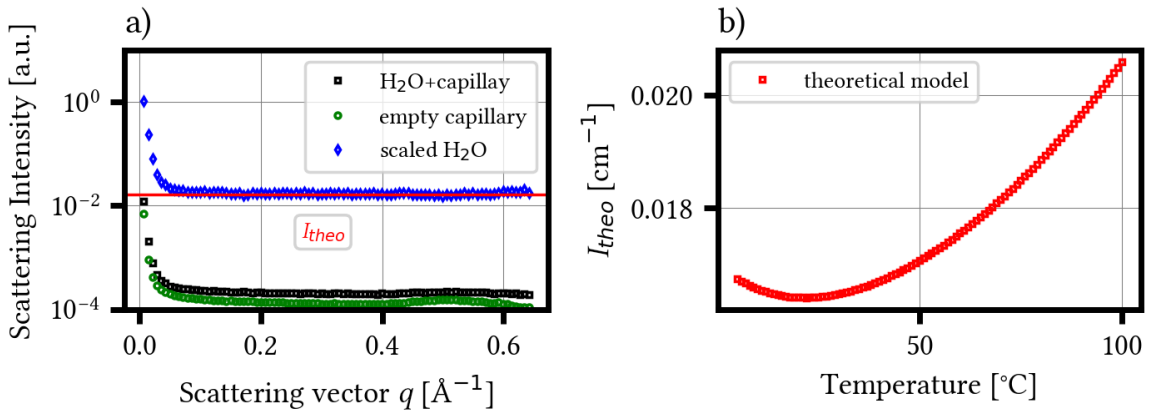

Figure 4.1. Illustration of the necessary steps for the background subtraction routine and determination of the calibration scaling factors. a) scattering curves for water inside the capillary, the pure scattering of the capillary and the background-subtracted and scaled curve for water, which was scaled to match the theoretical value I_{theo}. b) the theoretical model from equation (1.99) for the scattering cross section of water at different temperatures.

consisted of dead pixels or if two detector tiles overlapped. During integration the intensities are normalized by the incoming flux and the measurement time, i.e. the time in which the shutter is open and photons can hit the sample. These two normalizations replace a necessary transmission measurement. After integration, it is necessary to "remove" the scattering signal of the solvent and capillary, which were both measured separately and independently (see figure 4.1, a), from the scattering signal of the aqueous Pluronic solutions. The pure Pluronic scattering curve can be obtained by

$$I_{\text{scatt}}^{\text{P123}} = \frac{SF}{d_{\text{sample}}} \left(I_{\text{exp}}^{\text{P123}} - I_{\text{exp}}^{\text{H}_2\text{O}} \right) , \tag{4.5}$$

where SF is a scaling factor, d_{sample} the sample thickness and $I_{\text{exp}}^{\text{P123}}$ as well as $I_{\text{exp}}^{\text{H}_2\text{O}}$ are the experimentally obtained integrated scattering images of the aqueous Pluronic solutions and distilled water, respectively. After applying equation (4.5), the scattering intensity should be equivalent with the differential cross section $\frac{\mathrm{d}\sigma}{\mathrm{d}\Omega}$ and have units of $\frac{1}{\text{cm}}$, but the instrumental and experimental limitations outlined in chapter 1.3.4 maintain.

In order to reach absolute intensities, which correspond to $\frac{\mathrm{d}\sigma}{\mathrm{d}\Omega}$, the scaling factors SF in equation (4.5) are determined using the theoretical model for the scattering of water (see equation (1.99) in chapter 1.3.4). After subtracting the scattering curve of the empty capillary from the scattering curve of water, the mean of the scattering intensity $\overline{I}_{\text{H}_2\text{O}}$ is calculated between q = 0.2 and 0.5 Å^{-}1. This value is then compared to the one obtained by equation (1.99) at the respective temperature, I_{theo}, (see figure 4.1) leading to

$$SF = \frac{I_{\text{theo}}}{\overline{I}_{\text{H}_2\text{O}}} . \tag{4.6}$$

After each scaling factor is determined, it is used during the background subtraction at all measured temperatures.

Since all measurements were repeated several times, it is also possible to clarify whether the experiments can be reproduced. For all three Pluronic solutions the strongest deviations can be expected at the highest measured temperatures of 95°C (see figure 4.2). The overall form of the scattering curve remains the same for succeeding measurement runs and slight deviations only occur at very low q-values. In the following, each temperature run will be analyzed individually, but the results will later be compared and averaged providing the most convincing uncertainty evaluation during data analysis.

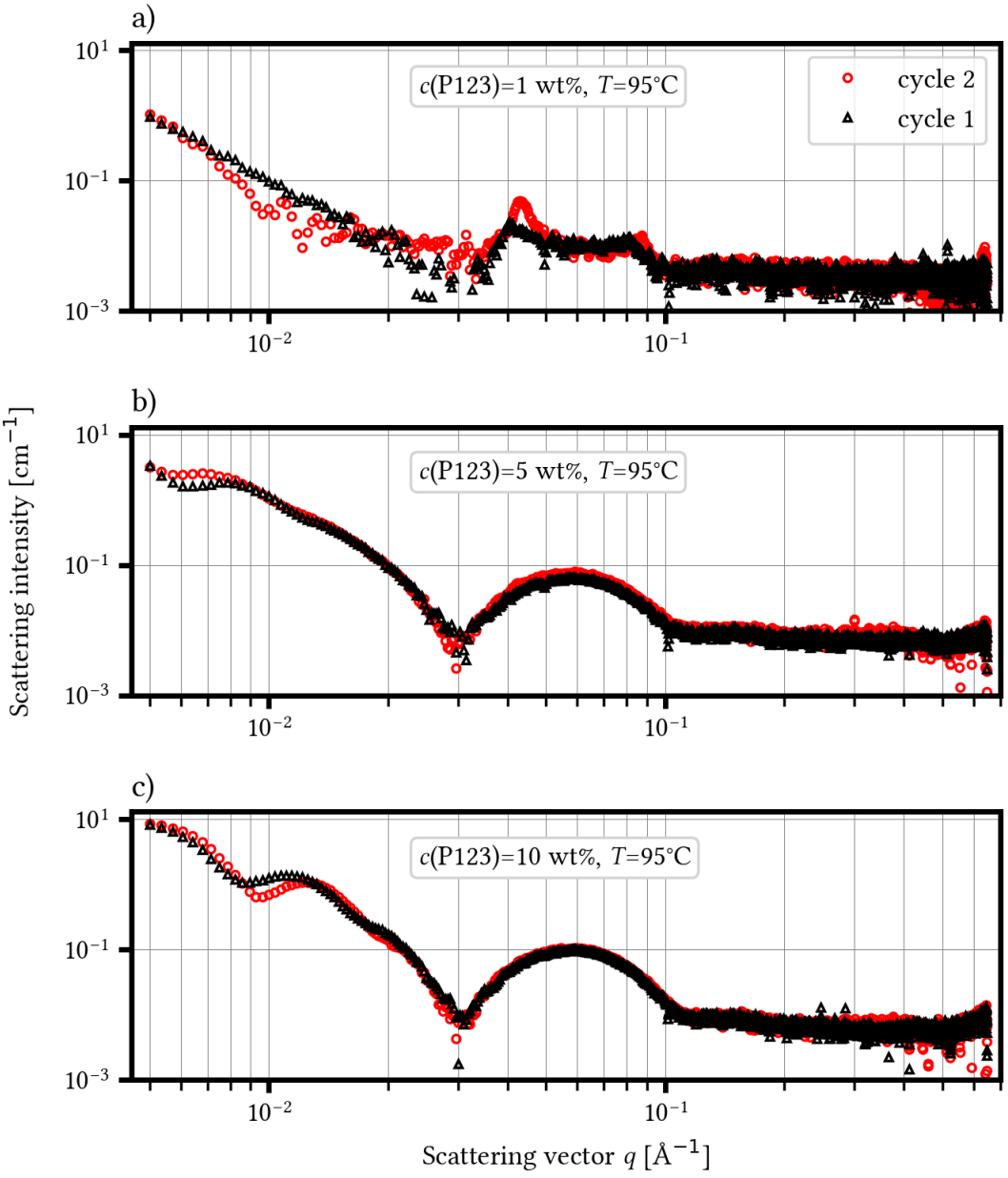

Figure 4.2. SAXS data of Pluronic samples with concentrations of a) 1 weight percent (wt%), b) 5wt% and c) 10 wt% at the highest measured temperatures (T = 95°C). All scattering curves are scaled to absolute intensities and were background-subtracted accroding to equation (4.5).

4.3. Small-angle neutron scattering

Sample preparation

The samples were prepared using the same procedure decribed in section 4.1. In addtion to the standard samples containing 1, 5 and 10 weight percent, which were dissolved in heavy water, a second batch of the same concentrations were prepared using a mixture of distilled and heavy water. Since both water variations have very distinct differences in their neutron scattering lengths (see table 4.1), it is possible to adjust the scattering length density of the solvent in the samples. For micelles with a cores-shell structure, this so-called contrast matching can be

Sample	b_n [fm][a)]	ρ [g/cm^3]	ρ_X^s [10^{10} cm^{-2}]	ρ_n^s [10^{10} cm^{-2}]
Hydrogen (^{1}H)	-3.741			
Deuterium (D=^{2}H)	6.671			
Carbon ($_6$C)	6.646			
Oxygen ($_8$O)	5.803			
Distilled water (H_2O)		0.996[b)]	9.39	-0.56
Heavy water (D_2O)		1.103[b)]	9.36	6.35
Pluronic P123 ($C_{290}O_{111}H_{588}$)				
$HO(EO)_{20}(PO)_{70}(EO)_{20}H$				
Micelle core			9.2[c)]	0.34
shell			9.8[c)]	0.59

Table 4.1. Neutron scattering lengths b_n, densities ρ and X-ray and neutron scattering length densities ρ_X^s and ρ_n^s of those elements and compounds, which are used for the experiments. a) values taken from [112], b) theoretical model values at 30°C taken from [322], c) experimentally obtained values for an aqueous P123 solution with 5 weight percent at 30°C taken from [231].

used to modify the solvent scattering length density to be equal to one of the components. The matched component has then zero contrast and is invisible for the incoming neutrons, which gives the opportunity to individually measure both the micellar core or shell. To obtain a certain scattering length density ρ_{target}^s, the mass ration between distilled and heavy water is

$$\frac{m_{H_2O}}{m_{D_2O}}(\rho_{\text{target}}^s) = \frac{(\rho_{D_2O}^s - \rho_{\text{target}}^s) \cdot \rho_{D_2O}^s \cdot x}{\rho_{\text{target}}^s \left[\rho_{D_2O}^s + \rho_{H_2O}^s (1-x)\right] - \rho_{D_2O}^s \rho_{H_2O}^s (2-x)}, \tag{4.7}$$

where $\rho_{D_2O}^s$ and $\rho_{H_2O}^s$ are the **neutron** scattering lengths of heavy and distilled water, respectively, as well as x is the degree of deuteration. If only the X-ray scattering length is known,

it can be converted to its neutron counterpart using equations (1.52):

$$\rho_n^{\mathrm{s}}(\rho_X^{\mathrm{s}}) = \frac{1}{r_e}\frac{\sum_i n_i \cdot b_i}{\sum_i n_i \cdot Z_i}\,\rho_X^{\mathrm{s}} \tag{4.8}$$

with the neutron and X-ray scattering lengths, ρ_n^{s} and ρ_X^{s}, of the system, the classical electron radius r_e as well as the neutron scattering lengths b_i, atomic number Z_i of each element in the compound and its stoichiometric composition n_i. For the presented small-angle neutron scattering experiments, the samples were preapred on-site in Dubna using the provided heavy water (ρ = 1.1052 $\frac{\mathrm{g}}{\mathrm{cm}^3}$ at 20°C, x = 0.99) following equation (4.2). For the contrast match experiments, the solvent of the aqueous solutions was set to match the scattering length density of the shell of the spherical micelles formed by Pluronic. Since the small-angle X-ray scattering experiments at the APS were yet to be performed at this time, the value for the the shell scattering length density was taken from preliminary SAXS data of the spherical micelles using laboratory equipment [231] (see table 4.1). This value was transformed using equation (4.8) and inserted into equation (4.7) to yield

$$\frac{m_{\mathrm{H_2O}}}{m_{\mathrm{D_2O}}} = 0.431 \tag{4.9}$$

as the desired ration between distilled and used heavy water. All prepared aqueous Pluronic solutions were stored at 5°C until they were used.

Experimental parameters

Before each experiment the samples were stirred, filled into standard hellma cells made of quartz glass with an optical path length of 1 cm and transferred to the beamline inside the temperature-controlled rack for up to 10 cells. During the experiment the samples and two pure solvents (pure D_2O, distilled and heavy water mixture) were measured at 5 different temperatures (5, 35, 45, 70 and 95°C) for 20 minutes each using the full neutron spectrum (λ_n = 0.5 – 8 Å) and a resolution of $\frac{\Delta\lambda}{\lambda}$ = 7%.

Data handling

Since the YuMO-spectrometer uses a ring detector and a white neutron spectrum, the scattering curves cannot be obtained in the same way as described in chapter 4.2. The neutrons hitting each individual ring element at different times are counted and the subsequent scattering signal is then drift-time corrected to obtain a better q-sampling. Afterwards, the scattering profiles of each individual ring are merged to cover the full q-range. For the background subtraction, the sample transmission, thickness and illumination time are taken into account. The scaling factors for the absolute intensity calibration are determined using the scattering signal of two vanadium standards, which are measured simultaneously with the samples. The whole data reduction routine is done using the customized software SAS, which was accessible at the beamline [323].

4.4. Neutron reflectometry

Sample preparation

All samples were prepared on-site in the chemical laboratories of the ILL using heavy water (degree of deuteration: 99.9%) as solvent and the procedure described in chapter 4.1. After their preparation, the samples were stored at 5°C. In addition to the Pluronic solution, hydrophillic and hydrophobic surfaces were necessary for the experiments. Both were prepared using silicon blocks (CrysTec (Berlin), Germany, dimensions: 70x70x10 cm) with polished surfaces, which were either cleaned or coated with octadecyltrichlorosilane (OTS) following the recipes in chapter 2.3. All blocks were loaned from the Chair of Crystallography at the University Nürnberg-Erlangen, which is gratefully acknowledged here again. To form hydrophilic surfaces, the blocks were first cleaned with ethanol, acetone and toluene before they were put into Caro's acid for 15 minutes each. Afterwards, they were rinsed until they reached chemical neutrality (ph=7) and then stored in distilled water at the beamline. Some of the blocks were already OTS-coated and were used as received. The surface energy of each silicon block was determined using contact angle measurements (see table 4.2).

Experimental parameters

In the present experiments a commercial rheometer by Anton Paar with the plate-plate geometry was used, which was mounted on a damped steel construction and modified to use the custom-made silicon blocks exploiting the inverse scattering geometry (see figures 1.12, b and 3.4). Prior to their use, each silicon block was rinsed with water and cleaned with dry air to remove dust and other residues. For the experiments, the rheometer caviaty (distance between silicon surface and the rotator of the rheometer) was set to 60 µm and overfilled with roughly 5 ml of the Pluronic solutions to allow for a uniform sample thickness. The samples were heated and cooled between 10 and 70°C and measured continously during the applied temperature ramps. In order to obtain reasonable results in short illumination times, the wavelength spectrum was used from 2 – 20 Å with a resolution of $\frac{\Delta\lambda}{\lambda} = 7\%$ and a rectangular slit collimation. Two incident angles, -1.5° and -2.5°, were used for the measurements. At 10, 38 and

Silicon Block number	Contact angle θ_c [°]	Surface energy γ [mN/m]
#1 (hydrophilic)	≤ 10	≥ 71
#2 (hydrophobic)	100.8 ± 0.3	12.0 ± 0.2

Table 4.2. Properties of the used hydrophilic and hydrophobic silicon surfaces. The contact angle was measured using distilled water ($\gamma_{H_2O}(20°C) = 72.75\frac{mN}{m}$) [324] at different locations on the surfaces. The shown values represent the mean over the whole surface. For the hydrophilic surface it was not possible to measure the contact angle, since the water droplet immediately dispersed. The values for γ were calculated using equation (2.28).

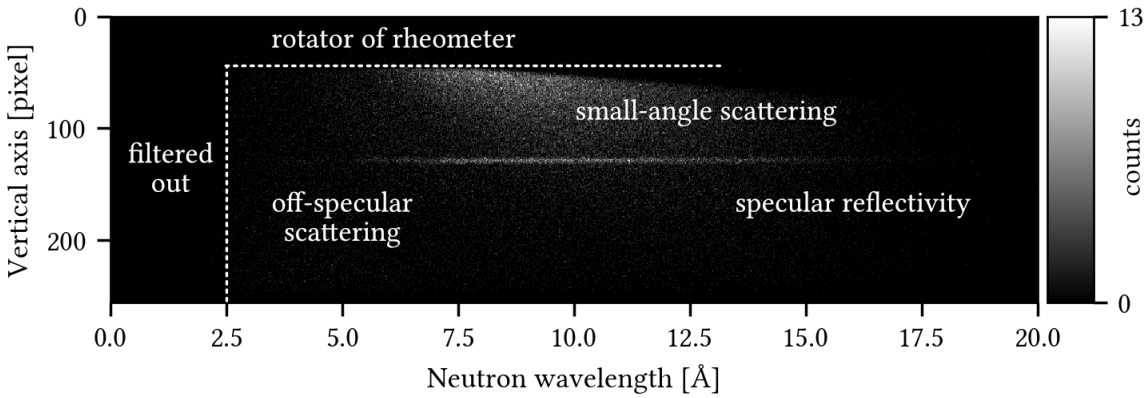

Figure 4.3. Example of recorded data at the FIGARO beamline. The data is presented over the full neutron spectrum (0 – 20 Å) and each wavelength bin represents the horizontally integrated detector signal. The regions of specular and off-specular reflectivity as well as the small-angle scattering signal are marked in the picture.

70°C, the samples were measured for 20 minutes under −1.5°. During the subsequent heating and cooling ramps between these temperature, each measurement was performed under −2.5° and lasted only 60 seconds each to track small structural changes near the surfaces. The data of both angles was later merged to cover a wide q-range during data analysis.

Data handling

The obtained detector images of the Pluronic samples were normalized using a direct beam (no sample in the path of the neutron beam) and pure solvent measurement. In both cases, the slit configuration was kept exactly the same. The solvent measurement time was 20 minutes to allow for good statics on the detector. To finally obtain the specluar reflectivity curve, the off-specular and incoherent backgorund scattering has to be subtracted (see figure 4.3). All the described steps were performed using the COSMOS software [318], which is an integrated reflectometry macro for the universal data handling software LAMP at the ILL [325].

4.5. Kinetic measurements

In addition to the experiments described in chapters 4.1-4.3, the kinetics of the transition from spherical to worm-like micelles were investigated following a unified procedure for all methods based on prior experimental studies by Kadam et al. [222] and Landazuri et al. [40].

Experimental parameters

During the kinetic experiments, all measured samples were rapidly brought to the transition temperature at which spherical micelles start to fuse and form worm-like aggregates. After initial equilibria at 5°C and 25°C to form spherical micelles, the Pluronic solutions were heated to 55°C as fast as possible using the accessible experimental equipment. Then, the samples were kept at this temperature for several hours (DLS: 8 hours, SAXS: 5 hours, SANS: 3 hours), while data was continuously acquired. Despite the total measurement time, the experimental parameters of each technique were kept the same as in the chapters before.

Data handling

The experimental data was treated and analyzed using the same techniques and recipes from the previous chapters (4.1-4.3). Each measurement was time-stamped, which was later used to calculate the temporal sampling for each experiment and obtain the correct kinetic parameters of the fusion process.

5. Results and Discussion

This chapter will provide the main results of the different experiments outlined in chapter 4. The theoretical concepts behind most of the analysis methods used here, unless otherwise stated, can be found in chapter 1. Following the experimental determination of the form-phase diagram of Pluronic P123 in 5.1 using the light scattering data, the structural properties and formation kinetics of P123's worm-like and lamellar micelles at elevated temperatures will be shown in 5.2. At last, the aggregation behaviour of P123 under confinement near surfaces and different surface energies will be presented in 5.4, highlighting a possible explanation for the observed gelation of bulk solutions near their cloud point.

5.1. Form-phase diagram of Pluronic P123

In chapter 2.2.2, the different temperature-dependent form phases of Pluronic P123 known in literature were already mentioned (see fig 2.6). At low temperatures, the individual P123 chains move independently in the solvent and are called unimers. By surpassing a certain temperature, the critical micellization temperature (cmt), the polymer chains start to agglomerate and form spherical micelles with a core-shell structure, which undergo two more form phase transitions towards worm-like and lamellar structures. To measure the precise transition temperatures, the data obtained by the dynamic light scattering (DLS) experiments can be used.

Following form scattering theory, the scattered intensity from a particle is proportional to its size. Especially in the backscattering geometry of the Zetasizer (see chapter 3.1), where no anisotropy in the scattering signal due to the shape or alignment of the particles is expected, this correlation is valid. Since the particle size increases for unimers, spherical micelles as well as worm-like and lamellar aggregates, the observed scattering intensity has to increase accordingly (see figure 5.1, a and b). At low temperatures, the observed intensities are significantly lower compared to the one at the highest measured temperature (88°C). In addition, the scattering intensity systematically increases with increasing concentration, which is also expected from theory, since the scattering intensity is proportional to the number of particles in the solution or their volume fraction (see equations (1.34) and (1.38)). There are certain temperature regimes in which the intensity is almost constant followed by sharp and steep increases. Since the micelllization and the following shape transitions of the micelles happen in narrow temperature gaps [36, 41, 40], these plateaus and inclines can be associated with the different shapes or aggregation states of Pluronic P123 and the transition regions connecting them. Similar interpretations have been made for Pluronic P85 using the intensities of small-angle neutron scattering experiments [41].

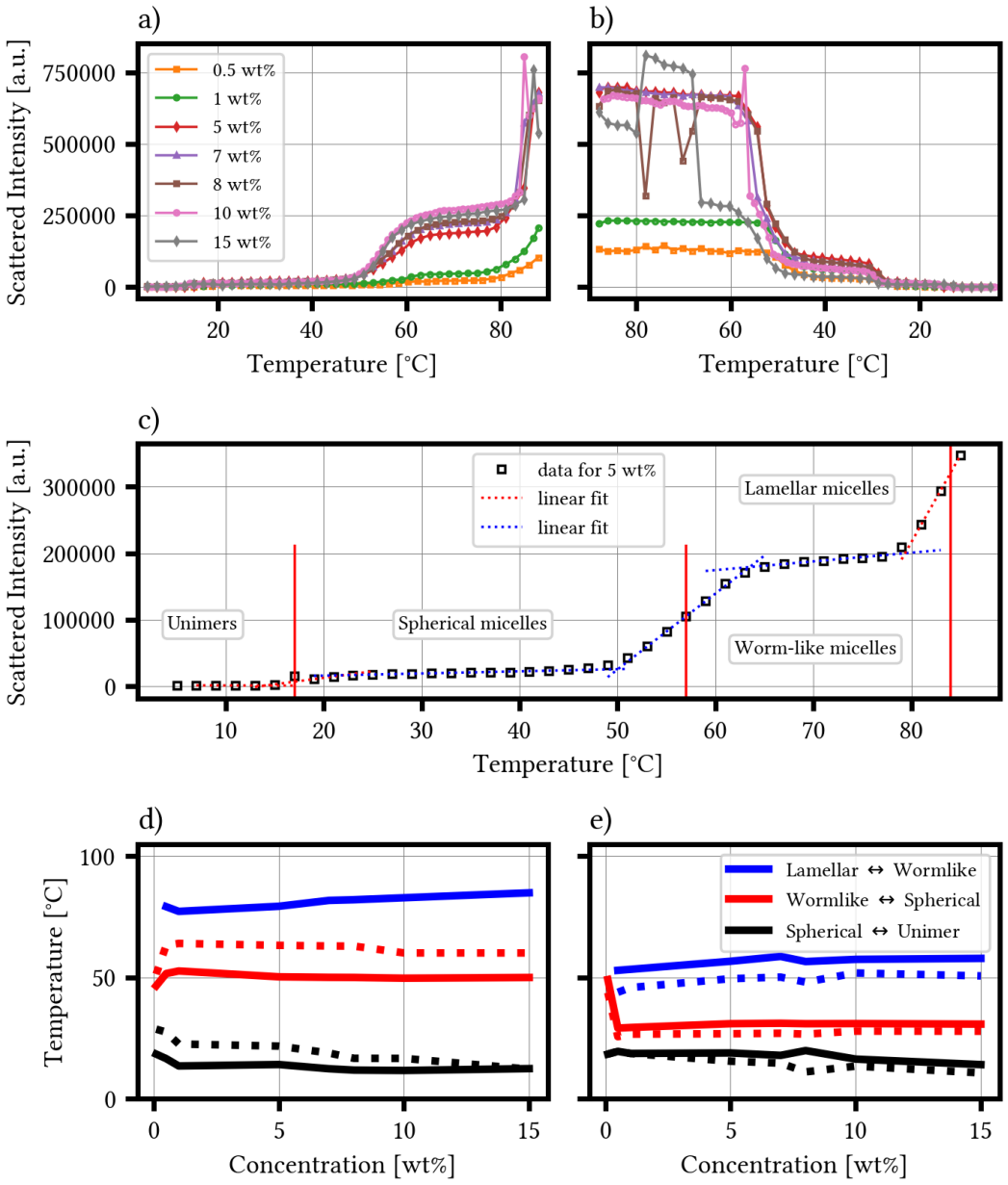

Figure 5.1. a) Light scattering intensity of Pluronic solutions with different concentrations during the heating and b) the cooling process of the samples. The scattering intensities were corrected for the different apertures sizes, which were used during the experiments to prevent the photo diode from overflowing. c) Example of the procedure to extract the transition points using linear fits. The uncertainties of the intensities follow the Poisson distribution are were too small to show in the graphs. d) Phase diagram of Pluronic P123 for heating and e) subsequent cooling of the solutions. The solid lines represent the beginning of the phase transition, while the dotted line shows its end. The numerical uncertainties are too small to accurately represent the errors of this crude fitting approach. It is estimated to be at least 1°C and the thickness of the lines in d) and e) was chosen to represent this uncertainty.

Between the heating (see figure 5.1, a) and the cooling of the solutions (see figure 5.1, b), an apparent hysteresis in the scattering intensities is visible. For all concentrations the highest intensities, which can be connceted to the large lamellar aggregates in the solution, remain down to temperatures of around 55°C. This is a 25°C difference between their formation (during heating) and dissolution (during cooling). The following transition are also shifted towards lower temperatures for the remaining reversed transitions. Only the phase boundaries of the demicellization are equivalent to the micellization process during heating.

To determine the precise transition temperature from the light scattering intensity data, linear fits can be used. Then, the crossing of two fit functions gives the onset and the end of each phase transition (see figure 5.1, c). This is a very crude but analytically solvable method and the transition temperatures are almost visible with the bare eye. An alternative model would be a sigmoid or logistic function, although both need at least one more parameter to refine and thus come with some numerical penalties compared to linear model. The transition temperatures for every measured P123 concentration can then be combined to form-phase diagrams for the heating (see figure 5.1, d) and cooling process (see figure 5.1, e). Following the description of the scattering intensities, the hysteresis between heating and cooling is clearly shown in the phase diagrams as well. The lamellar micelles, which stay present until 50°C, have the largest shift in the two phase diagrams, which is probably due to a supercooling of the lamellar structure. Especially the spherical micelles only have a small temperature gap in which they are present during cooling before they dissolve into individual unimers again. Hence, it is important to always cool aqueous P123-solutions down to at least 25°C, or below, to prevent shifted or altered micellar shapes between consecutive experimental runs! These form-phase boundaries and their hysteresis will appear throughout the following chapters and the reader will be referred to the two phase diagrams and the measured transition temperatures in different parts of the subsequent data analysis and discussion.

5.2. Structural analysis of Pluronic P123 and the formation of micelles

The following chapters will analyze the structural properties of Pluronic P123 and its micelles in the different temperature regimes outlined by its form-phase diagram (see figure 5.1, d and e) focusing on the high-temperature transitions to worm-like and lamellar structures. A detailed analysis of the unimers and spherical micelles can be found in reviews of Pluronics [36] and the excellent literature by Mortensen et al. and Pedersen et al. [39, 42, 66, 175, 326]. Throughout the next chapters, the results of three selected P123 concentrations will be presented: 1, 5 and 10 weight percent. Here, the solutions with 1 weight percent show no measurable structure factors in the scattering exerpiments, while the aqueous solutions with 5 and 10 weight percent of P123 show mild or even dominant texturization and micelle-interactions, respectively. Using these concentrations will make it possible to study the influence of inter-particle and micelles interactions on the aggregation process.

5.2.1. Hydrodynamic diameter and size distribution

Besides using the scattering intensities of the dynamic light scattering to determine the form-phase diagram of Pluronic P123 (see chapter 5.1), the goal of these experiments was to determine the temperature-dependent size and size distribution of the polymeric particles in the solutions. The Malvern instrument calculates the autocorrelation function (ACF) of the electric field g^1 internally using equation (4.3) (see figure 5.2, a). At low temperatures in the unimer phase of P123, the ACF decays or vanishes the slowest, which would indicate the biggest particles. This is counterintuitive and probably due to dust or another contamination. With increasing temperature, the ACF decays slower due to the presence of micelles and even larger aggregates. The instruments software is also capable of using different algorithms to either model the g^1-function by a cummulant approach (see equation (1.38)), or by the inverse Laplace-transformation (see equation (4.4)) with the CONTIN software package [320]. Although both methods yielded almost identical size distributions, only the results by the CONTIN algorithm will be used (see figure 5.2, b), since this method is model-independent and could detect multiple particle populations with different distributions. The transformed real-space data was then fitted using a log-normal distribution

$$D(d) = \frac{1}{\sqrt{2\pi}\,\sigma d}\, \mathrm{e}^{-\frac{(\ln(d)-\mu)^2}{2\sigma^2}} \tag{5.1}$$

with the transformed particle diameters d, the mean of the distribution μ and the shape parameter σ. For $\sigma = 1$, the log-normal distribution becomes a symmetric function and special case of the Gaussian distribution. If $\sigma \neq 1$, it has an asymmetric shape, which is ideal to describe the size distributions obtained by dynamic light scattering. The maximum of the distribution, which is the most probable particle diameter in the solution, is then obtained by

$$d_{\max} = \mu - \mathrm{e}^{\sigma^2} \tag{5.2}$$

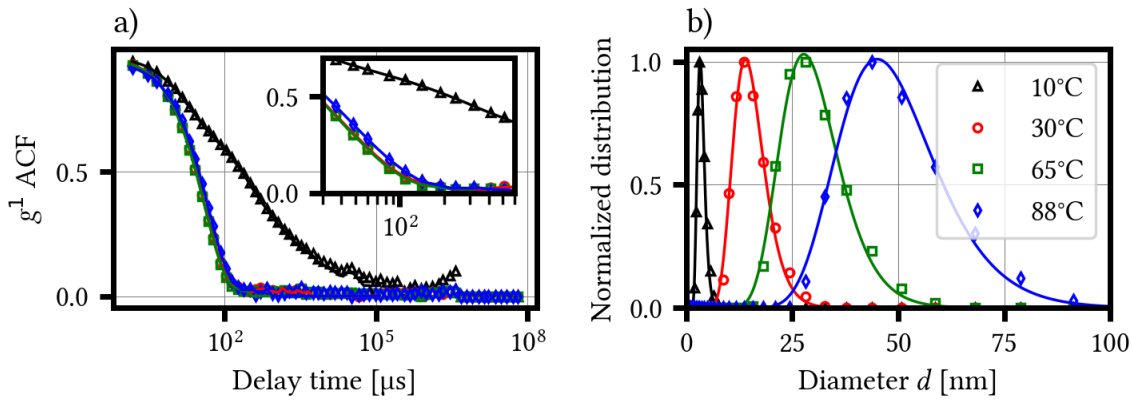

Figure 5.2. Exemplary data of a) the electric fields temporal auto-correlation function (ACF) $g^1(t)$ and b) the associated size distributions from the dynamic light scattering experiments using an aqeous solution with 5 weight percent of P123. The colored lines are fits through the data points, which were either done a) by the instrument using the CONTIN algorithm or b) by hand using a log-normal distribution function.

with the standard deviation

$$\mathrm{STD} = d_{\max} \cdot \sqrt{e^{\sigma^2/2} - 1} \ . \tag{5.3}$$

In case of dynamic light scattering, this maximum is called the hydrodynamic diameter. In contrast to the radius of gyration in equation (1.63), the hydrodynamic diameter/radius is not an averaged, model-independent quantity, but gives a sphere around the particle and its surrounding solvent shell.

In the temperature-dependent hydrodynamic diameter of the aqueous Pluronic P123 solutions, different size regimes are visible (see figure 5.3, a), which coincides with the transition borders of the measured form-phase diagram of the heating process (see figure 5.2, d). The numerical fit errors of the distribution parameters were smaller than the chosen symbols and, although it is possible to calculate the standard deviations using equation (5.3), errorbars were omitted in figure 5.3, a and b for reasons of clarity. Up to 17°C, P123 does not aggregate and the unimers have a mean size of 2 nm, which is in fair agreement with radii of gyration between 1 and 1.4 nm as reported in literature for various other Pluronics [39]. By surpassing the critical micellization temperature at around 18 to 19°C, the resulting spherical micelles have an average hydrodynamic radius between 16 and 18 nm. Interestingly, the micellar size seems to stay almost constant over their whole phase regime. Similar values have been observed before using small-angle X-ray [231] and small-angle neutron scattering experiments [61, 62, 39]. Interestingly, the spherical micelles seem to become smaller for higher concentrated solutions. A similar effect has been reported for Pluronic P85 [39]. After surpassing the second transition temperature at 50°C for the formation of worm-like structures, these larger aggregates almost double in size and stay constant in size after the transition is completed. Towards the could point, a third transition is visible with even larger, lamellar aggregates starting to form. In the

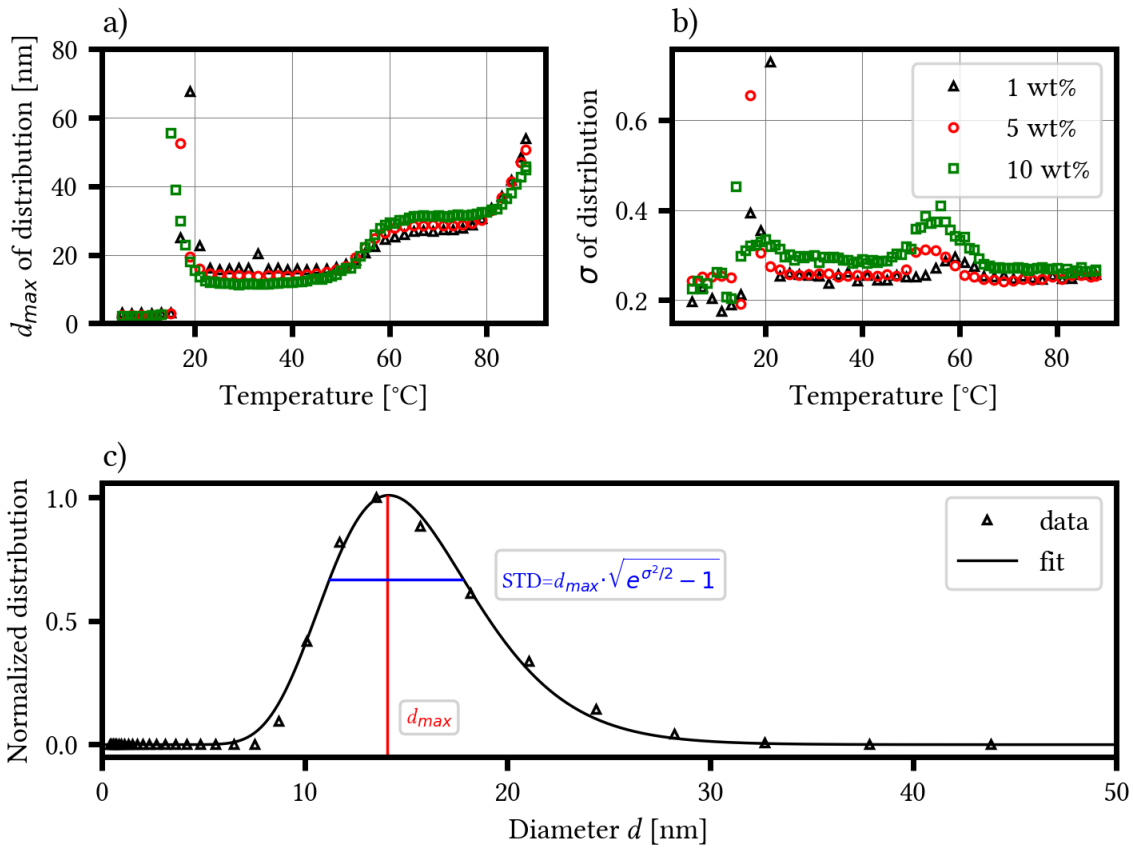

Figure 5.3. Results of the log-normal distribution fit to the dynamic light scattering data of the heating process: a) Maximum of the distribution, which represents the hydrodynamic radius of the observed particles, and b) the shape parameter σ of the log-normal distribution. c) Graphic representation of the distribution parameters and the associated standard deviation.

higher temperature regime, similar hydrodynamic diameter were reported for the worm-like micelles using light scattering experiments [40], but the structure and aggregate sizes near the cloud point are undocumented.

The shape parameter σ of the size distributions is nearly constant for the whole temperature range, with its only deviation in the transition regions (see figure 5.3, b). This could indicate that the observed particles are almost uniform in shape. Only during the form-phase transitions, multiple shapes and hence sizes would be present, which would lead to a wider distribution with different shapes. Dynamic light scattering experiments in the backscattering geometry provide information about particle sizes and do not allow for a direct analysis of their form and shape. This is done using the small-angle X-ray and neutron scattering data, but the shown results will act as initial guesses and constrains for the modeling and data analysis in the following chapters.

5.2.2. Structural properties

In contrast to the dynamic light scattering experiments, which can be used for the determination of the hydrodynamic radius and its distribution, small-angle scattering offers the possibility to access more detailed information about the particles in the aqueous solutions, e.g. their shape, size, inner structure and electron density difference compared to the solvent. Depending on the probe, i.e. whether neutrons or X-rays are used during the experiments, the resulting scattering curves will differ but consequently give the same set of information (see figure 5.4).

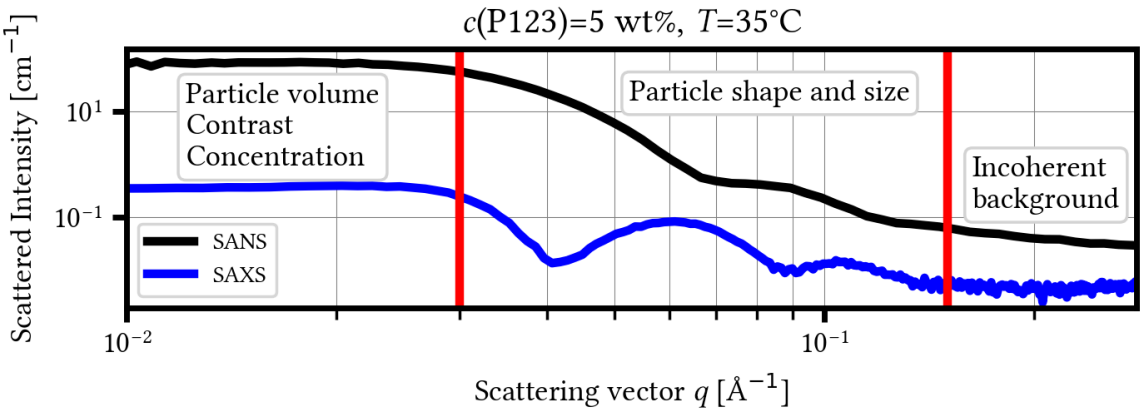

Figure 5.4. Explanation of the different scattering vector regimes and their importance for data analysis. Both small-angle neutron (SANS) and X-ray scattering (SAXS) data of the same sample (P123 concentration: 5 weight percent) at the same temperature (T = 35°C) is shown.

When comparing SANS and SAXS curves of organic samples like Pluronic P123, the scattered neutron intensities will be several orders higher than the equivalent X-ray data. This is due to the significantly higher scattering contrast $(\Delta\rho)^2 = (\rho^s_{\text{solvent}} - \rho^s_{\text{sample}})^2$ when using heavy water as a solvent in SANS experiments (4.1). At the same time, the scattering background, which is a combination of both incoherent scattering of the sample and the intrumental set-up, is systematically higher for neutrons when measuring organic samples due to the large amounts of hydrogen and its incoherent scattering cross-section. In addition, the intrinsic, finite q-resolution of a neutron experiment (see chapter 1.3.3), will result in smeared curves, which are more featureless compared to X-ray experiments. Even with an excellent q-resolution way below 1%, the features in SANS curves are generally less pronounced and shifted compared to the corresponding SAXS curve. In case of Pluronic P123, this is due to different contrasts between the PEO and PPO blocks with distilled or heavy water for X-rays or neutrons, respectively (see equation (1.81)). In the following, the data of both SANS and SAXS experiments will be analyzed to give model-independent information about the shape, size and aggregation number of P123 and its micelles. A thorough model-based analysis of the inner structure, especially of the worm-like and lamellar micelles can be found in chapter 5.3.

Radius of gyration and shape parameter

In the different temperature regimes, the observed small-angle neutron and (SANS) X-ray scattering (SAXS) data varies significantly depending on the present, dominant polymer or micelle shape (see figure 5.5). At low temperatures, both SANS and SAXS experiments show featureless and simply exponential decaying scattering curves (see figure 5.5, a and b). This is indicative of small particle sizes as they are expected for the free unimers by the dynamic light scattering (DLS) experiments (see figure 5.3, a). After surpassing the critical micellization temperature, spherical micelles are formed. At temperatures above 30°C this transition is finished and the scattering intensity is dominated by the signal of these spherical aggregates (see figure 5.5, c and d). Both SANS and SAXS data show the characteristic micelle oscillation in the q-range between 0.04 and 0.08 $Å^{-1}$, while the SAXS data even shows a smaller second-order peak of the spherical form factor (see figure 5.5, d). The higher concentrated P123 solutions with polymer concentrations of 5 and 10 weight percent (wt%) exhibit another peak between 0.02 and 0.03 $Å^{-1}$ due to a pronounced average distance between the micelles, which can be modeled using a structure factor (see chapter 1.3.3). In the worm-like micelle regime, the plateau intensity increases and the beginning of the exponential decay is shifted towards smaller q-values indicating the presence of larger particles (see figure 5.5, e and f). But here the obtained neutron and X-ray scattering data also show the most prominent differences. While the neutron data would suggest a simple increase in size due to the higher palteau intensity and the shifted oscillation, the SAXS data shows three very distinct and unique peaks (see figure 5.5, f). Such a scattering curve has not been reported in literature before and it will be discussed in more in chapter 5.3.1. A possible explanation for the observed differences could be the different illumination and hence averaging times during both SANS (20 minutes) and SAXS (0.2 seconds) experiments. At the highest measured temperatures of 95°C, the scattering curves do not exhibit a plateau region at the lowest measured q-values but still rising intensities (see figure 5.5, g and h). In addition, two distinct slopes are visible at low q-values before the oscillation due to the form factor appears. This is a clear indication for, firstly, the presence of very large aggregates and, secondly, a clear shape shift.

To quantify the above mentioned observations and interpretations, the scattering data was fitted using the Hammouda-model [174]. Since it was intended for the shape-independent analysis of SANS data, the q-range for modeling was adjusted to the plateau region and exponential decay regime. The scattering curves of both spherical and worm-like micelles showed a sructural peak at low q-values due to micelle interactions. This was taken into account by extending the Hammouda-model with the Beaucage structure factor S_{BM} [172]:

$$I_{\mathrm{scatt}}(q) = I_{\mathrm{H}}(q, G, R_G, s, d)_{\mathrm{BM}}(\mathrm{q}, \xi, \kappa) \,, \tag{5.4}$$

with I_{H} and S_{BM} being the formulas from equation (1.71) and (1.96), respectively, the Guinier-factor G, the radius of gyration R_G, the shape parameter s, the slope of the exponential decay d, the inter-micelle distance ξ and their packing parameter κ. The resulting radii of gyration from the SANS data are almost the same within their uncertainties for all three investigated Pluronic concentrations (see table 5.1) and coincide within their uncertainties with the light

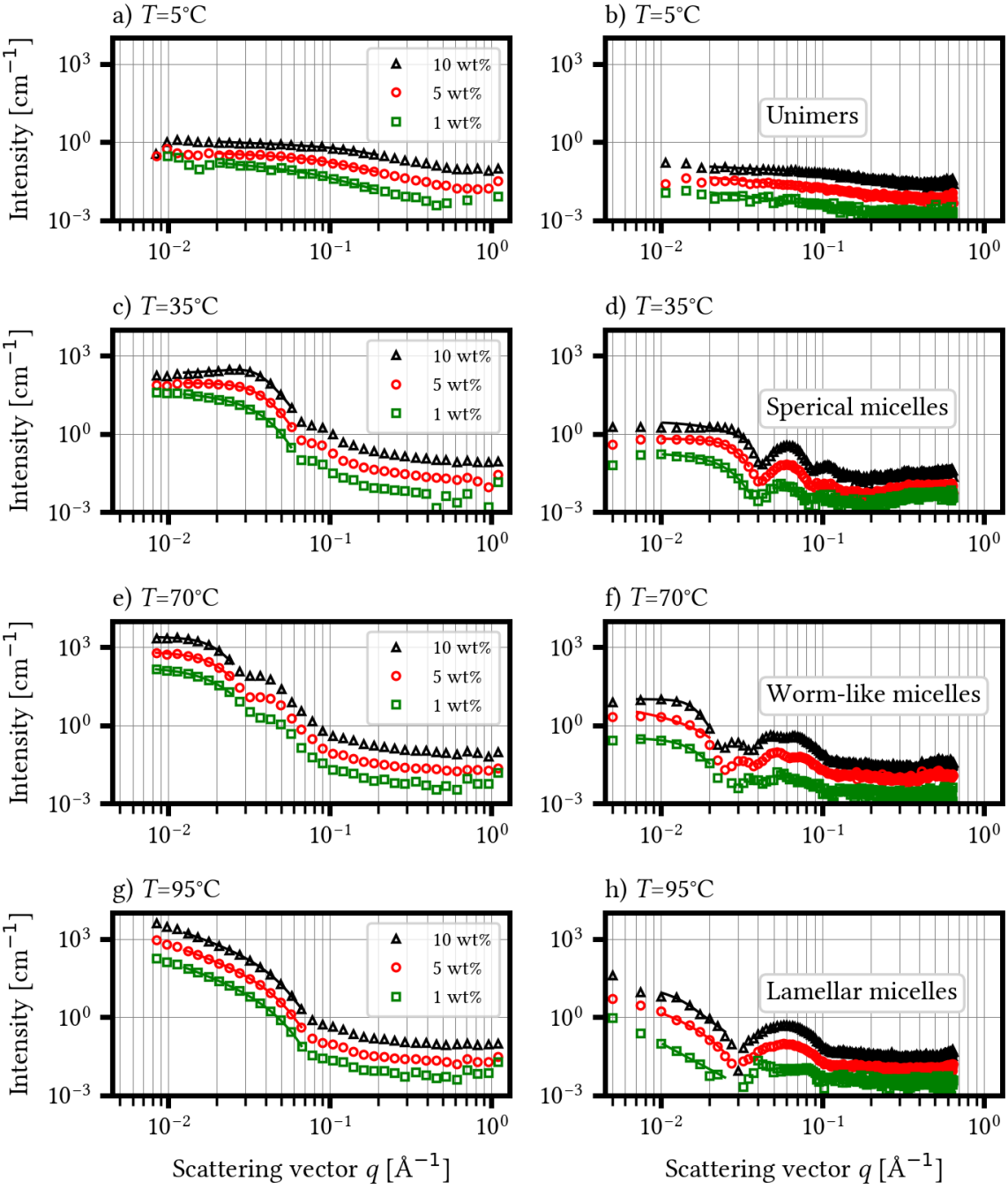

Figure 5.5. Overview of the small-angle neutron (a+c+e+g) and X-ray (b+d+f+h) scattering data of aqueous solutions with P123 concentrations of 1, 5 and 10 weight percent (wt%) at 5, 35, 70 and 95°C. Only a reduced number of data points is shown. In addition, the data of P123-solutions with 5 and 10 wt% were scaled by a factor of 1.5 and 5, respectively, to enhance visibility. The solid lines in the low-q regime are fits to the data points using the Hammouda-model in equation (1.71).

1 wt%	5°C	30°C	45°C	70°C	95°C
G	0.0225 ± 0.0094	11.4 ± 1.9	48.1 ± 5.7	200 ± 94	0.0154 ± 0.0014
R_G [Å]	11.7 ± 4.7	61 ± 15	69.0 ± 9.0	111 ± 38	29.2 ± 5.1
s	0.511 ± 0.015	0.343 ± 0.044	0	0	1.989 ± 0.011
d	1.5365 ± 0.0091	9.24 ± 0.16	9.97 ± 0.41	5.9 ± 1.8	9.854 ± 0.023
ξ [Å]		147 ± 19	405 ± 58	348 ± 63	
κ		0.326 ± 0.035	0.279 ± 0.040	0.108 ± 0.065	
5 wt%					
G	0.1414 ± 0.0033	181 ± 52	234 ± 57	1210 ± 245	0.1046 ± 0.0068
R_G [Å]	10.69 ± 0.47	63.9 ± 3.7	68 ± 11	121 ± 45	30.9 ± 5.2
s	0.2536 ± 0.0014	0	0	0	1.902 ± 0.017
d	1.2568 ± 0.0027	9.47 ± 0.22	7.78 ± 0.56	9.70 ± 0.96	8.07 ± 0.65
ξ [Å]		162.0 ± 4.3	169 ± 11	279 ± 26	
κ		1.041 ± 0.014	0.923 ± 0.029	0.715 ± 0.077	
10 wt%					
G	0.1704 ± 0.0018	293 ± 12	269 ± 34	2315 ± 623	0.276 ± 0.018
R_G [Å]	7.0 ± 1.5	61.3 ± 1.7	59.7 ± 4.6	125 ± 26	32.3 ± 3.4
s	0.2301 ± 0.0059	0	0	0	1.821 ± 0.016
d	1.107 ± 0.018	9.78 ± 0.90	6.08 ± 0.22	6.59 ± 0.71	7.72 ± 0.31
ξ [Å]		164 ± 12	169 ± 34	292 ± 8	
κ		2.62 ± 0.11	2.60 ± 0.13	1.25 ± 0.52	

Table 5.1. Fit parameters of the model-independent analysis of the small-angle neutron scattering data using equation (1.71). The values without a numerical error vanished during the fitting and were fixed afterwards.

scattering data (see figure 5.3, a) as well as the values reported in literature for Pluronic P85 [41]. In addition, the shape parameter clearly indicates that both the unimers and spherical micelles can be described by a spherical shape (low or vanishing s-value). Interestingly, the same holds for the worm-like micelles. Here, $s = 1$ would have been expected due to a more elongated shape of the worm-like aggregates [152]. A possible explanation could be the co-existence of both worm-like and spherical micelles or prolate, but very short "worms". At the highest measured temperatures above the cloud point, the resulting fit with s =1.8 to 2 shows the presence of a lamellar system. When comparing the exponential slopes d with values found in theory and literature, they are systematically too high. The reason for that is, on one hand, the presence of a structure factor and, on the other hand, an apparent low polydispersity and good q-resolution (see figure 1.10). Regarding the parameters of the structure factor, κ increases as expected with higher polymer concentration, while ξ is almost independent of the polymer concentration (5 and 10 wt%) and increases with the radius of gyration. This behavior is expected, since more polymers in the solution should result in a denser packing and larger particles would result in a longer correlation length 2ξ between them (see figure 1.11). From the very large ξ- and very low κ-values for the 1 wt% concentrated P123 solution, it can be deduced that the structure factor would not be necessary during the fitting, but it was kept for reasons of comparability. When using the fit results, which were obtained from the SANS data, for a modeling of the SAXS curves, only the Guinier-factor needed to be adjusted, since the plateau intensity can be orders of magnitudes lower (see figure 5.5, b, d, f and h).

In order to get the shape-corrected temperature-dependent size of the particles in the solution, the definition of the half-size [167, 152, 41, 153]

$$\frac{S}{2} = R_G \cdot \sqrt{\frac{5-s}{3-s}} \tag{5.5}$$

can be used. For the unimers, spherical and worm-like micelles, $\frac{S}{2}$ gives the radius R. For lamellar micelles, $\frac{S}{2} = \frac{T}{2}$, where T is the lamellar thickness or periodicity. With the obtained fit results for R_G and s,

$$\begin{aligned} R_{\text{uni}} &= 9.2 - 15.7 \text{ Å} \\ R_{\text{mic}} &= 79.1 - 82.5 \text{ Å} \\ R_{\text{worm}} &= 143 - 159 \text{ Å} \\ T_{\text{lam}} &= 50.4 - 53.0 \text{ Å} \end{aligned} \quad . \tag{5.6}$$

The values in (5.6) mark the lowest and highest possible sizes for all the different Pluronic concentrations. They almost perfectly mimic the hydrodynamic diameter of the DLS experiments (see figure 5.3, a), further strengthening the use of the Hammouda and Beaucage-model as well as the validity of both results from DLS and small-angle scattering experiments.

Scattering contrast

Besides the radius of gyration, it is possible to obtain information about the internal structure of the particles without assuming a fitting model with an explicit particle shape. In a first step, the scattering invariant (see equation (1.68) in chapter 1.3.2) can be analyzed. If the samples volume fraction or concentration is known, the mean scattering contrast can be derived, which should stay constant and can be used to track any unwanted changes, e.g. precipitation or evaporation, or derive more complex properties like the aggregation number (number of polymer chains forming an aggregate or micelle). The mass concentration of an aqueous P123-solution can be transformed in its temperature-dependent volume fraction using its density [231, 327]:

$$\phi(T) = \frac{\rho_{\mathrm{sol}}(T)}{\rho_{\mathrm{P123}}(T)}\, c_{\mathrm{m}} \tag{5.7}$$

with the densities of the aqueous solution ρ_{sol} and the pure P123 ρ_{P123} as well as the mass con-

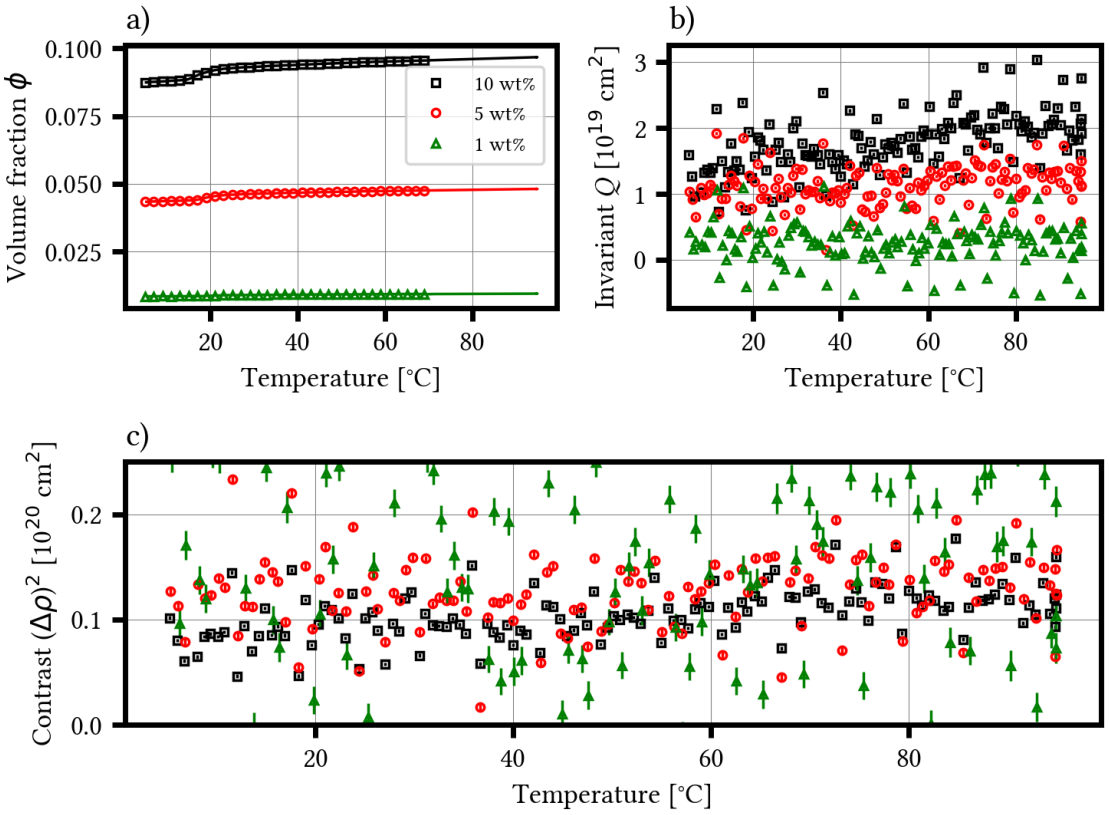

Figure 5.6. Overview of the experimental data for the invariant analysis. a) The volume fraction of the aqueous Pluronic solutions. The values were taken from [231] and the solid line is an interpolation using cubic-splines and a linear fit. b) The scattering invariant Q, which was calculated by integration of the SAXS data, was used to calculate the c) scattering contrast $(\Delta\rho^{\mathrm{s}})^2$ using equation (1.68).

centration c_m in weight percent. The solution densities for P123 concentrations of 1, 5 and 10 weight percent were measured in a previous study [231] and the pure P123 density was determined by subtracting the theoretically calculated water density [322] from the solution data [327]. As expected, the volume fraction increases slightly as a function of temperature due to thermal expansion and exhibit a characteristic feature at the respective critical micellization temperature (see figure 5.6, a). Since the experimental data was only measured up to 70°C and with a rough sampling, they were interpolated and extrapolated using cubic-spline-functions and a linear fit starting at 50°C.

To obtain the scattering contrast, it is necessary to calculate the scattering invariant Q from equation 1.68 by numerical integration of the scattering curves (see figure 5.6, b). The biggest possible errors of Q were calculated by integrating the curve with maximal and minimal intensity according to their uncertainties. With equation (1.68) and the interpolated volume fractions, the mean scattering contrast $(\Delta\rho^s)^2$ then follows, which is the mean electron-density difference between the polymer and the used solvent (see figure 5.6, c). For the solutions with P123 concentrations of 1 and 5 weight percent, the invariant Q and the contrast change very little and are almost constant over the whole investigated temperature range. Only for the highest P123 concentration of 10 weight percent, both increase slightly at temperatures above 60°C. Again, this falls into the region of worm-like and lamellar micelles. An increase in the mean scattering contrast indicates a different scattering length density of either polymer or solvent. But according to equation (1.68), a decreasing polymer concentration in the scattering volume would induce the same behavior. Both possibilities could be explained with more elongated polymer chains, which are packed more densely inside larger particles or lamellar structures with very low hydration levels. The resulting larger electron density would explain the increasing scattering contrast and the presence of larger particles in the scattering volume can cause local anomalies in the polymer distribution, which would result in locally lower volume fractions. This is a first clear indication for the dehydration and beginning phase separation towards the cloud point.

Aggregation number

In addition to the size, shape and scattering contrast, small-angle scattering can be used to determine the molar mass of the particles in the solution. The molar mass M is connected to the extrapolated intensity $I_{\text{scatt}}(q = 0)$ by [151, 328]:

$$M = \frac{I_{\text{scatt}}(q = 0) \cdot N_A}{c_m \cdot (\Delta\rho^s)^2 \cdot \rho_{\text{P123}}^{-2}}, \tag{5.8}$$

where N_A is Avogadro's constant, c_m the weight concentration of the polymers in the solution, $(\Delta\rho^s)^2$ its scattering contrast with the solvent and ρ_{P123} the polymer density. In order to determine $I_{\text{scatt}}(q = 0)$, which is the last missing component of equation (5.8), all temperature-dependent SAXS curves were fitted in the low q-regime using the same numerical approach as in equation (5.4) but changing the Hammouda with the simple Guinier-model from equation (1.61) (see figure 5.7). The reason is that the Hammouda-model does not give additional

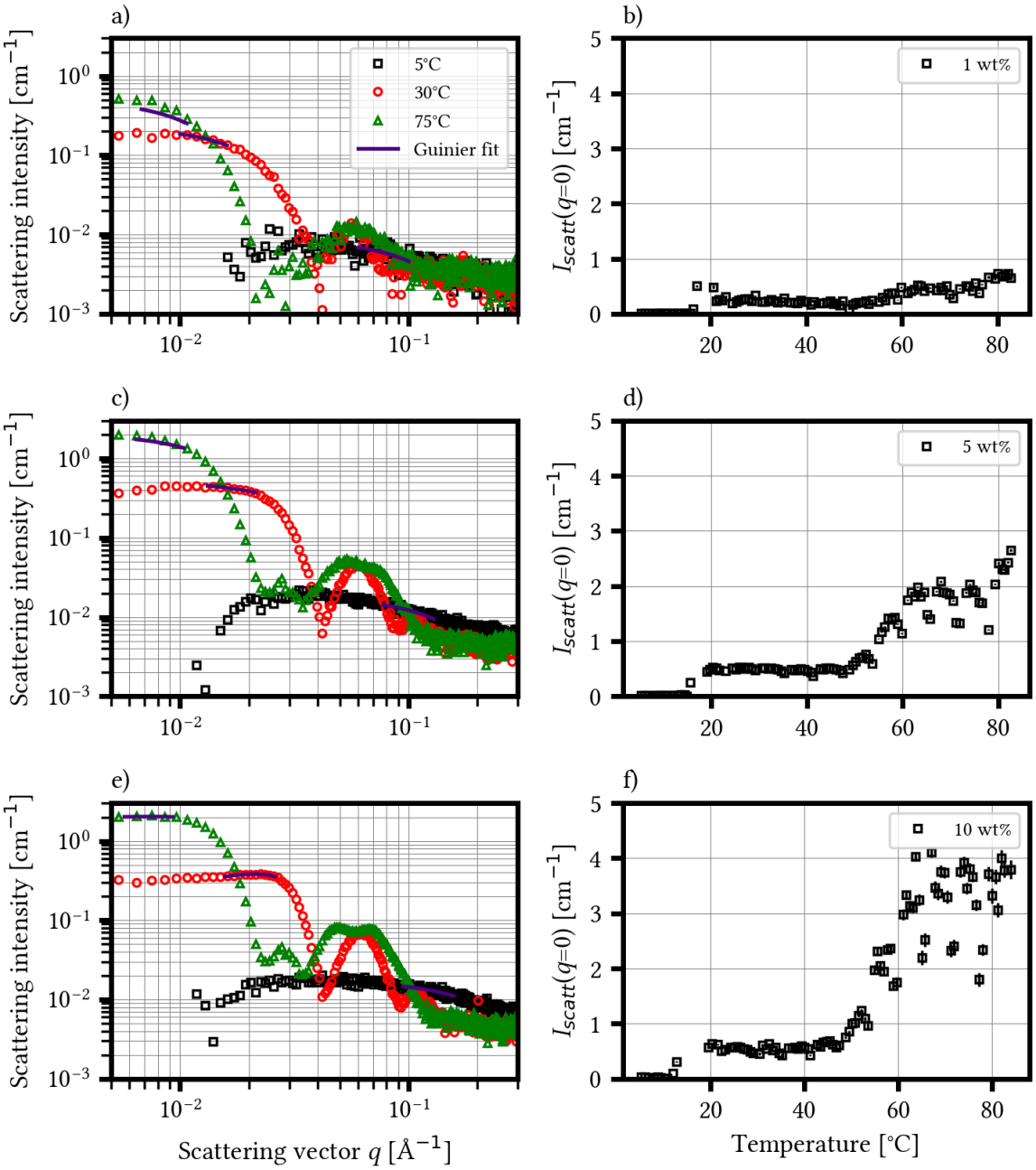

Figure 5.7. Overview of the Guinier-fits, which were used for the determination of $I_{\text{scatt}}(q = 0)$ of aqueous Pluronic solutions with a+b) 1 , c+d) 5 and e+f) 10 weight percent (wt%). The Guinier-fits are shown as purple lines through the points.

information and it is numerically favorable to reduce the number of free parameters during refinement. In addition, the previous results from the dynamic light (DLS) and small-angle neutron scattering (SANS) data were used. During the fitting of the vast amount of X-ray data sets, the q-range of the fit, the radius of gyration R_G were fixed by

$$\begin{aligned} R_G &= \sqrt{\frac{3}{5}}\,\frac{d_{\max}}{2} \\ q_{\min} &= \frac{0.9}{R_G} \\ q_{\max} &= \frac{1.3}{R_G} \end{aligned} \tag{5.9}$$

using the maximum diameter of the size distributions $d_{\max}$ obtained by DLS and theoretical limitations of the GUINIER-model [151, 152, 153]. To further reduce the number of free fit parameters, the micellar packing κ in the structure factor model was fixed according to the SANS data at 0.1, 1 and 2 for P123 concentrations of 1, 5 and 10 wt%, respectively (see table 5.1). In the end, the model only needs to adjust $I_{\text{scatt}}(q = 0)$ and the micelle correlation length 2ξ.

The extrapolated intensities (see figure 5.7) show the same characteristic plateau regions as they were already visible in the hydrodynamic diameter (see figure 5.3, a) and correlate with the different shape regimes according to the measured phase diagram (see figure 5.1, d). For temperatures $T > 80$°C, it was not possible to obtain reasonable fits, since there is no plateau intensity anymore due to the presence of very large, lamellar aggregates (see figure 5.5, g and h). The extracted intensities were used to calculate the molar masses M according to equation (5.8) and it was then possible to determine the aggregation number

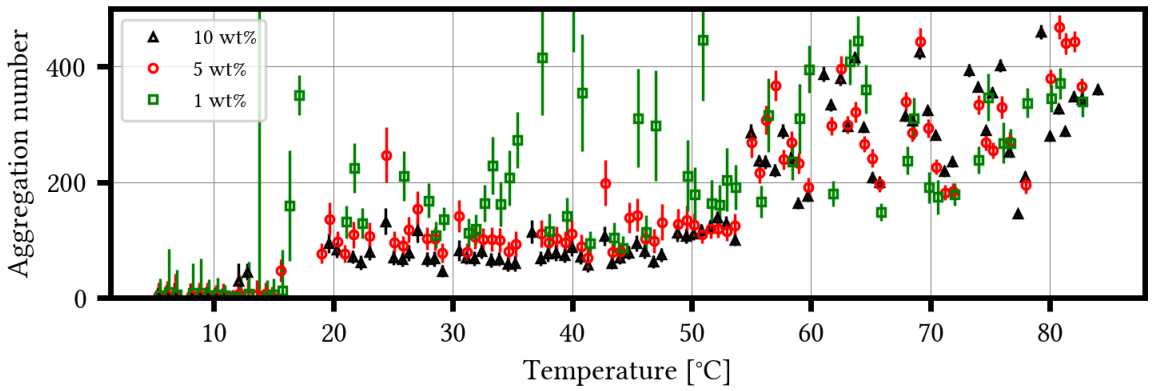

Figure 5.8. Temperature-dependent aggregation number of aqueous P123-solutions with different concentrations. The errors are due to the error propagation of all uncertainties in equation 5.8.

$$N_{agg} = \frac{M}{M_{P123}} \tag{5.10}$$

with the molar weight $M_{P123} = 5800 \frac{g}{mol}$ of one P123 macromolecule (see figure 5.8). At low temperatures, the aggregation number is negligibly small and the P123 chains acts as free unimers. Only after the critical micellization temperature, the aggregation number rises sharply and remains almost constant until 50°C due to the presence of spherical micelles. For a P123 concentration of 1 wt%, the values are highly scattered and follow no recognizable trend. This is probably due to the low concentration and a too low illumination time during the experiments. For 5 and 10 wt%, the spherical micelles have an average aggregation number $N_{agg}^{mic} = 98 \pm 10$.

There are numerous studies in literature, which provide experimental and theoretical values for the aggregation number of different Pluronics [174, 61, 329, 39, 42, 66, 71, 220, 68]. The observed temperature-dependence and negligible effect of the concentration is backed for several other Pluronic variations [61, 177, 220] while the obtained value N_{agg}^{mic} is in very good agreement with another study by Manet et al. investigating P123's spherical micelles using SANS and SAXS [329]. However, different experimental and simulation techniques came to other results with more than double the amount of polymers inside a micelle [44, 68]. A similar ambiguity exists for Pluronic P85, which was intensively studied during the 1990s and provides the majority of published data on the structural properties of Pluronic micelles. Compared to P123, its micelles have roughly the same size (around 16-18 nm in diameter) but tends to have lower aggregation numbers [174, 39, 42], which is likely due to its higher hydrophillicity, hydration levels and hence swollen chains. Mortensen and Pedersen studied the influence of the calculation model when neutron scattering data is used [42]. If only the micellar core of dehydrated PPO is used, the N_{agg}-values tended to be lower than in the case that the whole micelle and its PEO-corona were considered. A similar explanation could be used for the discrepancy between the presented X-ray and the published higher results based on static light scattering [44] and simulation data [68]. Light scattering in general observes slightly larger particles, which naturally gives larger aggregation numbers, and the theoretical work was based on highly concentrated micellar solutions. In case of P85, Pedersen and Gerstenberg developed a tailor-made fitting model for the spherical micelles of P85 [66], which combined both approaches and was successfully used for different Pluronics, including P123, as well [329].

Investigations on the structure of the worm-like aggregates are rare in literature [174, 71], which makes it hard to compare and validate the obtained aggregation numbers in this temperature regime. It appears that the worm-like micelles consist of roughly 2-3 spherical ones (see figure 5.8), but a more thorough analysis will follow in the next chapter.

5.3. Worm-like and lamellar aggregates

The structure and formation process of the worm-like (see chapter 5.3.1) and lamellar aggregates (see chapter 5.3.2) at higher temperatures was investigated using light, X-ray and neutron scattering experiments. Following the experimental approach of Landazuri et al. [40], the kinetics of the sphere-to-worm transition was studied with non-equilibrium measurements and all three scattering techniques. In addition, the kinetic small-angle X-ray scattering (SAXS) data was modeled using a combination of explicit form-factor models and phenomenological elements. These results were then used to get an interpretation for the structural changes during the subsequent transition to lamellar aggregates near the could-point.

5.3.1. Sphere-to-worm transition

The data shown here are based on the temperature-jump experiments, whose experimental description and parameters can be found in chapter 4.5.

Kinetics

The kinetics of a chemical reaction give an understanding for the rates at which they take place, i.e. how fast a reaction or transition takes place and when the equilibrium is reached. In case of the sphere-to-worm transition of Pluronic P123's micelles, it is triggered by surpassing a distinct temperature of 55°C (see figure 5.1, d). Due to experimental restrictions during the beamtimes, a complete data set using all three scattering techniques was only achieved for solutions with a Pluronic concentration of 5 weight percent (wt%). Hence, only the data for this concentration will be shown here, but similar results can be expected for the lower and higher concentrated solutions as well. With increasing time at the transition temperature, the micelles seem to grow (see figure 5.9). While the dynamic light scattering (DLS) data only hints an expected shift of the observed distributions towards bigger particle sizes, the small-angle X-ray (SAXS) and neutron (SANS) data clearly indicate changes in the shape and composition of the particles. To analyze the data in a more unified way, the time-dependent scattering intensity is used. For the DLS data, this is simply the accumulated photon counts on the photo diode. A similar parameter for the SAXS and SANS data is the extrapolated intensity $I(q = 0)$, which is again determined using a combination of the Guinier- and Beaucage-model (see chapter 5.2.2). Landazuri et al. narrowed the formation process of the worm-like micelles down to the random fusion of spherical ones and used a single exponential function to fit the kintetics curves [40]:

$$I(t) = I_1 - I_2 \, \mathrm{e}^{-\tau \cdot t} \, . \tag{5.11}$$

Here, I_1 and I_2 are two scaling intensities while τ is the kinetic rate of the transition. All extracted time-dependent scattering curves can be fitted using equation (5.11) and yield kinetic rates, which are in good agreement with those found in literature for P123 [69, 70, 63] and a different Pluronic variant (P103) [40]. Yet, there are distinct differences between the used techniques and solvents (see table 5.2 and figure 5.10, a).

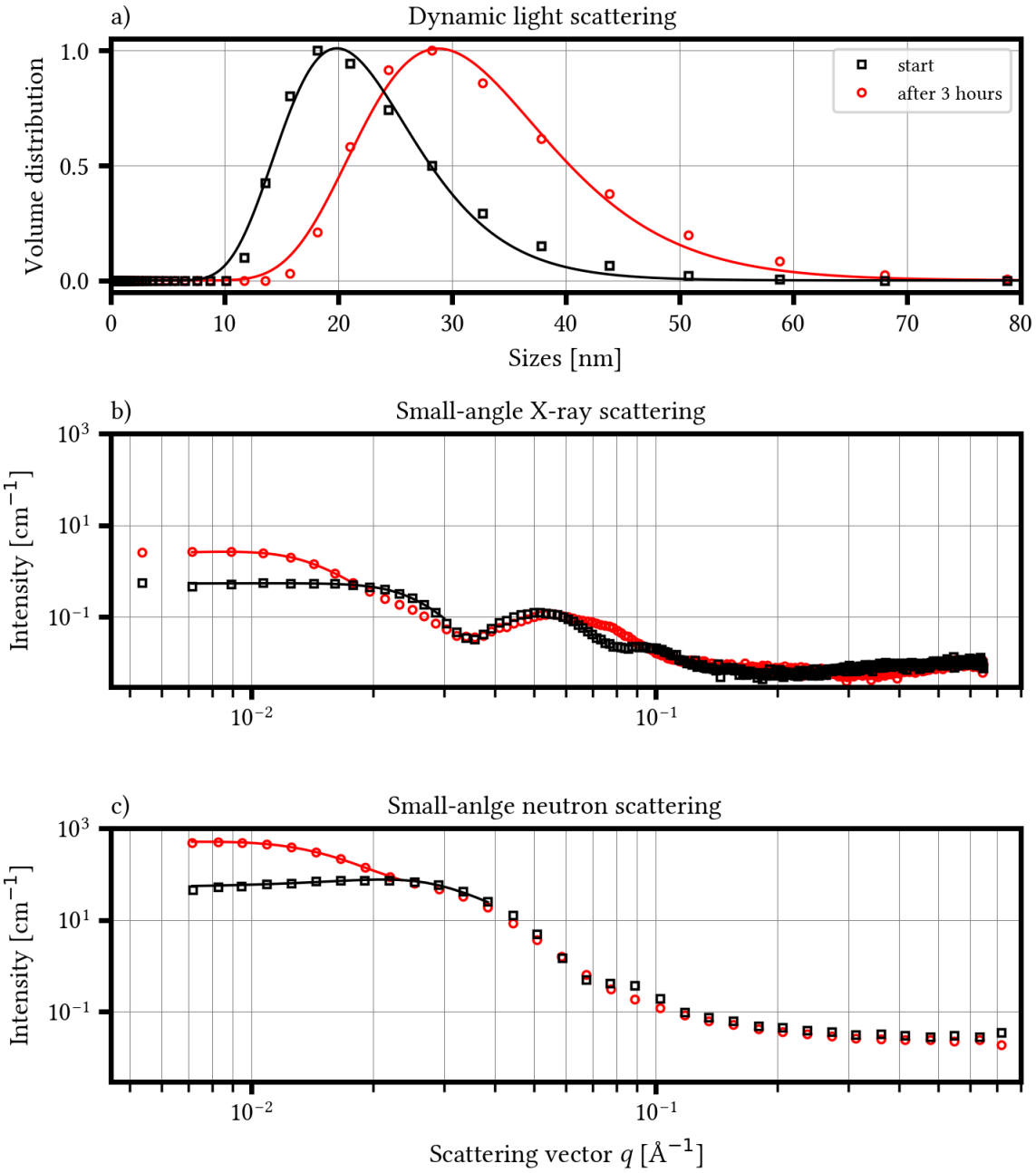

Figure 5.9. Data of the kinetic experiments of an aqueous solution with a Pluronic P123 concentration of 5 weight percent. a) Size distributions obtained by dynamic light scattering. The solid line is a fit using the log-normal distribution in equation (5.1). b) Small-angle X-ray and c) neutron scattering curves. For increased visibility only a third of the data points is shown and the solid lines in the low q-regime are fits using a combination of the Guinier-model from equation (1.61) and the Beaucage-model for the apparent structure factor from equation (1.96).

	SAXS	SANS		DLS	
		D_2O	CM	H_2O	D_2O
I_1	4.27 ± 0.56	729 ± 97	119.5 ± 34	153847 ± 106	170509 ± 372
I_2	2.93 ± 0.54	759 ± 141	120.7 ± 33	82808 ± 210	76497 ± 326
τ [10^{-2} min^{-1}]	0.80 ± 0.43	1.75 ± 0.95	1.77 ± 0.49	1.4170 ± 0.0086	0.534 ± 0.036

Table 5.2. Fit parameters of the single exponential to the time-dependent intensities.

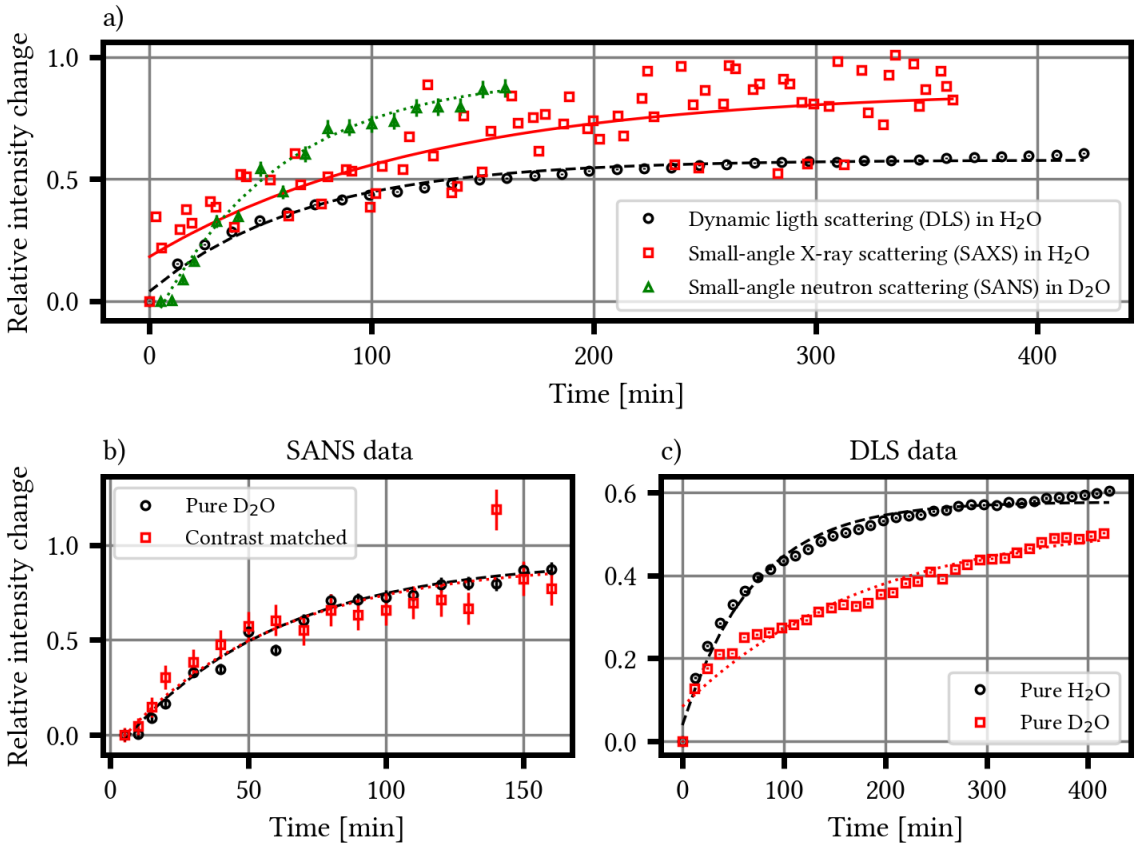

Figure 5.10. Time-dependent intensities of the kinetic experiments of an aqueous solution with a Pluronic P123 concentration of 5 weight percent. a) Each technique with their usual solvent. For better comparability, the relative intensity change $\frac{I(t)-I(t=0)}{I(t_{end})}$ is plotted. To increase visibility, only half the data points of the SAXS experiment is shown. The colored lines are the fits to the respective data points with the parameters of table 5.2. b) SANS data for heavy water D_2O and the D_2O/H_2O mixture. c) DLS data for P123 solutions in pure H_2O and D_2O.

The different techniques exhibit intensities, which vary over several orders of magnitude due to the different interaction mechanisms and scattering contrasts (see chapter 1.1). In addition, each technique has its usual, preferred solvent (distilles water H_2O for photons, heavy water D_2O for neutrons) and the respective values for τ almost agree within their uncertainties, but the SAXS measurements show a systematic lower kinetic rate. One possible explanations for this behavior could be a solvent-dependency of τ. When comparing the results using both SANS and DLS, which steem from experiments with both distilled and heavy water as a solvent, it becomes apparent, that there is no systematic influence of the solvent. While the SANS experiments with two different solvents provide almost identical intensity curves, the DLS data suggests a strong discrepancy (see figure 5.10, b and c). To lift any doubts on the comparability of these data sets, it has to be noted that the contrast matched solvent in the neutron scattering experiments exhibited a considerable amount of distilled water (almost 50%) and should hence show greater alterations. Due to the different masses of hydrogen and deuterium, there should be a measurable difference in the particle diffusion and τ. Nonetheless, these differences are only visible in the DLS data and the curves suggest a distinct deceleration of the formation process in case of heavy water as the solvent (see figure 5.10, c). Consequently, both SAXS and SANS as well as the DLS experiments show completely diverging trends leaving systematic and experimental influences as the remaining explanations. Any future experiments should always be performed with the same batch of sample solution to eliminate any contributions stemming from the sample preparation process. Pluronics are known to have impurities in their macromolecular structure, which can change for different lots and alter the aggregation process [64]. In order to investigate the discrepancy between the SANS and DLS data in distilled and heavy water, the SANS measurement could be repeated in both pure solvents as well. Furthermore, the experimental procedure should be refined. An immediate improvement would be the use of multiple angles during the DLS experiments, since it allows for the additional tracking of changes in the anisotropy of the observed particles, which is direct measure for the presence of worm-like aggregates [40].

Modeling approach

Although the kinetic measurements and their data analysis closely followed already published studies using either the temperature-jump method [40] or the addition of salts [69, 70, 63] to trigger the sphere-to-worm transition, the SAXS and SANS measurements allow for the time-dependent determination of the structural changes of P123's micelles in pure aqueous solution during the shape transition. Similar studies have been done by Sundblom et al., but with considerably higher concentrations leading to the formation of lyotropic liquid crystal phases and in an acidic environment [71].

When comparing the SAXS curves of a Pluronic solution with a concentration of 5 weight percent right after the transition temperature is reached and after 6 hours at this temperature, the plateau intensity increases and two distinct features at 0.022 as well as 0.08 $Å^{-1}$ appear (see figure 5.9, b and 5.11). In the first minute after the transition temperature is reached, the curves already show the additional wide shoulder at $q^* = 0.08$ $Å^{-1}$, which corresponds to a

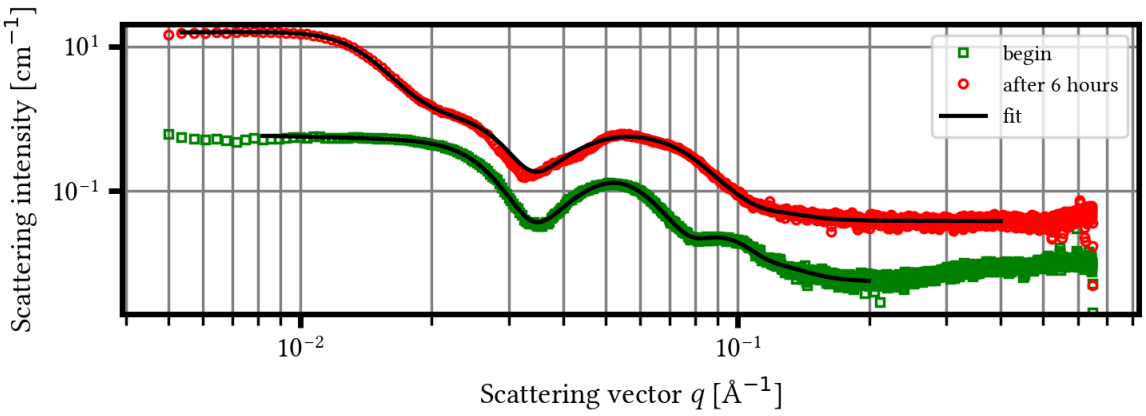

Figure 5.11. Small angle X-ray scattering (SAXS) data of the kinetic measurements (c(P123)=5 weight percent). The SAXS curves were taken when reaching 55°C and after staying there for 6 hours. The data is shifted by a constant factor to avoid overlap and the black solid lines represent fits to the data using the model in equation (5.12).

spacing of $d^* = \frac{2\pi}{q^*} = 78$Å. For the formation of such a pronounced shoulder or peak, this d-spacing has to be prominent in the sample solution. Since it is smaller than the micelle diameter, it is a first hint for a possible entanglement of the spherical micelles while they form larger aggregates. The second feature at $q = 0.022$ Å^{-1} or $d = 285$Å develops over time, which shows that larger aggregates are gradually formed. The shape of the scattering curve and the fixed position of the spherical micelle oscillation at $q = 0.05$ Å^{-1} also indicate that spherical aggregates will remain in the solution and that there will be a equilibrium between the worm-like and spherical micelles [69].

To start, the kinetic SAXS data can be modeled using a simple spherical core-shell model:

$$I_{\text{mic}} = \frac{\phi_{\text{mic}}}{V_{\text{p}}} \cdot P_0^{\text{CS}}(q, \rho_{\text{c}}^{\text{s}}, \rho_{\text{s}}^{\text{s}}, R_{\text{c}}, S) \cdot \mathcal{S}(q, R_{\text{HS}}) \tag{5.12}$$

with the volume fraction $\phi_{\text{mic}} = \frac{N \cdot V_{\text{p}}^{\text{mic}}}{V}$ and total volume V_{p} of the micelles as well as the spherical core-shell form-factor P_0^{CS} as defined in equation (1.81). To account for the structure factor in the low q-regime,

$$\mathcal{S}(q, R_{\text{HS}}) = [1 + \beta \cdot (S_{\text{HS}} - 1)] \ , \tag{5.13}$$

where S_{HS} is the hard-sphere structure factor model from equation (1.93) and β the decoupling factor from equation (1.92). In the following any polydispersity will be described by a Gaussian distribution of the total particle radius using the procedure in equation (1.82).

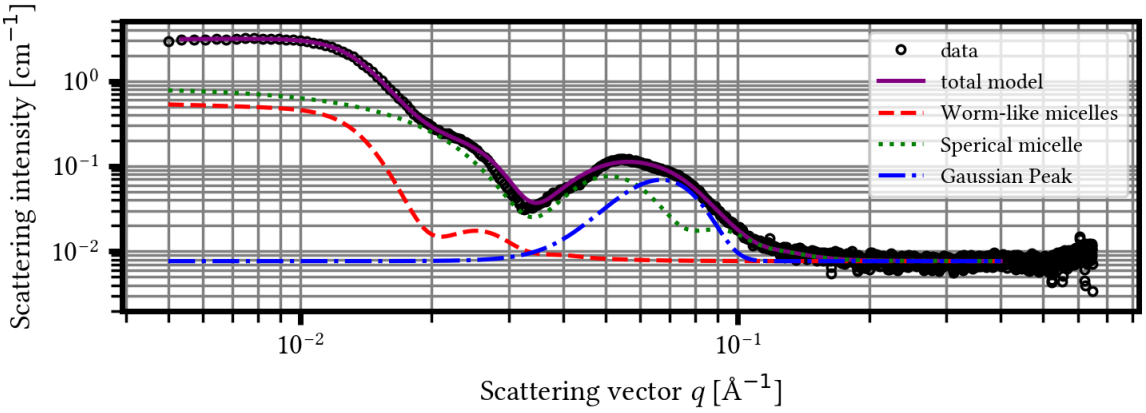

Figure 5.12. The fit model in equation (5.14) and its different contributions. The experimental data is taken from the measurements of the aqueous P123 solution with a concentration of 5 weigth percent.

In order to account for the mixture of both micelle species and the wide shoulder, the data was analyzed using the very simple model:

$$I_{\text{tot}} = I_{\text{mic}} + I_{\text{worm}} + I_{\text{peak}} \,, \tag{5.14}$$

where I_{mic}, I_{worm} and I_{peak} are the intensity contribution of the spherical micelles, worm-like aggregates and additional shoulder peak, respectively. I_{mic} is the same as in equation (5.12) without its structure factor $S(q, R_{\text{HS}})$. The elongated, larger aggregates should naturally be described using an ellipsoidal form-factor model (see figure 1.9), but during fitting both equatorial and polar radii converged to a simple spherical shape. This is probably due to the absence of a visible q^{-1}-slope in the low q-regime. To avoid the unnecessary numerical orientational averaging of the ellipsoidals, the larger aggregates are modeled using a simple spherical form-factor model:

$$I_{\text{worm}} = \phi_{\text{worm}} \cdot (\rho_{\text{s}}^{\text{s}} - \rho_{0}^{\text{s}})^2 \cdot V_{\text{p}} \cdot P_0^{\text{sphere}}(q, R) \cdot S(q, R_{\text{HS}}) \tag{5.15}$$

with the volume fraction ϕ_{worm}, the volume V_{p} of the spheres describing the worms, the spherical form-factor P_0^{sphere}, which is defined in equation (1.76) and the structure factor $S(q, R_{\text{HS}})$ from equation (5.13). Lastly, the peak at a certain q-value is assumed to have a Gaussian shape:

$$I_{\text{peak}} = A \cdot \mathrm{e}^{-\frac{(q-q_0)^2}{2\sigma_{\text{P}}^2}} \,. \tag{5.16}$$

Here, A is a scaling factor to adjust the height of the peak, q_0 is the peak position and σ_{P} is its standard deviation. When combining all three contributions (5.12), (5.15) and (5.16) in equation (5.14), the experimental data of the kinetic measurements can be sufficiently modeled (see figures 5.12 and 5.13).

The resulting model function has 11 free parameters, which makes it challenging to control the converging behavior during the fitting process. Both micellar volume fractions can be constrained

$$\phi_{\text{mic}} + \phi_{\text{worm}} = \phi_{\text{tot}} \,, \tag{5.17}$$

because they have to always add up to the total volume fraction or concentration of the P123 solution ϕ_{tot}. This still leaves 10 free parameters, which can only be handled with additional prior knowledge and assumptions. Since the very first scattering curve after reaching the transition temperature could be modeled only using the core-shell sphere model in equation (5.12), information about the associated sizes and scattering length densities of the micellar core and shell as well as the micelles overall polydispersity (see table A.1 in the appendix). The overall size of the spherical micelles (sum of core radius and shell thickness) and their size distribution (polydispersity) are independent of the concentration as already seen in the previous chapters (see figures 5.3 and 5.13, b). Since the characteristic oscillation of the spherical micelles at $q = 0.05$ Å^{-1} is still present after the 6 hours at the transition temperature (see figures 5.9, b and 5.11), it is assumed that their size, polydispersity and inner structure will only slightly change when worm-like micelles are present in the solution. Furthermore, the peak position in equation (5.16) can be confined to q-values larger than the micelle oscillation peak. During fitting, the volume fractions always approached a ration of $\phi_{\text{mic}}/\phi_{\text{worm}} = 1/10$ for all three measured concentrations and were consequently fixed at this ratio to futher reduce the model's degrees of freedom. With these restrictions, it was possible to determine the remaining fit parameters in a reproducible manner (see table A.1 in the appendix).

As already mentioned before, it is surprising that the worm-like micelles could not be described during the modeling using ellipsoids. Although the simple sphere model seems to produce inaccurate representation of the worm-like aggregates, it is still possible to extract valuable information from it. Using cryo transmission electron microscopy (TEM), Denkova et al. were able to take pictures of Pluronic solutions during the sphere-to-worm transition [69]. They did use different salts to trigger the shape change, but the cryo-TEM images clearly show the simultaneous presence of spherical and worm-like micelles, which are elongated but not thicker than one core-shell micelle. Using this information, the spheres in the fit model can give information about possible other particle shapes by calculating the subsequent ellipsoid parameter with equal volume or treating the sphere radius as a radius of gyration. An ellipsoid, which is as thick as one spherical micelle and has the same volume as the sphere in the fit model, will have an equatorial radius of

$$R_{\text{e}}^{\text{V}} = \frac{R_{\text{S}}^3}{R_{\text{M}}^2} \,, \tag{5.18}$$

where R_S is the radius of the sphere and R_M the total radius of one spherical micelle. If the spherical model for the worm-like micelles is interpreted as a surrounding shape due to the orientational averaging, similar to the radius of gyration, it is also possible to convert the spheres into corresponding elongated structures. By using the sphere radius as the radius of gyration, the equatorial radius of the resulting ellipsoid, which again has a thickness of exactly

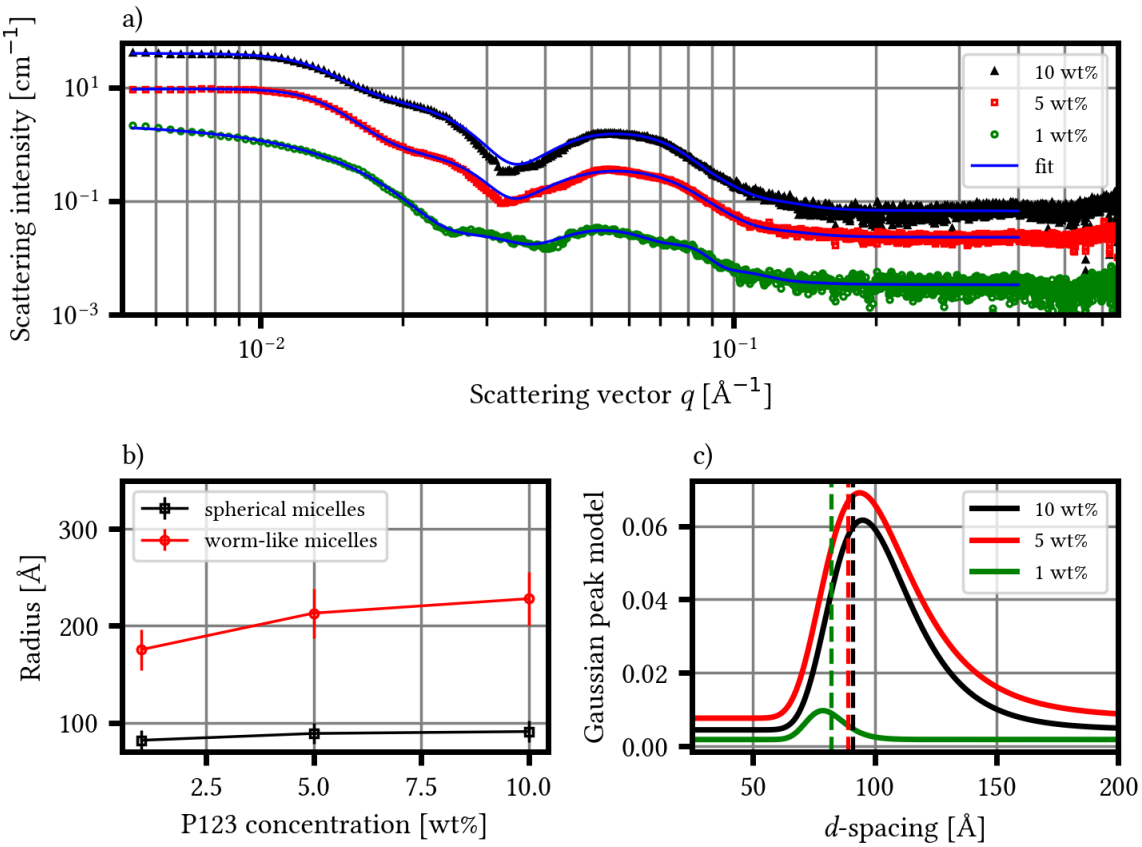

Figure 5.13. Fit results for aqueous P123 solutions with different concentrations. a) Scattering curves after 6 hours at transition temperature of 55°C. The blue solid lines are the optimized fits using the model in equation (5.14). b) Radii of the spherical and worm-like micelles. The radius of the core-shell particles is the sum of the core radius and the shell thickness. c) Normalized Gaussian peak from the fit model in equation (5.16) in the corresponding real-space $d = \frac{2\pi}{q}$. The dashed vertical lines represent the micelle

P123 concentration	1 wt%	5 wt%	10 wt%
N_W with equation (5.18)	9.7 ± 5.0	13.7 ± 7.1	15.7 ± 8.0
N_W with equation (5.19)	4.56 ± 0.85	5.16 ± 0.96	5.72 ± 0.99

Table 5.3. Number of spherical micelles forming one worm. The values for the radii of the sphere and spherical micelle were taken from table A.1 in the appendix. The uncertainties follow from the polydispersity of both the spheres and spherical micelles.

one micelle, will be [152]

$$R_e^G = \sqrt{5R_S - 2R_M} \tag{5.19}$$

with the same definitions as in equation (5.18). In a very crude approximation, these ellipsoids could be seen as pearl-necklace of touching micelles. Then it is possible to define the number of spherical micelles which form one worm-like aggregate

$$N_W = \frac{R_e}{R_M} \tag{5.20}$$

leading to distinct differences, whether equation (5.18) or (5.19) is used (see table 5.3). Depending on the approach, the values of N_W for each concentration vary up to a factor of 3. Yet, the results of both models can be explained. The method described in equation (5.19) would directly yield aggregation numbers, which are comparable to the results presented earlier (see figure 5.8). While the results from equation (5.18) seem to be very high, they would result in similar solution-averaged aggregation numbers due to the equilibrium between the micellar species. As a consequence, both approaches could be seen as lower and upper limits.

One of the key components for the good quality of the obtained fits is the Gaussian peak. It broadens the oscialltion of the spherical micelles towards higher q-value, which corresponds to smaller distances or sizes in real space. The dominant presence of smaller micelles would suggest a formation process of the worm-like aggregates based on insertion of individual polymer chains, which was already convincingly rules out in a prior study [40]. Interestingly, the fitted d-spacing of peak position correlates almost perfectly with the total radius of the micelles in these solutions (see figure 5.10, c). Since its appearance indicates the beginning of the transition towards worm-like aggregates, it has to be connected with the interaction between the spherical micelles. In the context of interaction potentials, like the hard-sphere structure factor, such a peak would result, if both potential radius and total micelle radius are equal as well as considerably large packing of the micelles (above 40 volume percent). The latter could be decreased when an attractive interaction between the micelles is assumed, e.g. in the sticky hard-sphere structure factor. Both interaction models have been tested, but failed to produce more meaningful or better fit results. Hence, a correct physical interpretation of the Gaussian peak is still missing and needs to be considered in future refinements of the model.

5.3.2. Lamellar system near the cloud point

With increasing temperature, another transition towards lamellar structures takes place (see figures 5.1, d and 5.14, a). The presence of lamellar aggregates at temperatures near the cloud point was already shown earlier using the SANS data(see figure 5.5 and table 5.1), but the associated SAXS data show more pronounced changes in the micellar structure due to the shorter significantly shorter measurement times. Using the model, which was introduced in equation (5.14), it is possible to analyze the scattering data over a wide temperature range (see figure 5.14, a). During modeling, the ratio between the simple and core-shell sphere contributions was kept at a ratio of 10/1 and no third particle population was introduced in the lamellar phase. These crude assumptions are up for debate, but were necessary to reduce the numerical complexity and track the parameters during the form-phase transition. Here, size-exclusion chromatography SAXS (SEC-SAXS) experiments or filtered solutions could yield valuable insight into the composition of the solutions and should be considered in the future. The feature, which appears at q = 0.03 Å^{-1} and is characteristic for the larger aggregates of spherical micelles, starts to move towards smaller q-values when approaching the cloud point. In the model, this results in an increase in the radius of the simple sphere contribution in equation (5.15). The numerical values are in excellent agreement with the hydrodynamic radii obtained by the previous DLS experiments (see figure 5.3, a) and those reported in the very sparse literature on the cloud point of Pluronics [229]. If the spherical model is believed to describe the overall shape of the lamellar aggregates, its size at high temperatures varies greatly from the assumption of micrometer sized particles in the milky solutions in this temperature regime [42].

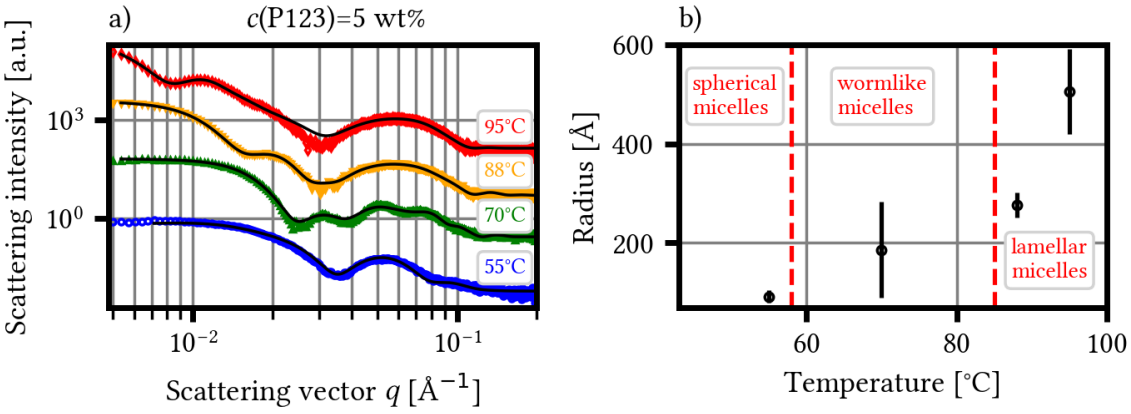

Figure 5.14. a) Scattering data before and during the transition from worm-like to lamellar micelles when approaching the cloud point. The solid black lines are fits to the data using either the core-shell sphere form factor (55°C) from equation (1.81) or the model introduced in equation (5.14). b) Temperature-dependent radius of the dominant micelle population. The red, dashed vertical lines show the transition boundaries between the different micelles species and were determined using dynamic light scattering experiments (see figure 5.1).

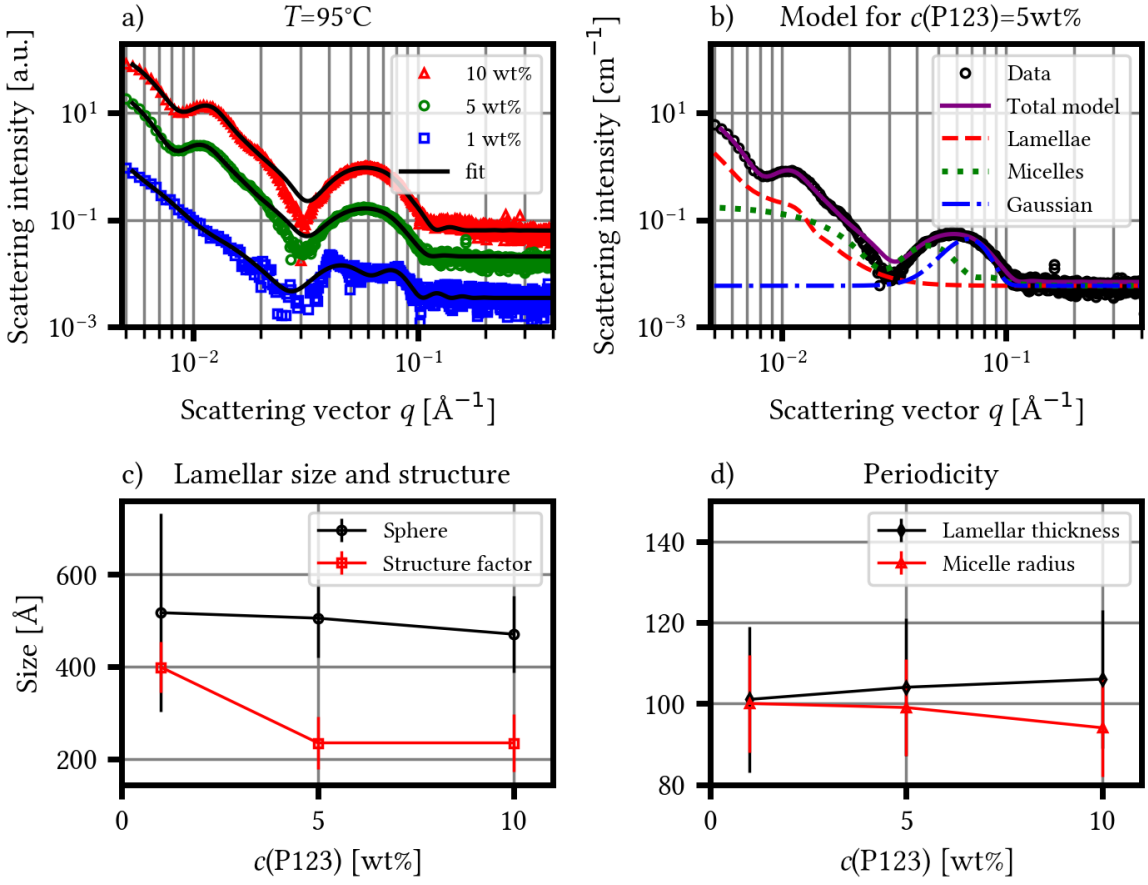

Figure 5.15. SAXS data and fit results of the lamellar system at the cloud point. a) Scattering curves at T = 95°C for different P123 concentrations in weight percent (wt%). The curves are shifted to avoid overlap. The solid lines are fits to the data using equation (5.14). b) Representation of the different components of the fit model. c) Fit results for the spherical contribution of the model in equations (5.12) and (5.15) representing the lamellar micelles. d) Comparison of the lamellar thicknesses in equation (5.6) obtained from the SANS data with the total radius of the spherical micelles in the model used to fit the data in a).

Interestingly, when modeling the data of all measured concentrations at T = 95°C, the feature near q = 0.01 Å^{-1} is only visible for higher P123 concentration and is not caused by the oscillation of the spherical form factor but by the used hard-sphere structure-factor model (see figures 5.15, a and b). In all cases, the hard-sphere radius is systematically lower than the sphere radius, which here represents the lamellar aggregates. Only for the solution with a P123 concentration of 1 weight percent, both radii are equal within their uncertainty (standard deviation of the Gaussian size distribution in case of the spherical form factor). Such a behavior is unusual, but is still explainable within the initial assumptions of the model and does not violate them [181, 182, 183] (see chapter 1.3.3). The interference of the scattered waves is due to the models hard spheres and their distance to each other. With them being

smaller than the "real" particles, the physical meaning of these spheres with radius R_{HS} and their volume fraction φ_{HS} has to be reconsidered. Since the micelles can move freely in the solution, it is very unlikely that the resulting lamellar system will only have one orientation [39, 228]. In analogy to solid-state crystallography, areas with a different orientation inside a crystal or crystallite are called grains [330]. The smaller spheres could then indicate the presence of such grains within the lamellar micelles and φ_{HS} would be their volume fraction or packing parameter in the micelle. In literature, hard-sphere structure factors were used to study the grain distribution inside solids [331, 332] and domain sizes of copolymers [333], due to their analytical formalism. Since the modeled interaction is always repulsive, it will be important to test new models for the structure of agglomerates [334] when refining the present fit model in the future. However, the obtained grain sizes are in good agreement with the reported lamellar periodicities for other Pluronic variants [39].

P123 concentration	1 wt%	5 wt%	10 wt%
N_D - number of domains per micelle	2.9 ± 2.2	9.9 ± 5.0	8.0 ± 4.3
N_L - number of lamellae per domain	7.9 ± 1.8	4.5 ± 1.3	4.4 ± 1.4
N_T - total number lamellae per micelle	23 ± 18	45 ± 26	35 ± 22

Table 5.4. Properties related to the internal structure of the lamellar micelles for different P123 concentrations. The numbers were calculated using equations (5.21), (5.22) and (5.23) as well as the fit results in table A.2 in the appendix.

Sticking to this very crude interpretation of the structure factor data, the number of domains inside a lamellar micelle can be determined. Under the assumption that the whole micelle is filled with domains, the number of domains per micelle is

$$N_D = \frac{R_{mic}^3}{R_{dom}^3} \tag{5.21}$$

with the micelle radius R_{mic} and the domain radius R_{dom}. Despite the large uncertainties, the solutions with P123 concentrations of 5 and 10 weight percent still have a systematically higher domain number, which is also the reason for the strong appearance of a feature in the scattering curves. Due to the higher quantity of polymer in the solutions, the lamellar micelles are more defined for higher P123 concentrations. Another important measure is the total number of lamellae per micelle

$$N_T = N_D \cdot N_L \,, \tag{5.22}$$

where N_D is the number of domains from equation (5.21) and

$$N_L = \frac{2R_{dom}}{T} \tag{5.23}$$

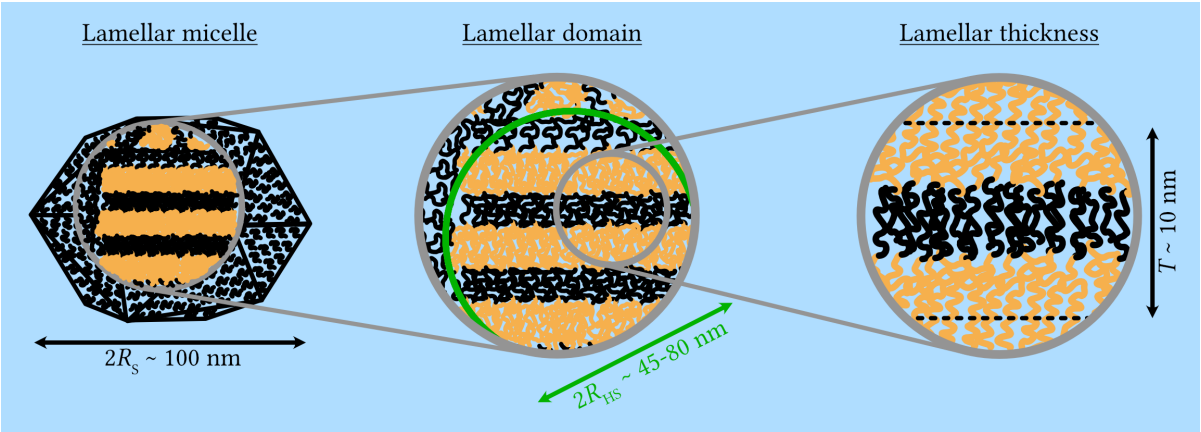

Figure 5.16. Cartoon to illustrate the different size regimes in the lamellar micelles. The orange and black chains symbolize the polypropylene oxide middle block or polyethylene oxide end groups of P123. The variables R_S, R_{HS} and T are the sphere radius, the radius of the hard-sphere structure factor and the lamellar thickness, respectively. The numerical values are from the associated fits (see figures 5.15, c and d).

is the number of lamellae per domain with the lamellar thickness T (see table 5.4). With the values for T from equation (5.6), the total number of lamellae per micelle is constant within the limits of uncertainties for all measured concentrations further corroborating the correlation between the peak at low q-values and the appearance of structural domains inside the micelle at higher polymer concentrations in the solutions.

Despite the mentioned inaccuracies of the very simple fit model, it still provides information to aid with the correct structural interpretation of the lamellar thickness. Even at the cloud point, a spherical micelle population was necessary in order to fit the oscillation at $q = 0.06$ Å^{-1}, which is characteristic for P123 (see figures 5.5 and 5.14, a). For all P123 concentrations, the fit results suggest that the total micelle radius (core radius+ shell thickness) almost perfectly coincides with the determined lamellar thicknesses using the SANS data earlier (see figure 5.15, d). Although the exact formation mechanism of the lamellar micelles is not known, the continuing dehydration and stretching of both P123's block groups has to play a key role [227, 335, 42, 218]. For the micelle to reach radii of 10 nm, both propoylene and ethylene oxide blocks need to be almost fully stretched, which strongly favors the formation of lamellar structures to minimize solvent contact. Since this aggregation lowers the entropic penalty of the system, the polymer chains do not have to be extended anymore due to their increased inter-chain interactions in the resulting lamellae. In addition, it is hard to imagine how the lamellar thickness and periodictiy would look like if it would be simply the micellar radius. A possible geometry could be the entanglement of the ethylene oxide blocks (see figure 5.16). It would explain the observed phase separation of polyethylene glycol in this temperature regime [218], explain the equivalence of the lamellar thickness with the micellar radius (see figure 5.15, d) and agree with the suggested micellar stacking found in molecular dynamics simulations [53].

Gelation near cloud point

During the experiments at various beamlines, the higher concentrated aqueous P123 solutions (c(P123)=10 weight percent) showed a fascinating behavior: the solutions gelated after they were kept at temperatures around T = 95°C for several hours (see figure 5.17). The gelation of Pluronic solutions is a well-studied phenonmenon and most of the liquid crystalline phases are already well-described [36, 54, 55], but were observed for drastically higher concentrations (above 27 weight percent) [44, 336] or by modifying the solvent properties [36]. To the knowledge of the author, this is the first report of a pure temperature-driven skip of the concentration-hurdle in a Pluronic system.

The gelation has to take place due to the ordering of the lamellar micelles and appears to start at the walls of the sample cell or container. It then grows inside the bulk solutions until a full gelation is reached after several hours. Near surface crystallization of Pluronic solutions in the temperature regime of spherical and worm-like micelle was demonstrated using shear [57]. Nonetheless, this ordering never translated further than a few micrometers away from the surfaces [263]. Since the observed gelation is due to a unique interplay between the aggregation behavior in solution and at surfaces, it will be investigated using neutron reflectometry in the following chapter. In the future, the time-dependency of this gelation should be further analyzed as well, e.g. using combined rheology and small-angle scattering. Here, new and refined experimental set-ups and sample environments will be required, since the temperatures near the boiling point of the aqueous solutions ask for additional precautions to ensure reproducible and meaningful results.

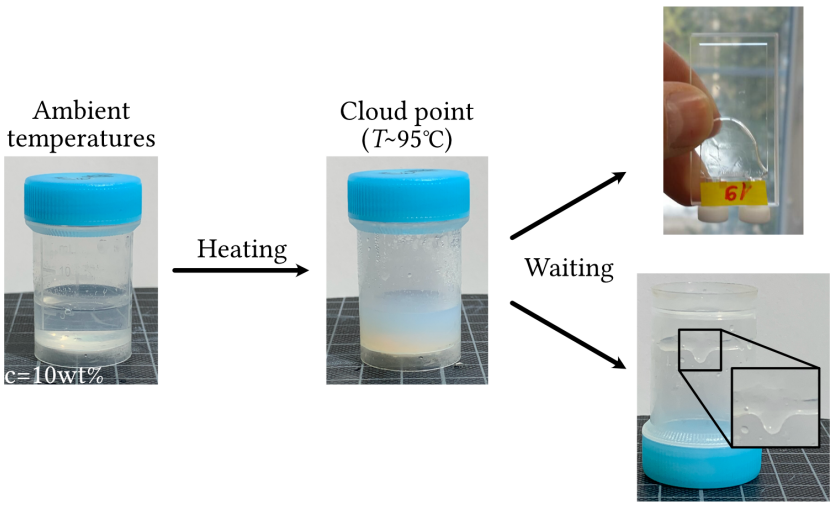

Figure 5.17. Experimental observation of the gelation near the cloud point. The gelation takes several hours and appears on both hydrophillic (quartz glas, upper right) and hydrophobic (polypropylene, lower right) container materials.

5.4. Aggregation under confinement

Using reflectometry, it is possible to study the aggregation behavior of P123 under confinement, e.g. near a surface. The experiments were performed on two different silicon surfaces, where one was activated through acidic cleaning and the other was coated with strong hydrophobic octadecyltrichlorosilane (OTS) (see chapter 2.3). As a result, both surfaces had very different surface energies, which lead to distinct differences in the temperature-dependent near surface aggregation of the polymers in the aqueous solutions (see figures 5.18 and 5.19). All fits were done using refnx [337], which is a python package for reflectiviy data anaylsis by NELSON and PRESCOTT based on the MOTOFIT macro in Igor Pro [338] and a matrix representation of the PARRATT formalism (see chapter 1.4.2).

5.4.1. Unimer regime

After filling the sample cavity of the rheometer, the solutions were cooled down to 10°C and kept there for multiple minutes to ensure the complete demicellization and presence of only unimers.

The reflectivtiy of the unimers on the cleaned and hydrohillic silicon interface is very similar for all three measured concentrations. During modeling, it was sufficient to use a simple FRESNEL-transition from the silicon surface into the aqueous bulk solution of polymers. In addition, a 12 – 20 Å thick layer of silicon dioxide as well as a Gaussian model for all interface roughnesses was used (see figure 1.16). The scattering length density of both silicon and silicon dioxide were taken from [112] while the one of the bulk solution was fitted using the reflectivity edge around $q = 0.015$ Å^{-1}. The scattering length density of the bulk solutions is always lower than the literature value for heavy water and decreases with increasing polymer concentration, as expected for a binary mixture (see table 4.1). In this temperature regime, the resulting scattering length density profiles suggest that there are apparently no polymers present on or near the hydrophillic silicon surface (see figure 5.18, b). The adsorption behavior of Pluronics on different hydrophillic surfaces was studied in literature [243, 246, 238, 253, 251], but almost never in the unimer regime. Even with the presence of micelles in the solutions, the observed adsorbed amounts of polymer could easily be rinsed or removed from the surfaces [243]. For the respective thickness of these weakly adsorbed layers near the critical micellization temperatures or concentrations, the reported values are diverging between few angstroms [246, 251] and almost 50 nm [238]. The very large layers were observed for Pluronic F127, a more hydrophillic variation compared to P123. Using the presented data such a similarly large layer thickness can clearly be ruled out. Yet, the complete absences of a polymer layer near the surface is also questionable since it will not be possible to detect polymer layer thickness below 20 Å using the presented reflectivity experiments due to limitations in the obtained q-range.

The reflectivity curves of all three concentrations in the unimer regime are very similar as well (see figure 5.19, a). Compared to the curves using the hydrophillic surface, they all exhibit a characteristic oscillation at $q = 0.15$ Å^{-1} and a shallower slope in the intermediate q-regime.

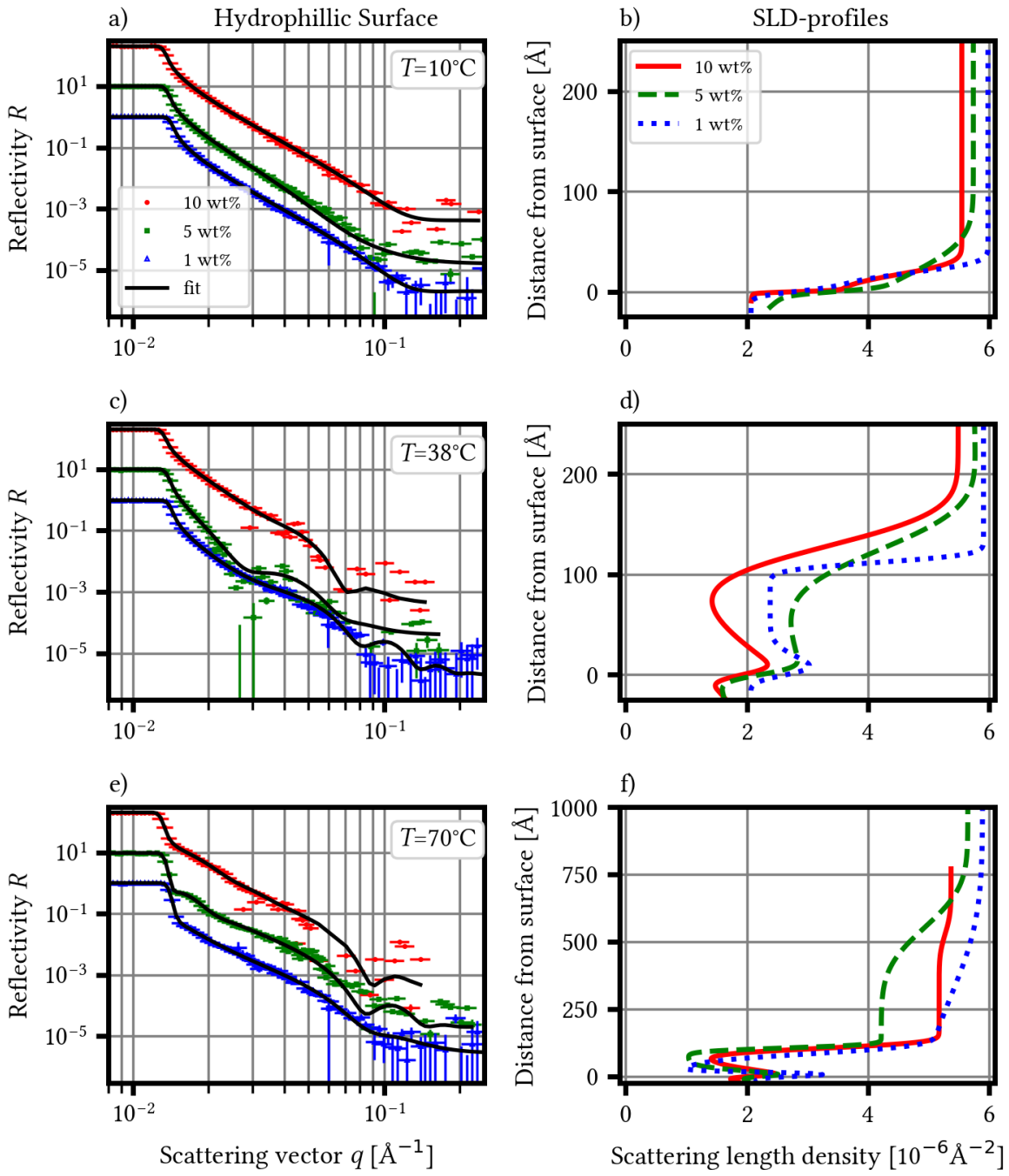

Figure 5.18. Reflectivity data of aqueous Pluronic solutions on a hydrophillic surface. The reflectivity curves are shifted by a constant factor to increase visibility and avoid overlap.

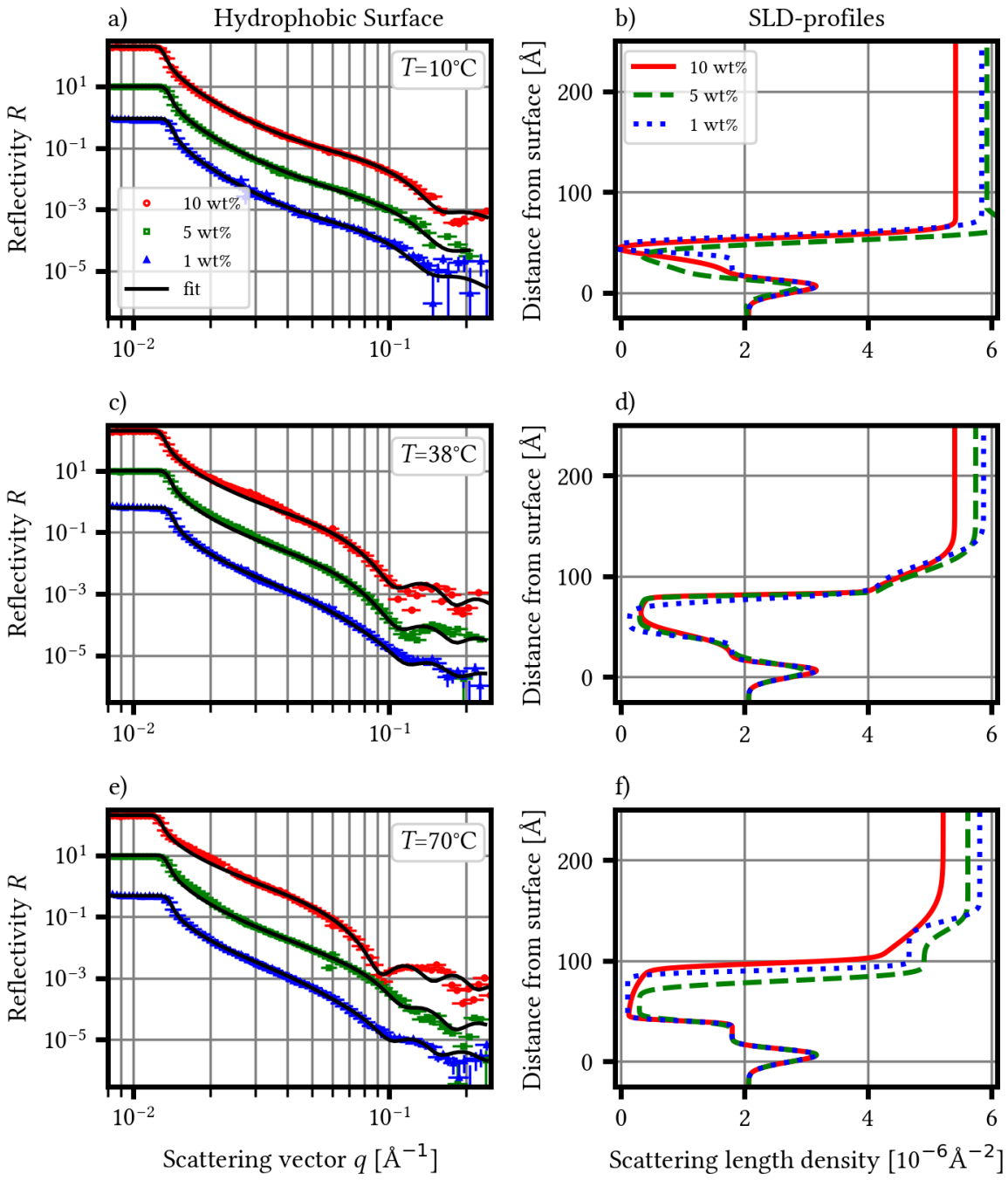

Figure 5.19. Reflectivity data of aqueous Pluronic solutions on a hydrophobic surface. The reflectivity curves are shifted by a constant factor to increase visibility and avoid overlap.

During modeling, there were two additional layers on top of the silicon dioxide, which represented the OTS coating and adsorbed polymer layer, respectively. Since the oxide layer is hidden under the very stable and durable coating [265], the parameters of both layers were determined once and then fixed for the remaining analysis of the data on the hydrophobic surfaces. The additional layer between the coating and the bulk solutions suggests the presence of polymers near the surface with a layer thickness of 20-30 Å (see tables A.3 to A.5 in the appendix). Since these thicknesses are very similar to the hydrodynamic diameter (see figure 5.3, a) and sizes according to the radius of gyration (see table 5.1) of the unimers, the layer will most likely consist of single polymer chains forming a monolayer on the surface [241, 242, 238, 335]. The obtained scattering length densities for the polymer layer are negative and have a very high contrast to the surrounding bulk solution. A possible work-around with the introduction of one or more layers did not yield more reasonable results and the unphysical values are probably due to the cutoff in the q-range and the very thin layer.

5.4.2. Spherical micelle regime

The sample solutions were subsequently heated to 38°C to reach the spherical micelle temperature regime (see figure 5.1, d).

In contrast to the unimer phase, the reflectivity curves of all three measured concentrations on the hydrophillic surface show distinct features and oscillations, which hint the presence of a surface layer of polymers (see figure 5.18, c). For all concentrations, the parameters of the silicon dioxide on the surface were kept the same and a second layer was added before the bulk solutions are reached. As a result, the this second layer approached scattering length density values of $2.1 - 2.2 \cdot 10^{-6}$ Å^{-1} and thicknesses of 90-110 Å (see figure 5.18, d). For micellar solutions of P123, a drastic increase in the adsorption of polymers to the surface is reported [243, 251, 253]. Lin et al. claim the presence of full micelles near the surface, where the interaction then has to be governed by the more hydrophillic corona consisting of polyethylene oxide [238]. The resulting layer thickness would be close to the hydrodynamic radius of one micelle. Yet, the majority of experimental [235, 249, 251] and theoretical work [253] strongly suggests that the polypropylene oxide middle block is the driving force for the interaction with hydrophillic surfaces. Using a similar Pluronic variant (P103) and cleaned, polished and heat-treated gold surfaces, Liou et al. measured very similar layer thicknesses of 100 Å. For the internal structure of the adsorbed polymer layer, different models exist, which range from "pancake-like" unordered films [247] up to half-dome micelles or even polymer brushes [247, 252]. Due to the high and uniform scattering length density of the modeled polymer layer, it is not possible to give a final judgment on the internal structure. All proposed geometries would yield similar results, when they are assumed to be hydrated and averaged.

The reflectivity curves on the hydrophobic surface in the micellar temperature regime show a shift of the oscillation, which was already present in the unimer phase, towards lower q-values (see figure 5.19, c). This is already a clear indication for the growth of the adsorbed polymer layer. During modeling it was necessary to add another layer before the bulk solution is reached. In the final fit, the both polymer layers have a total thickness between 60

and 65 Å and approach scattering length densities, which are indicative for completely dehydrated polypropylene oxide on the OTS coating and very hydrated polyethylene oxide chains dangling in the bulk solution (see figure 5.19, d). Similar "brush-like" structures have been reported for Pluronics on hydrophobic surfaces using total internal reflection microscopy (TIRM) [240], atomic force microscopy (AFM) [241], photon correlation spectroscopy (PCS) [246, 250], quartz-crystal microbalance (QCM) [247], small-angle neutron scattering (SANS) [248] and molecular dynamics simulations (MDS) [252]. The associated layer thicknesses between 40 [252] and 90 Å [247] are in very good agreement with the ones obtained from modeling. The proposed structure with the propylene oxide blocks closer to the surface and hydrated ethylene oxide, which are stretched in the solvent, is further corroborated by theoretical calculations of Linse et al. [335], MALMSTEEN et al. [246] and SONG et al. [252]. Here, it is clearly stated that hydrophobic-hydophobic interactions with the surface lead to a strong dehydration of the Pluronics middle block, which then forms a melt-like structure as a strongly bond first layer.

5.4.3. Worm-like micelle regime

In the last step of the experiment, the confined samples were further heated to 70°C, which brings the bulk solutions into the worm-like micelle regime (see figure 5.1, d).

All measured reflectivtiy curves on the hydrophillic surface show the same characteristic oscillations, which are indicative of a surface layer as seen in the micelle regime. In addition, a new feature becomes visible at even lower q-values (see figure 5.18, e). For P123 concentrations of 1 and 5 weight percent (wt%), there are peaks close to the reflectivity edge, which are more prominent when the curves are normalized with FRESNEL's q^{-4} decay (see figure 5.20, a) and were modeled using another layer. The fit results yield a polymer layer close to the surface, which is roughly half the size of one spherical P123 micelle and scattering length densities

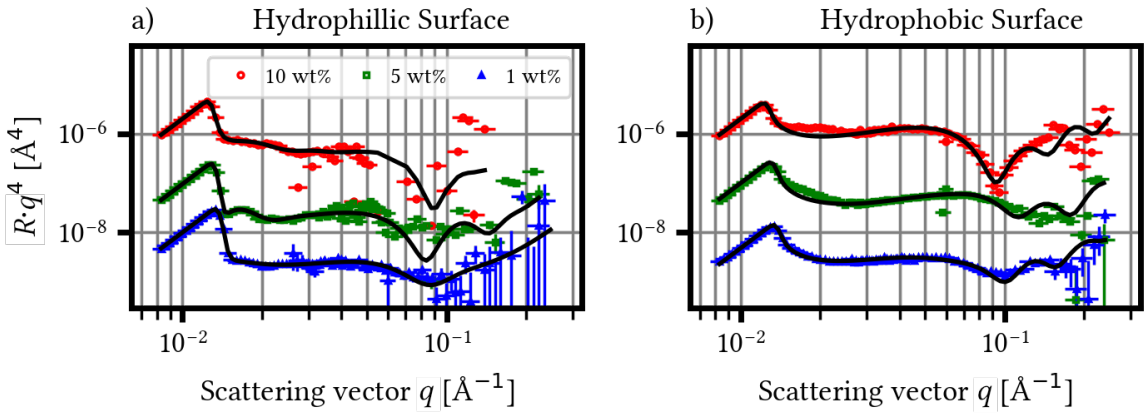

Figure 5.20. FRESNEL-normalized reflectivity $R \cdot q^4$ of the data at $T = 70$°C using a) the hydrophillic and b) the hydropphobic surface. The solid black lines are fits to the data, which are also visible in figures 5.18 and 5.19.

between 1 and $1.5 \cdot 10^{-6}$ Å^{-2}, followed by a 200 Å wide layer with a scattering length density close to the bulk solutions (see figure 5.18, f). The size of the polymer layer on the surface is almost identical with the one observed in the micelle regime and its decreasing scattering length density is a result of the continuing dehydration of the middle block and end groups of P123 [61, 39, 42]. Since the newly formed layer, which is needed to explain the peak at low q-values, is roughly the diameter or width of one spherical or worm-like micelle, repectively, it could be hint for an interaction between the surface layer and the micelles in the bulk solution. Micellar ordering was observed for hydrophillic silicon surfaces in this temperature regime even leading to the formation of different crystalline structures depending of the micelles architecture [57, 51]. However, the interaction between the micelles and with the polymer layer on the surface must be weak, since it can be disturbed with rather small shear rates [57]. The high scattering length density of the layer further corroborates this, because it implies that there must be considerable amount of solvent between the micelles. Nonetheless, a micelle stacking, as it is hinted here, could be an explanation for the drastically increasing adsorption [253] as well as the gelation of low-concentrated bulk solutions near the cloud point (see chapter 5.3.2).

On the hydrophobic surface, the brush-like, near-surface layer seems to grow in size, since the characteristic oscillations continue to move towards lower q-values (see figure 5.19, e). Using the same model as described in the prior temperature regime, the first layer on the coating, which represents the propylene oxide melt, increased to thicknesses between 40 and 60 Å, while the second layer remained at sizes between 30 and 35 Å. The growth of the propylene oxide layer on top of the OTS coating is probably due to the stretching of the block chains. When reaching sizes of 50 Å, P123's middle block is believed to be fully stretched and in a complete all-trans conformation [61], which is also a discussed explanation for the formation of worm-like micelles [39, 42]. The fact of fully elongated propylene oxide chains is further strengthened by the continued decreasing of the obtained scattering length density (see figure 5.19, f). As seen in the measurements on the hydrophillic surface, an additional feature also appears close to the reflectivity edge for the higher concentrated Pluronic solutions (5 and 10 weight percent) when using the hydrophobic surface (see figure 5.20, b). However, the introduction of an additonal layer into the model was not enough in this case. The obtained scattering length densities for such a layer would always higher than the ones of the bulk solution. This would mean that micelles are repelled of the surface layer producing a lower local polymer concentration. Such a process is unheard of and not documented in literature for soft matter systems, rendering it unphysical. Here, a more refined model is necessary, which could be based on the Bragg-diffraction of a multilayer [263]. Yet, the striking equivalence of the PPO thickness with the periodicidty of the lamellar structure as well as the formation of the observed peak in the low q-regime, is a further indication for the development of a multilayer system [253], which can act as the seed for the observed gelation of the bulk solution at the cloud point.

Conclusion

In summary, this thesis re-investigated the form-phase diagram of Pluronic P123 and its different micelle morphologies in their associated temperature regimes. The obtained phase boundaries complete the missing high-temperature regions in literature [44] and coincide with the reported ones of another Pluronic variant (P85) [41]. A strong hysteresis between heating and cooling is observed (see figure 5.1, d and e), which is indicative for a supercooling of the lamellar and worm-like structures. In the individual phases, the corresponding overall sizes of the micelles remain almost constant and show no pronounced concentration dependency (see table 5.1 and figure 5.3, a).

At the transition temperature towards worm-like micelles, out-of-equilibrium-measurements were used to investigate the underlying kinetics and structural changes during the transition process. The obtained growth rates of the micelles (see table 5.2) are in the order of hours and in fair agreement with those reported in literature [40, 69, 222]. However, the results for the different measurement techniques show distinct deviations, whose origin could not be clearly attributed to the different solvents and thus remains unknown. The obtained small-angle X-ray scattering data were fitted using a simple model, which took the presence of both and spherical and worm-like aggregates into account (see figure 5.11). In the data, a shoulder appears in the high q-regime immediately after the transition temperature is reached, which could only be accounted for by an additional Gaussian peak (see figure 5.12). The physical interpretation for this peak is still missing, but it is indicative for the beginning of the transition at low and high concentrations. By assuming that the worm-like aggregates have a pearl-necklace structure [69, 71], it was possible to determine the number of spherical micelles per worm-like aggregate, which was in good agreement with the average aggregation number obtained by a shape-independent approach (see table 5.3 and figure 5.8).

With increasing temperatures towards the cloud point, the aggregates started to grow in size. The neutron scattering data clearly demonstrated the presence of lamellae, while X-ray data revealed that the spherical micelles in the solution reached a state in which the middle block and end groups were almost completely dehydrated and stretched. By combining the fit results of both neutron and X-ray scattering data, a model for the inner structure of the lamellar micelles is proposed (see table 5.4 and figure 5.16). The large aggregates, which are responsible for the clouding in this temperature regime, consist of domains, which are responsible for the characteristic oscillation in the X-ray scattering data (see figure 5.14, a). Inside these domains the lamellae have a preferred orientation and certain periodicity according to their thickness. Lamellar micelles with such a structure explain and connect previous results, which are reported in literature [39, 41, 68].

During the experiments, a time-dependent crystallization of the Pluronic solutions with a concentration of 10 weight percent was observed (see figure 5.17). After several hours at the cloud point, the solutions started to gelate, which is only documented for significantly higher polymer concentration [44] or close to surfaces [57]. Indeed, P123 develops a monolayer on both hydrophillic and hydrophobic as shown by neutron reflectometry. These layers grow in size with increasing temperature due to a continuing dehydration and stretching of the polymer chains until they reach the same thickness as the lamellae near the cloud point (see figures 5.18 and 5.19). Here, these layers start to influence the bulk solution, since there are hints for a Bragg-like feature arising from a micellar stacking (see figure 5.20). For even higher temperatures, these surface layers could act as a seeding point for a growing lamellar crystal phase causing the gelation inside the bulk solutions. Additional kinetic measurements in the temperature regime near the cloud point using a combination of reflectometry, rheology and neutron or X-ray scattering techniques could help to validate this hypothesis in the future.

Zusammenfassung

Im Rahmen dieser Dissertation wurden das Form-Phasendiagram von Pluronic P123 sowie dessen verschiedene Mizellenfromen in ihrem jeweiligen Temperaturbereich erneut untersucht. Die so gewonnenen Phasengrenzen komplettieren die bestehenden Lücken in der Literatur bei hohen Temperaturen [44] und stimmen mit den bereits bekannten Daten eines anderen Pluronic-Typs (P85) überein [41]. Es besteht eine starke Hysterese zwischen dem Heiz- und Kühlvorgang (siehe Abbildung 5.1, d und e), die auf eine Unterkühlung der lamellaren und wurmartige Strukturen schließen lässt. Innerhalb der einzelnen Phasengrenzen ist die jeweilige Gesamtgröße der Mizellen nahezu konstant und zeigt keine Konzentrationsabhängigkeit (siehe Tabelle 5.1 und Abbildung 5.3, a).

An der Übergangstemperatur der wurmartigen Mizellen wurden Messungen außerhalb des Gleichgewichtszustandes durchgeführt, um die zugrunde liegenden kinematischen Prozesse und strukturellen Änderungen während des Übergangs zu untersuchen. Die gemessenen Wachstumsraten der Mizellen (siehe Tabelle 5.2) liegen in der Größenordnung von Stunden und stimmen einigermaßen mit den gefunden Literaturwerten überein [40, 69, 222]. Allerdings zeigten sich eindeutige Unterschiede zwischen den Ergebnissen der einelnen Messmethoden, deren Ursache nicht auf die unterschiedlichen verwendeten Lösungsmittel zurückgeführt werden konnte und nach wie vor unbekannt ist. Die aufgenommenen Röngtenstreudaten wurden mit einem einfachen Model analysiert, welches die gleichzeitige Anwesenheit von sphärischen und wurmartigen Mizellen in der Lösung berücksichtigt (siehe Abbildung 5.11). In den Streukurven zeigte sich sofort nach Erreichen der Übergangstemperatur eine Verbreiterung im Bereich hoher q-Werte, welche nur mit Hilfe eines zusätzlichen gaußförmigen Peaks angepasst werden konnte (siehe Abbidung 5.12). Eine physikalische Erklärung für diese Verbreiterung konnte nicht gefunden werden, aber ihr Auftreten zeigt das Einsetzen des Übergangsprozesses für niedrige und hohe Konzentrationen. Durch die Annahme, dass die wurmartigen Aggregate wie eine Perlenkette aufgebaut sind [69, 71], war es möglich die Anzahl sphärischer Mizellen innerhalb einer wurmartigen Struktur zu berechnen, welche gut mit der durchschnittlichen Aggregationszahl übereinstimmt, die mittels eines formunabhängigen Models bestimmt wurde (siehe Tabelle 5.3 und Abbildung 5.8).

Mit steigender Temperatur nahe des Trübungspunktes fingen die besteheneden Aggregate erneut an zu wachsen. Die Neutronenstreudaten zeigten klar die Präsenz von Lamellen, während die Röntgenstreudaten einen Zustand der sphärischen Mizellen offenbarten, in dem der Mittel- und beide Enblöcke des Polymers fast völlig dehydriert und vollständig gestreckt sind. Durch die Kombination der Ergebnisse der Neutronen- und Röntgendaten konnte ein Model für die innere Strucktur der lamellaren Mizellen vorgeschlagen werden (siehe Tabelle 5.4 und Abbildung 5.16). Die großen Aggregate, welche für die Trübung der Lösungen bei diesen

Temperaturen verantwortlich sind, bestehen aus Domänen, welche wiederum für die charakteristische Oszillation in den Röntgenstreudaten verantwortlich sind (siehe Abbildung 5.14, a). Innerhalb dieser Domänen richten sich die Lamellen in einer gewiseen Vorzugsrichtung aus und haben eine Periodizität, die mit ihrer Dicke zusammenhängt. Mit Hilfe dieses Models der lamellaren Mizellen lassen sich die bisherigen Ergebnisse in der Literatur [39, 41, 68] erklären und zu einem schlüssigen Bild zusammensetzen.

Während der Experimente trat eine zeitabhängige Kristallisation der Pluronic-Lösung mit einer Konzentration von 10 Gewichtsprozent auf (siehe Abbildung 5.17). Nach mehreren Studen bei der Temperatur des Trübungspunktes gelierten die Lösungen aus, was zuvor nur für deutlich höhere Polymerkonzentrationen [44] oder nahe einer Grenzfläche [57] dokumentiert worden war. Tatsächlich bildet P123 eine Monolage auf hydrophilen und hydrophoben Oberflächen aus, was mittels Neutronenreflektometriemessungen gezeigt werden konnte. Diese Oberflächenschichten wachsen mit steigender Temperatur aufgrund der voranschreitenden Dehydrierung und Streckung der Polymerketten, bis diese dieselbe Dicke wie die Lamellen nahe des Trübungspunktes erreicht haben (siehe Abbildungen 5.18 und 5.19). An diesem Punkt beginnen diese Zwischenschichten die Mizellen in der Lösung zu beeinflußen, da es Hinweise in den Reflektivitätskurven auf ein Bragg-artiges feature gibt, dass mit einer Anordnung der Mizellen oberhalb der Grenzfläche zu tun haben kann (siehe Abbildung 5.20). Bei noch höheren Temperaturen könnten diese Polymerschichten nahe der Oberfläche als Andockpunkt für die lamellaren Aggregate dienen, was letzlich zur Gelierung der gesamten Lösung führen würde. Um diese Arbeitshypothese zu unterstützen, sind weitere kinematische Messungen nahe des Trübungspunktes mit einer Kombination aus Reflektometrie-, Rheologie- und Streu-Experimenten nötig.

A. Tabulated fit results

Fits of the kinetic SAXS data

	1 wt%		5 wt%		10 wt%	
	start	end	start	end	start	end
background [10^{-3} cm^{-1}]	1.8	3.4	5.4	7.7	5.9	4.5
$\rho^{s}_{solvent}$ [10^{-6} Å^{-2}]	9.3					
ϕ_{mic}	0.01	0.001	0.05	0.005	0.1	0.01
R_{core} [Å]	62.0	50.5	59.1	61.0	54.7	61.6
S_{shell} [Å]	30.8	31.1	28.6	27.8	32.8	29.3
σ_{mic} [Å]	9.3	20.2	9.0	12.2	13.1	18.2
ρ^{s}_{core} [10^{-6} Å^{-2}]	9.2	7.4	8.6	8.6	8.8	8.9
ρ^{s}_{shell} [10^{-6} Å^{-2}]	9.7	10.7	10.6	10.6	10.1	10.2
ϕ_{sphere}		0.009		0.045		0.09
R_{sphere} [Å]		175.5		213.1		228.1
σ_{sphere} [Å]		26.2		25.6		34.2
ρ^{s}_{sphere} [10^{-6} Å^{-2}]		9.0		9.5		9.2
R_{HS} [Å]			115.4	214.5	109.2	222.3
ϕ_{HS}			0.18	0.19	0.20	0.20
ϕ_{Gaus}		0.008		0.061		0.057
R_{Gaus} [Å^{-1}]		0.080		0.067		0.066
σ_{Gaus} [Å^{-1}]		0.008		0.013		0.011

Table A.1. Fit parameters of the kinetic SAXS data.

Fits of the SAXS data near and at the cloud point

	5 wt%				1 wt%	10 wt%
	55°C	70°C	88°C	94°C	94°C	94°C
background [10^{-3} cm^{-1}]	6.1	7.0	6.3	7.0	3.5	6.4
$\rho^{s}_{solvent}$ [10^{-6} Å^{-2}]				9.3		
ϕ_{mic}	0.05	0.005	0.005	0.005	0.001	0.01
R_{core} [Å]	53.7	59.2	67.0	61.4	76.0	60.5
S_{shell} [Å]	38.0	32.2	24.5	38.3	24.3	33.5
σ_{mic} [Å]	13.8	18.2	4.6	3.0	4.9	12.5
ρ^{s}_{core} [10^{-6} Å^{-2}]	8.4	8.4	8.8	8.7	8.7	8.6
ρ^{s}_{shell} [10^{-6} Å^{-2}]	10.6	10.1	10.2	9.8	10.3	9.9
ϕ_{sphere}		0.045	0.045	0.045	0.009	0.09
R_{sphere} [Å]		186.0	276.5	504.9	516.8	470.2
σ_{sphere} [Å]		96.7	27.7	85.7	214.5	83.7
ρ^{s}_{sphere} [10^{-6} Å^{-2}]		9.5	9.4	9.5	9.5	9.5
R_{HS} [Å]	234.2	179.5	279.6	234.8	398.6	234.8
ϕ_{HS}	0.06	0.10	0.08	0.25	0.14	0.27
ϕ_{Gaus}		0.031	0.038	0.038	0.007	0.066
R_{Gaus} [Å]		0.077	0.068	0.068	0.072	0.070
σ_{Gaus} [Å]		0.008	0.012	0.012	0.010	0.012

Table A.2. Fit parameters of the SAXS data at elevated temperatures.

Parameter of the reflectivity models - c(P123)=1 wt%

	Hydrophillic surfaces			Hydrophobic surfaces		
	10°C	38°C	70°C	10°C	38°C	70°C
scale	1.0	0.97	1.0	0.90	0.63	0.48
background [10^{-6}]	2.0	2.0	2.9	2.0	2.0	2.0
ρ^{s}_{Si} [10^{-6} Å^{-2}]	2.07					
d_{SiO_2} [Å]	15.0					
σ_{SiO_2} [Å]	6.0					
$\rho^{s}_{SiO_2}$ [10^{-6} Å^{-2}]	3.5					
d_{OTS} [Å]				28.0		
σ_{OTS} [Å]				3.8		
ρ^{s}_{OTS} [10^{-6} Å^{-2}]				1.8		
d_{poly1} [Å]		96.9	67.9	17.1	36.9	50.1
σ_{poly1} [Å]		12.5	5.0	3.0	4.2	2.0
ρ^{s}_{poly1} [10^{-6} Å^{-2}]		2.4	0.8	-0.5	0.1	0.1
d_{poly2} [Å]			223.1		37.0	48.8
σ_{poly2} [Å]			23.0		5.0	3.0
ρ^{s}_{poly2} [10^{-6} Å^{-2}]			4.9		4.1	4.7
σ_{bulk} [Å]	7.7	5.9	226.4	6.0	13.9	6.8
ρ^{s}_{bulk} [10^{-6} Å^{-2}]	6.0	6.1	5.9	5.8	5.9	5.8

Table A.3. Fit parameters of the reflectivity curves for the P123 solutions with a concentration of 1 weight percent (wt%).

Parameter of the reflectivity models - c(P123)=5 wt%

	Hydrophillic surfaces			Hydrophobic surfaces		
	10°C	38°C	70°C	10°C	38°C	70°C
scale	1.0	1.0	0.95	1.0	1.0	1.0
background [10^{-6}]	1.6	1.6	2.0	3.9	2.0	1.7
ρ^s_{Si} [10^{-6} Å^{-2}]	2.07					
d_{SiO_2} [Å]	15.0					
σ_{SiO_2} [Å]	6.0					
$\rho^s_{SiO_2}$ [10^{-6} Å^{-2}]	3.5					
d_{OTS} [Å]				28.0		
σ_{OTS} [Å]				3.8		
ρ^s_{OTS} [10^{-6} Å^{-2}]				1.8		
d_{poly1} [Å]		108.5	89.7	8.6	41.0	39.5
σ_{poly1} [Å]		102.8	17.3	25.2	6.4	3.0
ρ^s_{poly1} [10^{-6} Å^{-2}]		2.4	1.0	-2.1	0.3	0.3
d_{poly2} [Å]			447.3		22.0	50.0
σ_{poly2} [Å]			10.0		1.5	5.2
ρ^s_{poly2} [10^{-6} Å^{-2}]			4.2		3.9	4.9
σ_{bulk} [Å]	27.9	34.4	118.6	7.0	15.7	63.6
ρ^s_{bulk} [10^{-6} Å^{-2}]	5.7	5.7	5.7	5.7	5.7	5.5

Table A.4. Fit parameters of the reflectivity curves for the P123 solutions with a concentration of 5 weight percent (wt%).

Parameter of the reflectivity models - c(P123)=10 wt%

	Hydrophillic surfaces			Hydrophobic surfaces		
	10°C	38°C	70°C	10°C	38°C	70°C
scale	1.0					
background [10^{-6}]	2.0					
ρ^{s}_{Si} [10^{-6} Å^{-2}]	2.07					
d_{SiO_2} [Å]	15.0					
σ_{SiO_2} [Å]	6.0					
$\rho^{s}_{SiO_2}$ [10^{-6} Å^{-2}]	3.5					
d_{OTS} [Å]				28.0		
σ_{OTS} [Å]				3.8		
ρ^{s}_{OTS} [10^{-6} Å^{-2}]				1.8		
d_{poly1} [Å]		113.0	88.6	13.3	39.6	56.9
σ_{poly1} [Å]		42.8	17.3	10.3	8.8	1.9
ρ^{s}_{poly1} [10^{-6} Å^{-2}]		1.1	1.3	-1.7	0.3	0.1
d_{poly2} [Å]			424.0		19.0	17.1
σ_{poly2} [Å]			17.0		1.5	3.3
ρ^{s}_{poly2} [10^{-6} Å^{-2}]			5.2		3.7	3.6
σ_{bulk} [Å]	9.1	27.1	59.5	6.0	16.4	29.5
ρ^{s}_{bulk} [10^{-6} Å^{-2}]	5.6	5.5	5.4	5.4	5.4	5.2

Table A.5. Fit parameters of the reflectivity curves for the P123 solutions with a concentration of 10 weight percent (wt%).

List of Figures

List of Tables

Bibliography

[1] D. Halliday, R. Resnick, and J. Walker, *Fundamentals of Physics*. WILEY, 2013.

[2] H. Alfvén, "Plasma universe," *Physica Scripta*, vol. T18, pp. 20–28, jan 1987.

[3] H. Alfven, "Cosmology in the plasma universe: an introductory exposition," *IEEE Transactions on Plasma Science*, vol. 18, no. 1, pp. 5–10, 1990.

[4] Y. Wang, J. Xiao, H. Zhu, Y. Li, Y. Alsaid, K. Y. Fong, Y. Zhou, S. Wang, W. Shi, Y. Wang, A. Zettl, E. J. Reed, and X. Zhang, "Structural phase transition in monolayer MoTe2 driven by electrostatic doping," *Nature*, vol. 550, pp. 487–491, oct 2017.

[5] E. Ehrenreich-Petersen, M. B. Nielsen, and M. Bremholm, "Experimental equation of state of 11 lanthanide nitrides (NdN to LuN) and pressure induced phase transitions in NdN, SmN, EuN, and GdN," *Journal of Applied Physics*, vol. 128, p. 135902, oct 2020.

[6] Y. V. Kuznetsova, I. Letofsky-Papst, B. Sochor, B. Schummer, A. A. Sergeev, F. Hofer, and A. A. Rempel, "Greatly enhanced luminescence efficiency of CdS nanoparticles in aqueous solution," *Colloids and Surfaces A: Physicochemical and Engineering Aspects*, vol. 581, p. 123814, nov 2019.

[7] M. Hecht, P. Leowanawat, T. Gerlach, V. Stepanenko, M. Stolte, M. Lehmann, and F. Würthner, "Self-sorting supramolecular polymerization: Helical and lamellar aggregates of tetra-bay-acyloxy perylene bisimide," *Angewandte Chemie International Edition*, vol. 59, pp. 17084–17090, aug 2020.

[8] F. Würthner, "Aggregation-induced emission (AIE): A historical perspective," *Angewandte Chemie International Edition*, vol. 59, pp. 14192–14196, jul 2020.

[9] M. Hecht, T. Schlossarek, S. Ghosh, Y. Tsutsui, A. Schmiedel, M. Holzapfel, M. Stolte, C. Lambert, S. Seki, M. Lehmann, and F. Würthner, "Nanoscale columnar bundles based on multistranded core–shell liquid crystals of perylene bisimide j-aggregate donor–acceptor dyads for photoconductivity devices with enhanced performance through macroscopic alignment," *ACS Applied Nano Materials*, vol. 3, pp. 10234–10245, sep 2020.

[10] H. Ø. Rasmussen, J. J. Enghild, D. E. Otzen, and J. S. Pedersen, "Unfolding and partial refolding of a cellulase from the SDS-denatured state: From β-sheet to α-helix and back," *Biochimica et Biophysica Acta (BBA) - General Subjects*, vol. 1864, p. 129434, jan 2020.

[11] C. Dincer, R. Bruch, E. Costa-Rama, M. T. Fernández-Abedul, A. Merkoçi, A. Manz, G. A. Urban, and F. Güder, "Disposable sensors in diagnostics, food, and environmental monitoring," *Advanced Materials*, p. 1806739, may 2019.

[12] R. K. Jha, Y. I. Wu, J. S. Zawistowski, C. MacNevin, K. M. Hahn, and B. Kuhlman, "Redesign of the PAK1 autoinhibitory domain for enhanced stability and affinity in biosensor applications," *Journal of Molecular Biology*, vol. 413, pp. 513–522, oct 2011.

[13] X. Wu, Z.-Y. Yang, Y. Li, C.-M. Hogerkorp, W. R. Schief, M. S. Seaman, T. Zhou, S. D. Schmidt, L. Wu, L. Xu, N. S. Longo, K. McKee, S. O'Dell, M. K. Louder, D. L. Wycuff, Y. Feng, M. Nason, N. Doria-Rose, M. Connors, P. D. Kwong, M. Roederer, R. T. Wyatt, G. J. Nabel, and J. R. Mascola, "Rational design of envelope identifies broadly neutralizing human monoclonal antibodies to HIV-1," *Science*, vol. 329, pp. 856–861, jul 2010.

[14] A. Krueger, "Diamond nanoparticles: Jewels for chemistry and physics," *Advanced Materials*, vol. 20, pp. 2445–2449, jun 2008.

[15] A. Krueger, "New carbon materials: Biological applications of functionalized nanodiamond materials," *Chemistry - A European Journal*, vol. 14, pp. 1382–1390, feb 2008.

[16] A. Krueger, "The structure and reactivity of nanoscale diamond," *Journal of Materials Chemistry*, vol. 18, no. 13, p. 1485, 2008.

[17] J. J. Escobar-Chávez, M. López-Cervantes, A. Naïk, Y. N. Kalia, D. Quintanar-Guerrero, and A. Ganem-Quintanar, "Applications of thermo-reversible pluronic f-127 gels in pharmaceutical formulations.," *Journal of pharmacy pharmaceutical sciences : a publication of the Canadian Society for Pharmaceutical Sciences, Societe canadienne des sciences pharmaceutiques*, vol. 9, pp. 339–358, 2006.

[18] A. V. Kabanov, E. V. Batrakova, and V. Y. Alakhov, "Pluronic® block copolymers for overcoming drug resistance in cancer," *Advanced Drug Delivery Reviews*, vol. 54, pp. 759–779, sep 2002.

[19] L. mei HAN, J. GUO, L. jun ZHANG, Q. song WANG, and X. ling FANG, "Pharmacokinetics and biodistribution of polymeric micelles of paclitaxel with pluronic p1231," *Acta Pharmacologica Sinica*, vol. 27, pp. 747–753, jun 2006.

[20] M. M. Lübtow, L. Hahn, M. S. Haider, and R. Luxenhofer, "Drug specificity, synergy and antagonism in ultrahigh capacity poly(2-oxazoline)/poly(2-oxazine) based formulations," *Journal of the American Chemical Society*, vol. 139, pp. 10980–10983, aug 2017.

[21] E. Gioffredi, M. Boffito, S. Calzone, S. M. Giannitelli, A. Rainer, M. Trombetta, P. Mozetic, and V. Chiono, "Pluronic f127 hydrogel characterization and biofabrication in cellularized constructs for tissue engineering applications," *Procedia CIRP*, vol. 49, pp. 125–132, 2016.

[22] L. Hahn, M. Maier, P. Stahlhut, M. Beudert, V. Flegler, S. Forster, A. Altmann, F. Töppke, K. Fischer, S. Seiffert, B. Böttcher, T. Lühmann, and R. Luxenhofer, "Inverse thermogelation of aqueous triblock copolymer solutions into macroporous shear-thinning 3d printable inks," *ACS Applied Materials & Interfaces*, vol. 12, pp. 12445–12456, mar 2020.

[23] T. Lorson, S. Jaksch, M. M. Lübtow, T. Jüngst, J. Groll, T. Lühmann, and R. Luxenhofer, "A thermogelling supramolecular hydrogel with sponge-like morphology as a cytocompatible bioink," *Biomacromolecules*, vol. 18, pp. 2161–2171, jun 2017.

[24] T. Lorson, M. M. Lübtow, E. Wegener, M. S. Haider, S. Borova, D. Nahm, R. Jordan, M. Sokolski-Papkov, A. V. Kabanov, and R. Luxenhofer, "Poly(2-oxazoline)s based biomaterials: A comprehensive and critical update," *Biomaterials*, vol. 178, pp. 204–280, sep 2018.

[25] P. T. Smith, A. Basu, A. Saha, and A. Nelson, "Chemical modification and printability of shear-thinning hydrogel inks for direct-write 3d printing," *Polymer*, vol. 152, pp. 42–50, sep 2018.

[26] E. V. Batrakova and A. V. Kabanov, "Pluronic block copolymers: Evolution of drug delivery concept from inert nanocarriers to biological response modifiers," *Journal of Controlled Release*, vol. 130, pp. 98–106, sep 2008.

[27] S. Jaksch, O. Holderer, M. Gvaramia, M. Ohl, M. Monkenbusch, and H. Frielinghaus, "Nanoscale rheology at solid-complex fluid interfaces," *Scientific Reports*, vol. 7, jun 2017.

[28] S. Jaksch, F. Lipfert, A. Koutsioubas, S. Mattauch, O. Holderer, O. Ivanova, H. Frielinghaus, S. Hertrich, S. F. Fischer, and B. Nickel, "Influence of ibuprofen on phospholipid membranes," *Physical Review E*, vol. 91, feb 2015.

[29] S. F. Khattak, S. R. Bhatia, and S. C. Roberts, "Pluronic f127 as a cell encapsulation material: Utilization of membrane-stabilizing agents," *Tissue Engineering*, vol. 11, pp. 974–983, may 2005.

[30] S. C. Miller and M. D. Donovan, "Effect of poloxamer 407 gel on the miotic activity of pilocarpine nitrate in rabbits," *International Journal of Pharmaceutics*, vol. 12, pp. 147–152, oct 1982.

[31] S. MIYAZAKI, S. TAKEUCHI, C. YOKOUCHI, and M. TAKADA, "Pluronic f-127 gels as a vehicle for topical administration of anticancer agents.," *CHEMICAL & PHARMACEUTICAL BULLETIN*, vol. 32, no. 10, pp. 4205–4208, 1984.

[32] I. Schmolka, "A review of block polymer surfactants," *Journal of the American Oil Chemists' Society*, vol. 54, no. 3, pp. 110–116, 1977.

[33] T. H. Vaughn, H. R. Suter, L. G. Lundsted, and M. G. Kramer, "Properties of some newly developed nonionic detergents," *Journal of the American Oil Chemists' Society*, vol. 28, pp. 294–299, jul 1951.

[34] N. F. Billups and N. K. Patel, "In vitro release of medicament from ointment bases," *Am. J. Phram. Educ.*, vol. 34, pp. 190–196, 1970.

[35] P.-C. Chen-Chow and S. G. Frank, "In vitro release of lidocaine from pluronic f-127 gels," *International Journal of Pharmaceutics*, vol. 8, pp. 89–99, apr 1981.

[36] P. Alexandridis, J. F. Holzwarth, and T. A. Hatton, "Micellization of poly(ethylene oxide)-poly(propylene oxide)-poly(ethylene oxide) triblock copolymers in aqueous solutions: Thermodynamics of copolymer association," *Macromolecules*, vol. 27, pp. 2414–2425, apr 1994.

[37] C. Guo, H. Liu, and J. Chen, "A fourier transform infrared study of the phase transition in aqueous solutions of ethylene oxide–propylene oxide triblock copolymer," *Colloid and Polymer Science*, vol. 277, no. 4, pp. 376–381, 1999.

[38] C. Guo, J. Wang, H. Liu, and J. Chen, "Hydration and conformation of temperature-dependent micellization of peo-ppo-peo block copolymers in aqueous solutions by ft-raman," *Langmuir*, vol. 15, no. 8, pp. 2703–2708, 1999.

[39] K. Mortensen, "Structural studies of aqueous solutions of peo-ppo-peo triblock copolymers, their micellar aggregates and mesophases; a small-angle neutron scattering study," *Journal of Physics: Condensed Matter*, vol. 8, no. 25A, p. A103, 1996.

[40] G. Landazuri, V. Fernandez, J. Soltero, and Y. Rharbi, "Kinetics of the sphere-to-rod like micelle transition in a pluronic triblock copolymer," *The Journal of Physical Chemistry B*, vol. 116, no. 38, pp. 11720–11727, 2012. PMID: 22934621.

[41] B. Hammouda, "SANS from pluronic p85 in d-water," *European Polymer Journal*, vol. 46, pp. 2275–2281, dec 2010.

[42] K. Mortensen and J. S. Pedersen, "Structural study on the micelle formation of poly(ethylene oxide)-poly(propylene oxide)-poly(ethylene oxide) triblock copolymer in aqueous solution," *Macromolecules*, vol. 26, pp. 805–812, jul 1993.

[43] K. Mortensen, W. Brown, and B. Nordén, "Inverse melting transition and evidence of three-dimensional cubatic structure in a block-copolymer micellar system," *Physical Review Letters*, vol. 68, pp. 2340–2343, apr 1992.

[44] G. Wanka, H. Hoffmann, and W. Ulbricht, "Phase diagrams and aggregation behavior of poly(oxyethylene)-poly(oxypropylene)-poly(oxyethylene) triblock copolymers in aqueous solutions," *Macromolecules*, vol. 27, no. 15, pp. 4145–4159, 1994.

[45] M. Walz, M. Wolff, N. Voss, H. Zabel, and A. Magerl, "Micellar crystallization with a hysteresis in temperature," *Langmuir*, vol. 26, no. 18, pp. 14391–14394, 2010.

[46] L. F. Giraldo, B. L. López, L. Pérez, S. Urrego, L. Sierra, and M. Mesa, "Mesoporous silica applications," *Macromolecular Symposia*, vol. 258, pp. 129–141, nov 2007.

[47] C. T. Kresge, M. E. Leonowicz, W. J. Roth, J. C. Vartuli, and J. S. Beck, "Ordered mesoporous molecular sieves synthesized by a liquid-crystal template mechanism," *Nature*, vol. 359, pp. 710–712, oct 1992.

[48] M. Kruk, M. Jaroniec, C. H. Ko, and R. Ryoo, "Characterization of the porous structure of SBA-15," *Chemistry of Materials*, vol. 12, pp. 1961–1968, jul 2000.

[49] P. Yang, T. Deng, D. Zhao, P. Feng, D. Pine, B. F. Chmelka, G. M. Whitesides, and G. D. Stucky, "Hierarchically ordered oxides," *Science*, vol. 282, pp. 2244–2246, dec 1998.

[50] V. L. Zholobenko, A. Y. Khodakov, M. Impéror-Clerc, D. Durand, and I. Grillo, "Initial stages of SBA-15 synthesis: An overview," *Advances in Colloid and Interface Science*, vol. 142, pp. 67–74, oct 2008.

[51] N. Wolff, S. Gerth, P. Gutfreund, and M. Wolff, "Temperature dependent cubic and hexagonal close packing in micellar structures," *Soft Matter*, vol. 10, pp. 8420–8426, 2014.

[52] T. A. LaFollette and L. M. Walker, "Structural and mechanical hysteresis at the order-order transition of block copolymer micellar crystals," *Polymers*, vol. 3, pp. 281–298, jan 2011.

[53] J. Albano, D. Grillo, J. Facelli, M. Ferraro, and M. Pickholz, "Study of the lamellar and micellar phases of pluronic f127: A molecular dynamics approach," *Processes*, vol. 7, p. 606, sep 2019.

[54] P. Alexandridis and T. A. Hatton, "Poly(ethylene oxide)-poly(propylene oxide)-poly(ethylene oxide) block copolymer surfactants in aqueous solutions and at interfaces: thermodynamics, structure, dynamics, and modeling," *Colloids and Surfaces A: Physicochemical and Engineering Aspects*, vol. 96, pp. 1–46, mar 1995.

[55] P. Alexandridis, D. Zhou, and A. Khan, "Lyotropic liquid crystallinity in amphiphilic block copolymers: Temperature effects on phase behavior and structure for poly(ethylene oxide)-b-poly(propylene oxide)-b-poly(ethylene oxide) copolymers of different composition," *Langmuir*, vol. 12, no. 11, pp. 2690–2700, 1996.

[56] M. Almgren, W. Brown, and S. Hvidt, "Self-aggregation and phase behavior of poly(ethylene oxide)-poly(propylene oxide)-poly(ethylene oxide) block copolymers in aqueous solution," *Colloid & Polymer Science*, vol. 273, pp. 2–15, jan 1995.

[57] S. Gerth, M. Klimczak, A. Nelson, and A. Magerl, "Near surface crystallization of pluronic p123," *Journal of Physics: Conference Series*, vol. 340, p. 012088, feb 2012.

[58] P. N. Hurter, J. M. H. M. Scheutjens, and T. A. Hatton, "Molecular modeling of micelle formation and solubilization in block copolymer micelles. 2. lattice theory for monomers with internal degrees of freedom," *Macromolecules*, vol. 26, pp. 5030–5040, sep 1993.

[59] P. N. Hurter, J. M. H. M. Scheutjens, and T. A. Hatton, "Molecular modeling of micelle formation and solubilization in block copolymer micelles. 1. a self-consistent mean-field lattice theory," *Macromolecules*, vol. 26, pp. 5592–5601, oct 1993.

[60] P. Linse and M. Bjoerling, "Lattice theory for multicomponent mixtures of copolymers with internal degrees of freedom in heterogeneous systems," *Macromolecules*, vol. 24, pp. 6700–6711, dec 1991.

[61] P. Linse, "Phase behavior of poly(ethylene oxide)-poly(propylene oxide) block copolymers in aqueous solution," *The Journal of Physical Chemistry*, vol. 97, pp. 13896–13902, dec 1993.

[62] P. Linse, "Micellization of poly(ethylene oxide)-poly(propylene oxide) block copolymers in aqueous solution: Effect of polymer polydispersity," *Macromolecules*, vol. 27, pp. 6404–6417, oct 1994.

[63] S. Manet, J. Schmitt, M. Impéror-Clerc, V. Zholobenko, D. Durand, C. L. P. Oliveira, J. S. Pedersen, C. Gervais, N. Baccile, F. Babonneau, I. Grillo, F. Meneau, and C. Rochas, "Kinetics of the formation of 2d-hexagonal silica nanostructured materials by nonionic block copolymer templating in solution," *The Journal of Physical Chemistry B*, vol. 115, pp. 11330–11344, oct 2011.

[64] K. Mortensen, W. Batsberg, and S. Hvidt, "Effects of PEO-PPO diblock impurities on the cubic structure of aqueous PEO-PPO-PEO pluronics micelles: fcc and bcc ordered structures in f127," *Macromolecules*, vol. 41, pp. 1720–1727, mar 2008.

[65] J. S. Pedersen and M. C. Gerstenberg, "Scattering form factor of block copolymer micelles," *Macromolecules*, vol. 29, no. 4, pp. 1363–1365, 1996.

[66] J. S. Pedersen and M. C. Gerstenberg, "The structure of p85 pluronic block copolymer micelles determined by small-angle neutron scattering," *Colloids and Surfaces A: Physicochemical and Engineering Aspects*, vol. 213, pp. 175–187, feb 2003.

[67] M. Svensson, P. Alexandridis, and P. Linse, "Phase behavior and microstructure in binary block copolymer/selective solvent systems:â€‰ experiments and theory," *Macromolecules*, vol. 32, no. 3, pp. 637–645, 1999.

[68] Y. Zhao, X. Chen, C. Yang, and G. Zhang, "Mesoscopic simulation on phase behavior of pluronic p123 aqueous solution," *The Journal of Physical Chemistry B*, vol. 111, pp. 13937–13942, dec 2007.

[69] A. G. Denkova, E. Mendes, and M.-O. Coppens, "Kinetics and mechanism of the sphere-to-rod transition of triblock copolymer micelles in aqueous solutions," *The Journal of Physical Chemistry B*, vol. 113, no. 4, pp. 989–996, 2009. PMID: 19123834.

[70] R. Ganguly, M. Kumbhakar, and V. K. Aswal, "Time dependent growth of the block copolymer p123 micelles near cloud point: Employing heat cycling as a tool to form kinetically stable wormlike micelles," *The Journal of Physical Chemistry B*, vol. 113, pp. 9441–9446, jul 2009.

[71] A. Sundblom, C. L. P. Oliveira, A. E. C. Palmqvist, and J. S. Pedersen, "Modeling in situ small-angle x-ray scattering measurements following the formation of mesostructured silica," *The Journal of Physical Chemistry C*, vol. 113, pp. 7706–7713, apr 2009.

[72] K. Mortensen, W. Brown, and E. Jorgensen, "Lamellar mesophase of poly(ethylene oxide)-poly(propylene oxide)-poly(ethylene oxide) melts and water-swollen mixtures," *Macromolecules*, vol. 28, pp. 1458–1463, sep 1995.

[73] A. Schulz, S. Jaksch, R. Schubel, E. Wegener, Z. Di, Y. Han, A. Meister, J. Kressler, A. V. Kabanov, R. Luxenhofer, C. M. Papadakis, and R. Jordan, "Drug-induced morphology switch in drug delivery systems based on poly(2-oxazoline)s," *ACS Nano*, vol. 8, pp. 2686–2696, feb 2014.

[74] F. Cau and S. Lacelle, "H nmr relaxation studies of the micellization of a poly(ethylene oxide)-poly(propylene oxide)-poly(ethylene oxide) triblock copolymer in aqueous solution," *Macromolecules*, vol. 29, no. 1, pp. 170–178, 1996.

[75] C. Huygens, *Treatise on Light.* Macmillan London, 1912.

[76] I. Newton, *The Principia : mathematical principles of natural philosophy.* Berkeley: University of California Press, 1999.

[77] T. Young, "II. the bakerian lecture. on the theory of light and colours," *Philosophical Transactions of the Royal Society of London*, vol. 92, pp. 12–48, dec 1802.

[78] J. A. Fresnel, *Scientific Memoirs: The Wave-Theory of Light*, ch. Memoir On The Diffraction Of Light, pp. 79–144. American Book Company, 1900.

[79] J. Maxwell, "A dynamical theory of the electromagnetic field," *Philosophical Transactions of the Royal Society of London*, vol. 155, pp. 459–512, 1865.

[80] G. Kirchhoff, "Ueber das verhältniss zwischen dem emissionsvermögen und dem absorptionsvermögen der körper für wärme und licht," *Annalen der Physik und Chemie*, vol. 185, no. 2, pp. 275–301, 1860.

[81] W. Wien, "Ueber die energievertheilung im emissionsspectrum eines schwarzen körpers," *Annalen der Physik und Chemie*, vol. 294, no. 8, pp. 662–669, 1896.

[82] F. Paschen, "Ueber gesetzmässigkeiten in den spectren fester körper," *Annalen der Physik und Chemie*, vol. 296, no. 4, pp. 662–723, 1897.

[83] O. Lummer and E. Pringsheim, "Ueber die strahlung des schwarzen körpers für lange wellen," *Verh. Dtsch. Phys.Ges.*, vol. 2, p. 163, 1900.

[84] H. Rubens and F. Kurlbaum, "Uber die emission langwelliger warmestrahlen durch den schwarzen körper bei verschiedenen temperaturen," *S.B. Preuss. Akad. Wiss.*, 1900.

[85] M. Planck, "Über eine verbesserung des wienschen gesetzes für das normalspektrum," *Verhandl. Dtsch. phys. Ges.*, no. 2, p. 202, 1900.

[86] M. Planck, "Ueber irreversible strahlungsvorgänge," *Annalen der Physik*, vol. 306, no. 1, pp. 69–122, 1900.

[87] M. Planck, "Zur theorie des gesetzes der energieverteilung im normalspektrum," *Verhandl. Dtsch. phys. Ges.*, vol. 2, p. 237, 1900.

[88] E. Becquerel, "Mémoire sur les effets électriques produits sous l'influence des rayons solaires," *Comptes Rendus*, vol. 9, pp. 561–567, 1839.

[89] H. Hertz, "Ueber einen einfluss des ultravioletten lichtes auf die electrische entladung," *Annalen der Physik und Chemie*, vol. 267, no. 8, pp. 983–1000, 1887.

[90] W. Hallwachs, "Ueber die electrisirung von metallplatten durch bestrahlung mit electrischem licht," *Annalen der Physik*, vol. 270, no. 8A, pp. 731–734, 1888.

[91] J. J. Thomson, "XL. cathode rays," *The London, Edinburgh, and Dublin Philosophical Magazine and Journal of Science*, vol. 44, pp. 293–316, oct 1897.

[92] P. Lenard, "Erzeugung von kathodenstrahlen durch ultraviolettes licht," *Annalen der Physik*, vol. 307, no. 6, pp. 359–375, 1900.

[93] A. Einstein, "Über einen die erzeugung und verwandlung des lichtes betreffenden heuristischen gesichtspunkt," *Annalen der Physik*, vol. 322, no. 6, pp. 132–148, 1905.

[94] R. A. Millikan, "A direct photoelectric determination of planck's "h"," *Physical Review*, vol. 7, pp. 355–388, mar 1916.

[95] L. de Broglie, "Recherches sur la théorie des quanta," *Ann. de Physique*, vol. 3, no. 10, p. 22, 1925.

[96] C. J. Davisson and L. H. Germer, "Reflection of electrons by a crystal of nickel," *Proceedings of the National Academy of Sciences*, vol. 14, pp. 317–322, apr 1928.

[97] E. Schrödinger, "Zur einsteinschen gastheorie," *Phys. Z.*, vol. 27, p. 95, 1926.

[98] E. Schrödinger, "Quantisierung als eigenwertproblem," *Annalen der Physik*, vol. 385, no. 13, pp. 437–490, 1926.

[99] E. Rutherford, "Bakerian lecture: Nuclear constitution of atoms," *Proceedings of the Royal Society of London. Series A, Containing Papers of a Mathematical and Physical Character*, vol. 97, pp. 374–400, jul 1920.

[100] W. Bothe and H. Becker, "Künstliche erregung von kern-gamma-strahlen," *Zeitschrift für Physik*, vol. 66, no. 5-6, pp. 289–306, 1930.

[101] I. Joliot-Curie and F. Joliot, "Émission de protons de grande vitesse par les substances hydrogénées sous l'influence des rayons gamma très pénétrants," *Comptes Rendus*, vol. 194, p. 273, 1932.

[102] J. Chadwick, "The existence of a neutron," *Proceedings of the Royal Society of London. Series A, Containing Papers of a Mathematical and Physical Character*, vol. 136, pp. 692–708, jun 1932.

[103] C. G. Shull and E. O. Wollan, "X-ray, electron, and neutron diffraction," *Science*, vol. 108, pp. 69–75, jul 1948.

[104] E. O. Wollan and C. G. Shull, "Neutron diffraction and associated studies.," *Nucleonics*, vol. 3, pp. 17–31, Aug. 1948.

[105] E. Hecht, *Optics*. Boston: Pearson Education, Inc, 2017.

[106] D. Attwood and A. Sakdinawat, *X-Rays and Extreme Ultraviolet Radiation*. Cambridge University Press, 2016.

[107] J. Als-Nielsen, *Neutron and Synchrotron Radiation for Condensed Matter Studies: Theory, Instruments and Methods*, ch. Diffraction, Refraction and Absorption of X-rays and Neutrons - A comparative Exposition, pp. 3–33. Springer-Verlag, 1993.

[108] Beer, "Bestimmung der absorption des rothen lichts in farbigen flüssigkeiten," *Annalen der Physik und Chemie*, vol. 162, no. 5, pp. 78–88, 1852.

[109] P. Bouguer, "Essai d'optique sur la gradation de la lumière," *Claude Jombert*, pp. 16–22, 1729.

[110] J. H. Lambert, "Photometria, sive de mensura et gradibus luminis, colorum et umbrae," *Sumptibus Vidae Eberhardi Klett*, 1760.

[111] N. Bohr, "I. on the constitution of atoms and molecules," *Philosophical Magazine Series 6*, vol. 26, no. 151, pp. 1–25, 1913.

[112] V. F. Sears, "Neutron scattering lengths and cross sections," *Neutron News*, vol. 3, pp. 26–37, jan 1992.

[113] National Institute for Standards and Technolgy (NIST), "https://www.ncnr.nist.gov/resources/n-lengths/," 2013. [online version from April 27th 2020].

[114] A. J. de Witte, "Equivalence of huygens' principle and fermat's principle in ray geometry," *American Journal of Physics*, vol. 27, pp. 293–301, may 1959.

[115] R. Descartes, *Discourse on Method, Optics, Geometry, and Meteorology*. Hackett Publishing Co, Inc, 2001.

[116] I. H. Malitson, "Interspecimen comparison of the refractive index of fused silica," *Journal of the Optical Society of America*, vol. 55, p. 1205, oct 1965.

[117] J. Colvin, A. Shestakov, J. Stölken, and R. Vignes, "The role of radiation transport in the thermal response of semitransparent materials to localized laser heating," *Journal of Applied Physics*, vol. 109, p. 053506, mar 2011.

[118] M. S. del Rio and R. J. Dejus, "Status of XOP: an x-ray optics software toolkit," in *Advances in Computational Methods for X-Ray and Neutron Optics* (M. S. del Rio, ed.), SPIE, oct 2004.

[119] T. Shinohara, K. Hirota, T. Adachi, K. Ikeda, H. M. Shimizu, J. ichi Suzuki, and T. Oku, "Thermal neutron refraction by material prism," *Physica B: Condensed Matter*, vol. 385-386, pp. 1232–1235, nov 2006.

[120] C. Krywka, A. Last, F. Marschall, O. M. andSebastian Georgi, M. Müller, and J. Mohr, "Polymer compound refractive lenses for hard x-ray nanofocusing," *AIP Conference Proceedings*, vol. 1764, p. 020001, 2016.

[121] F. Pfeiffer, P. Hoghoj, I. S. Anderson, and V. Leiner, "Neutron waveguides: a new neutron optical device for the production of submicrometer neutron beams," in *Neutron Optics* (J. L. Wood and I. S. Anderson, eds.), SPIE, nov 2001.

[122] C. V. Raman, "A new radiation," *Indian J. Phys.*, vol. 2, p. 387, 1928.

[123] A. Compton, "A quantum theory of the scattering of x-rays by light elements," *Phys. Rev.*, vol. 21, pp. 483–502, May 1923.

[124] B. N. Brockhouse and A. T. Stewart, "Scattering of neutrons by phonons in an aluminum single crystal," *Physical Review*, vol. 100, pp. 756–757, oct 1955.

[125] G. L. Squires, *Introduction to the Theory of Thermal Neutron Scattering*. Cambridge University Press, 2009.

[126] J. J. Thomson, "On electrical oscillations and the effects produced by the motion of an electrified sphere," *Proceedings of the London Mathematical Society*, vol. s1-15, pp. 197–219, nov 1883.

[127] L. Rayleigh, "X. on the electromagnetic theory of light," *The London, Edinburgh, and Dublin Philosophical Magazine and Journal of Science*, vol. 12, pp. 81–101, aug 1881.

[128] L. Rayleigh, "XXXIV. on the transmission of light through an atmosphere containing small particles in suspension, and on the origin of the blue of the sky," *The London, Edinburgh, and Dublin Philosophical Magazine and Journal of Science*, vol. 47, pp. 375–384, apr 1899.

[129] J. Strutt, "LVIII. on the scattering of light by small particles," *The London, Edinburgh, and Dublin Philosophical Magazine and Journal of Science*, vol. 41, pp. 447–454, jun 1871.

[130] G. Mie, "Beiträge zur optik trüber medien, speziell kolloidaler metallösungen," *Annalen der Physik*, vol. 330, no. 3, pp. 377–445, 1908.

[131] H. C. van de Hulst, *Light Scattering by Small Particles*. Dover Publications Inc., 1981.

[132] P. Debye, "Light scattering in solutions," *Journal of Applied Physics*, vol. 15, pp. 338–342, apr 1944.

[133] B. H. Zimm, "Molecular theory of the scattering of light in fluids," *The Journal of Chemical Physics*, vol. 13, pp. 141–145, apr 1945.

[134] B. H. Zimm, "The scattering of light and the radial distribution function of high polymer solutions," *The Journal of Chemical Physics*, vol. 16, pp. 1093–1099, dec 1948.

[135] R. Pecora, "Doppler shifts in light scattering from pure liquids and polymer solutions," *The Journal of Chemical Physics*, vol. 40, pp. 1604–1614, mar 1964.

[136] H. Z. Cummins, N. Knable, and Y. Yeh, "Observation of diffusion broadening of rayleigh scattered light," *Physical Review Letters*, vol. 12, pp. 150–153, feb 1964.

[137] B. J. Berne and R. Pecora, "Laser light scattering from liquids," *Annual Review of Physical Chemistry*, vol. 25, pp. 233–253, oct 1974.

[138] R. Xu, "Light scattering: A review of particle characterization applications," *Particuology*, vol. 18, pp. 11–21, feb 2015.

[139] B. J. Berne and R. Pecora, *Dynamic Light Scattering*. Dover Publications Inc., 2000.

[140] A. Einstein, "Über die von der molekularkinetischen theorie der wärme geforderte bewegung von in ruhenden flüssigkeiten suspendierten teilchen," *Annalen der Physik*, vol. 322, no. 8, pp. 549–560, 1905.

[141] G. G. Stokes, "On the effect of the internal friction of fluids on the motion of pendulums," *Transactions of the Cambridge Philosophical Society*, vol. 9, p. 8, 1851.

[142] A. Guinier, "Structure of age-hardened aluminium-copper alloys," *Nature*, vol. 142, pp. 569–570, sep 1938.

[143] A. Guinier, "La diffraction des rayons x aux très petits angles : application à l'étude de phénomènes ultramicroscopiques," *Annales de Physique*, vol. 11, no. 12, pp. 161–237, 1939.

[144] J. P. Cotton, B. Farnoux, and G. Jannink, "Neutron diffraction in dilute and semidilute polymer solutions," *The Journal of Chemical Physics*, vol. 57, pp. 290–294, jul 1972.

[145] J. P. Cotton, B. Farnoux, G. Jannink, and R. Ober, "Study of polymer solution by small-angle neutron scattering in the intermediate momentum range," *Journal of Applied Crystallography*, vol. 7, pp. 189–189, apr 1974.

[146] R. G. Kirste, W. A. Kruse, and K. Ibel, "Determination of the conformation of polymers in the amorphous solid state and in concentrated solution by neutron diffraction," *Polymer*, vol. 16, pp. 120–124, feb 1975.

[147] G. Wignall, D. Ballard, and J. Schelten, "Measurements of persistence length and temperature dependence of the radius of gyration in bulk atactic polystyrene," *European Polymer Journal*, vol. 10, pp. 861–865, sep 1974.

[148] P. Debye, "Zerstreuung von röntgenstrahlen," *Annalen der Physik*, vol. 351, no. 6, pp. 809–823, 1915.

[149] R. Gans, "Strahlungsdiagramme ultramikroskopischer teilchen," *Annalen der Physik*, vol. 381, no. 1, pp. 29–38, 1925.

[150] L. A. Feigin and D. I. Svergun, *Structure Analysis by Small-Angle X-Ray and Neutron Scattering*. Plenum Press New York, 1987.

[151] O. Glatter, *Scattering Methods and their Application in Colloid and Interface Science*. Elsevier Science Publishing Co Inc, 2018.

[152] A. Guinier and G. Fournet, *Small-Angle Scattering of X-Rays*. Wiley & Sons, 1955.

[153] O. Kratky and O. Glatter, eds., *Small Angle X-ray Scattering*. Academic Press London, 1982.

[154] B. A. Lippmann, "Variational principles for scattering processes. II. scattering of slow neutrons by para-hydrogen," *Physical Review*, vol. 79, pp. 481–486, aug 1950.

[155] B. A. Lippmann and J. Schwinger, "Variational principles for scattering processes. i," *Physical Review*, vol. 79, pp. 469–480, aug 1950.

[156] L. D. Landau and E. M. Lifshitz, *Quantum mechanics : non-relativistic theory*. Oxford New York: Pergamon Press, 1977.

[157] J. J. Sakurai, *Modern Qauntum Mechanics Revised Edition*. Addison-Wesley, 1994.

[158] R. Newton, *Scattering theory of waves and particles*. New York: McGraw-Hill, 1966.

[159] M. Born, "Zur quantenmechanik der stossvorgänge," *Zeitschrift für Physik*, vol. 37, pp. 863–867, dec 1926.

[160] M. Born, W. Heisenberg, and P. Jordan, "Zur quantenmechanik. II.," *Zeitschrift für Physik*, vol. 35, pp. 557–615, aug 1926.

[161] M. Born and P. Jordan, "Zur quantenmechanik," *Zeitschrift für Physik*, vol. 34, pp. 858–888, dec 1925.

[162] E. Fermi, "Sul moto dei neutroni nelle sostanze idrogenate. (Italian) [On the motion of neutrons in hydrogenous substances]," *La Ricerca Scientifica*, vol. 7, no. 2, pp. 13–52, 1936.

[163] P. Debye and A. M. Bueche, "Scattering by an inhomogeneous solid," *Journal of Applied Physics*, vol. 20, pp. 518–525, jun 1949.

[164] R. Bracewell, *The Fourier transform and its applications*. Boston: McGraw Hill, 2000.

[165] O. Glatter, "A new method for the evaluation of small-angle scattering data," *Journal of Applied Crystallography*, vol. 10, pp. 415–421, oct 1977.

[166] D. Franke, M. V. Petoukhov, P. V. Konarev, A. Panjkovich, A. Tuukkanen, H. D. T. Mertens, A. G. Kikhney, N. R. Hajizadeh, J. M. Franklin, C. M. Jeffries, and D. I. Svergun, "ATSAS 2.8: a comprehensive data analysis suite for small-angle scattering from macromolecular solutions," *Journal of Applied Crystallography*, vol. 50, pp. 1212–1225, jun 2017.

[167] G. Beaucage, "Small-angle scattering from polymeric mass fractals of arbitrary mass-fractal dimension," *Journal of Applied Crystallography*, vol. 29, pp. 134–146, apr 1996.

[168] G. Porod, "Theorie der diffusen röntgenkleinwinkelstreuung an kolloiden systemen," *Z. Naturforschg*, vol. 4 a, pp. 401–114, 1949.

[169] G. Porod, "Die röntgenkleinwinkelstreuung von dichtgepackten kolloiden systemen," *Kolloid-Zeitschrift*, vol. 124, pp. 83–114, nov 1951.

[170] G. Porod, "Die röntgenkleinwinkelstreuung von dichtgepackten kolloiden systemen. II. teil," *Kolloid-Zeitschrift*, vol. 125, pp. 108–122, feb 1952.

[171] G. Porod, "Die röntgenkleinwinkelstreuung von dichtgepackten kolloiden systemen," *Kolloid-Zeitschrift*, vol. 125, pp. 51–57, jan 1952.

[172] G. Beaucage, T. Ulibarri, E. Black, and D. Schaefer, *Multiple Size Scale Structures in Silica-Siloxane Composites Studied by Small-Angle Scattering*, ch. 9, pp. 97–111. ACS Publications, 1995.

[173] G. Porod, "Zusammenhang zwischen mittlerem endpunktsabstand und kettenlänge bei fadenmolekülen," *Monatshefte für Chemie*, vol. 80, no. 2, pp. 251–255, 1949.

[174] B. Hammouda, "A new guinier–porod model," *Journal of Applied Crystallography*, vol. 43, pp. 716–719, may 2010.

[175] J. S. Pedersen, "Analysis of small-angle scattering data from colloids and polymer solutions: modeling and least-squares fitting," *Advances in Colloid and Interface Science*, vol. 70, pp. 171–210, jul 1997.

[176] L. Rayleigh, "LXXXII. on the motion of solid bodies through viscous liquid," *The London, Edinburgh, and Dublin Philosophical Magazine and Journal of Science*, vol. 21, pp. 697–711, jun 1911.

[177] J. S. Pedersen, "Resolution effects and analysis of small-angle neutron scattering data," *Le Journal de Physique IV*, vol. 03, pp. C8–491–C8–498, dec 1993.

[178] J. S. Pedersen, D. Posselt, and K. Mortensen, "Analytical treatment of the resolution function for small-angle scattering," *Journal of Applied Crystallography*, vol. 23, pp. 321–333, aug 1990.

[179] T. Freltoft, J. K. Kjems, and S. K. Sinha, "Power-law correlations and finite-size effects in silica particle aggregates studied by small-angle neutron scattering," *Physical Review B*, vol. 33, pp. 269–275, jan 1986.

[180] M. Kotlarchyk and S.-H. Chen, "Analysis of small angle neutron scattering spectra from polydisperse interacting colloids," *The Journal of Chemical Physics*, vol. 79, pp. 2461–2469, sep 1983.

[181] L. Ornstein and F. Zernike, "Accidental deviations of density and opalescence at the critical point of a single substance," *Koninklijke Nederlandsche Akademie van Wetenschappen Proceedings*, vol. 17, pp. 793–806, 1914.

[182] J. K. Percus and G. J. Yevick, "Analysis of classical statistical mechanics by means of collective coordinates," *Phys. Rev.*, vol. 110, no. 1, pp. 1–13, 1958.

[183] N. W. Ashcroft and J. Lekner, "Structure and resistivity of liquid metals," *Physical Review*, vol. 145, pp. 83–90, may 1966.

[184] C. A. Dreiss, K. S. Jack, and A. P. Parker, "On the absolute calibration of bench-top small-angle x-ray scattering instruments: a comparison of different standard methods," *Journal of Applied Crystallography*, vol. 39, pp. 32–38, jan 2006.

[185] U. Bonse and M. Hart, "An x-ray interferometer," *Applied Physics Letters*, vol. 6, pp. 155–156, apr 1965.

[186] D. Orthaber, A. Bergmann, and O. Glatter, "SAXS experiments on absolute scale with kratky systems using water as a secondary standard," *Journal of Applied Crystallography*, vol. 33, pp. 218–225, apr 2000.

[187] G. D. Wignall and F. S. Bates, "Absolute calibration of small-angle neutron scattering data," *Journal of Applied Crystallography*, vol. 20, pp. 28–40, feb 1987.

[188] F. Zhang, J. Ilavsky, G. G. Long, J. P. G. Quintana, A. J. Allen, and P. R. Jemian, "Glassy carbon as an absolute intensity calibration standard for small-angle scattering," *Metallurgical and Materials Transactions A*, vol. 41, pp. 1151–1158, aug 2009.

[189] G. S. Kell, "Density, thermal expansivity, and compressibility of liquid water from 0 to 150°c. correlations and tables for atmospheric pressure and saturation reviewed and expressed on 1968 temperature scale," *Journal of Chemical & Engineering Data*, vol. 20, pp. 97–105, jan 1975.

[190] J. D. Jackson, *Classical Electrodynamics*. John Wiley Sons Inc, 1998.

[191] J. Als-Nielsen and D. Mcmorrow, *Elements of Modern X-Ray Physics*. WILEY, 2011.

[192] C. Fermon, F. Ott, and A. Menelle, "Neutron reflectometry," in *Lecture Notes in Physics Monographs*, vol. 58, pp. 163–195, Springer Berlin Heidelberg, 1999.

[193] L. G. Parratt, "Surface studies of solids by total reflection of x-rays," *Physical Review*, vol. 95, pp. 359–369, jul 1954.

[194] I. W. Hamley and J. S. Pedersen, "Analysis of neutron and x-ray reflectivity data. i. theory," *Journal of Applied Crystallography*, vol. 27, pp. 29–35, feb 1994.

[195] S. Gayen, "A versatile simulator for specular reflectivity study of multi-layer thin films," *arXiv*, 2013.

[196] J. Als-Nielsen and K. Kjær, "X-ray reflectivity and diffraction studies of liquid surfaces and surfactant monolayers," in *Phase Transitions in Soft Condensed Matter*, pp. 113–138, Springer US, 1989.

[197] P. S. Pershan and J. Als-Nielsen, "X-ray reflectivity from the surface of a liquid crystal: Surface structure and absolute value of critical fluctuations," *Physical Review Letters*, vol. 52, pp. 759–762, feb 1984.

[198] J. S. Pedersen and I. W. Hamley, "Analysis of neutron and x-ray reflectivity data. II. constrained least-squares methods," *Journal of Applied Crystallography*, vol. 27, pp. 36–49, feb 1994.

[199] J. S. Pedersen, "Model-independent determination of the surface scattering-length-density profile from specular reflectivity data," *Journal of Applied Crystallography*, vol. 25, pp. 129–145, apr 1992.

[200] A. L. Patterson, "A direct method for the determination of the components of interatomic distances in crystals," *Zeitschrift für Kristallographie - Crystalline Materials*, vol. 90, jan 1935.

[201] H. Staudinger, "Über polymerisation," *Berichte der deutschen chemischen Gesellschaft (A and B Series)*, vol. 53, pp. 1073–1085, jun 1920.

[202] Association of Plastics Manufactures, "https://www.plasticseurope.org/."

[203] J. C. Gilbert, J. Hadgraft, A. Bye, and L. G. Brookes, "Drug release from pluronic f-127 gels," *International Journal of Pharmaceutics*, vol. 32, pp. 223–228, oct 1986.

[204] M. Amiji and K. Park, "Prevention of protein adsorption and platelet adhesion on surfaces by PEO/PPO/PEO triblock copolymers," *Biomaterials*, vol. 13, no. 10, pp. 682–692, 1992.

[205] M. L. Huggins, "Solutions of long chain compounds," *The Journal of Chemical Physics*, vol. 9, pp. 440–440, may 1941.

[206] P. J. Flory, "Thermodynamics of high polymer solutions," *The Journal of Chemical Physics*, vol. 9, pp. 660–660, aug 1941.

[207] S. F. Edwards, "The statistical mechanics of polymers with excluded volume," *Proceedings of the Physical Society*, vol. 85, pp. 613–624, apr 1965.

[208] P. de Gennes, "Exponents for the excluded volume problem as derived by the wilson method," *Physics Letters A*, vol. 38, pp. 339–340, feb 1972.

[209] P. de Gennes, *Scaling concepts in polymer physics*. Ithaca, N.Y: Cornell University Press, 1979.

[210] P. J. Flory, *Principles of Polymer Chemistry*. Cornell University Press, 1953.

[211] M. Rubinstein, *Polymer physics*. Oxford New York: Oxford University Press, 2003.

[212] J. E. Mayer, "Contribution to statistical mechanics," *The Journal of Chemical Physics*, vol. 10, pp. 629–643, oct 1942.

[213] S. Alexander, "Adsorption of chain molecules with a polar head a scaling description," *Journal de Physique*, vol. 38, no. 8, pp. 983–987, 1977.

[214] P. G. de Gennes, "Conformations of polymers attached to an interface," *Macromolecules*, vol. 13, pp. 1069–1075, sep 1980.

[215] I. Schmolka, "Aqueous gel composition containing polyether polyol gelling agents," July 24 1973. US Patent 3,748,276.

[216] I. Schmolka, "Polyoxyethylene-polyoxypropylene aqueous gels," June 19 1973. US Patent 3,740,421.

[217] G. N. Malcolm and J. S. Rowlinson, "The thermodynamic properties of aqueous solutions of polyethylene glycol, polypropylene glycol and dioxane," *Transactions of the Faraday Society*, vol. 53, p. 921, 1957.

[218] S. Saeki, N. Kuwahara, M. Nakata, and M. Kaneko, "Upper and lower critical solution temperatures in poly (ethylene glycol) solutions," *Polymer*, vol. 17, pp. 685–689, aug 1976.

[219] Z. Zhou and B. Chu, "Light-scattering study on the association behavior of triblock polymers of ethylene oxide and propylene oxide in aqueous solution," *Journal of Colloid and Interface Science*, vol. 126, no. 1, pp. 171 – 180, 1988.

[220] G. Wanka, H. Hoffmann, and W. Ulbricht, "The aggregation behavior of poly-(oxyethylene)-poly-(oxypropylene)-poly-(oxyethylene)-block-copolymers in aqueous solution," *Colloid & Polymer Science*, vol. 268, pp. 101–117, feb 1990.

[221] V. Singh, P. Khullar, P. N. Dave, and N. Kaur, "Micelles, mixed micelles, and applications of polyoxypropylene (PPO)-polyoxyethylene (PEO)-polyoxypropylene (PPO) triblock polymers," *International Journal of Industrial Chemistry*, vol. 4, no. 1, p. 12, 2013.

[222] Y. Kadam, R. Ganguly, M. Kumbhakar, V. K. Aswal, P. A. Hassan, and P. Bahadur, "Time dependent sphere-to-rod growth of the pluronic micelles: Investigating the role of core and corona solvation in determining the micellar growth rate," *The Journal of Physical Chemistry B*, vol. 113, no. 51, pp. 16296–16302, 2009. PMID: 19938845.

[223] R. Lund, L. Willner, M. Monkenbusch, P. Panine, T. Narayanan, J. Colmenero, and D. Richter, "Structural observation and kinetic pathway in the formation of polymeric micelles," *Physical Review Letters*, vol. 102, may 2009.

[224] R. Lund, L. Willner, D. Richter, and E. E. Dormidontova, "Equilibrium chain exchange kinetics of diblock copolymer micelles: tuning and logarithmic relaxation," *Macromolecules*, vol. 39, pp. 4566–4575, jun 2006.

[225] B. Michels, G. Waton, and R. Zana, "Dynamics of micelles of poly(ethylene oxide)-poly(propylene oxide)-poly(ethylene oxide) block copolymers in aqueous solutions," *Langmuir*, vol. 13, pp. 3111–3118, jun 1997.

[226] M. S. Turner and M. E. Cates, "The relaxation spectrum of polymer length distributions," *Journal de Physique*, vol. 51, no. 4, pp. 307–316, 1990.

[227] G. Karlstroem, "A new model for upper and lower critical solution temperatures in poly(ethylene oxide) solutions," *The Journal of Physical Chemistry*, vol. 89, pp. 4962–4964, nov 1985.

[228] D. J. Mitchell, G. J. T. Tiddy, L. Waring, T. Bostock, and M. P. McDonald, "Phase behaviour of polyoxyethylene surfactants with water. mesophase structures and partial miscibility (cloud points)," *Journal of the Chemical Society, Faraday Transactions 1: Physical Chemistry in Condensed Phases*, vol. 79, no. 4, p. 975, 1983.

[229] B. Bharatiya, C. Guo, J. Ma, P. Hassan, and P. Bahadur, "Aggregation and clouding behavior of aqueous solution of EO–PO block copolymer in presence of n-alkanols," *European Polymer Journal*, vol. 43, pp. 1883–1891, may 2007.

[230] G. Porte, J. Marignan, P. Bassereau, and R. May, "Sans diffuse pattern in very swollen lamellar phases," *Europhysics Letters (EPL)*, vol. 7, pp. 713–717, dec 1988.

[231] B. Sochor, "Form-phasendiagram von pluronic p123," Master's thesis, Universtiy Würzburg, 2017.

[232] J. Israelachvili, *Intermolecular and Surface Forces*. Academic Press, third edition ed., 2011.

[233] C. Freij-Larsson, T. Nylander, P. Jannasch, and B. Wesslén, "Adsorption behaviour of amphiphilic polymers at hydrophobic surfaces: effects on protein adsorption," *Biomaterials*, vol. 17, pp. 2199–2207, nov 1996.

[234] A. Higuchi, K. Sugiyama, B. O. Yoon, M. Sakurai, M. Hara, M. Sumita, S. ichi Sugawara, and T. Shirai, "Serum protein adsorption and platelet adhesion on pluronic™-adsorbed polysulfone membranes," *Biomaterials*, vol. 24, pp. 3235–3245, aug 2003.

[235] Y.-B. Liou and R.-Y. Tsay, "Adsorption of PEO–PPO–PEO triblock copolymers on a gold surface," *Journal of the Taiwan Institute of Chemical Engineers*, vol. 42, pp. 533–540, may 2011.

[236] A. K. Muszanska, H. J. Busscher, A. Herrmann, H. C. van der Mei, and W. Norde, "Pluronic–lysozyme conjugates as anti-adhesive and antibacterial bifunctional polymers for surface coating," *Biomaterials*, vol. 32, pp. 6333–6341, sep 2011.

[237] A. Kozak and Z. Sadowski, "Effect of pluronics and surfactant adsorption onto dolomite suspension zeta potential and stability," *Annales UMCS, Chemia*, vol. 70, jan 2015.

[238] Y. Lin and P. Alexandridis, "Temperature-dependent adsorption of pluronic f127 block copolymers onto carbon black particles dispersed in aqueous media," *The Journal of Physical Chemistry B*, vol. 106, pp. 10834–10844, oct 2002.

[239] V. Shah, T. Panchal, B. Bharatiya, N. S. Patel, A. D. Shukla, and D. O. Shah, "Colloidal PTFE dispersion in commercial engine oil: Lubrication by pluronic adsorption at the interface," *Colloids and Surfaces A: Physicochemical and Engineering Aspects*, vol. 597, p. 124775, jul 2020.

[240] M. A. Bevan and D. C. Prieve, "Forces and hydrodynamic interactions between polystyrene surfaces with adsorbed PEO-PPO-PEO," *Langmuir*, vol. 16, pp. 9274–9281, nov 2000.

[241] P. Brandani and P. Stroeve, "Adsorption and desorption of PEO-PPO-PEO triblock copolymers on a self-assembled hydrophobic surface," *Macromolecules*, vol. 36, pp. 9492–9501, dec 2003.

[242] P. Brandani and P. Stroeve, "Kinetics of adsorption and desorption of PEO-PPO-PEO triblock copolymers on a self-assembled hydrophobic surface," *Macromolecules*, vol. 36, pp. 9502–9509, dec 2003.

[243] P. Brandani and P. Stroeve, "Kinetics and equilibria of adsorption of peo-ppo-peo triblock copolymers on a hydrophilic self-assembled monolayer on gold," *Macromolecules*, vol. 37, no. 17, pp. 6640–6643, 2004.

[244] M. E. Cates and M. S. Turner, "Flow-induced gelation of rodlike micelles," *Europhysics Letters (EPL)*, vol. 11, pp. 681–686, apr 1990.

[245] É. Kiss, K. Erdélyi, I. Szendrö, and E. I. Vargha-Butler, "ADSORPTION AND WETTING PROPERTIES OF PLURONIC BLOCK COPOLYMERS ON HYDROPHOBIC SURFACES STUDIED BY OPTICAL WAVEGUIDE LIGHTMODE SPECTROSCOPY AND DYNAMIC TENSIOMETRIC METHOD," *The Journal of Adhesion*, vol. 80, pp. 815–829, sep 2004.

[246] M. Malmsten, P. Linse, and T. Cosgrove, "Adsorption of PEO-PPO-PEO block copolymers at silica," *Macromolecules*, vol. 25, pp. 2474–2481, apr 1992.

[247] M. R. Nejadnik, A. L. J. Olsson, P. K. Sharma, H. C. van der Mei, W. Norde, and H. J. Busscher, "Adsorption of pluronic f-127 on surfaces with different hydrophobicities probed by quartz crystal microbalance with dissipation," *Langmuir*, vol. 25, pp. 6245–6249, jun 2009.

[248] A. Nelson and T. Cosgrove, "Small-angle neutron scattering study of adsorbed pluronic tri-block copolymers on laponite," *Langmuir*, vol. 21, pp. 9176–9182, sep 2005.

[249] J. Rubio and J. Kitchener, "The mechanism of adsorption of poly(ethylene oxide) flocculant on silica," *Journal of Colloid and Interface Science*, vol. 57, pp. 132–142, oct 1976.

[250] J. Shar, T. Obey, and T. Cosgrove, "Adsorption studies of polyethers part 1. adsorption onto hydrophobic surfaces," *Colloids and Surfaces A: Physicochemical and Engineering Aspects*, vol. 136, pp. 21–33, apr 1998.

[251] J. Shar, T. Obey, and T. Cosgrove, "Adsorption studies of polyethers," *Colloids and Surfaces A: Physicochemical and Engineering Aspects*, vol. 150, pp. 15–23, may 1999.

[252] X. Song, S. Zhao, S. Fang, Y. Ma, and M. Duan, "Mesoscopic simulations of adsorption and association of PEO-PPO-PEO triblock copolymers on a hydrophobic surface: From mushroom hemisphere to rectangle brush," *Langmuir*, vol. 32, pp. 11375–11385, oct 2016.

[253] F. Tiberg, M. Malmsten, P. Linse, and B. Lindman, "Kinetic and equilibrium aspects of block copolymer adsorption," *Langmuir*, vol. 7, pp. 2723–2730, nov 1991.

[254] T. W. Haas and B. Maxwell, "Effects of shear stress on the crystallization of linear polyethylene and polybutene-1," *Polymer Engineering and Science*, vol. 9, pp. 225–241, jul 1969.

[255] J. F. Lutsko, "Molecular chaos, pair correlations, and shear-induced ordering of hard spheres," *Physical Review Letters*, vol. 77, pp. 2225–2228, sep 1996.

[256] P. G. de Gennes, "Wetting: statics and dynamics," *Reviews of Modern Physics*, vol. 57, pp. 827–863, jul 1985.

[257] H. Fox and W. Zisman, "The spreading of liquids on low-energy surfaces. III. hydrocarbon surfaces," *Journal of Colloid Science*, vol. 7, pp. 428–442, aug 1952.

[258] R. J. Good and L. A. Girifalco, "A theory for estimation of surface and interfacial energies. iii. estimation of surface energies of solids from contact angle data," *The Journal of Physical Chemistry*, vol. 64, pp. 561–565, may 1960.

[259] T. Young, "An essay on the cohesion of fluids," *Philosophical Transactions of the Royal Society of London*, vol. 95, pp. 65–87, dec 1805.

[260] P. Bryk, E. Korczeniewski, G. S. Szymański, P. Kowalczyk, K. Terpiłowski, and A. P. Terzyk, "What is the value of water contact angle on silicon?," *Materials*, vol. 13, p. 1554, mar 2020.

[261] K. Hermansson, U. Lindberg, B. Hok, and G. Palmskog, "Wetting properties of silicon surfaces," in *TRANSDUCERS '91: 1991 International Conference on Solid-State Sensors and Actuators. Digest of Technical Papers*, IEEE.

[262] H. Caro, "Zur kenntniss der oxydation aromatischer amine," *Zeitschrift für Angewandte Chemie*, vol. 11, pp. 815–846, sep 1898.

[263] S. Gerth, *Stabilität adsorbierter Polymerschichten an Grenzflächen.* Dissertation, Friedrich-Alexander-Universität Erlangen-Nürnberg, 2012.

[264] C. &. E. News, "Safety," *Chemical & Engineering News*, vol. 33, p. 3336, aug 1955.

[265] M. Lessel, O. Bäumchen, M. Klos, H. Hähl, R. Fetzer, M. Paulus, R. Seemann, and K. Jacobs, "Self-assembled silane monolayers: an efficient step-by-step recipe for high-quality, low energy surfaces," *Surface and Interface Analysis*, vol. 47, pp. 557–564, apr 2015.

[266] J. Barriga, B. Coto, and B. Fernandez, "Molecular dynamics study of optimal packing structure of OTS self-assembled monolayers on SiO2 surfaces," *Tribology International*, vol. 40, pp. 960–966, jun 2007.

[267] R. R. Rye, "Transition temperatures for n-alkyltrichlorosilane monolayers," *Langmuir*, vol. 13, pp. 2588–2590, apr 1997.

[268] S. R. Wasserman, Y. T. Tao, and G. M. Whitesides, "Structure and reactivity of alkylsiloxane monolayers formed by reaction of alkyltrichlorosilanes on silicon substrates," *Langmuir*, vol. 5, pp. 1074–1087, jul 1989.

[269] A. L. Schawlow and C. H. Townes, "Infrared and optical masers," *Physical Review*, vol. 112, pp. 1940–1949, dec 1958.

[270] F. R. Elder, A. M. Gurewitsch, R. V. Langmuir, and H. C. Pollock, "Radiation from electrons in a synchrotron," *Physical Review*, vol. 71, pp. 829–830, jun 1947.

[271] A. Einstein, "Strahlungs-emission und -absorption nach der quantentheorie," *Verh. Deutsch. Phys. Gesell.*, vol. 18, pp. 318–323, 1916.

[272] A. Einstein, "Zur quantentheorie der strahlung," *Phys. Z.*, vol. 18, pp. 121–128, 1917.

[273] T. H. Maiman, "Stimulated optical radiation in ruby," *Nature*, vol. 187, pp. 493–494, aug 1960.

[274] A. Javan, W. R. Bennett, and D. R. Herriott, "Population inversion and continuous optical maser oscillation in a gas discharge containing a he-ne mixture," *Physical Review Letters*, vol. 6, pp. 106–110, feb 1961.

[275] D. A. V. Baak, "Just how bright is a laser?," *The Physics Teacher*, vol. 33, pp. 497–499, nov 1995.

[276] E. M. McMillan, "The synchrotron—a proposed high energy particle accelerator," *Physical Review*, vol. 68, pp. 143–144, sep 1945.

[277] V. I. Veksler, "New method for the acceleration of relativistic particles," *Doklady Akademii Nauk USSR*, vol. 43, no. 8, pp. 346–348, 1944.

[278] H. Motz, "Applications of the radiation from fast electron beams," *Journal of Applied Physics*, vol. 22, pp. 527–535, may 1951.

[279] H. Motz, W. Thon, and R. N. Whitehurst, "Experiments on radiation by fast electron beams," *Journal of Applied Physics*, vol. 24, pp. 826–833, jul 1953.

[280] N. Bohr and J. A. Wheeler, "The mechanism of nuclear fission," *Physical Review*, vol. 56, pp. 426–450, sep 1939.

[281] B. Rossi, "Über die eigenschaften der durchdringenden korpuskularstrahlung im meeresniveau," *Zeitschrift für Physik*, vol. 82, pp. 151–178, mar 1933.

[282] G. T. Seaborg, *The interactions of fast neutrons with lead.* PhD thesis, University of California, Berkley, 1937.

[283] A. Taylor, M. Dunne, S. Bennington, S. Ansell, I. Gardner, P. Norreys, T. Broome, D. Findlay, and R. Nelmes, "A route to the brightest possible neutron source?," *Science*, vol. 315, pp. 1092–1095, feb 2007.

[284] H. Becquerel, "Sur les radiations invisibles émises par les corps phosphorescents," *Comptes rendus hebdomadaires des séances de l'Académie des science*, vol. 122, pp. 501–503, 1896.

[285] H. Becquerel, "Sur les radiations émises par phosphorescence," *Comptes rendus hebdomadaires des séances de l'Académie des science*, vol. 122, pp. 420–421, 1896.

[286] M. S. Curie, "Rayons émis par les composÃ©s de l'uranium et du thorium," *Comptes rendus hebdomadaires des séances de l'Académie des sciences*, vol. 126, pp. 1101–1103, 1898.

[287] P. Curie and M. S. Curie, "Sur la radio-activité provoquÃ©e par les rayons de becquerel," *Comptes rendus hebdomadaires des séances de l'Académie des sciences*, vol. 129, pp. 714–716, 1899.

[288] P. Curie and M. S. Curie, "Sur les corps radioactifs," *Comptes rendus hebdomadaires des séances de l'Académie des sciences*, vol. 134, pp. 85–87, 1902.

[289] K. H. Beckurts and K. Wirtz, *Neutron Physics.* Springer Berlin Heidelberg, 1964.

[290] E. Fermi, "Radioactivity induced by neutron bombardment," *Nature*, vol. 133, pp. 757–757, may 1934.

[291] E. Fermi, E. Amaldi, O. D'Agostino, F. Rasetti, and E. Segrè, "Artificial radioactivity produced by neutron bombardment," *Proceedings of the Royal Society of London. Series A, Containing Papers of a Mathematical and Physical Character*, vol. 146, pp. 483–500, sep 1934.

[292] O. R. Frisch, "Physical evidence for the division of heavy nuclei under neutron bombardment," *Nature*, vol. 143, pp. 276–276, feb 1939.

[293] O. Hahn and F. Strassmann, "Über die entstehung von radiumisotopen aus uran durch bestrahlen mit schnellen und verlangsamten neutronen," *Die Naturwissenschaften*, vol. 26, pp. 755–756, nov 1938.

[294] O. Hahn and F. Strassmann, "Über den nachweis und das verhalten der bei der bestrahlung des urans mittels neutronen entstehenden erdalkalimetalle," *Die Naturwissenschaften*, vol. 27, pp. 11–15, jan 1939.

[295] O. Hahn and F. Strassmann, "Nachweis der entstehung aktiver bariumisotope aus uran und thorium durch neutronenbestrahlung; nachweis weiterer aktiver bruchstücke bei der uranspaltung," *Die Naturwissenschaften*, vol. 27, pp. 89–95, feb 1939.

[296] L. Meitner and O. R. Frisch, "Disintegration of uranium by neutrons: a new type of nuclear reaction," *Nature*, vol. 143, pp. 239–240, feb 1939.

[297] L. Meitner, F. Strassmann, and O. Hahn, "Künstliche umwandlungsprozesse bei bestrahlung des thoriums mit neutronen auftreten isomerer reihen durch abspaltung von α-strahlen," *Zeitschrift für Physik*, vol. 109, pp. 538–552, jul 1938.

[298] U.S. Atomic Energy Commission, *The first reactor*. U.S. Atomic Energy Commission, Division of Technical Information, Oak Ridge, Tennessee, 1967.

[299] J. Erő and J. Szűcs, eds., *Nuclear Structure Study with Neutrons*. Springer US, 1974.

[300] K. A. Petrzhak and G. N. Flerov, "Spontaneous fission of uranium," *Physics-Uspekhi*, vol. 36, pp. 332–336, apr 1993.

[301] D. A. Hicks, J. Ise, and R. V. Pyle, "Multiplicity of neutrons from the spontaneous fission of californium-252," *Physical Review*, vol. 97, pp. 564–565, jan 1955.

[302] D. A. Hicks, J. Ise, and R. V. Pyle, "Spontaneous-fission neutrons of californium-252 and curium-244," *Physical Review*, vol. 98, pp. 1521–1523, jun 1955.

[303] E. Hjalmar, H. Slätis, and S. G. Thompson, "Energy spectrum of neutrons from spontaneous fission of californium-252," *Physical Review*, vol. 100, pp. 1542–1543, dec 1955.

[304] V. Shvetsov, "Neutron sources at the frank laboratory of neutron physics of the joint institute for nuclear research," *Quantum Beam Science*, vol. 1, p. 6, apr 2017.

[305] Malvern Panalyical, "Zetasizer nano zs - user manual," 2020.

[306] Argonne National Laboratory, "anl.gov," 2020. [checked: November 12th 2020].

[307] Argonne National Laboratory, "aps.anl.gov," 2020. [checked: November 12th 2020].

[308] G. S. Knapp, M. A. Beno, and H. You, "Hard x-ray synchrotron radiation applications in materials science," *Annual Review of Materials Science*, vol. 26, pp. 693–725, aug 1996.

[309] S. Seifert, R. Winans, D. Tiede, and P. Thiyagarajan, "Design and performance of a ASAXS instrument at the advanced photon source," *Journal of Applied Crystallography*, vol. 33, pp. 782–784, jun 2000.

[310] Frank Laboratory for Neutron Physics, "flnph.jinr.ru/en/," 2020. [checked: November 14th 2020].

[311] Flerov Laboratory for Nuclear Reactions, "flerovlab.jinr.ru," 2020. [checked: November 14th 2020].

[312] V. Shvetsov, "Pulsed fast reactor IBR-2 after modernization," *Journal of Surface Investigation: X-ray, Synchrotron and Neutron Techniques*, vol. 14, pp. S213–S217, oct 2020.

[313] E. P. Shabalin, V. L. Aksenov, G. G. Komyshev, and A. D. Rogov, "Neptunium-based high-flux pulsed research reactor," *Atomic Energy*, vol. 124, pp. 364–370, oct 2018.

[314] Y. M. Ostanevich, "Time-of-flight small-angle scattering spectrometers on pulsed neutron sources," *Makromolekulare Chemie. Macromolecular Symposia*, vol. 15, pp. 91–103, mar 1988.

[315] A. Kuklin, A. K. Islamov, Y. S. Kovalev, P. Utrobin, and V. Gordely, "Optimization two-detector system small-angle neutron spectrometer yumo for nanoobject investigation," *Journal of Surface Investigation: X-ray, Synchrotron and Neutron Techniques*, vol. 6, pp. 74–83, 2006.

[316] A. I. Kuklin, A. K. Islamov, and V. I. Gordeliy, "Scientific reviews: Two-detector system for small-angle neutron scattering instrument," *Neutron News*, vol. 16, pp. 16–18, jul 2005.

[317] R. A. Campbell, H. P. Wacklin, I. Sutton, R. Cubitt, and G. Fragneto, "FIGARO: The new horizontal neutron reflectometer at the ILL," *The European Physical Journal Plus*, vol. 126, nov 2011.

[318] P. Gutfreund, T. Saerbeck, M. A. Gonzalez, E. Pellegrini, M. Laver, C. Dewhurst, and R. Cubitt, "Towards generalized data reduction on a chopper-based time-of-flight neutron reflectometer," *Journal of Applied Crystallography*, vol. 51, pp. 606–615, apr 2018.

[319] D. E. Koppel, "Analysis of macromolecular polydispersity in intensity correlation spectroscopy: The method of cumulants," *The Journal of Chemical Physics*, vol. 57, pp. 4814–4820, dec 1972.

[320] S. W. Provencher, "A constrained regularization method for inverting data represented by linear algebraic or integral equations," *Computer Physics Communications*, vol. 27, pp. 213–227, sep 1982.

[321] J. C. Thomas, "The determination of log normal particle size distributions by dynamic light scattering," *Journal of Colloid and Interface Science*, vol. 117, pp. 187–192, may 1987.

[322] National Institute for Standards and Technolgy (NIST), "https://webbook.nist.gov/chemistry/fluid/," 2018. [online version from January 17th 2021].

[323] A. G. Soloviev, T. M. Solovjeva, O. I. Ivankov, D. V. Soloviov, A. V. Rogachev, and A. I. Kuklin, "SAS program for two-detector system: seamless curve from both detectors," *Journal of Physics: Conference Series*, vol. 848, p. 012020, may 2017.

[324] N. B. Vargaftik, B. N. Volkov, and L. D. Voljak, "International tables of the surface tension of water," *Journal of Physical and Chemical Reference Data*, vol. 12, pp. 817–820, jul 1983.

[325] D. Richard, M. Ferrand, and G. J. Kearley, "Analysis and visualisation of neutron-scattering data," *Journal of Neutron Research*, vol. 4, pp. 33–39, dec 1996.

[326] J. S. Pedersen, "Structure factors effects in small-angle scattering from block copolymer micelles and star polymers," *The Journal of Chemical Physics*, vol. 114, pp. 2839–2846, feb 2001.

[327] B. Sochor, O. Düdükcü, M. M. Lübtow, B. Schummer, S. Jaksch, and R. Luxenhofer, "Probing the complex loading-dependent structural changes in ultrahigh drug-loaded polymer micelles by small-angle neutron scattering," *Langmuir*, mar 2020.

[328] B. Plazzotta, J. S. Diget, K. Zhu, B. Nyström, and J. S. Pedersen, "Small-angle x-ray scattering as a useful supplementary technique to determine molecular masses of polyelectrolytes in solution," *Journal of Polymer Science Part B: Polymer Physics*, vol. 54, pp. 1913–1917, jun 2016.

[329] S. Manet, A. Lecchi, M. Impéror-Clerc, V. Zholobenko, D. Durand, C. L. P. Oliveira, J. S. Pedersen, I. Grillo, F. Meneau, and C. Rochas, "Structure of micelles of a nonionic block copolymer determined by SANS and SAXS," *The Journal of Physical Chemistry B*, vol. 115, pp. 11318–11329, oct 2011.

[330] C. Kittel, *Introduction to Solid State Physics*. WILEY, 2004.

[331] H. J. Frost and F. Spaepen, "Hard Sphere Models For The Structure Of Grain Boundaries," *Le Journal de Physique Colloques*, vol. 43, pp. C6–73–C6–82, dec 1982.

[332] A. L. Thorneywork, S. K. Schnyder, D. G. A. L. Aarts, J. Horbach, R. Roth, and R. P. A. Dullens, "Structure factors in a two-dimensional binary colloidal hard sphere system," *Molecular Physics*, vol. 116, pp. 3245–3257, jul 2018.

[333] D. J. Kinning and E. L. Thomas, "Hard-sphere interactions between spherical domains in diblock copolymers," *Macromolecules*, vol. 17, pp. 1712–1718, sep 1984.

[334] A. H. Larsen, J. S. Pedersen, and L. Arleth, "Assessment of structure factors for analysis of small-angle scattering data from desired or undesired aggregates," *Journal of Applied Crystallography*, vol. 53, pp. 991–1005, jul 2020.

[335] P. Linse, "Adsorption and phase behaviour of pluronic block copolymers in aqueous solution," *Colloids and Surfaces A: Physicochemical and Engineering Aspects*, vol. 86, pp. 137–142, jul 1994.

[336] M. Walz, S. Gerth, P. Falus, M. Klimczak, T. H. Metzger, and A. Magerl, "Nanoscale structures and dynamics of a boundary liquid layer," *Journal of Physics: Condensed Matter*, vol. 23, p. 324102, jul 2011.

[337] A. R. J. Nelson and S. W. Prescott, "refnx: neutron and x-ray reflectometry analysis in python," *Journal of Applied Crystallography*, vol. 52, pp. 193–200, feb 2019.

[338] A. Nelson, "Co-refinement of multiple-contrast neutron/x-ray reflectivity data using-MOTOFIT," *Journal of Applied Crystallography*, vol. 39, pp. 273–276, mar 2006.